Functionalization of Two-dimensional $Ti_3C_2T_x$ MXene and its Nanocomposites for Application in Catalysis and Optoelectronics

A Thesis Submitted to
Indian Institute of Technology Guwahati
For the Degree of

Doctor of Philosophy

By
KOUSHIK GHOSH

Department of Physics
Indian Institute of Technology Guwahati
Guwahati-781039, India

April 2025

Dedicated to

…..My beloved Family

Department of Physics
Indian Institute of Technology Guwahati
Guwahati-781039, India

STATEMENT

The work contained in the thesis entitled "**Functionalization of Two-dimensional $Ti_3C_2T_x$ MXene and its Nanocomposites for Application in Catalysis and Optoelectronics**" has been carried out by me at Indian Institute of Technology Guwahati under the supervision of **Prof. P. K. Giri**, Professor, Department of Physics, Indian Institute of Technology Guwahati. This work has not been submitted elsewhere for the award of any degree.

Koushik Ghosh

Roll No. - **196121015**

Senior Research Fellow
Department of Physics
Indian Institute of Technology Guwahati
Guwahati-781039, India

Prof. P. K. Giri
Professor
Department of Physics
Indian Institute of Technology Guwahati
Guwahati-781039, India
Phone: ***+91 361 2582703***, Fax: ***+91 361 2690762***
Email: ***giri@iitg.ac.in***

CERTIFICATE

This is to certify that the work contained in the thesis entitled "**Functionalization of Two-dimensional $Ti_3C_2T_x$ MXene and its Nanocomposites for Application in Catalysis and Optoelectronics**" has been carried out by **Mr. Koushik Ghosh** at Indian Institute of Technology Guwahati under my supervision. This work has not been submitted elsewhere for the award of any degree.

Prof. P. K. Giri

Thesis supervisor

Acknowledgment

My PhD journey and the evolution of this thesis would not have been possible without the unwavering support, guidance, and encouragement of many individuals. I would like to take this opportunity to express my sincere gratitude to them.

I would like to express my deepest gratitude to my supervisor, Prof. P. K. Giri, whose guidance and support were instrumental in initiating and shaping my Ph.D. journey. Without his mentorship, this research endeavour would not have been possible. I am sincerely thankful for the opportunity to work under his supervision in his esteemed laboratory. His continuous encouragement, insightful suggestions, spiritual motivation, and unwavering support have enabled me to overcome numerous challenges throughout this journey. His extensive knowledge and technical expertise have been invaluable in strengthening my research foundation, identifying key opportunities in the field, and preparing me for future challenges. I am also thankful for providing me the academic freedom, along with access to essential lab facilities, necessary resources, and moral support throughout my entire Ph.D. journey to achieve my research objectives.

I express my sincere gratitude to my Doctoral Committee members, Prof. A. K. Sharma, Prof. P. K. Padmanabhan, and Prof. Kalyan Raidongia, for their consistent evaluation of my research progress. Their constructive feedback, critical insights, and valuable suggestions have significantly contributed to the refinement and advancement of my work. I also extend my gratitude to the Head of the Department of Physics, the faculty members of the department, as well as the staff of the Central Instruments Facility and the Centre for Nanotechnology for providing a research-friendly environment and access to state-of-the-art research facilities.

A special thanks to the scientific and technical officers, Sujit Kumar Deb, Dr. Sidananda Sarma, Emlin Elsa Abraham, Dr. Kula K. Senapati, Ashim Malakar, Chandan Borgohain, and Madhurjya Borah, whose assistance and support were invaluable in completing my research work. I am also grateful to the Central Workshop of the Department of Mechanical Engineering for fabricating the essential components required for my experimental setup.

I would like to convey my appreciation and thanks to my friends and lab mates for their help and support. I am sincerely grateful to my seniors, Dr. Joydip Ghosh, Dr. Larionette P. L.

Mawlong, Dr. Sumana Paul, Dr. Ruma Das, Dr. Sumaiya Parveen, Dr. Somorjit Singh, Dr. Abhilasha Bora, and Dr. Tarik Hossain, for their guidance and warm gestures. I also extend my thanks to my lab mates Abdul, Ravinder, Tadasha, Sirsendu, Sanju, Subhankar, Sanjoy, Shipra, Debabrata, Sourav, Garima, and Shantanu for their companionship and support. A special thanks to Sanjoy for his continuous help and support throughout my Ph.D. journey.

Last but not least, I extend my heartfelt gratitude for the blessings of my father, Srikrishna Ghosh, and my mother, Chhabi Ghosh, whose support and encouragement have made this journey possible. I am deeply grateful to my wife, Ananya Ghosh, whose presence in my life has been a source of strength. Her unwavering support during difficult times and constant motivation have played a crucial role in helping me navigate challenges and complete this journey. I am also immensely thankful to Pallabi Ghosh (Didi) and Pijush Kanti Ghosh (Dada) for their continuous support and encouragement. Additionally, I feel truly fortunate to have friends like Sarmistha, Alok, Himanshu, Debabrata, and Amalika, who have always stood by me through difficult times.

Koushik Ghosh

IIT Guwahati

Contents

Synopsis

Over the past few decades, two-dimensional (2D) materials have captured immense research interest owing to their exceptional physical, chemical, and electronic properties. Since the revolutionary discovery of graphene, a new landscape of research opportunities has emerged. However, despite its many advantages, graphene's lack of an intrinsic bandgap poses limitations for its use in nanoelectronics applications. This challenge has prompted researchers to investigate other 2D materials with tuneable properties, such as transition metal dichalcogenides, perovskites, black phosphorus, hexagonal boron nitride, and MXenes. Among these, MXenes have gained significant attention due to their unique combination of physical, chemical, and electronic properties, making them highly promising candidates for applications in fields like catalysis, energy storage, electromagnetic interference (EMI) shielding, and electronics. More than 40 types of MXenes have been successfully synthesized experimentally so far, with theoretical studies predicting the existence of many more. These advances underscore the vast potential of MXenes to drive innovations in next-generation technologies across various fields.

MXenes are typically derived from a parent MAX phase, represented by the general formula $M_{n+1}AX_n$, where M represents a transition metal, A is an element from group IIIA or IVA, X denotes carbon (C) and/or nitrogen (N), and n can have a value between 1-3. The layered structure of MXenes is obtained by selectively etching out the "A" element layer from the MAX phase. Additionally, the suffix "ene" in their name signifies their layered nature, which is similar to that of graphene.

Titanium carbide ($Ti_3C_2T_x$) MXene stands out among the various MXene materials due to its exceptional properties, including a large surface area, hydrophilic and negatively charged surface, high metallic conductivity (~10^4 $S.cm^{-1}$), and a tuneable work function. These characteristics make $Ti_3C_2T_x$ highly versatile for applications in energy storage, catalysis, electromagnetic interference (EMI) shielding, and optoelectronics. In addition to these outstanding properties, $Ti_3C_2T_x$ MXene nanosheets face an inherent restacking issue caused by interlayer van der Waal interactions, which significantly diminishes their catalytically active surface area and hinders their performance in various catalytic applications. Addressing this restacking problem remains a significant challenge in $Ti_3C_2T_x$ MXene materials. Furthermore, previous research on $Ti_3C_2T_x$ has concentrated on its use in composite materials, where it acts

as a supportive matrix to enhance overall performance. Recent studies have been directed towards functionalized $Ti_3C_2T_x$ to improve their chemical, physical, and electronic properties. These advancements in $Ti_3C_2T_x$ aim to improve its performance in diverse areas such as wastewater remediation, electrochemical hydrogen production, and optoelectronic device applications, where the functionalized surface and high conductivity offer significant benefits. However, more comprehensive and systematic studies are necessary to bridge the gap between fundamental research and commercial applications. This includes advancement in material functionalization and deepening our understanding of their physical and chemical properties to optimize them for practical use.

In practical applications, $Ti_3C_2T_x$ MXene is commonly synthesized by etching the Al layers followed by exfoliation, using methods such as hydrofluoric (HF) etching, acid/fluoride salt etching, electrochemical etching, and molten salt etching. Among the etching methods, acid/fluoride salt (HCl/LiF) etching is commonly used due to its single-step process. In this method, the in-situ formation of HF selectively etches away the Al layers, while Li ions act as intercalants to produce single-layer or few-layer $Ti_3C_2T_x$ flakes. However, harsh HF etching not only selectively removes Al layers but also creates various defect sites in the $Ti_3C_2T_x$ lattice. Understanding and controlling these intrinsic defects during synthesis is essential for optimizing various catalytic performances. Additionally, to reduce restacking of $Ti_3C_2T_x$ layers due to the strong van der Waals forces between the layers, functionalization strategies, such as heteroatom doping, can offer a potential solution by increasing interlayer spacing and altering surface chemistry. Furthermore, constructing suitable heterostructures with cost-effective metal sulfides, like bismuth sulfide (Bi_2S_3), can provide beneficial band alignment and enhance electronic properties through interfacial charge transfer at the atomically thin heterojunction, supporting high-performance catalytic and optoelectronic device applications. Additionally, transforming $Ti_3C_2T_x$ into 1D nanoribbons significantly increases the exposed surface area and introduces defective edges, which provide numerous active sites for improved catalytic performance. Moreover, nitrogen (N)-doped $Ti_3C_2T_x$ nanoribbons combined with noble metal atomic clusters can further boost photoelectrochemical hydrogen production by enhancing the photothermal effect. Therefore, optimizing the defects/doping in 1D $Ti_3C_2T_x$ can be an effective approach to enhance the optical absorption and catalytic activity for advancing the efficiency of solar light-driven photocatalysts.

This thesis presents a systematic investigation into the synthesis of $Ti_3C_2T_x$ in its multilayer, monolayer, and nanoribbon forms, along with an in-depth analysis of its structural, optical, and

electronic properties. It explores the tunability of intrinsic defects in multilayer $Ti_3C_2T_x$ and addresses the self-stacking tendency in $Ti_3C_2T_x$ nanosheets through heteroatom doping. Additionally, it examines the formation of suitable heterostructures to enhance photochemical and photophysical properties. Finally, the study highlights N-doped $Ti_3C_2T_x$ nanoribbons with exposed defective edges, coupled with Ru atomic clusters, to improve photoelectrochemical performance through the photothermal effect. We believe these studies provide valuable insights into the fundamental properties of $Ti_3C_2T_x$ MXene and their potential applications in multifunctional fields, such as industrial wastewater remediation, photoelectrochemical hydrogen production, and optoelectronic devices. This thesis is organized into seven chapters, which are outlined below:

Chapter 1 presents an overview of the structural, electronic, and optical properties of $Ti_3C_2T_x$ MXene, as well as the synthesis procedures used to obtain them. It discusses their promising applications across various fields, including catalysis and optoelectronics. This chapter also addresses the fundamental challenges faced by pristine $Ti_3C_2T_x$, highlighting its limitations in becoming a next-generation material for real-world applications. Additionally, the recent advancements in functionalized $Ti_3C_2T_x$ nanostructures and $Ti_3C_2T_x$-based hybrids in catalytic wastewater treatment, photoelectrochemical hydrogen production, and broadband photodetection are discussed. This chapter concludes by outlining the motivation for the current work, setting the platform for further exploration and development of $Ti_3C_2T_x$ MXene for catalytic and optoelectronic applications.

Chapter 2 presents the synthesis of accordion-like, multi-layered $Ti_3C_2T_x$ (m-$Ti_3C_2T_x$) MXene and the optimization of low valent Ti states (Ti^{2+}, Ti^{3+}) or oxygen vacancy states (OVs) by controlling the concentration of HF etchant. Morphological and structural analysis confirmed the successful removal of Al layers. Moreover, XPS analysis showed an abundant presence of surface groups (-F, -O, and -OH) on m-$Ti_3C_2T_x$, along with lower-valent Ti states (Ti^{2+} and Ti^{3+}), which can enhance the catalytic degradation of organic pollutants through advanced oxidation processes (AOPs). The catalytic performance of m-$Ti_3C_2T_x$ in the degradation of methylene blue (MB), a cationic dye, was evaluated using a small amount of hydrogen peroxide (H_2O_2) as an oxidizer. MB was used as a model pollutant to evaluate degradation efficiency, with multiple factors influencing the process. The results revealed that m-$Ti_3C_2T_x$ is highly efficient in degrading MB via the Fenton reaction. Furthermore, post-annealing studies highlighted the essential roles of Ti^{2+} and Ti^{3+} species in the degradation process, and their

involvement was explored in detail. These findings indicate that m-$Ti_3C_2T_x$ could be an effective Fenton catalyst for eliminating cationic dyes from industrial wastewater.

Chapter 3 explores the impact of phosphorus (P) doping in $Ti_3C_2T_x$ MXene nanosheets, anchored onto a flexible, porous polyvinyl alcohol (PVA) -coated melamine sponge (PVA@MS) for enhanced performance in wastewater treatment via an advanced oxidation process. The P doping significantly improves the surface area of $Ti_3C_2T_x$ by increasing interlayer spacing and preventing layer restacking. When anchored to the MS, the P-$Ti_3C_2T_x$ forms a robust, flexible 3D architecture of P-$Ti_3C_2T_x$@PVA@MS aerogel that resolves the recollection issues associated with thin nanosheets during repeated cycles. The study delves into how P doping enhances the catalytic degradation rate of organic pollutants, such as the ciprofloxacin (CIP) antibiotic and methylene blue (MB) dye, examining the degradation mechanisms in detail. Density Functional Theory (DFT) simulations provide insight into the electronic density of states in P-$Ti_3C_2T_x$ and elucidate the role of phosphorus atoms in facilitating the improved degradation performance. This chapter highlights the advantages of P-doped-$Ti_3C_2T_x$/PVA@MS based aerogel in the degradation of organic pollutants for wastewater treatment through an advanced oxidation process.

Chapter 4 presents the synergistic effects and the interfacial charge transfer dynamics in Bi_2S_3@$Ti_3C_2T_x$ composite, which exhibits outstanding catalytic activity for the reduction of 4-nitrophenol and organic pollutants in the presence of $NaBH_4$, as well as for photoelectrochemical hydrogen production in alkaline media. In this composite, $Ti_3C_2T_x$ nanosheet reduces the agglomeration of Bi_2S_3 nanorods by immobilizing the Bi^{3+} ions on the negatively charged surface groups (-F, -O and -OH). Interestingly, fewer Bi^{3+} are reduced to metallic Bi nanoparticles, attributed to the self-reduction capability of $Ti_3C_2T_x$ MXene, which is also supported by DFT calculation. We investigate the catalytic reduction capability of the composite over various organic pollutants such as 4-nitrophenol (4-NP), Methylene blue (MB), Methyl orange (MO), and Rhodamine B (RhB) in the presence of $NaBH_4$, which demonstrates an outstanding reduction rate (up to 1.1 min^{-1}) of 4-NP with long cyclic stability. The reduction mechanism, role of Bi nanoparticles, and effective charge transfer were further supported by DFT analysis. Moreover, excellent light-harvesting capacity, reduced recombination of photogenerated charge carriers, and photothermal effects contribute to an enhanced rate of photoelectrochemical hydrogen production, achieving an overpotential of 73 mV and a Tafel slope of 85 mV/dec under visible light irradiation. This study provides valuable insights into the self-reduction capability of $Ti_3C_2T_x$ MXene and highlights the potential of the

Bi_2S_3@$Ti_3C_2T_x$ composite as a highly effective catalyst for wastewater treatment and sustainable hydrogen production.

Chapter 5 presents the development of N-doped, ultra-small Ru nano cluster (NC) -anchored onto 1D $Ti_3C_2T_x$ MXene nanoribbons for efficient photoelectrochemical hydrogen production in an alkaline medium. The high aspect ratio exposed oxygen vacancy (OV) sites of the N-doped $Ti_3C_2T_x$ MXene nanoribbons significantly reduce the aggregation of Ru NCs and provide strong electron-metal interaction for efficient electrochemical hydrogen production. The OV states and in-situ formation of TiO_2 nanoparticles (TiO_2 NPs) during 1D nano structuring and N doping enhances UV-Vis light absorption, improving photocatalytic efficiency. Electrochemical studies demonstrate the exceptional hydrogen evolution reaction (HER) performance of 5% Ru@N-MXNR under both dark and illuminated conditions, with low overpotentials of 22 mV and 12 mV and Tafel slopes of 50 mV/dec and 34 mV/dec, respectively, which is superior than commercial 20% Pt/C catalyst, which exhibits an overpotential of ~23 mV and a Tafel slope of 42 mV/dec. Furthermore, under Vis-NIR illumination, enhanced charge carrier generation by TiO_2 and photothermal effects improve electron mobility, further boosting HER efficiency. Additionally, these catalysts offer prolonged operational stability by maintaining a consistent current density, which is beneficial for stable hydrogen production. This study highlights the progress of $Ti_3C_2T_x$ MXene nanoribbon-based composite for sustainable hydrogen production.

Chapter 6 highlights the role of $Ti_3C_2T_x$ MXenes in optoelectronic device applications, focusing on the Bi_2S_3@$Ti_3C_2T_x$ composite due to their excellent broadband light absorption (UV-Vis-NIR), efficient photogenerated charge carrier separation. We fabricated a Schottky junction photodetector by spin-casting the Bi_2S_3@$Ti_3C_2T_x$ (BSMX4) composite onto an Au interdigitated electrode (IDE) pattern with an alumina base. This low-cost photodetector demonstrated impressive broadband responsivity across the ultraviolet to near-infrared range (300-1550 nm), achieving peak responsivities of 36.7 A/W at 300 nm and 26.2 A/W at 780 nm. Additionally, the device achieved an external quantum efficiency of approximately 3.9×10^3 % and a fast response time of around 300 μs under a 3 V bias in ambient conditions. The mechanism behind this high performance and the formation of the local Schottky junction was investigated using DFT calculations and verified through various microscopic and spectroscopic techniques. This work provides valuable insights into superior charge transport and ultra-broadband photodetection in MXene-based composites, advancing their potential for high-performance optoelectronic applications.

Chapter 7 provides a summary of the research conducted, highlighting the key contributions to the study of $Ti_3C_2T_x$ MXene, its properties, and its potential applications in catalysis and optoelectronics. It concludes by discussing the future directions for research on functionalized $Ti_3C_2T_x$, along with other MXene materials, focusing on their applications in environmental remediation, energy solutions, and broadband optoelectronics.

List of abbreviations

Abbreviation	Description
1D	One-dimensional
2D	Two-dimensional
3D	Three-dimensional
EDS	Energy Dispersive X-ray Spectroscopy
ESR	Electron Spin Resonance
FESEM	Field Emission Scanning Electron Microscopy
FETEM	Field Emission Transmission Electron Microscopy
FWHM	Full Width at Half Maxima
HER	Hydrogen Evolution Reaction
HRTEM	High Resolution Transmission Electron Microscopy
NC	Nanocrystal
NFCs	Nanofibers
NIR	Near Infrared
OV	Oxygen vacancy
PEC	Photoelectrochemical
PL	Photoluminescence
RHE	Reversible Hydrogen Electrode
LSPR	Localized Surface Plasmon Resonance
TEM	Transmission Electron Microscopy
UV-Vis	Ultraviolet Visible
XPS	X-ray Photoelectron Spectroscopy
UPS	Ultraviolet photoelectron spectroscopy

XRD	X-ray Diffraction
4-NP	4-nitrophenol
4-AP	4-aminophenol
SCFs	Supercritical fluids
AOPs	Advanced oxidation processes
MB	Methylene blue
CIP	Ciprofloxacin
RhB	Rhodamine B
CV	Crystal violet
MO	Methyl orange
BE	Binding energy
HF	Hydrofluoric acid
PMS	Peroxymonosulfate
MS	Melamine sponge
PVA	Polyvinyl alcohol
VASP	Vienna Ab Initio Simulation Package
GGA	Generalized gradient approximation
BET	Brunauer-Emmett-Teller
LSV	Linear sweep voltammetry
CV	Cyclic voltammetry
ECSA	Electrochemically active surface area
EIS	Electrochemical impedance spectroscopy
DFT	Density functional theory
DOS	Density of states
TDOS	Total density of states
PDOS	Partial density of states
PD	Photodetector

Chapter 1

Introduction

Two-dimensional (2D) materials have garnered significant attention in recent years as a unique class of functional materials owing to their extraordinary physical and chemical properties, which are fundamentally distinct from those of their bulk counterparts[1-3]. Graphene, a single layer of carbon atoms arranged in a honeycomb lattice, has been extensively studied due to its exceptional properties, including high electrical conductivity, outstanding mechanical strength, and remarkable optical properties[4-6]. These distinctive characteristics make graphene a highly promising material for diverse applications, such as catalysis, energy storage, and optoelectronic devices. The remarkable success of graphene has consequently driven extensive research into other 2D materials with tuneable properties, such as transition metal dichalcogenides (TMDs), perovskites, black phosphorus, hexagonal boron nitride, and MXenes. Notably, MXenes[7-9] have emerged as a particularly intriguing class of 2D materials due to their unique combination of electronic, chemical, and mechanical properties, making them attractive for a wide range of applications.

Since their discovery in 2011, MXenes have rapidly gained attention as a growing field of research, with applications spanning energy storage[10-12], catalysis[13, 14], electromagnetic interference (EMI) shielding[15, 16], electronics[17, 18], biomedicine[19, 20], etc. Their rising significance can be attributed to their distinctive properties, including high electrical conductivity, hydrophilicity, large surface-to-volume ratio, tuneable work function, biocompatibility, and excellent mechanical strength. MXenes belong to the family of 2D transition metal carbides, nitrides, and/or carbonitrides, which are synthesized primarily through the selective etching of MAX phase ceramics. The MAX phases are layered hexagonal materials with the general formula $M_{n+1}AX_n$, where n ranges from 1 to 4. In this structure, M represents an early transition metal, A corresponds to an element from groups IIIA to VA, and X denotes carbon and/or nitrogen. The M-A bonds in MAX phases exhibit greater chemical reactivity and are more prone to selective cleavage than the mixed covalent or ionic M-X bonds. Through appropriate etching methods, the M-A bonds are selectively broken, resulting in the formation of loosely stacked MXene layers. The final composition of MXenes is commonly represented as $M_{n+1}X_nT_x$, where T_x indicates surface functional groups such as -F, -OH, and -O, introduced based on the choice of etching agents and synthesis conditions. To date, more

than 40 MXene structures have been successfully synthesized, while theoretical predictions suggest the possibility of over 100 different MXene compositions[21, 22].

Among the diverse members of the MXene family, $Ti_3C_2T_x$ is one of the earliest discovered and most extensively investigated materials. Its structure consists of alternating Ti and C layers. After exfoliation from its MAX phase precursor, the surface of $Ti_3C_2T_x$ becomes functionalized with termination groups such as -OH, -O, and -F. With advancements in both experimental and theoretical studies, $Ti_3C_2T_x$ MXene has become a prominent focus of research due to its unique physicochemical properties. A significant advantage of $Ti_3C_2T_x$ lies in its relatively simple and cost-effective synthesis, which enhances its feasibility for commercial applications. Furthermore, $Ti_3C_2T_x$ can be engineered into various structural configurations, including multilayered accordion-like architectures, lamellar nanosheets, nanoribbons, and quantum dots, thereby broadening its applicability across diverse technological fields. Additionally, its electronic band structure and physicochemical properties can be tailored through surface functionalization. Notably, the incorporation of local defects in $Ti_3C_2T_x$ plays a crucial role in the development of MXene-based catalyst materials. Despite the presence of surface terminations and defects, $Ti_3C_2T_x$ exhibits outstanding electrical conductivity, reinforcing its potential for applications in catalysis, energy storage, EMI shielding, and electronic technologies.

1.1. Structure of $Ti_3C_2T_x$ MXene

Structurally, $Ti_3C_2T_x$ MXene exhibits a hexagonal symmetry and belongs to the $P6_3/mmc$ space group[1]. Its atomic structure consists of alternating three Ti and two C layers, predominantly

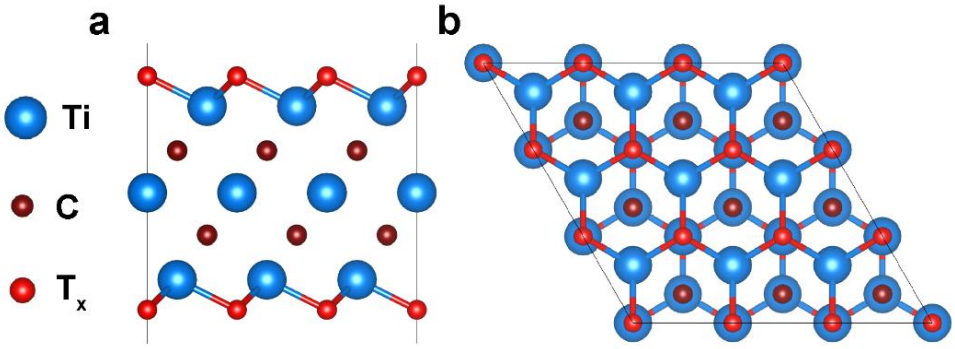

Fig. 1.1. A schematic illustration of the crystal structure of monolayer $Ti_3C_2T_x$ (T_x = -F, -O, and -OH) (a) front view and (b) top view.

connected through ionic bonding, forming the primary structural framework as shown in **Fig. 1.1**. The top-down etching process introduces surface terminations that chemically bond to the

exposed Ti atoms, resulting in a random distribution of functional groups[23]. The most common terminal groups include -O, -F, and -OH. Over time, -F groups are gradually substituted by -O groups[23] when exposed to air. The physicochemical properties of $Ti_3C_2T_x$ MXene are significantly influenced by both the composition and spatial distribution of these surface functional groups [24-27].

1.2. Properties of $Ti_3C_2T_x$ MXenes

1.2.1. Electronic Properties

The properties of $Ti_3C_2T_x$ MXenes are significantly influenced by their surface terminations and lateral size[28]. According to density functional theory (DFT) calculations, the electronic structure of $Ti_3C_2T_x$ MXenes is highly sensitive to surface terminations (**Fig. 1.2(a)**). Specifically, the introduction of -F and -OH groups convert the metallic Ti_3C_2 structure into narrow bandgap semiconductors, with bandgaps of 0.05 and 0.1 eV, respectively[1]. This alteration reduces the carrier density and, consequently, the conductivity[28]. Additionally, it has been reported that the electrical properties of $Ti_3C_2(OH)_2$ and $Ti_3C_2F_2$ monolayers exhibit a dependence on the spatial arrangement of the -OH and -F groups on the $Ti_3C_2T_x$ MXene surface, leading to either narrow bandgap semiconductors or metallic behavior[24]. Recent studies further emphasize that the electronic properties of MXenes can be modulated by optimizing their surface terminations.

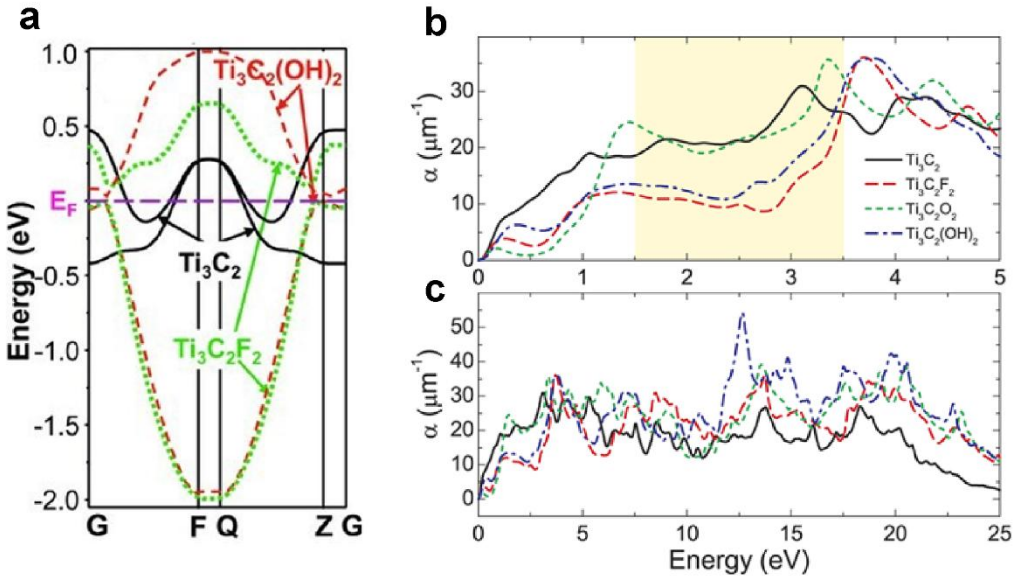

Fig. 1.2. The DFT simulations of pristine Ti_3C_2 and functionalized $Ti_3C_2T_x$ (T_x = -O, -F, and -OH) monolayers: (a) the electronic band structure. Adopted from ref. [1], (b) the absorption coefficient within a lower photon energy range (highlighted area shows visible region), and (c) its variation over a broader photon energy. Adopted from ref. [30].

Further, depending on the surface compositions, the work function of $Ti_3C_2T_x$ can be

modulated in the range of 3.9 to 4.8 eV by annealing at varying temperatures under an inert atmosphere[29]. This tunability is particularly advantageous for the development of heterostructures with compatible semiconducting materials.

1.2.2. Optical Properties

Berdiyorov et al.[30] investigated the absorption coefficient of pristine Ti_3C_2 and functionalized $Ti_3C_2T_x$ MXenes using DFT calculations. The peaks observed in the absorption spectrum (**Fig. 1.2(b-c)**) arise from both intra-band and inter-band transitions. Notably, the absorption spectrum undergoes significant changes upon surface functionalization. For instance, in -F and -OH-terminated $Ti_3C_2T_x$ samples, the absorption decreases considerably for photon energies below 3.5 eV. In contrast, -O termination leads to enhanced absorption in the visible range. A prominent absorption peak is observed at 1.4 eV for $Ti_3C_2O_2$, which is less pronounced in other functionalized samples. This distinct feature in the optical spectrum of $Ti_3C_2O_2$ can be attributed to the significant contribution of O atoms to the total density of states (DOS) near the Fermi energy. At higher photon energies (E > 5 eV), surface functionalization results in stronger absorption compared to pristine Ti_3C_2. These findings affirm that the absorption characteristics of Ti_3C_2 MXene are highly sensitive to surface terminations. Additionally, research shows that $Ti_3C_2T_x$ MXene films exhibit excellent light absorption in the UV-visible region, specifically within the 300-500 nm range[31]. A $Ti_3C_2T_x$ MXene film with a thickness of ~5 nm showed a transmittance of up to 91.2%, making it highly suitable for transparent electrode applications[31] . Additionally, depending on the film thickness, a strong and broad absorption band may appear around 700-800 nm, which is attributed to the surface plasmon resonance effect[31]. This characteristic is particularly significant for photothermal therapy applications[32].

1.2.3. Magnetic Properties

First-principles calculations have revealed that specific defective Ti-based MXenes display magnetic behaviour due to the presence of unpaired electrons in the d-orbitals[33]. Scheibe et al.[34] investigated the magnetic characteristics of $Ti_3C_2T_x$ MXenes modified with SO_3H and S_2 functional groups through chloro-sulfonic acid treatment. Similarly, Zhang et al.[35] explored the magnetic properties of $Ti_3C_2T_x$ MXenes and examined the effects of H_2 annealing, reporting a significant enhancement in magnetic saturation following the annealing process. The magnetic properties of $Ti_3C_2T_x$ MXenes can be tailored by modifying the transition metal composition, surface terminations, and synthesis or etching conditions[36].

1.2.4. Catalytic Properties

The surface functional groups of $Ti_3C_2T_x$ MXene, including -O, -F, and -OH, provide numerous anchoring sites for base catalysts, facilitating the formation of efficient heterojunctions by reducing agglomeration and enhancing catalytic performance[23]. Additionally, the presence of a significant number of exposed metal sites and defective surface states offers active sites for improved catalytic reactions. The surface chemical state of $Ti_3C_2T_x$ MXenes plays a crucial role in modulating their physical properties. Notably, the replacement of -F with -O groups on the surface has been shown to improve the electrochemical performance of the material[37].

Owing to these exceptional properties, $Ti_3C_2T_x$ MXenes have been extensively investigated for their potential in catalytic and optoelectronic applications, which are elaborated further in **section 1.5.**

1.3. Synthesis Strategy of $Ti_3C_2T_x$ MXenes

The synthesis of $Ti_3C_2T_x$ MXene is predominantly carried out through a top-down approach. This technique involves the selective etching of the MAX phase precursor, Ti_3AlC_2, followed by intercalation and sonication to obtain $Ti_3C_2T_x$ MXene nanosheets. The top-down approach offers several benefits, such as precise control over the composition, structure, and morphology of the resulting MXene materials. The removal of the A-layer from the MAX phase facilitates the creation of MXenes with large surface areas, tunable surface chemistry, and inherent metallic conductivity. Furthermore, this method is scalable, making it suitable for large-scale production, and does not require complex fabrication processes or expensive starting materials. Over time, the top-down approach has evolved with the development of various etching techniques, enabling the production of $Ti_3C_2T_x$ MXenes with enhanced purity and precise stoichiometric control. The use of these etching strategies has significantly improved the performance of $Ti_3C_2T_x$ MXenes, broadening their application in catalysis and optoelectronics. A detailed overview of these etching techniques is provided below.

1.3.1. Hydrofluoric (HF) Acid Etching

The synthesis of $Ti_3C_2T_x$ MXenes using HF etching involves three key steps: (1) the selective removal of the Al layer from the Ti_3AlC_2 MAX phase, (2) intercalation, and (3) exfoliation. Unlike other two-dimensional materials such as graphene, $Ti_3C_2T_x$ MXenes cannot be mechanically exfoliated and thus require chemical methods for effective delamination. In 2011, Naguib et al[1]. employed a 50 wt% concentrated HF solution to selectively etch the Al layer from the Ti_3AlC_2 MAX phase. This HF treatment effectively removes Al atoms, thereby

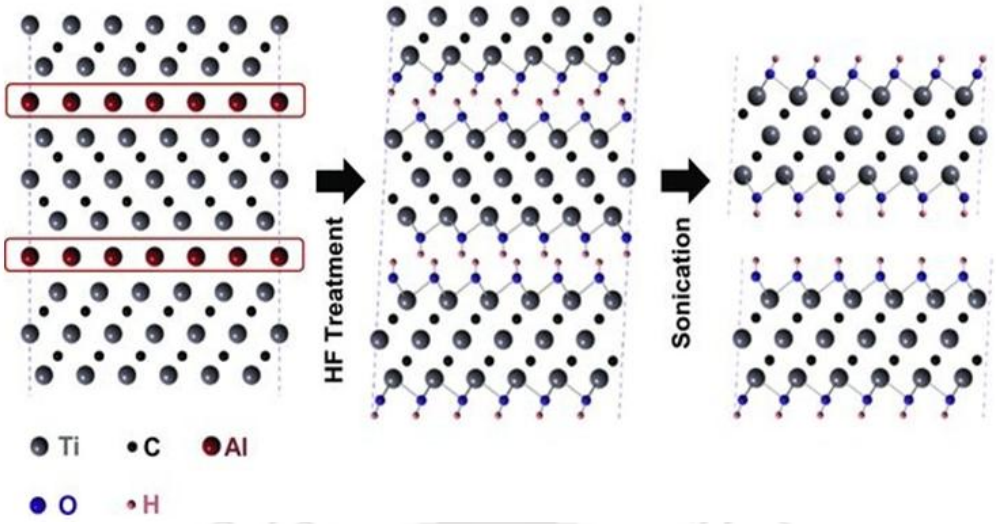

Fig. 1.3. Schematic of the synthesis of $Ti_3C_2T_x$ MXenes via the HF etching method. Adapted from ref. [1].

disrupting these bonds and allowing the Ti_3C_2 layers to separate (**Fig. 1.3**). Furthermore, the abundance of -OH, -O, and -F ions in the etching medium facilitates the attachment of these functional groups onto the MXene surfaces. The etching process of Ti_3AlC_2 in HF can be represented by the following reactions:

$$Ti_3AlC_2 + 3HF \rightarrow Ti_3C_2 + AlF_3 + \frac{3}{2}H_2 \qquad (1)$$

$$Ti_3C_2 + 2H_2O \rightarrow Ti_3C_2(OH)_2 + H_2 \qquad (2)$$

$$Ti_3C_2 + 2HF \rightarrow Ti_3C_2F_2 + H_2 \qquad (3)$$

During this process, HF interacts with the Al atoms in Ti_3AlC_2 and etch them from the structure. After that, the resultant mixture is centrifuged and washed with distilled water (DI) until the pH reaches ~6. The product was subsequently freeze-dried to obtain $Ti_3C_2T_x$, where the surfaces are functionalized with -OH, -O, and/or -F groups. The process is further continued by employing intercalation and delamination agents such as dimethyl sulfoxide (DMSO) and tetramethylammonium hydroxide (TMAOH) to obtain $Ti_3C_2T_x$ nanosheets.

1.3.2. LiF/HCl Etching

The synthesis of layered $Ti_3C_2T_x$ MXene through HF etching has been the most widely used and effective method. However, due to the corrosive nature of HF and the potential risks it poses, such as eye, skin, and respiratory irritation, there is a need to investigate safer alternative techniques. One promising approach is in-situ HF etching. In this context, Ghidiu et al[38]. developed a novel high-yield method that utilizes a LiF/HCl system for the in-situ production of $Ti_3C_2T_x$ MXene sheets. In this procedure, $Ti_3C_2T_x$ is synthesized by adding Ti_3AlC_2 powders

(3 gm) to a mixture of LiF (5 M) and HCl (6M, 30 ml), followed by heating the solution at 40 °C for 45 h. The mixture is then washed with DI water to remove by-products and adjust the pH to ~6 (**Fig. 1.4)**. This LiF/HCl-based etching approach results in $Ti_3C_2T_x$ exhibiting increased interlayer spacing and enlarged surface area. These mild etching conditions

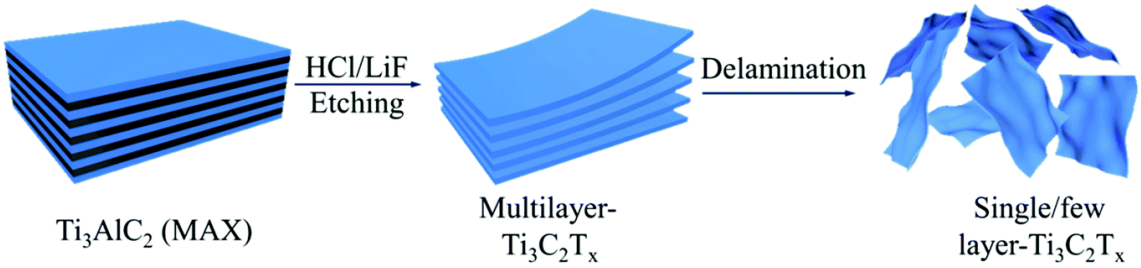

Fig. 1.4. Schematic of the synthesis of $Ti_3C_2T_x$ MXenes via the LiF/HCl etching method. Adapted from ref. [39]

associated with the LiF/HCl system, compared to pure HF, reduce the formation of surface defects in the final product. Consequently, the LiF/HCl method produces $Ti_3C_2T_x$ with superior surface characteristics, conductivity[39], and enhanced mechanical stability, making this one-step etching process a promising avenue for future research.

1.3.3. Electrochemical Etching

Electrochemical etching is a well-known top-down strategy for the synthesis of MXene materials. In this approach, an electrochemical cell is configured such that the precursor material serves as the anode, while an appropriate counter electrode acts as the cathode. The precursor is immersed in an electrolyte solution, which facilitates ion transport. When a voltage is applied between the electrodes, electrochemical reactions occur at the surface of the precursor, prompting the migration of ions from the anode to the cathode. By fine-tuning the parameters, such as the applied potential and the electrolyte composition, it is possible to selectively remove specific atomic layers while preserving the overall structural integrity of the MXene.

For example, Chen et al.[40] demonstrated the successful synthesis of $Ti_3C_2T_x$ MXene via electrochemical etching (**Fig. 1.5**). Their procedure began with cutting Ti_3AlC_2 blocks into smaller segments, followed by thorough rinsing with DI water. In a two-electrode system, the Ti_3AlC_2 pieces acted simultaneously as both the anode and the cathode while being immersed in an electrolyte containing 0.8 M LiOH and 1.0 M LiCl. The etching process was carried out under constant stirring at a fixed potential of 5.5 V for 5 h. After etching, centrifugation produced a three-layer black sediment. The topmost layer was collected initially, whereas the intermediate layer underwent additional washing and centrifugation before being freeze-dried

to obtain the final electrochemically etched $Ti_3C_2T_x$ flakes.

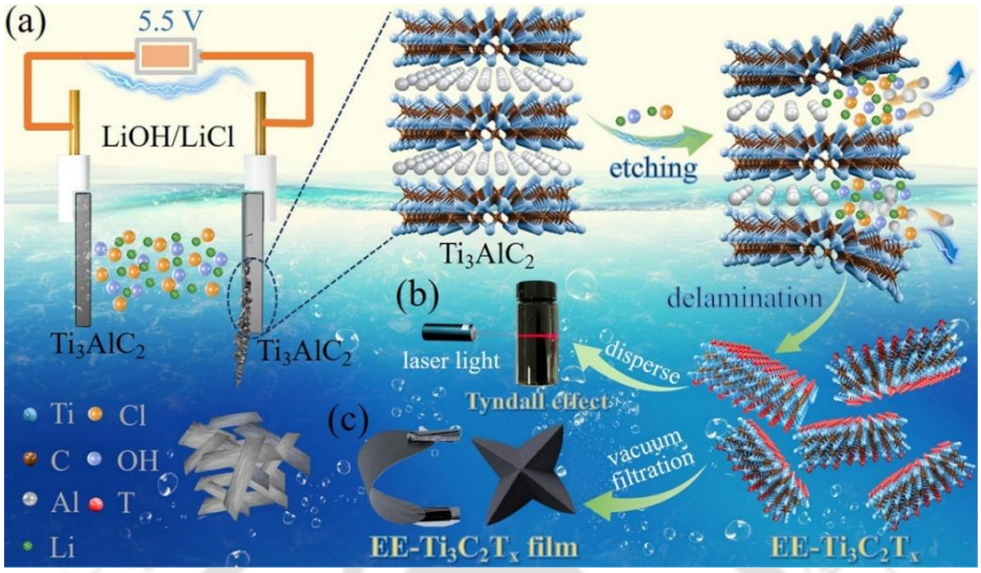

Fig. 1.5. (a) Schematic representation of the synthesis process of $Ti_3C_2T_x$ MXene through Electrochemical Etching (EE-$Ti_3C_2T_x$). (b) The accompanying photograph illustrates the dispersion of EE-$Ti_3C_2T_x$ and the observed Tyndall effect. (c) Illustration of the EE-$Ti_3C_2T_x$ film. Adopted from the ref. [40].

1.3.4. Molten Salt Etching

Molten salt etching has emerged as an efficient approach for the synthesis of MXenes, utilizing liquid salts as the reactive medium. However, a key limitation is that MXenes produced via molten salt etching are generally not dispersible in aqueous media, thereby limiting their application in water-based systems such as inks and coatings.

Li et al. demonstrated the synthesis of $Ti_3C_2T_x$ MXene through a two-step process. Initially, Al in the MAX phase was substituted with Zn, and subsequently, the Zn was removed through a reaction between Ti_3AlC_2 and $ZnCl_2$ at 550 °C [41, 42]. Further, Liu et al.[43] reported advanced molten salt synthesis by mixing Ti_3AlC_2 with molten salts in a molar ratio of 1: 3: 2: 2 (Ti_3AlC_2: $CuCl_2$: NaCl: KCl). The precursor mixture was ground for 10 min and then subjected to thermal treatment at 680 °C with a controlled heating ramp of 4 °C/min over 24 h in an Ar atmosphere. During this thermal process, $CuCl_2$, along with the NaCl/KCl mixture, facilitated the oxidation of Al in Ti_3AlC_2 to form Al^{3+} ions, while in-situ reducing Cu^{2+} ions on the $Ti_3C_2T_x$ MXene surface. The Cu^{2+} ions react with Ti atoms to produce metallic Cu, while Cl ions combine with the Ti_3C_2 structure to form $Ti_3C_2Cl_2$. The obtained $Ti_3C_2Cl_2$ MXene was subjected to treatment with ammonium persulfate to eliminate Cu particles and incorporate -O surface groups, thereby forming MS-$Ti_3C_2T_x$ MXene. Conventional delamination using DMSO becomes ineffective, resulting in the formation of thick, multilayer MXene flakes. However, exfoliation was successfully achieved by treating the material with tetrabutylammonium hydroxide (TBAOH)

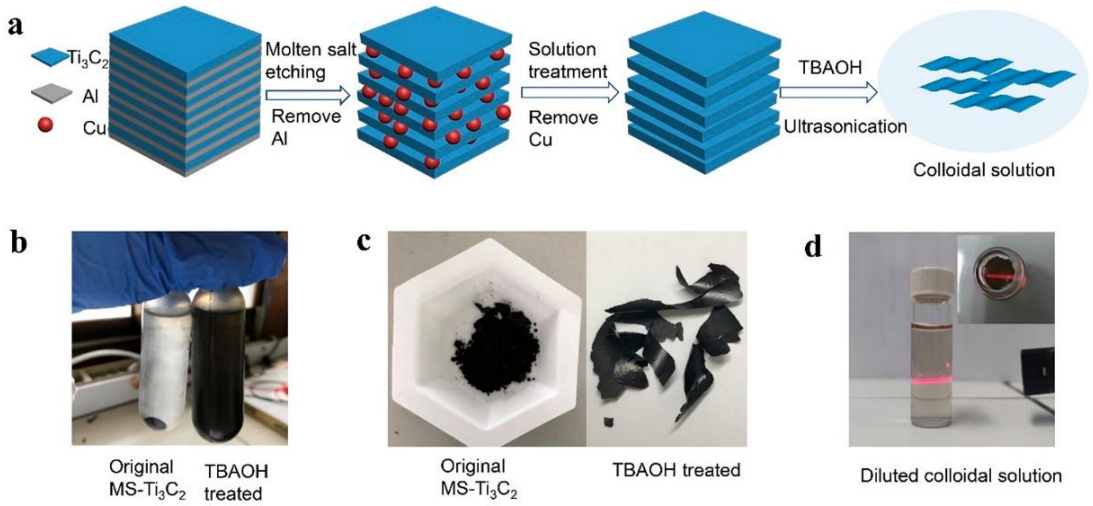

Fig. 1.6. Schematic representations of the synthesis and exfoliation of MXene via the Lewis acidic etching approach. Images of pristine MS-$Ti_3C_2T_x$ before (left) and after (right) treatment with TBAOH following (b) centrifugation at 3500 rpm for 30 min and (c) subsequent collection through filtration. (d) Illustration of the Tyndall effect observed in MS-$Ti_3C_2T_x$ nanoflakes. Adopted from the ref. [43]

and applying sonication, followed by centrifugation to remove residual sediment. The schematic representation of the synthesis process is illustrated in **Fig. 1.6**.

The conventional etching method using HF and LiF/HCl poses significant environmental hazards and is not suitable for large-scale industrial applications due to safety concerns. While alternative approaches such as electrochemical etching and molten salt etching offer more environmentally friendly routes for $Ti_3C_2T_x$ MXene synthesis, they suffer from limitations, such as lower yield and poor dispersion, particularly in the case of molten salt etching. These challenges hinder their viability for large-scale production. Therefore, the development of an environmentally sustainable, cost-effective, and scalable synthesis strategy is necessary to enable the industrial application of $Ti_3C_2T_x$ MXene.

1.3.5. Other Etching Methods

The alkali etching method uses alkaline solutions, such as sodium hydroxide (NaOH) or potassium hydroxide (KOH), to selectively etch the MAX phase. Li et al.[44] demonstrated the successful synthesis of $Ti_3C_2T_x$ MXene with a purity of 92wt% using an alkali-assisted hydrothermal method. In this approach, the Ti_3AlC_2 MAX phase was exposed to an aqueous NaOH solution under hydrothermal conditions, with an Ar atmosphere maintained to prevent oxidation. Compared to HF etching, alkali etching offers a safer alternative while also enabling the tailoring of MXene surface chemistry and improving its environmental stability.

Supercritical fluids (SCFs) are widely employed for the intercalation and delamination of densely packed layered materials, such as graphite and clay, due to their high efficiency and

yield. Their ability to diffuse between layers, coupled with enhanced shear forces, enables rapid exfoliation while preserving the structural integrity of the material. This approach supports the large-scale production of few-layer, defect-free nanomaterials. N. Chen et al.[45] have developed a supercritical etching technique for the synthesis of $Ti_3C_2T_x$ MXene, achieving a remarkable yield of ~ 1 kg within 4 h. This method improves the penetration of HF, which is generated in situ from ammonium bifluoride (NH_4HF_2), into the MAX phase while simultaneously ensuring the efficient removal of by-products. The SCF-based strategy demonstrates significant potential for the scalable and rapid synthesis of high-quality MXenes.

1.4. Functionalization and $Ti_3C_2T_x$ MXene-based Composite Formation

Since the discovery of $Ti_3C_2T_x$ MXenes, it has attracted considerable interest due to their exceptional surface properties. In contrast to other 2D materials, where catalytic activity is predominantly localized at the edge sites, MXenes possess active sites distributed across their basal planes. Their combination of high electrical conductivity and intrinsic hydrophilicity makes them highly promising for catalytic applications. However, despite surface functionalization, pristine $Ti_3C_2T_x$ MXenes exhibit lower catalytic efficiency compared to transition metal-based electrocatalysts. This limitation arises primarily from their inherently low activity in hydrogen evolution reactions (HER) and advanced oxidation processes (AOPs). The low catalytic performance is largely attributed to a limited number of active sites and non-ideal adsorption energy, which hinder their overall reactivity in these processes.

Despite their promising potential, $Ti_3C_2T_x$ MXenes encounter several challenges, including limited mechanical flexibility, a tendency to undergo stacking, and instability in oxygen-rich environments. These factors hinder the development of pure $Ti_3C_2T_x$ MXene-based materials for catalytic applications. To improve their catalytic activity, two primary strategies, 1. heteroatom doping and 2. composite formation, have been extensively explored. Heteroatom doping has emerged as a highly effective approach for improving MXene-based catalysts by tailoring their chemical composition, surface characteristics, and electronic structure. This doping process can be classified into three main approaches based on the site of incorporation and the corresponding mechanistic effects. The first approach, surface adsorption, involves the attachment of heteroatoms onto the exposed surfaces of MXene sheets through either non-covalent interactions or direct chemical bonding. The second method, functional substitution, entails replacing surface termination groups such as -O, -OH and -F with alternative functional moieties containing the dopant element. Heteroatom doping provides multiple advantages,

including (i) enhanced electrical conductivity and the transformation of inert regions into catalytically active sites, (ii) modulation of the Fermi energy level, and (iii) reduction of nanosheet restacking by introducing surface functional groups or chemical bonds. A more intricate approach, lattice substitution, involves the direct incorporation of heteroatoms into the MXene crystal lattice by replacing either the metal or carbon atoms. This substitution, which can occur through in-situ or ex-situ doping, may introduce partial lattice mismatches, leading to substantial modifications in the material's electronic properties.

Beyond doping strategies, composite formation represents another effective method for enhancing the activity of MXene-based catalysts. The surface functionalities of MXenes provide nucleation centres that facilitate uniform dispersion of active catalysts on their surface, preventing agglomeration and thereby increasing the catalytically active surface area. The incorporation of MXenes into composite materials significantly enhances overall electrical conductivity, leading to improved ionic and electronic transport. Furthermore, MXene addition has been shown to enhance light absorption in the UV-Vis-NIR range, thereby augmenting the photothermal effect. This characteristic improves photoelectrochemical performance and enhances the functionality of MXene-based composite materials.

1.5. Application of $Ti_3C_2T_x$ MXenes in Catalysis and Optoelectronics

1.5.1. Fenton Oxidation of Organic Pollutants

The rapid expansion of industrial activities has led to severe organic water pollution, posing significant environmental challenges. In recent years, heterogeneous Fenton-like oxidation has garnered considerable attention due to its high efficiency and ease of operation[45, 46]. Fenton oxidation is an advanced oxidation process (**Fig. 1.7**) that involves the reaction of hydrogen peroxide (H_2O_2) with ferrous ions (Fe^{2+}) to generate hydroxyl radicals[47] (•OH). These •OH are highly reactive and non-selective oxidants capable of breaking down a wide range of organic pollutants. The overall reaction typically occurs under acidic conditions ~at pH 3, which is shown in eq'n (4). In this process, the generated •OH radicals attack and oxidize organic contaminants, ultimately converting them into less harmful

$$Fe^{2+} + H_2O_2 \rightarrow Fe^{3+} + \cdot OH + OH - \qquad (4)$$

compounds such as CO_2, H_2O, and various inorganic ions. Fenton oxidation is widely used in wastewater treatment and environmental remediation due to its efficiency in degrading

complex organic molecules. Among the commonly utilized oxidants in Fenton-like processes, H_2O_2 and persulfate (PS) play crucial roles.

The unique properties of 2D MXene-based materials, including exceptional electrical conductivity, a large surface area, and abundant active sites, offer enhanced potential for the

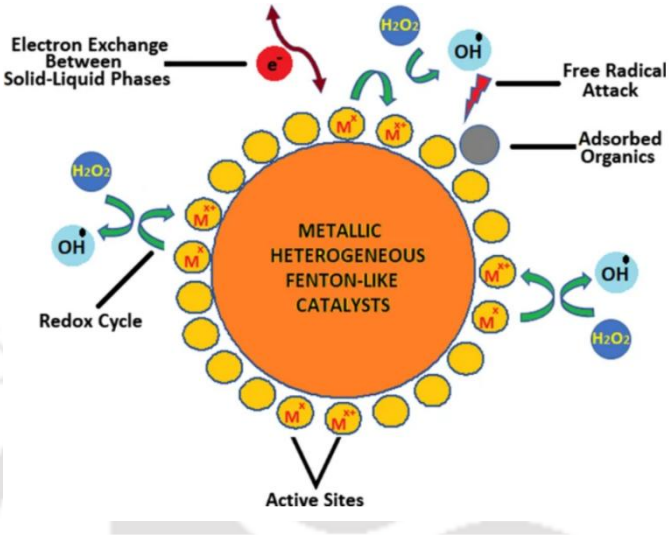

Fig. 1.7. Schematic representations of the heterogeneous Fenton oxidation process. Adopted from ref. [47]

activation of H_2O_2 or PS[48, 49]. Research indicates that the primary reactive species generated in the H_2O_2-based system include $^{\bullet}OH$ and superoxide radicals ($O_2^{\bullet-}$). In addition to these, the PS-based system also produces sulfate radicals ($SO_4^{\bullet-}$) and singlet oxygen ($^1O_2$), which contribute to the degradation of organic pollutants in wastewater treatment[50-52].

The activation of H_2O_2 has attracted significant interest in the degradation of organic pollutants[53], with Fe^{2+} serving as a catalyst to generate reactive free radicals[54]. MXenes, characterized by their lamellar structure and surface electronegativity, provide an ideal platform for Fe particle loading, both on their surface and within their interlayer spaces[55]. Furthermore, 2D MXene facilitates the uniform dispersion of Fe nanoparticles, effectively preventing their agglomeration [56]. Notably, MXene loaded with Fe particles exhibits a higher specific surface area and an improved pore structure compared to pristine MXene. The pores within this composite function as micro-reactors, enhancing H_2O_2 activation. Studies have demonstrated that H_2O_2 activated by magnetic (nZVI)@Ti_3C_2 nanosheets can achieve 91.1% removal of ranitidine within 30 min[57]. Consequently, MXene@Fe composites serve as highly efficient catalysts for H_2O_2 activation, facilitating the degradation of organic contaminants. The PS-based AOPs also have gained significant attention for the degradation of organic pollutants [58]. Typically, PS exists in two primary ionic forms: peroxodisulfate (PDS, $S_2O_8^{2-}$) and

peroxymonosulfate (PMS, HSO_5^-) [59]. The oxidation potentials of PDS and PMS are 2.01 V and 1.82 V, respectively [60]. These persulfates can be activated by suitable catalysts, facilitating pollutant degradation through both radical ($SO_4^{\bullet-}$, $^{\bullet}OH$, and $O_2^{\bullet-}$) formation as well as non-radical pathways such as electron transfer [61, 62].

To date, most research has concentrated on $Ti_3C_2T_x$-based hybrid materials for Fenton oxidation of organic pollutants, while the development of pristine $Ti_3C_2T_x$ Fenton catalysts remains limited. Therefore, advancing MXene-based Fenton catalysis through surface defect engineering or heteroatom doping is highly desirable.

1.5.2. Catalytic Reduction of Organic Pollutants

Catalytic reduction plays a vital role in sustainable development and wastewater treatment, offering a more environment-friendly alternative to Fenton oxidation, which generates CO_2 as a by-product and enhances environmental concerns. In the catalytic reduction process, highly toxic organic pollutants are transformed into less harmful by-products with minimal environmental impact, which can be reused for the production of pharmaceuticals and medicinal compounds. The selection of an appropriate catalyst is a key factor influencing the efficiency of this process. Typically, catalytic reduction involves the presence of sodium borohydride ($NaBH_4$) as a reducing agent combined with an active catalyst to facilitate the reduction of organic pollutants. However, the widespread use of precious noble metal catalysts[63, 64] presents a significant limitation to the practical implementation of this approach. Therefore, the development of high-performance non-precious metal catalysts is essential for advancing catalytic reduction technologies and expanding their applicability.

Recent studies have indicated that $Ti_3C_2T_x$ MXene is ineffective[65, 66] in catalyzing the reduction of 4-nitrophenol (4-NP) to 4-aminophenol (4-AP) in the presence of $NaBH_4$. This limitation is attributed to the negative zeta potential of $Ti_3C_2T_x$ nanosheets, suggesting that the surface of MXene is predominantly covered with negatively charged functional groups (-F, -O, and -OH). Consequently, these negatively charged groups hinder the adsorption of BH_4^- ions and 4-NP due to electrostatic repulsion, inhibiting the occurrence of the reduction reaction. However, certain $Ti_3C_2T_x$-based composite[65, 66] materials have demonstrated enhanced catalytic activity in the reduction of 4-NP to 4-AP. In these composites, $Ti_3C_2T_x$ plays a crucial role in improving the overall electrical conductivity of the material and facilitating efficient charge transfer across the heterojunction, thereby enhancing catalytic performance.

1.5.3. Electrocatalytic Hydrogen Production

The hydrogen evolution reaction is fundamentally a two-electron process that can proceed via two primary mechanisms[67, 68]: the Volmer-Heyrovsky mechanism or the Volmer-Tafel mechanism. In acidic environments, the reaction is initiated by the Volmer step, during which a proton (H^+) accepts an electron and becomes adsorbed onto the catalyst surface, forming an intermediate hydrogen species (H*). The subsequent reaction pathway depends upon the surface coverage of H*: if the surface is densely populated with H*, two neighbouring H* species can combine to yield molecular hydrogen (H_2) via the Tafel mechanism; alternatively, when the H* coverage is low, the Heyrovsky mechanism dominates, whereby a single H* reacts with additional protons and electrons to produce H_2. In contrast, in alkaline media, the formation of H* primarily results from the dissociation of water rather than direct proton adsorption, leading to a lower concentration of protons at the catalyst interface. This reduction in proton availability necessitates a higher activation energy for the HER. Nonetheless, the reaction in alkaline conditions still proceeds through pathways analogous to the Volmer-Heyrovsky and Volmer-Tafel mechanisms. A schematic diagram of the HER reaction mechanism and corresponding reactions in acidic and alkaline media is illustrated in **Fig. 1.8**.

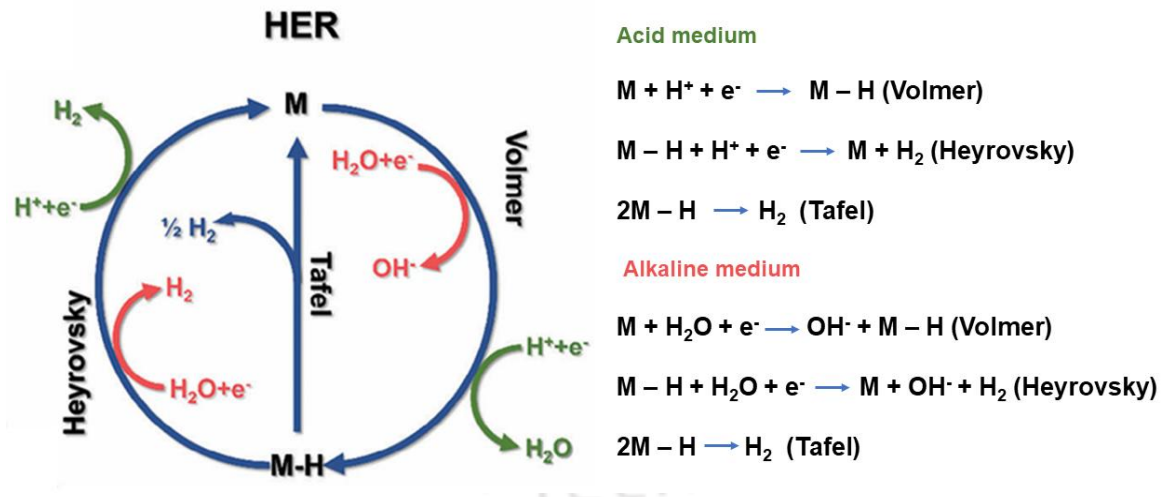

Fig. 1.8. A schematic illustration of the HER reaction mechanism, along with the associated reactions in both acidic and alkaline media. In this diagram, red font indicates reactions occurring in the alkaline electrolyte, while green font denotes those in the acidic electrolyte. Adopted from ref. [68]

2D MXene-based electrocatalysts have emerged as promising candidates for the HER, attracting considerable interest in both experimental and theoretical research. Several strategies have been employed to improve the catalytic efficiency of MXenes through structural engineering, including modifications of termination groups, nanostructure design, and hybridization approaches. Owing to their remarkable properties, $Ti_3C_2T_x$ MXene based

composite materials exhibit great potential as electrocatalysts for the HER, positioning them as promising alternatives to traditional Pt-based electrocatalysts.

1.5.3.1. Modification in Surface Termination

Modifying the surface terminations of MXenes is pivotal for boosting their HER performance, primarily by enhancing their electrical conductivity. Such modifications optimize the electronic structure of MXenes, thereby intrinsically improving their catalytic activity. Recent experimental and theoretical investigations have extensively explored these termination modifications. For example, MXenes with -O or -OH terminal groups exhibit metallic behaviour[69] that facilitates efficient charge transfer, as evidenced by surface Pourbaix diagrams that also attest to their chemical stability. The improved HER activity observed in -O/OH terminated MXenes was attributed to a higher exchange current and enhanced hydrogen evolution efficiency. Additionally, calculated Gibbs free energy (ΔG_{H^*}) values indicate that O atoms on the surface served as active sites, reinforcing the interaction with adsorbed hydrogen (H*). Further studies reveal that O-terminated MXenes predominantly follow the Heyrovsky mechanism, with HER activity varying among different surface groups[70] (-O, -OH, and -F); notably, O-termination proves to be the most effective. These findings collectively confirm that tailoring the surface terminations of MXenes is a critical factor in modulating their catalytic activity for HER applications. Numerous studies into termination modifications have underscored their essential role in enhancing the performance of MXene-based electrocatalysts for the HER. For instance, Jiang et al.[71] reported the development of ultrathin, -O terminated Ti_3C_2 MXenes, demonstrating that -F termination on the basal plane adversely affects HER performance by diminishing the kinetics of hydrogen adsorption. In their approach, $Ti_3C_2O_x$ was synthesized by treating $Ti_3C_2T_x$ in an aqueous KOH solution to replace the F-terminations with -OH groups[72], followed by calcination at 450 °C under Ar atmosphere to convert these -OH groups into -O terminations. The resulting $Ti_3C_2O_x$ exhibited enhanced HER activity, achieving an overpotential of 190 mV at 10 mA cm^{-2}, which outperformed both $Ti_3C_2(OH)_x$ (217 mV) and $Ti_3C_2T_x$-450 (266 mV). Additionally, a Tafel slope of 60.7 mV dec^{-1} was observed. These findings underscore that a higher -F content diminishes HER efficiency, whereas Ti_3C_2 MXenes with -O terminations demonstrate exceptional catalytic performance for the HER.

1.5.3.2. Composite Formation

Integrating $Ti_3C_2T_x$ MXenes with other HER-active materials has been demonstrated to synergistically enhance HER performance. In these hybrid composites, $Ti_3C_2T_x$ MXenes play

a crucial role in the uniform dispersion of catalytic components, boosting overall conductivity and supplying numerous active sites for H* adsorption. **Table 1.1** provides a summary of $Ti_3C_2T_x$ MXene-based composite catalysts used in electrochemical HER, clearly showing their superior electrochemical HER performance.

Table 1.1. *Comparison of the electrochemical HER performance of $Ti_3C_2T_x$ based composites.*

Electrocatalyst	Electrolyte	Overpotential (mV)	Tafel slope (mV dec^{-1})	Refs.
Cu/Co TiO_2@N-$Ti_3C_2T_x$	1 M KOH	78	119	[73]
Co_3O_4/MXene	1 M KOH	118	113	[74]
$Ti_3C_2T_x$@ MOF (Fe/Co)	1 M KOH	104	79	[75]
B-$T_{3-x}C_2T_y$@$MoSe_2$	1 M KOH	52.7	77.4	[76]
Ru-E-MXene/rGA	1 M KOH	42	36.6	[77]
Co_2P/N@$Ti_3C_2T_x$@NF	1 M KOH	15	30	[78]
Ru@B-$Ti_3C_2T_x$	0.5 M H_2SO_4	62.9	100	[79]

Despite the extensive research on $Ti_3C_2T_x$ MXene-based catalysts for HER, most studies have overlooked the benefits derived from their superior light absorption and photothermal effects in photoelectrochemical hydrogen production. Consequently, there remains a notable gap in understanding how enhanced light absorption and photothermal properties influence the performance of $Ti_3C_2T_x$ MXene-based composites. Furthermore, additional research is necessary to develop broad-spectrum light-absorbing materials that extend into the infrared region to achieve efficient photoelectrochemical hydrogen production.

1.5.3.3. $Ti_3C_2T_x$ Nanostructures

Nanostructure engineering is a powerful approach to enhance the electrocatalytic performance of MXenes for the HER, particularly through the fabrication of nanoribbons and nanodots. MXenes with engineered nanostructures exhibit a rapid electrochemical response, distinctive electronic properties, and a high density of active sites, all of which contribute to their promise as efficient HER electrocatalysts. Moreover, this nanostructuring not only broadens the application range of MXenes but also aids in the effective assembly of active catalytic components. The DFT simulations[80] further revealed that the edges of MXene nanoribbons, comprising both metal and carbon atoms, are highly effective at capturing hydrogen species, thereby serving as active sites that facilitate hydrogen evolution with favourable kinetics.

Recent reports demonstrate that $Ti_3C_2T_x$ nanofibers (NFs) show excellent HER performance [81], with an overpotential of 169 mV at 10 mA cm^{-2}, which is significantly lower than the 385 mV observed for $Ti_3C_2T_x$ flakes. Correspondingly, the Tafel slopes are 97 mV dec^{-1} for the NFs compared to 188 mV dec^{-1} for the flakes. Additionally, the NFs possess a much higher surface area (58.5 m^2 g^{-1}) than the flakes (8.5 m^2 g^{-1}), thereby enhancing the exposure of active sites. Moreover, constructing a three-dimensional (3D) porous structure from alkalized Ti_3C_2 (a-Ti_3C_2) nanoribbons results in increased interlayer spacing, which enhances reaction kinetics. Additionally, the combination of this expanded spacing with a reduced nanoribbon width further improves both the reaction kinetics and the morphological stability [82].

1.5.4. Photodetector

Suitable nanocomposites based on $Ti_3C_2T_x$ MXenes demonstrate exceptional electronic and optoelectronic characteristics, positioning them as ideal candidates for photodetector (PD) applications. Their tuneable work function and high electronic conductivity facilitate their use as electrode materials in photodetector devices, underscoring the significant potential of $Ti_3C_2T_x$ MXenes in photodetector device applications. **Table 1.2** illustrates an overview of the photodetection performance of $Ti_3C_2T_x$ MXene-based composite materials reported in the literature.

Table 1.2. *Comparison of the $Ti_3C_2T_x$ composite-based photodetectors.*

Material	Wavelength (nm)	Responsivity (AW^{-1})	Detectivity (Jones)	Refs.
$Ti_3C_2T_x$/$CsPbBr_3$	450	44.9×10^{-3}	6.4×10^{8}	[83]
Ti_3C_2/ZnO	200 - 400	128.3×10^{-3}	5.7×10^{11}	[84]
MoS_2/$Ti_3C_2T_x$	700 - 800	1.9 (Negative photo responsivity)	2.1×10^{10}	[85]
ReS_2/$Ti_3C_2T_x$	Visible - NIR	40.8 (Visible) 26.9 (NIR)	1.07×10^{12} (Visible)	[86]
$MoSe_2$/$Ti_3C_2T_x$	554 - 780	6.58×10^{-3} (Visible) 9.82×10^{-3} (NIR)	2.27×10^{9} (Visible)	[87]
$Ti_3C_2T_x$-TiO_2	300 - 800	0.078×10^{-3}	8.4×10^{4}	[88]
MXene/InGaN	470	6	9×10^{11}	[89]

Nonetheless, most investigations on $Ti_3C_2T_x$ MXene-based PDs have reported a restricted photodetection range, typically covering either the UV-Vis or Vis-NIR regions. Consequently, developing truly broadband $Ti_3C_2T_x$ MXene-based PDs is imperative to meet the requirements of next-generation optoelectronic applications. Further, the specific role of MXene in PD performance needs a thorough investigation.

1.6. Problems and Challenges of Functionalized $Ti_3C_2T_x$ MXenes and its Nanocomposites for Catalysis and Photodetection Application

Recent studies have focused extensively on $Ti_3C_2T_x$ MXene and its derived nanocomposites for a broad spectrum of catalytic and optoelectronic applications. However, numerous challenges associated with $Ti_3C_2T_x$ MXene-based nanocomposites need to be addressed to meet future technological demands.

1. Synthesis of high-purity, scalable, monolayer $Ti_3C_2T_x$ MXenes nanosheet with a very high surface-to-volume aspect ratio is still challenging. Most of the recent studies adopted the in-situ HF formation (LiF/HCl) technique for $Ti_3C_2T_x$ MXene synthesis, which results in a nonuniform distribution of MXene sheet size and hence, the MXene nanosheet with a higher lateral size and uniformity is desired.

2. Pristine $Ti_3C_2T_x$ MXene tends to undergo face-to-face re-stacking of layers due to interlayer van der Waals interactions. This stacking reduces the available catalytically active sites and, in turn, diminishes catalytic performance. Therefore, a reduction in layer stacking is crucial for enhancing its catalytic activity and optoelectronic applications.

3. $Ti_3C_2T_x$ MXene exhibits limited stability under ambient conditions, and maintaining its integrity during functionalization or compositional modifications presents a significant challenge.

4. Typically, the synthesis of $Ti_3C_2T_x$ MXenes under harsh chemical conditions induces intrinsic surface defects. Consequently, a thorough understanding and optimization of these defect states are imperative for enhancing catalytic applications.

5. Furthermore, incorporating conventional nanomaterials (0D, 1D, and 2D) with 2D $Ti_3C_2T_x$ MXenes can impart unique properties owing to their excellent light absorption capabilities. Nevertheless, fabricating composite or hybrid structures that achieve the desired catalytic and optoelectronic performance remains challenging.

Thus, a comprehensive understanding of synthesis strategies, transport, optical, and defect-

induced properties is essential to address the challenges associated with $Ti_3C_2T_x$ MXene-based nanocomposites and to enhance their commercial viability for catalytic and optoelectronic applications.

1.7. Focus of the Present Thesis

2D $Ti_3C_2T_x$ MXenes hold significant promise for catalytic and optoelectronic applications due to their exceptional surface and electronic properties. However, a thorough understanding of how synthesis parameters and functionalization techniques can be leveraged to optimize surface defects as well as the influence of heterostructure formation and nanostructuring on catalytic behaviour, remains primary. Therefore, this thesis investigates the optimization of surface defects, the development of heterostructures, and the application of nanostructuring, assessing their crucial roles in enhancing catalytic and optoelectronic performance. The focus of the present thesis is

1. Optimization of surface defect states in multi-layered $Ti_3C_2T_x$ MXene through controlled modulation of synthesis parameters and investigation of their role in catalytic Fenton degradation of organic pollutants.

2. Investigation of the impact of heteroatom doping on the surface properties of few-layer $Ti_3C_2T_x$ MXene nanosheets and their application in catalytic degradation of organic pollutants via advanced oxidation process.

3. Fabrication of a composite based on 2D $Ti_3C_2T_x$ nanosheets and semiconducting 1D Bi_2S_3 nanorods to investigate their catalytic performance in the reduction of organic pollutants, elucidate interlayer charge transfer mechanisms, and explore their application in photoelectrochemical hydrogen production.

4. Investigation of the effect of ultrasmall Ru atomic cluster anchoring on N-doped $Ti_3C_2T_x$ nanoribbons and its influence on the enhanced photothermal effect and photoelectrochemical hydrogen production.

5. Development of a composite integrating 2D $Ti_3C_2T_x$ nanosheets with 1D Bi_2S_3 nanorods to investigate interlayer charge transfer and broadband light absorption for application in UV-Vis-NIR broadband photodetection.

1.8. Organization of the Thesis

Chapter 1 provides a brief introduction to 2D $Ti_3C_2T_x$ MXenes, covering their crystal

structure, properties, synthesis routes, and applications, with a particular focus on catalysis and optoelectronics. **Chapter 2** explores the modulation of surface defect states in $Ti_3C_2T_x$ and their influence on the Fenton degradation of organic pollutants. **Chapter 3** investigates the effect of phosphorous-doped $Ti_3C_2T_x$ MXene/carbon foam hybrid aerogel in the oxidative degradation of organic pollutants through an advanced oxidation process. **Chapter 4** highlights the study of interfacial charge transfer between 1D Bi_2S_3 nanorods and 2D $Ti_3C_2T_x$ MXene nanosheets for catalytic reduction of organic pollutants and photoelectrochemical hydrogen evolution reaction. **Chapter 5** investigates the impact of Ru atomic cluster anchoring on N-doped $Ti_3C_2T_x$ nanoribbons and its role in enhancing photoelectrochemical hydrogen production through the photothermal effect. **Chapter 6** investigates the broadband photodetection performance of the 1D Bi_2S_3/2D $Ti_3C_2T_x$ MXene-based composites. **Chapter 7** presents a summary of the key findings and significant conclusions of this thesis, along with potential future research directions.

References

(1) Naguib, M.; Kurtoglu, M.; Presser, V.; Lu, J.; Niu, J.; Heon, M.; Hultman, L.; Gogotsi, Y.; Barsoum, M. W. Two-Dimensional Nanocrystals Produced by Exfoliation of Ti_3AlC_2. *Adv. Mater.* **2011**, *23* (37), 4248-4253.
(2) Liu, C.; Chen, H.; Wang, S.; Liu, Q.; Jiang, Y.-G.; Zhang, D. W.; Liu, M.; Zhou, P. Two-dimensional materials for next-generation computing technologies. *Nat. Nanotechnol.* **2020**, *15* (7), 545-557.
(3) Cheng, Z.; Cao, R.; Wei, K.; Yao, Y.; Liu, X.; Kang, J.; Dong, J.; Shi, Z.; Zhang, H.; Zhang, X. 2D Materials Enabled Next-Generation Integrated Optoelectronics: from Fabrication to Applications. *Adv. Sci.* **2021**, *8* (11), 2003834.
(4) Castro Neto, A. H.; Guinea, F.; Peres, N. M. R.; Novoselov, K. S.; Geim, A. K. The electronic properties of graphene. *Rev. Modern Phys.* **2009**, *81* (1), 109-162.
(5) Papageorgiou, D. G.; Kinloch, I. A.; Young, R. J. Mechanical properties of graphene and graphene-based nanocomposites. *Progress in Mater. Sci.* **2017**, *90*, 75-127.
(6) Naumis, G. G.; Barraza-Lopez, S.; Oliva-Leyva, M.; Terrones, H. Electronic and optical properties of strained graphene and other strained 2D materials: a review. *Reports on Progress in Phys.* **2017**, *80* (9), 096501.
(7) Gogotsi, Y.; Huang, Q. MXenes: Two-Dimensional Building Blocks for Future Materials and Devices. *ACS Nano* **2021**, *15* (4), 5775-5780.
(8) Murali, G.; Rawal, J.; Modigunta, J. K. R.; Park, Y. H.; Lee, J.-H.; Lee, S.-Y.; Park, S.-J.; In, I. A review on MXenes: new-generation 2D materials for supercapacitors. *Sustainable Energy & Fuels* **2021**, *5* (22), 5672-5693, 10.1039/D1SE00918D.
(9) Bai, S.; Yang, M.; Jiang, J.; He, X.; Zou, J.; Xiong, Z.; Liao, G.; Liu, S. Recent advances of MXenes as electrocatalysts for hydrogen evolution reaction. *npj 2D Materials and Applications* **2021**, *5* (1), 78.
(10) Solangi, N. H.; Karri, R. R.; Mubarak, N. M.; Mazari, S. A.; Azad, A. K. Emerging 2D MXenes as next-generation materials for energy storage applications. *Journal of Energy Storage* **2023**, *70*, 108004.

(11) Nan, J.; Guo, X.; Xiao, J.; Li, X.; Chen, W.; Wu, W.; Liu, H.; Wang, Y.; Wu, M.; Wang, G. Nanoengineering of 2D MXene-Based Materials for Energy Storage Applications. *Small* **2021**, *17* (9), 1902085.
(12) Li, X.; Huang, Z.; Shuck, C. E.; Liang, G.; Gogotsi, Y.; Zhi, C. MXene chemistry, electrochemistry and energy storage applications. *Nat. Rev. Chem.* **2022**, *6* (6), 389-404.
(13) Hamzehlouy, A.; Soroush, M. MXene-based catalysts: A review. *Mater. Today Catal.* **2024**, *5*, 100054.
(14) Yang, Y.; Xu, Y.; Li, Q.; Zhang, Y.; Zhou, H. Two-dimensional carbide/nitride (MXene) materials in thermal catalysis. *J. Mater. Chem. A* **2022**, *10* (37), 19444-19465, 10.1039/D2TA03481F.
(15) Iqbal, A.; Hassan, T.; Naqvi, S. M.; Gogotsi, Y.; Koo, C. M. MXenes for multispectral electromagnetic shielding. *Nat. Rev. Electrical Eng.* **2024**, *1* (3), 180-198.
(16) Zhang, H.; Wan, J.; Wu, R.; Chen, Y.; Yu, H.; Shi, S. MXenes for electromagnetic interference shielding: Insights from structural design. *Carbon* **2024**, *218*, 118716.
(17) Hu, Y.; Wang, F.; Ye, H.; Jiang, J.; Li, S.; Dai, B.; Li, J.; Yang, J.; Song, X.; Zhang, J.; et al. MXene-based flexible electronic materials for wound infection detection and treatment. *npj Flexible Electronics* **2024**, *8* (1), 30.
(18) Iravani, S.; Rabiee, N.; Makvandi, P. Advancements in MXene-based composites for electronic skins. *J. Mater. Chem. B* **2024**, *12* (4), 895-915, 10.1039/D3TB02247A.
(19) Wang, Q.; Su, X.; Jia, Y.; Liu, Y.; Shahzad, F. Microwave absorption properties and electromagnetic characteristics of MoS_2/MXene sandwich composites. *Ceram. Int.* **2025**, *51* (8), 9833-9841.
(20) Avinashi, S. K.; Mishra, R. K.; Singh, R.; Shweta; Rakhi; Fatima, Z.; Gautam, C. R. Fabrication Methods, Structural, Surface Morphology and Biomedical Applications of MXene: A Review. *ACS Appl. Mater. Interfaces* **2024**, *16* (36), 47003-47049.
(21) Eghbali, P.; Hassani, A.; Wacławek, S.; Andrew Lin, K.-Y.; Sayyar, Z.; Ghanbari, F. Recent advances in design and engineering of MXene-based catalysts for photocatalysis and persulfate-based advanced oxidation processes: A state-of-the-art review. *Chem. Eng. J.* **2024**, *480*, 147920.
(22) Cao, W.; Nie, J.; Cao, Y.; Gao, C.; Wang, M.; Wang, W.; Lu, X.; Ma, X.; Zhong, P. A review of how to improve $Ti_3C_2T_x$ MXene stability. *Chem. Eng. J.* **2024**, *496*, 154097.
(23) Li, X.; Bai, Y.; Shi, X.; Su, N.; Nie, G.; Zhang, R.; Nie, H.; Ye, L. Applications of MXene ($Ti_3C_2T_x$) in photocatalysis: a review. *Mater. Adv.* **2021**, *2* (5), 1570-1594, 10.1039/D0MA00938E.
(24) Tang, Q.; Zhou, Z.; Shen, P. Are MXenes promising anode materials for Li ion batteries? Computational studies on electronic properties and Li storage capability of Ti_3C_2 and $Ti_3C_2X_2$ (X= F, OH) monolayer. *J. Am. Chem. Soc.* **2012**, *134* (40), 16909-16916.
(25) Hope, M. A.; Forse, A. C.; Griffith, K. J.; Lukatskaya, M. R.; Ghidiu, M.; Gogotsi, Y.; Grey, C. P. NMR reveals the surface functionalisation of Ti_3C_2 MXene. *Phys. Chem. Chem. Phys.* **2016**, *18* (7), 5099-5102, 10.1039/C6CP00330C.
(26) Karlsson, L. H.; Birch, J.; Halim, J.; Barsoum, M. W.; Persson, P. O. Å. Atomically Resolved Structural and Chemical Investigation of Single MXene Sheets. *Nano Letters* **2015**, *15* (8), 4955-4960.
(27) Lashgari, H.; Abolhassani, M. R.; Boochani, A.; Elahi, S. M.; Khodadadi, J. Electronic and optical properties of 2D graphene-like compounds titanium carbides and nitrides: DFT calculations. *Solid State Commun.* **2014**, *195*, 61.
(28) Pei, Y.; Zhang, X.; Hui, Z.; Zhou, J.; Huang, X.; Sun, G.; Huang, W. $Ti_3C_2T_X$ MXene for Sensing Applications: Recent Progress, Design Principles, and Future Perspectives. *ACS Nano* **2021**, *15* (3), 3996-4017.

(29) Schultz, T.; Frey, N. C.; Hantanasirisakul, K.; Park, S.; May, S. J.; Shenoy, V. B.; Gogotsi, Y.; Koch, N. Surface Termination Dependent Work Function and Electronic Properties of $Ti_3C_2T_x$ MXene. *Chem. Mater.* **2019**, *31* (17), 6590-6597.
(30) Berdiyorov, G. R. Optical properties of functionalized $Ti_3C_2T_2$ (T = F, O, OH) MXene: First-principles calculations. *AIP Adv.* **2016**, *6* (5).
(31) Xing, C.; Chen, S.; Liang, X.; Liu, Q.; Qu, M.; Zou, Q.; Li, J.; Tan, H.; Liu, L.; Fan, D. Two-dimensional MXene (Ti_3C_2)-integrated cellulose hydrogels: toward smart three-dimensional network nanoplatforms exhibiting light-induced swelling and bimodal photothermal/chemotherapy anticancer activity. *ACS Appl. Mater. Interfaces* **2018**, *10* (33), 27631-27643.
(32) Hantanasirisakul, K.; Zhao, M.-Q.; Urbankowski, P.; Halim, J.; Anasori, B.; Kota, S.; Ren, C. E.; Barsoum, M. W.; Gogotsi, Y. Fabrication of $Ti_3C_2T_x$ MXene Transparent Thin Films with Tunable Optoelectronic Properties. *Adv. Electron. Mater.* **2016**, *2* (6), 1600050.
(33) Bandyopadhyay, A.; Ghosh, D.; Pati, S. K. Effects of point defects on the magnetoelectronic structures of MXenes from first principles. *Phys. Chem. Chem. Phys.* **2018**, *20* (6), 4012-4019.
(34) Scheibe, B.; Tadyszak, K.; Jarek, M.; Michalak, N.; Kempiński, M.; Lewandowski, M.; Peplińska, B.; Chybczyńska, K. Study on the magnetic properties of differently functionalized multilayered $Ti_3C_2T_x$ MXenes and Ti-Al-C carbides. *Appl. Surf. Sci.* **2019**, *479*, 216-224.
(35) Zhang, K.; Di, M.; Fu, L.; Deng, Y.; Du, Y.; Tang, N. Enhancing the magnetism of 2D carbide MXene $Ti_3C_2T_x$ by H_2 annealing. *Carbon* **2020**, *157*, 90-96.
(36) Madhu, S.; MacKenzie, J.; Grewal, K. S.; Farooque, A. A.; Koleilat, G. I.; Selopal, G. S. Titanium Carbide ($Ti_3C_2T_x$) MXene for Sequestration of Aquatic Pollutants. *ChemSusChem* **2024**, *17* (21), e202400421.
(37) Jiang, Y.; Sun, T.; Xie, X.; Jiang, W.; Li, J.; Tian, B.; Su, C. Oxygen-Functionalized Ultrathin Ti3C2T MXene for Enhanced Electrocatalytic Hydrogen Evolution. *ChemSusChem* **2019**, *12* (7), 1368-1373.
(38) Ghidiu, M.; Lukatskaya, M. R.; Zhao, M.-Q.; Gogotsi, Y.; Barsoum, M. W. Conductive two-dimensional titanium carbide 'clay' with high volumetric capacitance. *Nature* **2014**, *516* (7529), 78-81.
(39) Bian, R.; He, G.; Zhi, W.; Xiang, S.; Wang, T.; Cai, D. Ultralight MXene-based aerogels with high electromagnetic interference shielding performance. *J. Mater. Chem. C* **2019**, *7* (3), 474-478, 10.1039/C8TC04795B.
(40) Chen, J.; Chen, M.; Zhou, W.; Xu, X.; Liu, B.; Zhang, W.; Wong, C. Simplified Synthesis of Fluoride-Free $Ti_3C_2T_x$ via Electrochemical Etching toward High-Performance Electrochemical Capacitors. *ACS Nano* **2022**, *16* (2), 2461-2470.
(41) Naguib, M. Two-dimensional transition metal carbides. *ACS Nano* **2012**, *6* (2), 1322.
(42) Arole, K.; Blivin, J. W.; Saha, S.; Holta, D. E.; Zhao, X.; Sarmah, A.; Cao, H.; Radovic, M.; Lutkenhaus, J. L.; Green, M. J. Water-dispersible $Ti_3C_2T_z$ MXene nanosheets by molten salt etching. *iScience* **2021**, *24* (12), 103403.
(43) Liu, L.; Orbay, M.; Luo, S.; Duluard, S.; Shao, H.; Harmel, J.; Rozier, P.; Taberna, P.-L.; Simon, P. Exfoliation and Delamination of $Ti_3C_2T_x$ MXene Prepared via Molten Salt Etching Route. *ACS Nano* **2022**, *16* (1), 111-118.
(44) Li, T.; Yao, L.; Liu, Q.; Gu, J.; Luo, R.; Li, J.; Yan, X.; Wang, W.; Liu, P.; Chen, B.; et al. Fluorine-Free Synthesis of High-Purity Ti_3C_2T (T=OH, O) via Alkali Treatment. *Angew. Chem. Int. Ed.* **2018**, *57* (21), 6115-6119.
(45) Oh, W.-D.; Lim, T.-T. Design and application of heterogeneous catalysts as peroxydisulfate activator for organics removal: an overview. *Chem. Eng. J.* **2019**, *358*, 110-133.

(46) Ramirez, J. H.; Maldonado-Hódar, F. J.; Pérez-Cadenas, A. F.; Moreno-Castilla, C.; Costa, C. A.; Madeira, L. M. Azo-dye Orange II degradation by heterogeneous Fenton-like reaction using carbon-Fe catalysts. *Appl. Catal. B: Environ.* **2007**, *75* (3-4), 312-323.
(47) Hussain, S.; Aneggi, E.; Goi, D. Catalytic activity of metals in heterogeneous Fenton-like oxidation of wastewater contaminants: a review. *Environ. Chem. Lett.* **2021**, *19* (3), 2405-2424.
(48) Dixit, F.; Zimmermann, K.; Dutta, R.; Prakash, N. J.; Barbeau, B.; Mohseni, M.; Kandasubramanian, B. Application of MXenes for water treatment and energy-efficient desalination: A review. *J. Hazard. Mater.* **2022**, *423*, 127050.
(49) Jun, B.-M.; Kim, S.; Heo, J.; Park, C. M.; Her, N.; Jang, M.; Huang, Y.; Han, J.; Yoon, Y. Review of MXenes as new nanomaterials for energy storage/delivery and selected environmental applications. *Nano Res.* **2019**, *12*, 471-487.
(50) Fayyaz, A.; Saravanakumar, K.; Talukdar, K.; Kim, Y.; Yoon, Y.; Park, C. M. Catalytic oxidation of naproxen in cobalt spinel ferrite decorated $Ti_3C_2T_x$ MXene activated persulfate system: Mechanisms and pathways. *Chem. Eng. J.* **2021**, *407*, 127842.
(51) Jin, L.; You, S.; Yao, Y.; Chen, H.; Wang, Y.; Liu, Y. An electroactive single-atom copper anchored MXene nanohybrid filter for ultrafast water decontamination. *J. Mater. Chem. A* **2021**, *9* (46), 25964-25973.
(52) Liu, Y.; Luo, R.; Li, Y.; Qi, J.; Wang, C.; Li, J.; Sun, X.; Wang, L. Sandwich-like Co3O4/MXene composite with enhanced catalytic performance for Bisphenol A degradation. *Chem. Eng. J.* **2018**, *347*, 731-740.
(53) Wan, Z.; Wang, J. Ce-Fe-reduced graphene oxide nanocomposite as an efficient catalyst for sulfamethazine degradation in aqueous solution. *Environ. Sci. Pollution Res.* **2016**, *23*, 18542-18551.
(54) Cui, Y.; Liu, M.; Huang, H.; Zhang, D.; Chen, J.; Mao, L.; Zhou, N.; Deng, F.; Zhang, X.; Wei, Y. A novel one-step strategy for preparation of Fe3O4-loaded Ti3C2 MXenes with high efficiency for removal organic dyes. *Ceram. Int.* **2020**, *46* (8), 11593-11601.
(55) Mashtalir, O.; Naguib, M.; Mochalin, V. N.; Dall'Agnese, Y.; Heon, M.; Barsoum, M. W.; Gogotsi, Y. Intercalation and delamination of layered carbides and carbonitrides. In *MXenes*, Jenny Stanford Publishing, 2023; pp 359-377.
(56) Shi, W.; Fu, Y.; Hao, C.; Guo, F.; Tang, Y. Heterogeneous photo-Fenton process over magnetically recoverable $MnFe_2O_4$/MXene hierarchical heterostructure for boosted degradation of tetracycline. *Mater. Today Commun.* **2022**, *33*, 104449.
(57) Ma, Y.; Lv, X.; Xiong, D.; Zhao, X.; Zhang, Z. Catalytic degradation of ranitidine using novel magnetic Ti3C2-based MXene nanosheets modified with nanoscale zero-valent iron particles. *Appl. Catal. B: Environ.* **2021**, *284*, 119720.
(58) Li, N.; Wang, Y.; Cheng, X.; Dai, H.; Yan, B.; Chen, G.; Wang, S. Influences and mechanisms of phosphate ions onto persulfate activation and organic degradation in water treatment: A review. *Water Res.* **2022**, *222*, 118896.
(59) Devi, P.; Das, U.; Dalai, A. K. In-situ chemical oxidation: principle and applications of peroxide and persulfate treatments in wastewater systems. *Sci. Total Environ.* **2016**, *571*, 643-657.
(60) Peng, W.; Dong, Y.; Fu, Y.; Wang, L.; Li, Q.; Liu, Y.; Fan, Q.; Wang, Z. Non-radical reactions in persulfate-based homogeneous degradation processes: A review. *Chem. Eng. J.* **2021**, *421*, 127818.
(61) Li, N.; Li, R.; Duan, X.; Yan, B.; Liu, W.; Cheng, Z.; Chen, G.; Hou, L. a.; Wang, S. Correlation of active sites to generated reactive species and degradation routes of organics in peroxymonosulfate activation by Co-loaded carbon. *Environ. Sci. Technol.* **2021**, *55* (23), 16163-16174.
(62) Wang, Y.; Peng, W.; Wang, J.; Chen, G.; Li, N.; Song, Y.; Cheng, Z.; Yan, B.; Hou, L. a.; Wang, S. Sulfamethoxazole degradation by regulating active sites on distilled spirits lees-

derived biochar in a continuous flow fixed bed peroxymonosulfate reactor. *Appl. Catal. B: Environ.* **2022**, *310*, 121342.
(63) Mejía, Y. R.; Reddy Bogireddy, N. K. Reduction of 4-nitrophenol using green-fabricated metal nanoparticles. *RSC Adv.* **2022**, *12* (29), 18661-18675, 10.1039/D2RA02663E.
(64) Zhao, P.; Feng, X.; Huang, D.; Yang, G.; Astruc, D. Basic concepts and recent advances in nitrophenol reduction by gold- and other transition metal nanoparticles. *Coord. Chem. Rev.* **2015**, *287*, 114-136.
(65) Qin, X.; Ding, C.; Tian, Y.; Dong, J.; Cheng, B. Multifunctional $Ti_3C_2T_x$ MXene/Silver Nanowire Membranes with Excellent Catalytic, Antifouling, and Antibacterial Properties for Nitrophenol-Containing Water Purification. *ACS Appl. Mater. Interfaces* **2023**, *15* (41), 48154-48167.
(66) Yu, C.; Peng, L.; Zhu, Y.; Xie, G.; Wu, Z.; Xie, X.; Zhang, N. Electrostatically confined Bi/$Ti_3C_2T_x$ on a sponge as an easily recyclable and durable catalyst for the reductive transformation of nitroarenes. *J. Mater. Chem. A* **2021**, *9* (35), 19847-19853, 10.1039/D1TA02736K.
(67) Bai, S.; Yang, M.; Jiang, J.; He, X.; Zou, J.; Xiong, Z.; Liao, G.; Liu, S. Recent advances of MXenes as electrocatalysts for hydrogen evolution reaction. NPJ 2D Mater. Appl. 5: 78. 2021.
(68) Wang, J.; Yang, G.; Jiao, Y.; Yan, H.; Fu, H. Subtle 2D/2D MXene-based heterostructures for high-performance electrocatalytic water splitting. *Small Methods* **2025**, *9* (2), 2301602.
(69) Gao, G.; O'Mullane, A. P.; Du, A. 2D MXenes: a new family of promising catalysts for the hydrogen evolution reaction. *Acs Catal.* **2017**, *7* (1), 494-500.
(70) Ran, J.; Gao, G.; Li, F.-T.; Ma, T.-Y.; Du, A.; Qiao, S.-Z. Ti_3C_2 MXene co-catalyst on metal sulfide photo-absorbers for enhanced visible-light photocatalytic hydrogen production. *Nat. Commun.* **2017**, *8* (1), 13907.
(71) Jiang, Y.; Sun, T.; Xie, X.; Jiang, W.; Li, J.; Tian, B.; Su, C. Oxygen-functionalized ultrathin $Ti_3C_2T_x$ MXene for enhanced electrocatalytic hydrogen evolution. *ChemSusChem* **2019**, *12* (7), 1368-1373.
(72) Xie, Y.; Naguib, M.; Mochalin, V. N.; Barsoum, M. W.; Gogotsi, Y.; Yu, X.; Nam, K.-W.; Yang, X.-Q.; Kolesnikov, A. I.; Kent, P. R. Role of surface structure on Li-ion energy storage capacity of two-dimensional transition-metal carbides. *J. Am. Chem. Soc.* **2014**, *136* (17), 6385-6394.
(73) Khalid, A.; Choi, H. W.; Zafar, U.; Hassan, T.; Kim, J.; Koo, C. M.; Yoon, D. H. Zeolitic imidazole framework derived Cu doped Co decorated N-Ti3C2Tx MXene nanosheets for enhanced hydrogen evolution performance. *J. Alloys Compd.* **2024**, *978*, 173395.
(74) Ghaemmaghami, M.; Yamini, Y. Three-Dimensional Network of Highly Uniform Cobalt Oxide Microspheres/MXene Composite as a High-Performance Electrocatalyst in Hydrogen Evolution Reaction. *ACS Appl. Mater. Interfaces* **2024**, *16* (15), 18782-18789.
(75) Zhao, Y.; Wang, S.; Zhang, Z.; Hu, Y.; Ge, K.; Liu, B.; Yang, Y. Effect of electron transfer of 2D $Ti_3C_2T_x$@MOF heterostructure on hydrogen evolution reaction activity. *Int. J. Hydrogen Energy* **2024**, *55*, 225-233.
(76) Du, M.; Yang, X.; Zhang, J.; Chen, W.; Huang, H.; Zhu, X.; Li, X. a. Defect-modulated and heteroatom-functionalized $Ti_{3-x}C_2T_y$ MXene 3D nanocavities induce growth of MoSe2 nanoflakes toward electrocatalytic hydrogen evolution in all pH electrolytes. *Nano Res.* **2024**.
(77) Yu, X.; Li, Y.; Pei, C.; Lu, Y.; Kim, J. K.; Park, H. S.; Pang, H. Interfacial Design of $Ti_3C_2T_x$ MXene/Graphene Heterostructures Boosted Ru Nanoclusters with High Activity Toward Hydrogen Evolution Reaction. *Adv. Sci.* **2024**, *11* (22), 2310013.
(78) Lv, Z.; Ma, W.; Wang, M.; Dang, J.; Jian, K.; Liu, D.; Huang, D. Co-Constructing Interfaces of Multiheterostructure on MXene ($Ti_3C_2T_x$)-Modified 3D Self-Supporting

Electrode for Ultraefficient Electrocatalytic HER in Alkaline Media. *Adv. Funct. Mater.* **2021**, *31* (29), 2102576.
(79) Bat-Erdene, M.; Batmunkh, M.; Sainbileg, B.; Hayashi, M.; Bati, A. S. R.; Qin, J.; Zhao, H.; Zhong, Y. L.; Shapter, J. G. Highly Dispersed Ru Nanoparticles on Boron-Doped $Ti_3C_2T_x$ (MXene) Nanosheets for Synergistic Enhancement of Electrocatalytic Hydrogen Evolution. *Small* **2021**, *17* (38), 2102218.
(80) Yang, X.; Gao, N.; Zhou, S.; Zhao, J. MXene nanoribbons as electrocatalysts for the hydrogen evolution reaction with fast kinetics. *Phys. Chem. Chem. Phys.* **2018**, *20* (29), 19390-19397.
(81) Yuan, W.; Cheng, L.; An, Y.; Wu, H.; Yao, N.; Fan, X.; Guo, X. MXene nanofibers as highly active catalysts for hydrogen evolution reaction. *ACS Sustainable Chem. Eng.* **2018**, *6* (7), 8976-8982.
(82) Lian, P.; Dong, Y.; Wu, Z.-S.; Zheng, S.; Wang, X.; Wang, S.; Sun, C.; Qin, J.; Shi, X.; Bao, X. Alkalized Ti_3C_2 MXene nanoribbons with expanded interlayer spacing for high-capacity sodium and potassium ion batteries. *Nano Energy* **2017**, *40*, 1-8.
(83) Deng, W.; Huang, H.; Jin, H.; Li, W.; Chu, X.; Xiong, D.; Yan, W.; Chun, F.; Xie, M.; Luo, C.; et al. All-Sprayed-Processable, Large-Area, and Flexible Perovskite/MXene-Based Photodetector Arrays for Photocommunication. *Adv. Optical Mater.* **2019**, *7* (6), 1801521.
(84) Song, W.; Liang, Z.; Guo, Y.; Luo, X.; He, X.; Liu, Q.; Sun, Y.; Li, S. 2D Ti_3C_2 nanoflakes anchored ZnO photodetector with substantially improved deep-ultraviolet photoresponse and on/off ratio. *J. Alloys Compd.* **2022**, *909*, 164816.
(85) Zhu, J.; Wang, H.; Ma, L.; Zou, G. Observation of ambipolar photoresponse from 2D MoS2/MXene heterostructure. *Nano Res.* **2021**, *14* (10), 3416-3422.
(86) Selamneni, V.; Adepu, V.; Raghavan, H.; Sahatiya, P. Ultra-High Responsivity and Enhanced Trap Assisted Charge Transfer by utilizing $Ti_3C_2T_x$(MXene) as a Transport Layer for ReS_2 based Flexible Broadband Photodetector: A better Alternative to Graphene. *FlatChem* **2022**, *33*, 100363.
(87) Polumati, G.; Adepu, V.; Kolli, C. S. R.; Reji, J.; Sahatiya, P. Band alignment study of 2D-2D heterointerface of $MoSe_2$ with $Ti_3C_2T_x$ (transport layer) for flexible broadband photodetection. *Mater. Sci. Semiconductor Process.* **2023**, *153*, 107161.
(88) Xiong, D.; Deng, W.; Tian, G.; Zhang, B.; Zhong, S.; Xie, Y.; Yang, T.; Zhao, H.; Yang, W. Controllable in-situ-oxidization of 3D-networked $Ti_3C_2T_x$-TiO_2 photodetectors for large-area flexible optical imaging. *Nano Energy* **2022**, *93*, 106889.
(89) Kong, D.; Lin, T.; Chai, J.; Zhu, Z.; Liu, P.; Lin, Z.; Lin, T.; Li, L.; Chen, L.; Li, G.; et al. A self-powered MXene/InGaN van der Waals heterojunction mini-photodetector for visible light communication. *Appl. Phys. Lett.* **2023**, *122* (14).

Chapter 2

Surface Defect Engineered Multi-layered $Ti_3C_2T_x$ MXene as Advanced Fenton Catalyst for Organic Pollutant Degradation

In this chapter, the surface defect states of multi-layered $Ti_3C_2T_x$ (m-$Ti_3C_2T_x$) MXenes were optimized by adjusting synthesis parameters, and their influence on the degradation of organic pollutants via Fenton oxidation was examined. Morphological and structural characterizations confirmed the successful synthesis, whereas XPS revealed the presence of abundant surface functional groups (-F, -O, and -OH), lower-valent Ti states (Ti^{2+} and Ti^{3+}), and oxygen vacancies. The modulation of these surface defect states was further verified by electron spin resonance (ESR) analysis. The catalytic performance of m-$Ti_3C_2T_x$ was evaluated using various organic pollutants, with methylene blue degradation showing the highest efficiency. Under optimal conditions, m-$Ti_3C_2T_x$ exhibited a high catalytic activity for MB degradation, achieving an average degradation rate of 0.22 min^{-1}. Post-annealing studies further highlighted the significant role of surface defects in the degradation process, offering detailed insights into their contribution. These findings suggest that m-$Ti_3C_2T_x$ can be a promising Fenton catalyst for the removal of organic pollutants from industrial wastewater.

2.1. Introduction

The rapid expansion of the human population and escalating consumption patterns have significantly accelerated water pollution. However, the polluted wastewater, characterized by high chemical oxygen demand, low biodegradability, and inherent toxicity, raises substantial environmental and health concerns[1]. Consequently, the effective removal of organic contaminants from such wastewater before environmental discharge is imperative. Over the years, various methods for wastewater treatment, such as photocatalytic oxidation[2, 3], adsorption[4], membrane filtration[5], and precipitation[6], have been investigated. While these techniques are useful, they often encounter limitations, including high operational costs, significant energy consumption, and excessive sludge production[1]. In contrast, advanced oxidation processes (AOPs) have emerged as a particularly promising alternative, given their ability to oxidize nearly all organic contaminants into harmless products, surpassing the mere phase transformation achieved by adsorption and precipitation. Among the AOPs, Fenton oxidation is the most effective[7], as discussed in **Chapter 1**. However, its practical application

is constrained by the need for harsh acidic conditions (pH < 3) and concerns related to the high dosages of H_2O_2 required. Therefore, the development of high-performance, cost-effective catalysts remains crucial for advancing wastewater treatment technologies.

Two-dimensional (2D) $Ti_3C_2T_x$ MXenes (T = -F, -O, and -OH) are the most extensively studied materials due to their exceptional properties[8-11], such as large specific surface area, excellent electronic conductivity, abundant surface-terminated functional groups (-F, -O, and -OH), and negatively charged surfaces. These excellent surface properties make them ideal for catalytic wastewater treatment applications. Although these promising characteristics are evident, only a few studies are exploring the use of $Ti_3C_2T_x$ MXenes-based hybrid materials[12-14] in wastewater treatment via the Fenton reaction, and the application of pristine $Ti_3C_2T_x$ MXenes for this purpose remains rare.

In this chapter, a three-dimensional (3D), accordion-like $Ti_3C_2T_x$ microstructure was synthesized, and its intrinsic surface defect states were tuned by adjusting the synthesis parameters. Structural and morphological characterizations confirmed the successful synthesis, while ESR analysis verified the modulation of surface defects. The synthesized materials were subsequently applied as a Fenton catalyst for degrading various organic pollutants, with methylene blue (MB) showing the highest degradation efficiency. Furthermore, the effects of several parameters on MB degradation were systematically evaluated, and the underlying degradation mechanism was explored in detail.

2.2. Experimental Details

2.2.1. Synthesis of Multi-layered $Ti_3C_2T_x$ MXene

Multi-layered $Ti_3C_2T_x$ MXenes were synthesized via a single-step HF etching process[15].

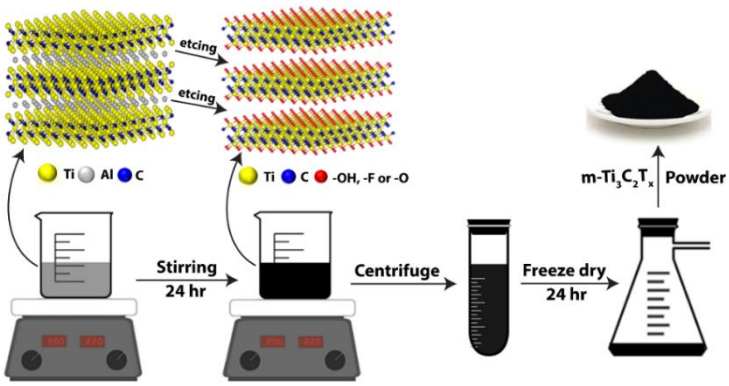

Fig. 2.1. Schematic representation of m-$Ti_3C_2T_x$ MXene synthesis through chemical etching of Ti_3AlC_2 by HF.

As shown in **Fig. 2.1**, 1 g of Ti_3AlC_2 MAX powder was added to 20 mL of HF solutions having

various concentrations, such as 20, 40, and 48 wt%, under continuous stirring at 250 rpm for 24 h. After that, the mixture was centrifuged multiple times with DI water at 4500 rpm until the pH of the solution reached ~6. The resulting sediment was then freeze-dried for 24 h. The final product was obtained as a black powder and labeled as m-TC20, m-TC40, and m-TC48, corresponding to the HF concentrations used in each case.

2.2.2. Experimental Procedure for Pollutant Degradation

Pollutant degradation experiments were conducted in the dark at room temperature using a 50 mL (20 μM) solution. The pH of these solutions was adjusted with 0.1 M NaOH and HCl. In a typical experiment, a predetermined amount of the synthesized catalyst powder was added to the pollutant solution and continuously stirred at 500 rpm for 25 min to establish an adsorption-desorption equilibrium. Subsequently, 100 μL of 10 M H_2O_2 was introduced into the system, and 2 mL of the pollutant solution was withdrawn at 3-min intervals, followed by filtration. The filtered samples were then analyzed using a UV-Vis spectroscope, and the degradation efficiency was calculated using the following formula.

$$\text{Degradation efficiency (\%)} = (C_0-C_t)/C_0 \quad (1)$$

Here, C_0 and C_t represent the absorbance of the pollutant solution initially and at any given time t after the achievement of adsorption-desorption equilibrium.

2.2.3. Characterization Techniques

The crystallinity and phase of Ti_3AlC_2 MAX were characterized before and after HF etching using X-ray diffraction (XRD) (Rigaku SmartLab 9 kW with Cu Kα radiation, λ = 0.15406 nm) and micro-Raman spectroscopy (HORIBA LabRam HR, λ_{ex}= 532 nm). The specific surface area and pore size distribution were determined at 77 K through nitrogen adsorption-desorption isotherms using a Quantachrome Autosorb-iQ MP analyzer, applying the BET method for surface area analysis and the BJH method for pore size estimation. Electron Spin Resonance (ESR) spectroscopy was conducted using a JEOL JES-FA200 spectrometer to investigate the defect states associated with oxygen vacancies in the synthesized samples. Structural, morphological, and elemental features were examined via FESEM (Zeiss Sigma) and TEM (JEM-JEOL 2010, operating at 200 kV). X-ray photoelectron spectroscopy (XPS) was performed on a Thermo Fisher ESCALAB Xi^+ to assess the oxidation states of various elements, surface defects, and surface functional groups, with spectral data processed using XPSPEAK 41. Additionally, UV-Visible (UV-Vis) absorption spectra of the organic pollutants were recorded using a Shimadzu UV-2600 spectrometer.

2.3. Results and Discussion

2.3.1. Morphology and Composition Studies

The morphology of Ti_3AlC_2 before and after HF treatment was examined using FESEM and TEM. In **Fig. 2.2(a, b)**, the FESEM images display a tightly packed layered structure of Ti_3AlC_2 MAX. After HF treatment, the tightly packed multi-layered structure transforms into a loosely packed accordion-like structure, as shown in **Fig. 2.2(c)**, due to the selective etching

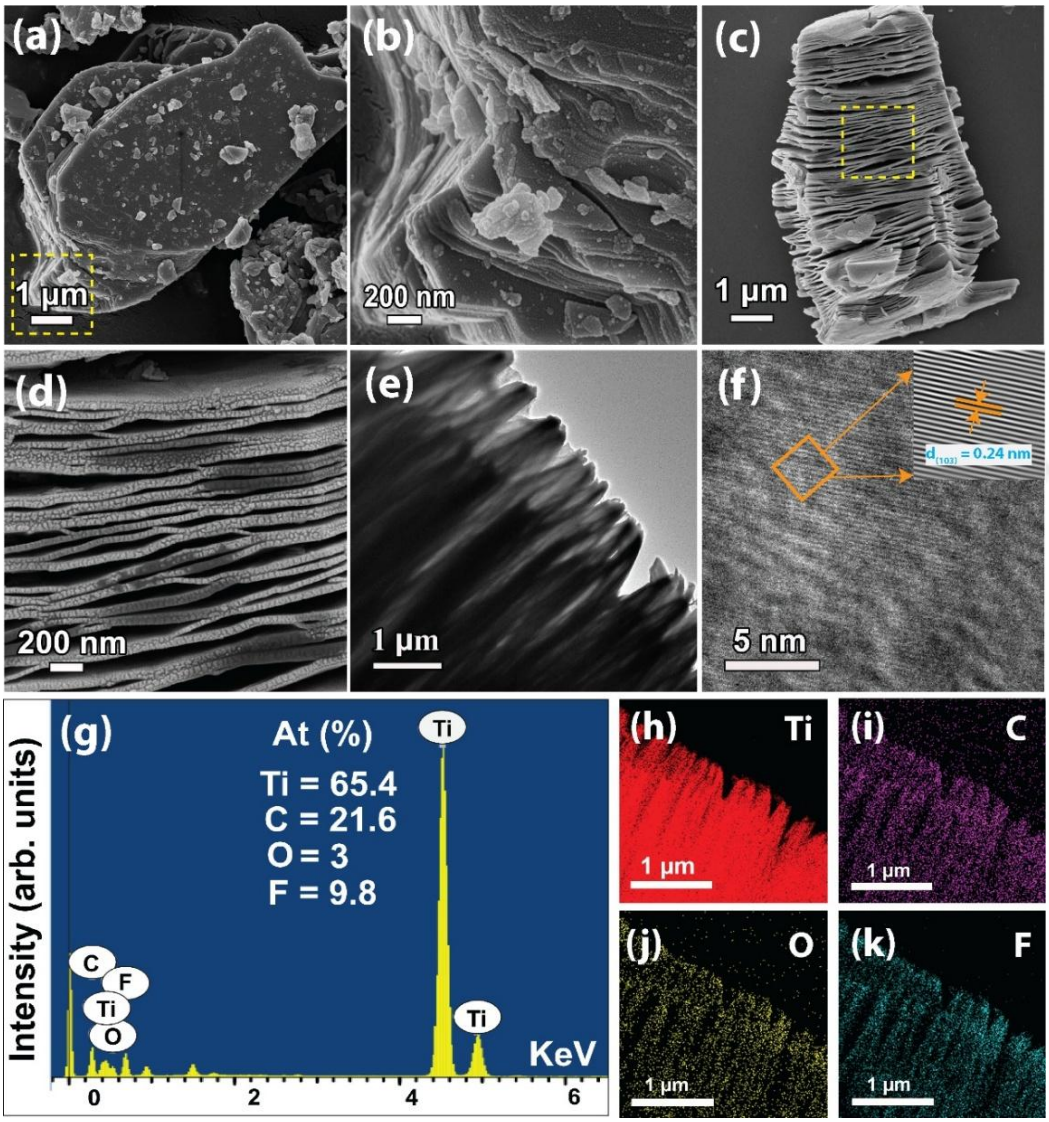

Fig. 2.2. FESEM images of (a) bulk Ti_3AlC_2 and (b) magnified edge view of the Ti_3AlC_2 bulk. (c) Ti_3AlC_2 after HF etching (m-TC40) and (d) a close-up view of the highlighted section of m-TC40. (e) TEM and (f) HRTEM lattice image of m-TC40. The inset displays an inverse fast Fourier transform (IFFT) lattice image. (g) Energy-dispersive spectrometry (EDS) and (h-k) elemental mapping of m-TC40, illustrating the elemental distribution of Ti, C, O, and F.

of Al layers. A magnified view of **Fig. 2.2(c)**, presented in **Fig. 2.2(d)**, emphasizes the presence of open channels between the layers. These channels significantly enhance the catalytically active surface area, thereby promoting the adsorption of various molecules on the material's

surface. In **Fig. 2.2 (e)**, the TEM image of m-TC40 displays a stacked layered microstructure with noticeable interlayer open channels similar to FESEM. The HRTEM image of m-TC40 (**Fig. 2.2(f)**) reveals a crystalline structure with an interplanar spacing of 0.24 nm, corresponding to the (103) lattice plane[16], which is consistent with the XRD pattern of m-TC40 as discussed later. Moreover, the EDS analysis in **Fig. 2.2(g)** indicates the atomic composition of Ti, C, O, and F at 65.4%, 21.6%, 3%, and 9.8%, respectively, with no detectable presence of Al, confirming the successful removal of Al layers. The elemental mapping in **Fig. 2.2(h-k)** further confirms the presence and distribution of Ti, C, F, and O in m-TC40.

2.3.2. Structural Characterizations

XRD analysis was conducted to investigate the structural characteristics of Ti_3AlC_2 MAX both before and after treatment with hydrofluoric acid (HF). The XRD pattern of pristine Ti_3AlC_2, depicted in **Fig. 2.3(a)**, exhibits sharp diffraction peaks at 2θ values of 9.6°, 19.1°, 34°, 36.8°, 39°, 41.8°, 45°, 48.5°, 52.3°, 56.4°, and 60.2°, which closely align with the standard diffraction data of Ti_3AlC_2 (JCPDS No. 52-0875)[17]. After HF treatment, the disappearance of the most intense diffraction peak at 2θ = 39° confirms the effective removal of Al atoms[15] from Ti_3AlC_2. Additionally, diffraction peaks at 2θ = 9°, 18.4°, and 27.8° appear with reduced intensity in comparison to pristine Ti_3AlC_2, corresponding to the (002), (004), and (006) lattice planes, respectively. A noticeable shift of the (002) and (004) peaks toward lower angles is observed in the as-prepared samples, accompanied by an increase in the full width at half maximum (FWHM) compared to pristine Ti_3AlC_2. This shift suggests an expansion of the c-lattice parameter[15], while the broadening of the peaks indicates a decrease in crystallinity. Moreover, a systematic increase in FWHM is observed with increasing HF concentration, signifying a progressive reduction in crystallinity with higher etchant concentrations. The calculated c-lattice parameters of Ti_3AlC_2 before and after HF treatment are 18.45 Å and 19.45 Å, respectively, reflecting a 5.2% expansion in the interlayer spacing along the c-axis. Such structural modifications imply the formation of a new phase, designated as multi-layered $Ti_3C_2T_x$ (m-TC) MXene. In the XRD pattern of m-TC, additional diffraction peaks at 2θ = 36.18° and 41.98° are identified, corresponding to TiC[18], which exists as an impurity in the precursor Ti_3AlC_2.

To gain further insights into the structural and surface modifications of m-TC samples, Raman spectroscopy was conducted. The Raman spectra of Ti_3AlC_2 before and after HF treatment are illustrated in **Fig. 2.3(b)**. In the Raman spectra of pristine Ti_3AlC_2, three primary peaks were identified: peak I at 269 cm^{-1}, corresponding to Ti-Al bond vibrations, and peaks II and III at

405 cm^{-1} and 612 cm^{-1}, respectively, which are associated with Ti-C bond vibrations[19]. After HF treatment, peak I in the Raman spectra of all m-TC samples nearly disappeared, signifying the effective removal of Al atoms[20] from Ti_3AlC_2. Furthermore, peaks II and III exhibited broadening and reduced intensity, which suggests lower crystallinity[20] of m-TC samples compared to the pristine Ti_3AlC_2. This observation aligns well with the XRD analysis. Additionally, a noticeable shift in peaks II and III was detected in m-TC samples, likely due to the strong interaction of surface functional groups[20] such as -F, -OH, and -O.

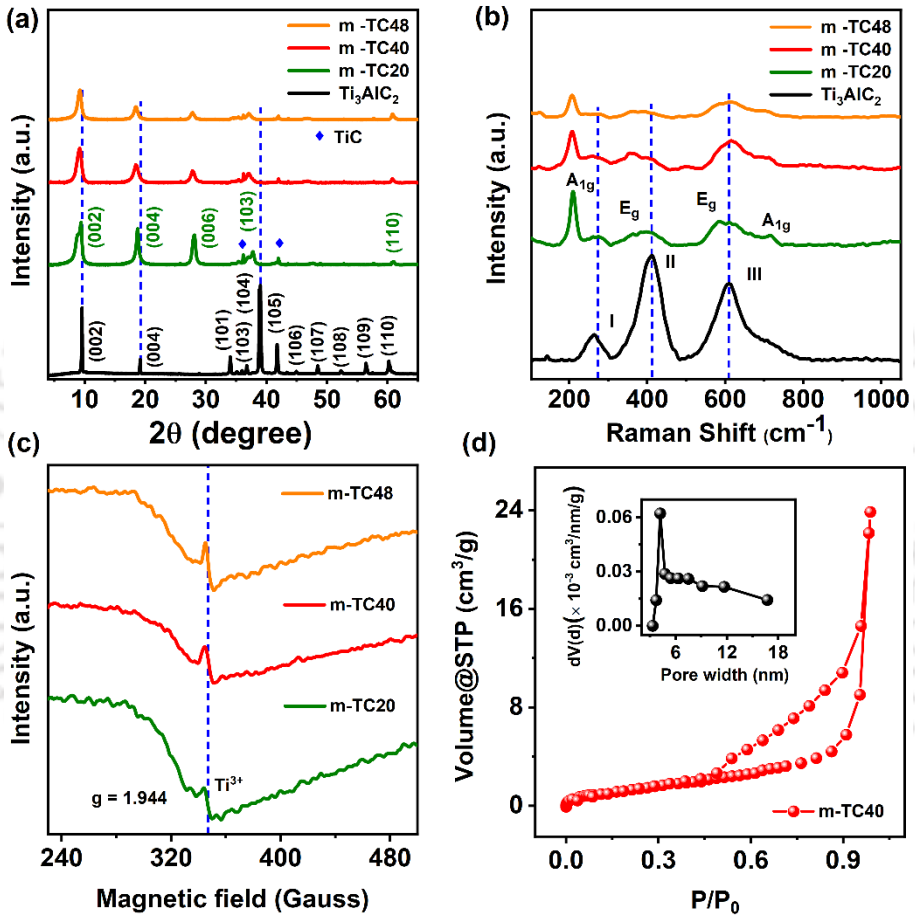

Fig. 2.3. Comparisons in (a) XRD patterns and (b) Raman spectra of Ti_3AlC_2 before and after HF treatment. (c) comparisons in the ESR signal of m-TC20, m-TC40, and m-TC48 (d) Nitrogen adsorption-desorption isotherm and BJH pore size distribution (inset) of m-TC40.

The Raman peak in m-TC samples appears at 207.6 cm^{-1} (A_{1g}), while a smaller peak is observed at 711.5 cm^{-1} (A_{1g}), corresponding to out-of-plane vibrations of the Ti-C atomic bonds[21]. A broad spectral region between 230 and 470 cm^{-1} is attributed to the in-plane (E_g) vibrations of surface groups (-F, -OH, and -O) chemically bonded to Ti atoms[21]. Additionally, vibrational modes in the range of 540-730 cm^{-1} primarily correspond to carbon-related vibrations[21] in both E_g and A_{1g} modes.

2.3.3. ESR and BET Analysis

Further, the ESR signal depicted in **Fig. 2.3(c)** displays prominent peaks at "g" values of 1.94 corresponding to Ti^{3+}.[22] It's noteworthy that as the concentration of HF increases, the peak intensity of the Ti^{3+} state also increases. This confirms that a higher concentration of HF can produce higher defect states. Therefore, the defect states can be controlled by precisely controlling the concentration of HF etchant. The porosity of micro-structured m-TC40 surfaces was analyzed using nitrogen adsorption-desorption isotherms, as shown in **Fig. 2.3(d)**. The type IV isotherm confirms the mesoporous structure, with a BET surface area of 5.442 m^2/g. The BJH method revealed a pore size distribution between 2.6 and 13.3 nm. This mesoporous characteristic improves the adsorption of various pollutants on its surface and enhances their degradation rate.

2.3.4. XPS Analysis

XPS was employed to analyze the chemical composition and oxidation states of elements in the as-prepared m-TC40 sample. The survey scan XPS spectrum, shown in **Fig. 2.4(a)**, was recorded over a binding energy (BE) range of 200 - 800 eV and confirms the presence of Ti,

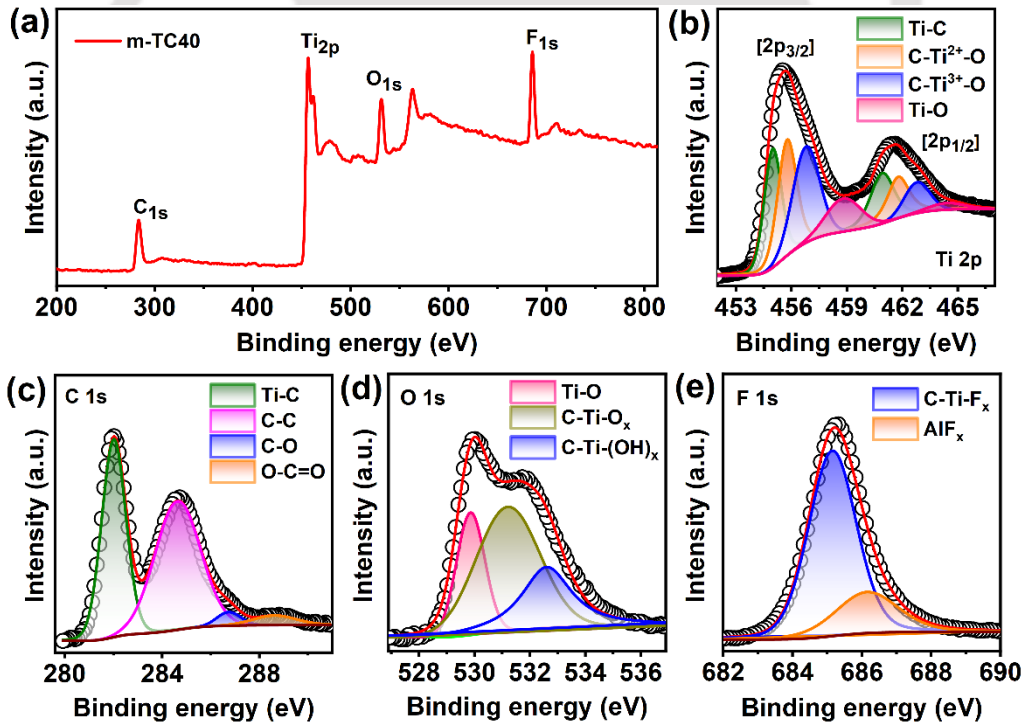

Fig. 2.4. (a) XPS survey scan of m-TC40. High-resolution XPS spectra of m-TC40 for (b) Ti 2p, (c) C 1s, (d) O 1s, and (e) F 1s. The symbols represent experimental data, while the solid lines indicate Gaussian-Lorentzian fitted spectra with a Shirley background.

C, O, and F in the sample. The core-level XPS spectrum of Ti 2p, depicted in **Fig. 2.4(b)**, displays a characteristic doublet at approximately 455.3 eV (Ti $2p_{3/2}$) and 461.3 eV (Ti $2p_{1/2}$).

Deconvolution of the Ti $2p_{3/2}$ region reveals four distinct peaks entered at ~ 455.1, 456, 456.9, and 458.7 eV, corresponding to Ti-C, O-Ti^{2+}-C, O-Ti^{3+}-C, and Ti^{4+} states, respectively[23]. The relative percentages of various low-valent Ti states are summarized in **Table 2.1**. **Fig. 2.4(c)** illustrates the core-level XPS spectrum of C 1s, which has been fitted with four peaks located at ~ 282, 284.7, 286.6, and 288.6 eV. These peaks are assigned to Ti-C, C-C, C-O[23], and O=C-O, respectively[24]. The presence of the C-O peak is likely a result of solvent residues from the drying process. The O 1s core-level spectrum, shown in **Fig. 2.4(d)**, was deconvoluted into three peaks centred at ~ 529.8, 531.1, and 531.9 eV, which are attributed to Ti-O, C-Ti-O_x, and C-Ti-$(OH)_x$, respectively[23]. Additionally, their relative percentages are summarized in **Table 2.1**. The high-resolution F 1s spectrum in **Fig. 2.4(e)** was fitted with two peaks at ~685.1 and 686.2 eV, corresponding to C-Ti-F_x and AlF_x, respectively[23]. These XPS findings confirm the presence of surface functional groups such as -F, -O, and -OH in the as-prepared m-TC40 sample. Furthermore, XPS analysis of the high-resolution Ti 2p spectrum indicates that the majority of Ti species exist in Ti^{2+} and Ti^{3+} oxidation states, suggesting the presence of oxygen vacancies within the lattice structure.

2.3.5. Catalytic Degradation of Organic Pollutants

Here, we have explored the potential of m-TC40 as a Fenton catalyst for degrading various pollutants, including MB, 4-NP, and ciprofloxacin, from wastewater, focusing on its surface, structural, and compositional characteristics. The presence of low-valent Ti elements (Ti^{2+} and Ti^{3+}) can play a significant role in enhancing the degradation of organic pollutants by serving

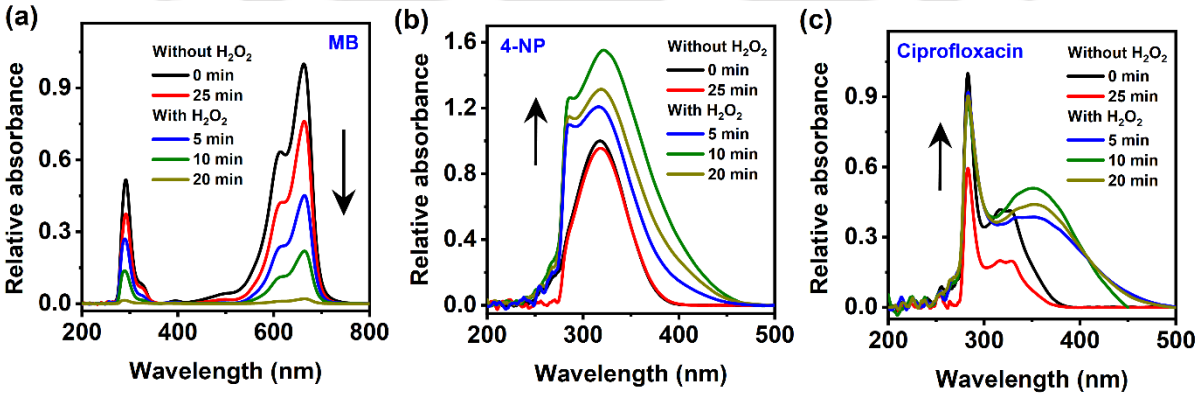

Fig. 2.5. UV-Vis absorption spectra of (a) MB, (b) 4-NP, and (c) CIP before and after the addition of H_2O_2.

as active sites for pollutant adsorption and facilitating electron transfer for H_2O_2 activation. As shown in **Fig. 2.5(a)**, MB degradation occurs spontaneously after the addition of H_2O_2, which is evident from the decreasing absorbance over time. However, for 4-nitrophenol (4-NP) and ciprofloxacin (CIP) (**Fig. 2.5(b, c)**), the absorbance increases instead, possibly due to the

formation of reaction intermediates with higher absorbance than their parent compounds.[25] Consequently, the m-TC40 + H_2O_2 system is ineffective for degrading 4-NP and CIP. Therefore, our study focuses on the catalyst's performance in MB dye degradation, which is detailed in the following sections.

2.3.5.1. Zeta Potential and MB Dye Adsorption Study

The surface polarity of the synthesized m-TC40 was evaluated through Zeta potential measurements across different pH values (2 - 12) of the solvent, as depicted in **Fig. 2.6(a)**. The results indicate a significant decrease in Zeta potential from -3.4 mV to -37.1 mV, with

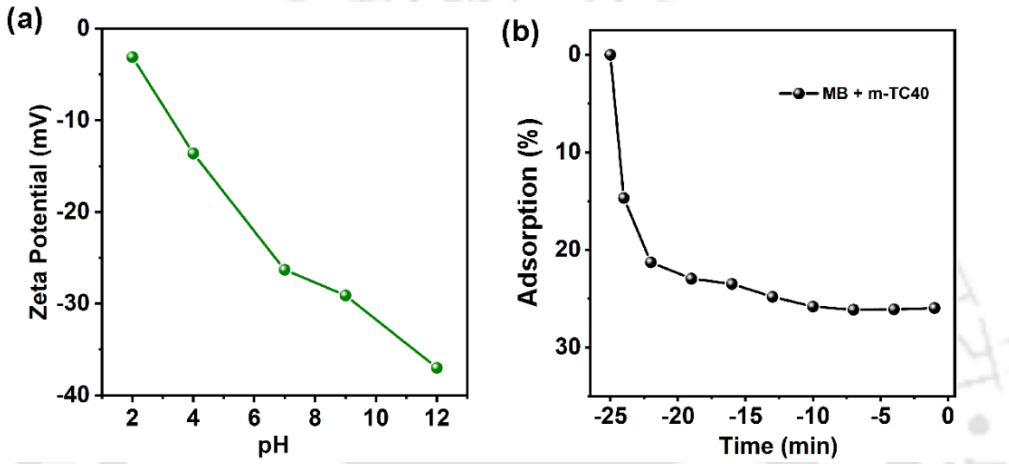

Fig. 2.6. (a) Dependence of the Zeta potential of m-TC40 on the pH of the solution. (b) Adsorption efficiency of MB on m-TC40 in the absence of H_2O_2 under dark conditions.

increasing pH value 2 to 12, confirming the negatively charged surface[11, 18] of m-TC40. This negatively charged surface facilitates the adsorption of cationic MB dye molecules through electrostatic attraction. Furthermore, in the dark, MB adsorption-desorption process reached equilibrium within 20 min (**Fig. 2.6(b)**), which can be attributed to the strong adsorption of MB molecules onto the negatively charged surface of m-TC40, which demonstrated an MB removal efficiency of ~24%.

2.3.5.2. Catalytic MB Degradation

The dye degradation performance of the as-synthesized catalysts was evaluated by monitoring the decomposition of MB in the presence of H_2O_2 under dark conditions. **Fig. 2.7(a)** illustrates the colour change in the MB solution after H_2O_2 (0-24 min) addition with the presence of m-TC40. The UV-Vis absorption spectra depicted in **Fig. 2.7(b)** reveal the spectral alterations of the MB solution, where the characteristic absorption peak at 664 nm steadily decreases within 24 min after the addition of H_2O_2. After the degradation process, the absorption spectra of the remaining solution showed no peak within the 400-800 nm range, indicating the complete

breakdown of the MB dye molecules. **Fig. 2.7(c)** compares the degradation efficiency of different catalysts. In dark conditions, the adsorption-desorption process of MB achieved equilibrium in 20 min, which is likely due to the adsorption of MB molecules on the surface of bare m-TC40, resulting in around 24% MB removal efficiency. The as-prepared m-TC40 has a negative zeta potential, signifying a negatively charged surface. This negative charge enhances the attachment of cationic MB dye molecules to the m-TC40 surface through electrostatic attraction. Further, the introduction of a small amount of H_2O_2 (100 µL, 10 M) led to the complete degradation of MB within 24 min. Interestingly, m-TC48 and m-TC20 exhibited 100% and 35% MB degradation efficiency in 18 and 24 min, respectively.

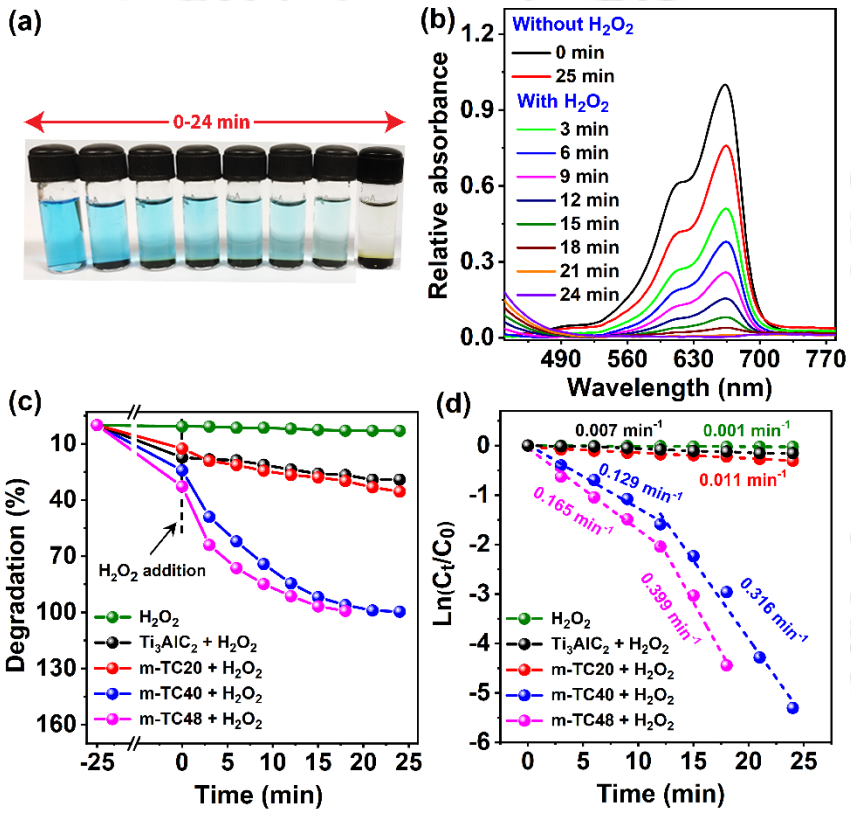

Fig. 2.7. (a) Digital images illustrating the MB degradation process. (b) UV-Vis absorption spectra of MB were recorded at an interval of 3 min during the degradation process. (c) Comparative analysis of the catalytic efficiency of various catalysts in MB degradation under dark conditions. (d) A plot of $\ln(C_t/C_0)$ vs time (t) with linear fitting shows the first-order degradation rate constant.

On the other hand, H_2O_2 alone can degrade only 3% of the MB dye under dark conditions. Moreover, the combination of the MAX precursor Ti_3AlC_2 with H_2O_2 showed a degradation efficiency of about 28% in 24 min, which is significantly lower than that achieved by m-TC40 + H_2O_2. The results mentioned above clearly demonstrate the combined effect of m-TC40 and H_2O_2 in degrading MB molecules. The degradation kinetics of MB dye can be characterized by pseudo-first-order rate kinetics, described by the Langmuir-Hinshelwood equation:

$$\ln (C_t/C_0) = -kt \qquad (1)$$

Where C_0 and C_t represent absorbance of dye solution initially and at any given time t (min) after the introduction of H_2O_2, and k is the rate constant (min^{-1}). Our experimental results indicate that MB degradation follows pseudo-first-order kinetics. We plotted this relationship for H_2O_2, m-TC20 + H_2O_2, m-TC40 + H_2O_2, and m-TC48 + H_2O_2, as illustrated in **Fig. 2.7(d)**. The plot of $ln(C_t/C_0)$ versus time (t) for bare H_2O_2 and m-TC20 + H_2O_2 reveals a single linear decay with rate constants of 0.001 and 0.011 min^{-1}, respectively. In contrast, the $ln(C_t/C_0)$ vs t plots for m-TC40 + H_2O_2 and m-TC48 + H_2O_2 display two distinct linear decay phases, each characterized by different rate constants. For the first phase, the rate constants (k_1) are 0.129 and 0.165 min^{-1}, while for the second phase (k_2), they are 0.316 and 0.399 min^{-1}, respectively. The physical reasons behind the dual rate constants observed in the MB degradation kinetics will be discussed later. Although m-TC40 and m-TC48 have comparable dye degradation rates, we chose m-TC40 as the optimal material for our experiments due to its higher crystalline structure.

2.3.5.3. Effect of m-$Ti_3C_2T_x$ Loading

In this study, m-TC40 plays a pivotal role in the degradation of MB by facilitating its adsorption and enhancing the generation of ·OH radicals in the presence of H_2O_2. To determine the optimal catalyst loading for MB degradation, experiments were conducted by varying the amount of m-TC40 while maintaining a fixed H_2O_2 concentration of 100 µL (10 M). As illustrated in **Fig. 2.8(a)**, the degradation efficiency of MB increased significantly from 49% to 88% within 24 min as the catalyst dosage was raised from 20 mg to 25 mg. Further increasing the m-TC40 dosage to 30 mg resulted in complete (100%) MB degradation within the same duration. This enhancement in degradation efficiency can be attributed to the increased total surface area, which provides additional active sites for H_2O_2 activation and subsequent ·OH radical formation. Interestingly, when the catalyst loading was further increased to 35 mg, the rate of MB degradation did not improve; instead, a slight reduction was observed, although the overall degradation efficiency remained unchanged. This phenomenon could be attributed to the overlapping of active sites or the excessive generation of ·OH radicals, which may react with H_2O_2 to form less reactive HO_2· radicals, thereby limiting MB degradation efficiency. Consequently, 30 mg of m-TC40 was identified as the optimal catalyst dosage and was used for all subsequent experiments.

2.3.5.4. Effect of H_2O_2 Concentration

Here, H_2O_2 played a crucial role as both an oxidizing agent and a source of ·OH radicals in the presence of m-TC40 MXene. To evaluate its influence on MB degradation efficiency by

enhancing ·OH radical production, experiments were conducted by varying the H_2O_2 concentration (12 - 28 mM) while maintaining a fixed m-TC40 catalyst dosage of 30 mg. As shown in **Fig. 2.8(b)**, the MB degradation efficiency increased significantly from 59% to 94% within 24 min as the H_2O_2 concentration was raised from 12 mM to 16 mM. When the concentration was further increased to 20 mM, nearly complete (~100%) MB degradation was achieved within the same duration. However, a further increase in H_2O_2 concentration to 28 mM resulted in a slight decline in degradation efficiency to ~ 97%. Therefore, 20 mM was identified as the optimal H_2O_2 concentration for this study and was maintained for all subsequent experiments. The observed decrease in efficiency at higher H_2O_2 concentrations could be attributed to the formation of less reactive HO_2· radicals, which may arise from the reaction between excess ·OH radicals and H_2O_2.

2.3.5.5. Effect of MB Concentration

The effect of varying MB concentrations (20-50 µM) on degradation efficiency was investigated to determine the maximum MB degradation capacity of the m-TC40 + H_2O_2-based AOP system. These experiments were conducted using 30 mg of m-TC40 and 100 µL of H_2O_2 in a dark environment, with different MB concentrations (20 - 50 µM) prepared in 50 mL of an aqueous solution. As illustrated in **Fig. 2.8(c)**, the degradation efficiency of MB was found to be strongly influenced by its initial concentration. An increase in MB concentration led to a decline in degradation efficiency over a 24 min reaction period. Specifically, the degradation efficiency was ~91% and 82% for MB concentrations of 30 µM and 40 µM, respectively, while it dropped to 52% at 50 µM. This trend is expected, as the production rate of ·OH radicals remains limited for a fixed amount of m-TC40 and H_2O_2, making it insufficient to completely degrade higher concentrations of MB.

2.3.5.6. Effect of Solution pH

The Fenton oxidation reaction is generally more efficient under acidic conditions due to the higher oxidative potential of ·OH radicals in acidic media compared to neutral and basic environments. To examine the influence of the initial pH on MB degradation efficiency, a series of experiments was conducted at room temperature with solution pH values of ~ 2, 4, 9, and 12. The natural pH of the MB solution, without any acid or base addition, was measured to be 6.7. The pH levels of the MB dye solutions were adjusted using 0.1 M HCl and NaOH solutions, while the concentrations of m-TC40 and MB dye were kept constant at 30 mg and 20 µM, respectively. As depicted in **Fig. 2.8(d)**, MB degradation efficiency varied significantly with the pH of the solutions. A decrease in pH led to a substantial increase in degradation

efficiency. At pH 2, ~95% degradation was achieved within 9 min, whereas at pH 4, the efficiency was 83% in the same duration. With an extended reaction time of 24 min, the degradation efficiency further increased to ~97% and ~98% at pH 2 and 4, respectively,

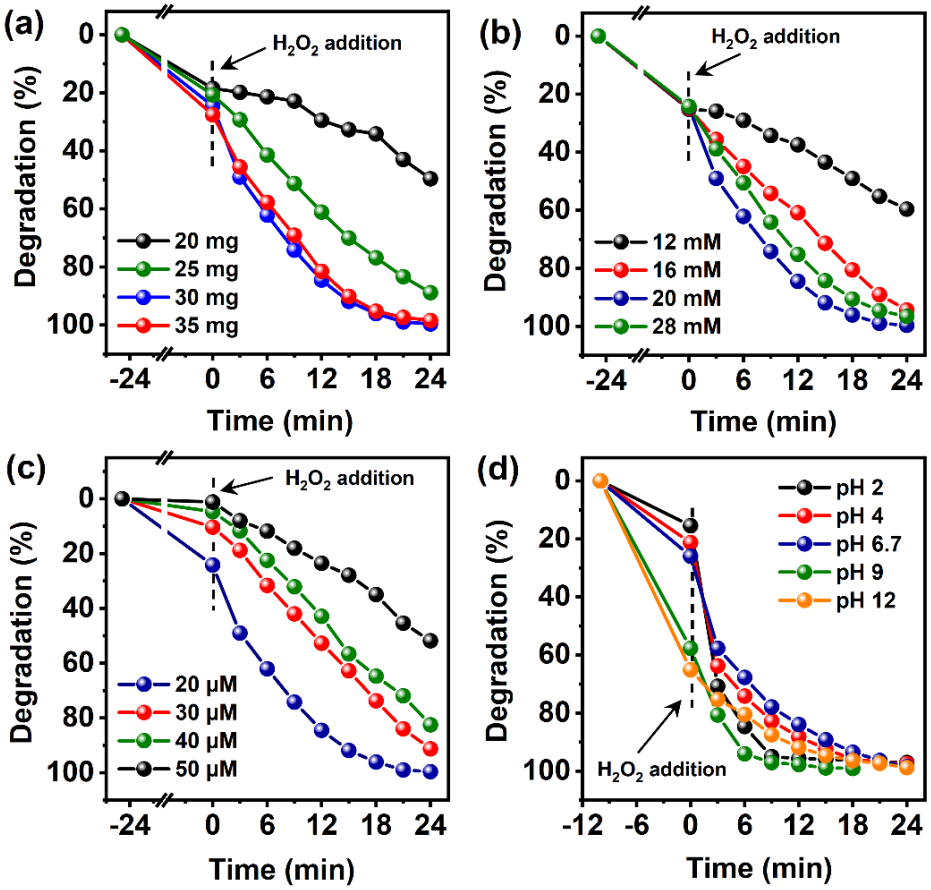

Fig. 2.8. The efficiency of MB dye degradation was evaluated by examining the influence of the following parameters: (a) the loading of the m-TC40 catalyst with a fixed H_2O_2 concentration of 20 mM; (b) the concentration of H_2O_2 with fixed m-TC40 loading of 30 mg; (c) the initial MB concentration and (d) the solution pH, with the H_2O_2 concentration set at 20 mM and m-TC40 loading fixed at 30 mg.

indicating a higher reaction rate in acidic conditions. This enhanced degradation at lower pH can be attributed to the negatively charged surface of m-TC40 (**Fig. 2.6(a)**), which facilitates greater adsorption of positively charged species, thereby promoting interactions between m-TC40 and H_2O_2 through electrostatic attraction. The observed decrease in Zeta potential with increasing pH suggests an increase in negative surface charge density. At pH 9 and 12, MB degradation efficiencies of 98% and 92% were achieved in 12 min. With an extended reaction time of 24 min, the efficiencies increased to ~99% and ~98% at pH 9 and 12, respectively. The improved degradation performance in basic conditions can be attributed to the increased negative surface charge of m-TC40 (**Fig. 2.6(a)**), which enhances the adsorption of cationic MB molecules. However, it is well documented that ·OH radicals exhibit lower degradation

efficiency in alkaline media, which is evident from the slower degradation observed at pH 12 compared to pH 9. This suggests a reduction in the effectiveness of ·OH radicals in MB degradation with increasing pH. Nevertheless, the combined effects of surface adsorption and ·OH radical generation contributed to the overall enhancement in MB degradation efficiency. These findings highlight the ability of the m-TC40 catalyst to facilitate dye degradation over a broad pH range, underscoring its potential for practical applications.

2.3.6. Scavenging Test and Cyclic Stability

To confirm the generation of ·OH radicals and their role in MB degradation, a scavenging test was performed using DMSO as a ·OH radical scavenger and p-BQ as an O_2·- scavenger. DMSO reacts with ·OH radicals to form ·CH_3 radicals, which produce methane and ethane. **Fig. 2.9(a)** shows that adding 0.03 mol/L DMSO reduced MB degradation efficiency from 100% to 57%, and increasing DMSO to 0.06 mol/L further decreased degradation to 37%. Conversely, adding 0.01 mol/L p-BQ had little effect, with degradation efficiency remaining at 98% after 24 min. These results confirm that ·OH radicals are the main active species driving MB degradation. For practical use and commercial application in wastewater treatment, the recyclability of catalysts is crucial.

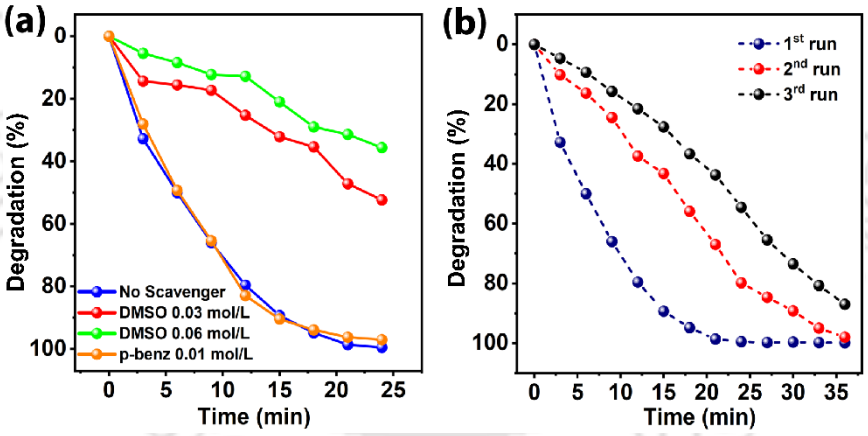

Fig. 2.9. (a) Influence of free radical scavengers on the degradation of MB. (b) Cyclic stability of the m-TC40 catalyst in MB degradation under identical conditions.

The cyclic stability of m-TC40 in MB degradation is illustrated in **Fig. 2.9(b)**. To compensate for the loss of material during the centrifugation and cleaning process, 6 mg of pure m-TC40 was added for the 2nd and 3rd cycles. In the 1st cycle, complete MB degradation was achieved within 24 min. However, degradation efficiency decreased from 100% to 80% in the 2nd and 55% in the 3rd cycle within the same timeframe. Extending the reaction time to 36 min improved degradation efficiency to 98% and 87% in the 2nd and 3rd cycles, respectively. The decline in efficiency may be due to the oxidation of Ti^{2+} and Ti^{3+} states to Ti^{4+}, as discussed in

the later section, and leading to a reduced production rate of ·OH radicals in subsequent cycles. Another possible reason could be the adsorption of degraded products on the active sites of m-TC40.

2.3.7. Post-Degradation Catalyst Stability

XRD analysis of m-TC40 before and after MB degradation (**Fig. 2.10(a)**) indicates a significant decrease in peak intensity, reflecting reduced crystallinity due to the reaction with H_2O_2. The increased TiO_2 peak suggests the formation of Ti^{4+} states, which diminishes catalytic activity.

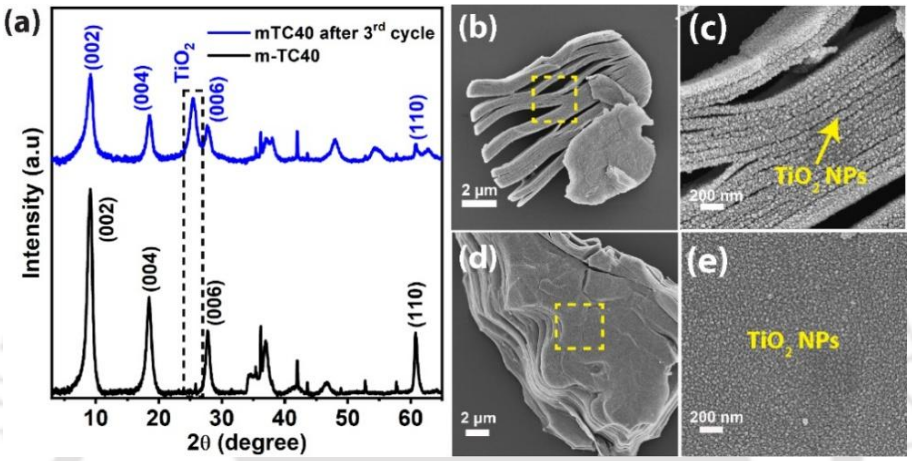

Fig. 2.10. (a) The XRD patterns of m-TC40 before and after the 3rd cycle of MB degradation. (b, d) FESEM images of m-TC40 following the third cycle of MB degradation. (c, e) Enlarged views of the selected regions from images (b) and (d), respectively.

The FESEM images in **Fig. 2.10(b, d)** reveal that m-TC40 maintains its multi-layered structure after MB degradation. The magnified views in **Fig. 2.10(c, e)** indicate the formation of TiO_2 nanoparticles within the interlayer spaces and on the surface, which leads to a reduction in its catalytic activity. Further, XPS analysis in **Fig. 2.11(a)** reveals the changes in Ti 2p core-level spectrum, before and after MB degradation, as summarized in **Table 2.1**. Initially, the percentages of Ti^{2+} and Ti^{3+} states are 23.8% and 24.7%, respectively, with a minor presence of Ti^{4+} (9.1%). After the degradation process, Ti^{2+} decreases to 15.8%, while Ti^{3+} rises to 29.7%, indicating conversion from Ti^{2+} to Ti^{3+}, whereas the Ti^{4+} state increases significantly to 36.2%, with BE shifts to 459.02 eV for Ti $2p_{3/2}$ and 464.8 eV for Ti $2p_{1/2}$, signifying the formation of titanium peroxide. Further, O1s XPS spectrum in **Fig. 2.11(b)** displays an increased Ti-O peak at 530.3 eV and a shifted Ti-OH peak at 531.8 eV, consistent with titanium peroxide. The decrease in the relative percentages of the Ti-OH peak (**Table 2.1**) implies that -OH acts as an MB adsorption site and plays a crucial role in the degradation process. Hence, XPS confirms the conversion of Ti^{2+} and Ti^{3+} to Ti^{4+} and reduces m-TC40's catalytic efficiency. Additionally, **Fig. 2.11(c)** presents a comparative analysis of the core-level XPS spectra of

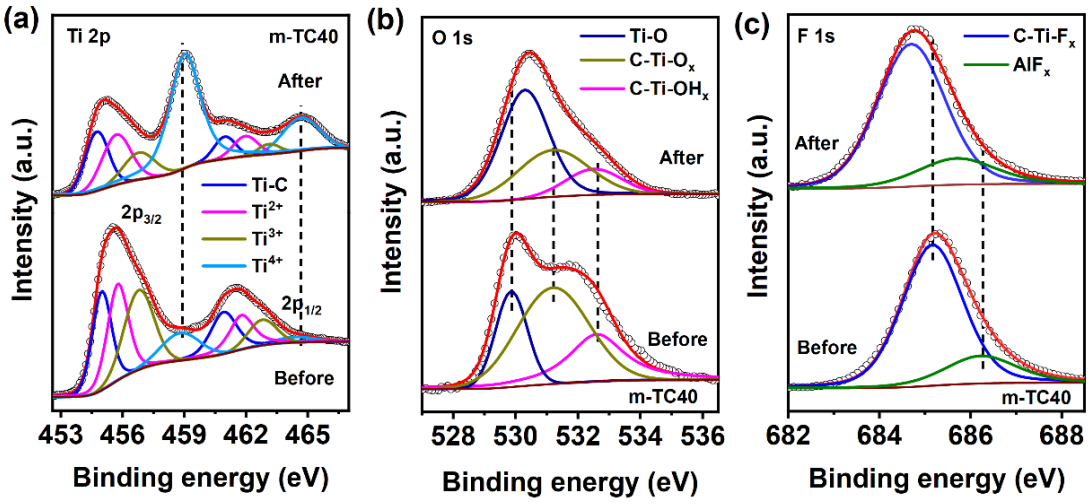

Fig. 2.11. High-resolution XPS spectra of (a) Ti 2p, (b) O 1s, and (c) F 1s recorded after the first cycle of the MB degradation experiment. The symbol represents experimental data, while the solid lines correspond to Gaussian-Lorentzian fitted spectra using a Shirley baseline.

F 1s before and after degradation. The results indicate a shift in the peak corresponding to the -F surface group to a lower binding energy of 684.8 eV. This shift suggests that the -F surface groups serve as active sites for adsorption. However, almost no change in the relative percentage of the C-Ti-F_x peak was observed.

Table 2.1. *The relative area under the peaks from XPS data represents the various elemental states of as-synthesised, post MB degradation, and air-annealed m-TC40 samples.*

Sample	**Ti 2p (%)**				**F 1s (%)**		**O 1s (%)**		
m-TC40	Ti-C	Ti^{2+}	Ti^{3+}	Ti^{4+}	Ti-F_x	AlF_x	Ti-O	Ti-OH_x	Ti-O_x
as-synthesized	30	31	28	11	80	20	22	27	50
Post-MB degradation	18	19	11	53	81	19	54	14	32
Air annealed	-	-	-	100	-	-	70.5	17.2	12.2

2.3.8. Mechanism of Catalytic Dye Degradation

The XPS spectra of m-TC40 before MB degradation indicate that the majority of Ti is in the Ti^{2+} and Ti^{3+} states, which are associated with surface oxygen vacancies and serve as active sites for H_2O_2 adsorption and activation. Upon contact with H_2O_2, the Ti^{2+} on the surface of m-

TC40 reacts with H_2O_2, generating Ti^{3+} and ·OH radicals. Similarly, Ti^{3+} reacts with H_2O_2 to produce Ti^{4+} and ·OH radicals. This transformation is evident in the XPS spectra of Ti 2p after MB degradation (**Fig. 2.11(a)**). Interestingly, the formed Ti^{4+} state is the combination of TiO_2 and Ti-O-O-Ti (titanium peroxide) complex, as confirmed by the XPS spectra of Ti 2p and O 1s after the 1st cycle of MB degradation (**Fig. 2.11(b)**). The BE of Ti^{4+} at 459.02 eV in Ti 2p, Ti-O at 530.3 eV, and Ti-OH at 531.8 eV in the O 1s spectra are consistent with reported values for titanium peroxide. This titanium peroxide further reacts with H_2O to produce ·OH radicals and improve degradation kinetics, the possible reaction mechanism is provided below:

$$Ti^{2+} + H_2O_2 \rightarrow Ti^{3+} + {\cdot}OH + OH^-$$

$$Ti^{3+} + H_2O_2 \rightarrow Ti^{4+} + {\cdot}OH + OH^-$$

$$Ti^{4+}(Ti\text{-}O\text{-}O\text{-}Ti) + H_2O \rightarrow Ti^{4+} + {\cdot}OH + OH^-$$

$$H_2O_2 + {\cdot}OH \rightarrow H_2O + HO_2{\cdot}$$

$$\text{Organic wastes} + {\cdot}OH \rightarrow \text{Degraded products}$$

The observed dual-slope behaviour in the MB degradation kinetics can be attributed to the distinct reactivities of Ti^{2+} and Ti^{3+} with H_2O_2. In the initial stage, the higher reducing

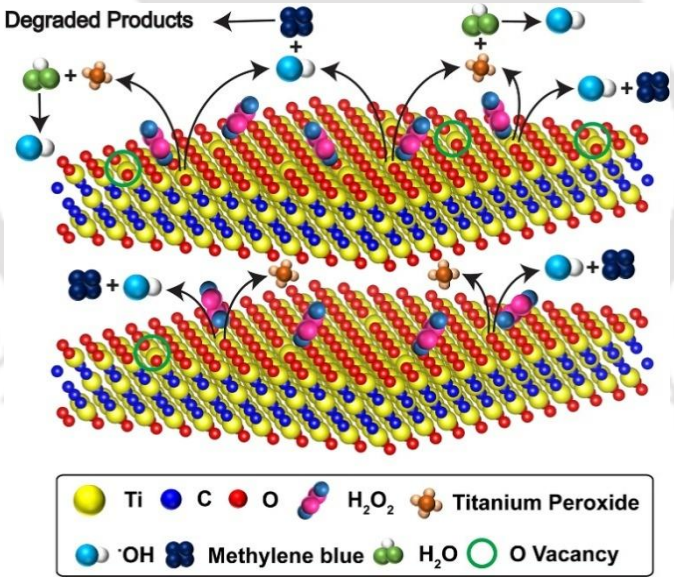

Fig. 2.12. Schematic illustration of the mechanism underlying MB dye degradation on the surface of m-TC40 in the presence of H_2O_2.

capability of Ti^{2+} facilitates the electron transfer necessary to activate H_2O_2, leading to the generation of hydroxyl radicals and the conversion of Ti^{2+} to Ti^{3+}. In the subsequent stage, both Ti^{2+} and Ti^{3+} participate in the degradation process, thereby enhancing the overall degradation rate. A schematic representation of MB degradation on the surface of m-TC40 in the presence

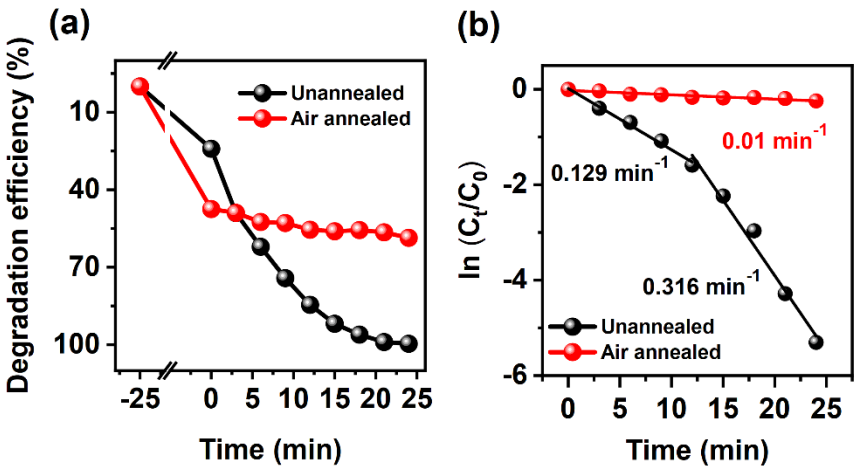

Fig. 2.13. (a) Comparative analysis of the catalytic efficiency of unannealed and air-annealed m-TC40 for MB degradation. (b) Linear fitting of ln (C_t/C_0) versus time (t) plots shows the MB degradation rate constant.

of H_2O_2 is illustrated in **Fig. 2.12**. To further validate the proposed degradation mechanism, we annealed m-TC40 samples at 300 °C for 1 h in air and conducted MB degradation experiments with the air-annealed samples. The conditions were kept identical to compare the catalytic performance of unannealed and air-annealed m-TC40. As shown in **Fig. 2.13**, the air-annealed m-TC40 exhibited significantly lower dye degradation efficiency (~ 10%) with a degradation

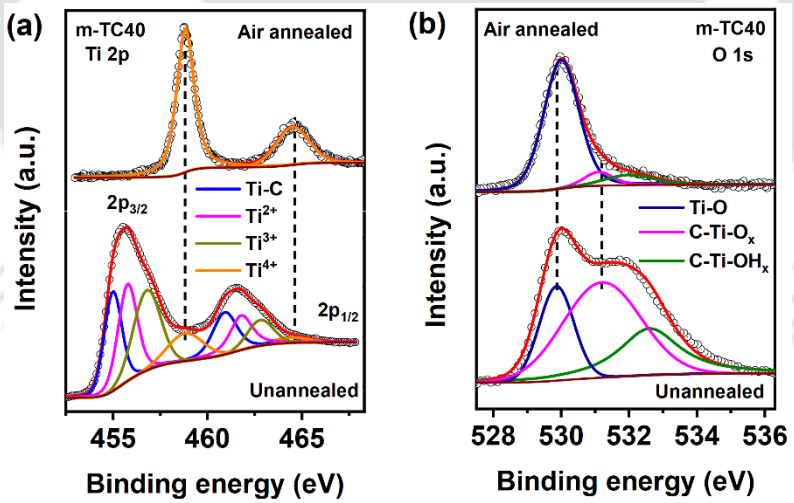

Fig. 2.14. High-resolution XPS spectra comparison of (a) Ti 2p and (b) O 1s for unannealed and air-annealed m-TC40 samples. The experimental data are represented by symbols, while the solid lines indicate Gaussian-Lorentzian fitted spectra based on a Shirley baseline.

rate of 0.01 min^{-1} despite having a higher MB adsorption capacity (~48%) than the unannealed sample. To investigate the reasons for the reduced catalytic efficiency, a comparative XPS analysis was performed on both unannealed and air-annealed samples. **Fig. 2.14(a)** shows that the Ti 2p XPS spectra of unannealed m-TC40 have Ti^{2+}, Ti^{3+}, and Ti^{4+} states at 23.8%, 24.7%, and 9.1%, respectively, while the air-annealed m-TC40 contains only Ti^{4+} at 100%. This indicates that Ti^{2+} and Ti^{3+} states are eliminated after annealing, leading to the removal of low-

valence Ti states and oxygen vacancies, which destroy the catalytic activity of m-TC40. **Fig. 2.14(b)** compares the O 1s XPS spectra, revealing a reduction in -OH groups from 46.7% in unannealed m-TC40 to 17.2% in air-annealed m-TC40 and a decrease in $-O_x$ groups from 21.6% to 12.2%. Thus, it can be concluded that the catalytic dye degradation is primarily due to the low-valence Ti sites (Ti^{2+} and Ti^{3+}) and oxygen vacancies in m-TC40.

2.3.9. Degradation of Cationic and Anionic Dyes

To evaluate the degradation efficiency of other dyes, Rhodamine B (RhB) and Methyl orange (MO) were selected respectively. **Fig. 2.15(a and b)** display the UV-Vis absorption

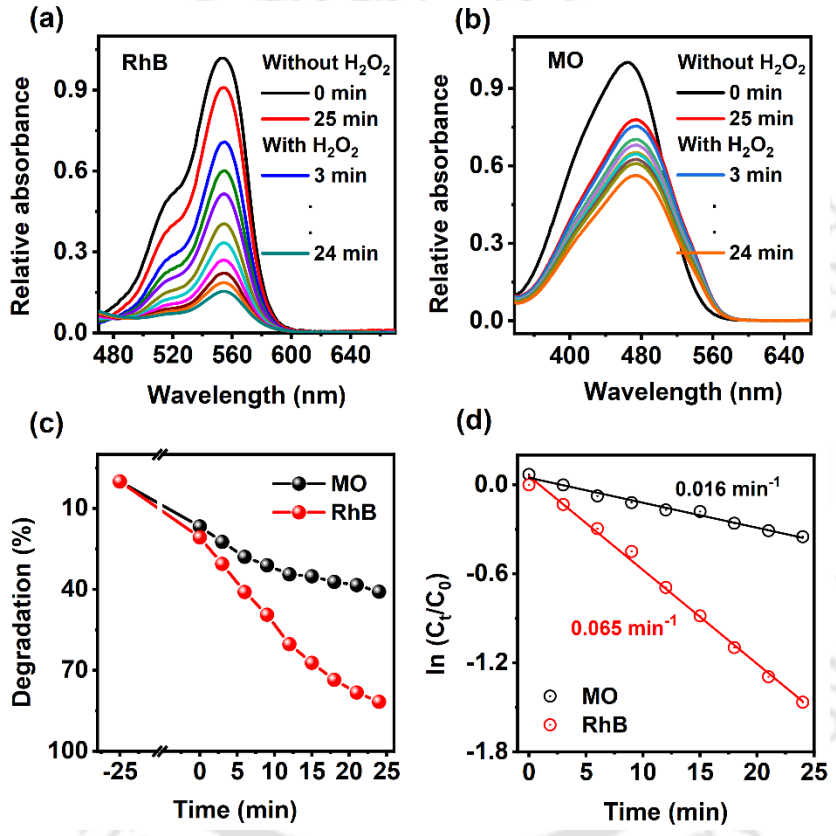

Fig. 2.15. UV-visible absorption spectra of (a) RhB and (b) MO dyes (c) Comparative analysis of the degradation efficiency of RhB and MO dyes (d) A plot of ln (C_t/C_0) vs time (t) with linear fitting shows their first-order degradation rate constant

spectra of RhB and MO solutions, before and after the introduction of H_2O_2, along with the catalyst. **Fig. 2.15(c)** shows their degradation efficiencies. Initially, RhB achieved an adsorption efficiency of ~21% in 25 min. However, after adding H_2O_2, its degradation efficiency becomes ~82% in 24 min, attributed to the rapid oxidation by ·OH radicals generated on the m-TC40 surface. In contrast, the anionic nature of MO leads to electrostatic repulsion from the negatively charged m-TC40, resulting in a lower degradation efficiency of ~40%. The degradation kinetics in **Fig. 2.15(d)** illustrated the reaction rate constants of 0.065 min^{-1} for

RhB and 0.013 min^{-1} for MO. Moreover, these results indicate that MB degrades at a faster rate than both RhB and MO. Although both MB and RhB are cationic dyes, MB exhibits a much higher degradation rate. This difference is likely attributable to their molecular size disparity; MB is approximately 1 nm in size, while RhB measures around 1.6 nm. The larger dimensions of RhB result in less efficient surface adsorption compared to MB, which ultimately reduces its degradation rate. Additionally, a comparative analysis of the degradation performance of bare m-TC40 catalyst, with reported $Ti_3C_2T_x$-based composites, is summarized in **Table 2.2**.

Table 2.2. *Comparison of MB and RhB* degradation *performance of bare m-$Ti_3C_2T_x$ with reported literatures.*

Catalyst	Pollutant	Experimental Conditions	Reaction Time (min)	Degradation efficiency (%)/Adsorption capacity (mg/g)	Ref.
mp-MXene/TiO_{2-x} nanodots (NDs)	RhB (30mg/L)	Catalyst (150mg/L) + sunlight irradiation + H_2O_2 (0.7mM)	10	96	[12]
MXene–Co_3O_4 nanoco-mposites	MB (12.5mg/L)	Catalyst (10 mg) + H_2O_2 (15 ml)	300	128.91 mg/g	[26]
(111) TiO_{2-x}/Ti_3C_2 -12 hr	MB (20mg/L)	Catalyst (50 mg/L) + 500 W Xe lamp, <400 nm	150	75	[27]
Ti_3C_2-Fe_3O_4 MNPs	MB (20 mg/L)	Catalyst (0.5g/L) + H_2O_2 (50 mM/L)	6	100	[28]
CdS@Ti_3C_2@TiO_2 nanocom-posite	MB (20mg/L)	Catalyst (250 mg/L) + vis light irradiations 300 W Xe lamp (λ < 400 nm)	88	100	[29]
m-$Ti_3C_2T_x$	MB (6.4 mg/L)	Catalyst (0.6 gm/L) + H_2O_2 (20 mM)	24	100	**This work**
m-$Ti_3C_2T_x$	RhB (6.4 mg/L)	Catalyst (0.6 gm/L) + H_2O_2 (20 mM)	24	82	**This work**

2.4. Conclusions

We have successfully synthesized an accordion-like microstructure of Ti_3C_2Tx MXenes (m-TC40) via a single-step HF etching of Ti_3AlC_2, as confirmed by both morphological and structural analyses. By modulating the HF concentration during the etching process, the surface

defect states were optimized. Further, XPS analysis revealed the presence of low-valent titanium species (Ti^0, Ti^{2+}, and Ti^{3+}) along with oxygen vacancy sites, and ESR demonstrated the modulation of low-valent Ti states (Ti^{3+}) with HF concentration. Subsequently, the performance of m-TC40 as a Fenton catalyst was evaluated for the degradation of various pollutants, with MB exhibiting the most effective. The effects of different parameters on MB degradation were also systematically examined. Under optimized conditions, complete degradation (100%) of MB was achieved in 24 min with only a minimal amount of H_2O_2. Additionally, a detailed discussion of the degradation mechanism was provided. XPS analyses of samples subjected to MB degradation and subsequent air annealing reveal that the Ti^{2+} and Ti^{3+} states, along with oxygen vacancy sites, significantly contribute to the degradation process of MB. Furthermore, m-TC40 demonstrated broad pH tolerance and good reusability. Its superior performance for cationic dyes (MB and RhB) compared to anionic dyes (MO) is ascribed to its negatively charged surface, which facilitates favourable electrostatic interactions. Overall, these findings underscore the potential of m-TC40 MXenes as effective Fenton catalysts for wastewater treatment, with further enhancements achievable through tailored surface defect state engineering.

References

(1) Javaid, R.; Qazi, U. Y. Catalytic Oxidation Process for the Degradation of Synthetic Dyes: An Overview. *Int. J. Environ. Res. and Public Health* **2019**, *16* (11), 2066.
(2) Liu, Z.; Xu, Z.; Xu, L.; Buyong, F.; Chay, T. C.; Li, Z.; Cai, Y.; Hu, B.; Zhu, Y.; Wang, X. Modified biochar: synthesis and mechanism for removal of environmental heavy metals. *Carbon Res.* **2022**, *1* (1), 8.
(3) Zhang, Y.; Liu, H.; Gao, F.; Tan, X.; Cai, Y.; Hu, B.; Huang, Q.; Fang, M.; Wang, X. Application of MOFs and COFs for photocatalysis in CO_2 reduction, H_2 generation, and environmental treatment. *Energy Chem.* **2022**, *4* (4), 100078.
(4) Dutta, S.; Gupta, B.; Srivastava, S. K.; Gupta, A. K. Recent advances on the removal of dyes from wastewater using various adsorbents: a critical review. *Mater. Adv.* **2021**, *2* (14), 4497-4531, 10.1039/D1MA00354B.
(5) Hassani, A. H.; Mirzayee, R.; Nasseri, S.; Borghei, M.; Gholami, M.; Torabifar, B. Nanofiltration process on dye removal from simulated textile wastewater. *Int. J. Environ. Sci. Technol.* **2008**, *5* (3), 401-408.
(6) Zhu, M.-X.; Lee, L.; Wang, H.-H.; Wang, Z. Removal of an anionic dye by adsorption/precipitation processes using alkaline white mud. *J. Hazard. Mater.* **2007**, *149* (3), 735-741.
(7) Babuponnusami, A.; Muthukumar, K. A review on Fenton and improvements to the Fenton process for wastewater treatment. *J. Environ. Chem. Eng.* **2014**, *2* (1), 557-572.
(8) Mashtalir, O.; Naguib, M.; Mochalin, V. N.; Dall'Agnese, Y.; Heon, M.; Barsoum, M. W.; Gogotsi, Y. Intercalation and delamination of layered carbides and carbonitrides. *Nat. Commun.* **2013**, *4* (1), 1716.

(9) Yu, M.; Zhou, S.; Wang, Z.; Zhao, J.; Qiu, J. Boosting electrocatalytic oxygen evolution by synergistically coupling layered double hydroxide with MXene. *Nano Energy* **2018**, *44*, 181-190.
(10) Lim, G. P.; Soon, C. F.; Ma, N. L.; Morsin, M.; Nayan, N.; Ahmad, M. K.; Tee, K. S. Cytotoxicity of MXene-based nanomaterials for biomedical applications: A mini review. *Environ. Res.* **2021**, *201*, 111592.
(11) Ling, Z.; Ren, C. E.; Zhao, M.-Q.; Yang, J.; Giammarco, J. M.; Qiu, J.; Barsoum, M. W.; Gogotsi, Y. Flexible and conductive MXene films and nanocomposites with high capacitance. *Proc. Natl. Acad. Sci.* **2014**, *111* (47), 16676-16681.
(12) Cheng, X.; Zu, L.; Jiang, Y.; Shi, D.; Cai, X.; Ni, Y.; Lin, S.; Qin, Y. A titanium-based photo-Fenton bifunctional catalyst of mp-MXene/TiO_{2-x} nanodots for dramatic enhancement of catalytic efficiency in advanced oxidation processes. *Chem. Commun.* **2018**, *54* (82), 11622-11625, 10.1039/C8CC05866K.
(13) Cui, Y.; Zhang, D.; Shen, K.; Nie, S.; Liu, M.; Huang, H.; Deng, F.; Zhou, N.; Zhang, X.; Wei, Y. Biomimetic anchoring of Fe_3O_4 onto Ti_3C_2 MXene for highly efficient removal of organic dyes by Fenton reaction. *J. Environ. Chem. Eng.* **2020**, *8* (5), 104369.
(14) Ma, Y.; Lv, X.; Xiong, D.; Zhao, X.; Zhang, Z. Catalytic degradation of ranitidine using novel magnetic Ti_3C_2-based MXene nanosheets modified with nanoscale zero-valent iron particles. *Appl. Catal. B: Environ.* **2021**, *284*, 119720.
(15) Naguib, M.; Kurtoglu, M.; Presser, V.; Lu, J.; Niu, J.; Heon, M.; Hultman, L.; Gogotsi, Y.; Barsoum, M. W. Two-Dimensional Nanocrystals Produced by Exfoliation of Ti_3AlC_2. *Adv. Mater.* **2011**, *23* (37), 4248-4253.
(16) Du, Y.; Zhang, X.; Wei, L.; Yu, B.; Ma, D.; Ye, S. Electrodeposition of a Ni–P–TiO_2/$Ti_3C_2T_x$ Coating with In Situ Grown Nanoparticles TiO_2 on $Ti_3C_2T_x$ Sheets. *Coatings* **2019**, *9* (11), 750.
(17) Chen, X.; Sun, X.; Xu, W.; Pan, G.; Zhou, D.; Zhu, J.; Wang, H.; Bai, X.; Dong, B.; Song, H. Ratiometric photoluminescence sensing based on Ti_3C_2 MXene quantum dots as an intracellular pH sensor. *Nanoscale* **2018**, *10* (3), 1111-1118, 10.1039/C7NR06958H.
(18) My Tran, N.; Thanh Hoai Ta, Q.; Sreedhar, A.; Noh, J.-S. $Ti_3C_2T_x$ MXene playing as a strong methylene blue adsorbent in wastewater. *Appl. Surf. Sci.* **2021**, *537*, 148006.
(19) Low, J.; Zhang, L.; Tong, T.; Shen, B.; Yu, J. TiO_2/MXene Ti_3C_2 composite with excellent photocatalytic CO_2 reduction activity. *J. Catal.* **2018**, *361*, 255-266.
(20) Cheng, L.; Chen, Q.; Li, J.; Liu, H. Boosting the photocatalytic activity of $CdLa_2S_4$ for hydrogen production using Ti_3C_2 MXene as a co-catalyst. *Appl. Catal. B: Environ.* **2020**, *267*, 118379.
(21) Sarycheva, A.; Gogotsi, Y. Raman Spectroscopy Analysis of the Structure and Surface Chemistry of $Ti_3C_2T_x$ MXene. *Chem. Mater.* **2020**, *32* (8), 3480-3488.
(22) Li, J.; Zhang, M.; Guan, Z.; Li, Q.; He, C.; Yang, J. Synergistic effect of surface and bulk single-electron-trapped oxygen vacancy of TiO_2 in the photocatalytic reduction of CO_2. *Appl. Catal. B: Environ.* **2017**, *206*, 300-307.
(23) Halim, J.; Cook, K. M.; Naguib, M.; Eklund, P.; Gogotsi, Y.; Rosen, J.; Barsoum, M. W. X-ray photoelectron spectroscopy of select multi-layered transition metal carbides (MXenes). *Appl. Surf. Sci.* **2016**, *362*, 406-417.
(24) Rakhi, R. B.; Ahmed, B.; Hedhili, M. N.; Anjum, D. H.; Alshareef, H. N. Effect of Postetch Annealing Gas Composition on the Structural and Electrochemical Properties of Ti_2CT_x MXene Electrodes for Supercapacitor Applications. *Chem. Mater.* **2015**, *27* (15), 5314-5323.
(25) Xiao, S.; Wu, J.; Kang, M.; Dong, Z. Aptamer regulated peroxidase-like activity of cobalt oxyhydroxide nanosheets for colorimetric detection of kanamycin. *Analytical Sci.* **2024**, *40* (12), 2181-2190.

(26) Luo, S.; Wang, R.; Yin, J.; Jiao, T.; Chen, K.; Zou, G.; Zhang, L.; Zhou, J.; Zhang, L.; Peng, Q. Preparation and Dye Degradation Performances of Self-Assembled MXene-Co_3O_4 Nanocomposites Synthesized via Solvothermal Approach. *ACS Omega* **2019**, *4* (2), 3946-3953.
(27) Peng, C.; Wang, H.; Yu, H.; Peng, F. (111) TiO_{2-x}/Ti_3C_2: Synergy of active facets, interfacial charge transfer and Ti^{3+} doping for enhance photocatalytic activity. *Materials Research Bulletin* **2017**, *89*, 16-25.
(28) Liu, Q.; Tan, X.; Wang, S.; Ma, F.; Znad, H.; Shen, Z.; Liu, L.; Liu, S. MXene as a non-metal charge mediator in 2D layered CdS@Ti_3C_2@TiO_2 composites with superior Z-scheme visible light-driven photocatalytic activity. *Environ. Sci.: Nano* **2019**, *6* (10), 3158-3169, 10.1039/C9EN00567F.
(29) Cui, Y.; Liu, M.; Huang, H.; Zhang, D.; Chen, J.; Mao, L.; Zhou, N.; Deng, F.; Zhang, X.; Wei, Y. A novel one-step strategy for preparation of Fe_3O_4-loaded Ti_3C_2 MXenes with high efficiency for removal organic dyes. *Ceram. Int.* **2020**, *46* (8, Part B), 11593-11601.

Chapter 3

Catalytic Activity of Phosphorous-doped Ti_3C_2Tx MXene/ Carbon Foam Hybrid Aerogel for the Degradation of Organic Pollutants Through Advanced Oxidation Process

In **Chapter 2**, we discussed that the accordion-like microstructure of $Ti_3C_2T_x$ MXene consists of numerous stacked layers, resulting in a relatively low surface area available for catalytic reactions. To further improve the catalytically active surface area, here we synthesized few-layer $Ti_3C_2T_x$ MXene nanosheets using the LiF/HCl etching method. However, pristine $Ti_3C_2T_x$ tends to undergo face-to-face restacking due to interlayer van der Waals interactions, which reduces its catalytic activity. Additionally, the effective recollection and separation of thin $Ti_3C_2T_x$ nanosheets after catalytic reactions are challenging due to their excellent dispersion in aqueous media.

To address these limitations, we adopted an innovative strategy involving heteroatom doping within the $Ti_3C_2T_x$ framework, along with the fabrication of a hierarchical 3D porous aerogel structure. Specifically, phosphorus (P) doping was introduced to reduce multilayer restacking by modifying the surface chemical properties of $Ti_3C_2T_x$, while the hydrophilic 3D hierarchical porous aerogel enhances surface adsorption and effectively minimizes the loss of active catalysts during multiple recycling cycles. Finally, the catalytic performance of the aerogel catalyst was evaluated in the degradation of ciprofloxacin (CIP) and the organic dyes via PMS activation. The key factors influencing the catalytic degradation process are discussed in detail.

3.1. Introduction

The advanced oxidation process (AOPs) is widely recognized for its efficacy in eliminating micropollutants from water. In particular, AOPs activated by peroxymonosulfate (PMS) (PMS-AOPs) offer significant advantages over traditional Fenton oxidation, such as higher redox potential, a wider effective pH range, extended radical lifespan, and reduced energy requirements[1, 2]. Unlike H_2O_2, which produces only •OH radicals, the decomposition of PMS through O-O bond cleavage primarily generates both $SO_4^{\bullet-}$ and •OH radicals, which are essential for the degradation of organic pollutants[3]. Recent studies have also underscored the significance of $^1O_2$ as an important non-radical oxidizing agent[4] in PMS-AOPs. While $SO_4^{\bullet-}$ and •OH radicals facilitate the breakdown of organic pollutants into smaller inorganic

molecules, the moderate half-life of $^1O_2$ benefits greater environmental stability[4]. Thus, the integration of both radical and non-radical oxidation mechanisms offers a highly effective strategy for organic pollutant degradation.

Compared to the accordion-like 3D microstructure, 2D $Ti_3C_2T_x$ MXene nanosheets exhibit a substantially higher surface area and are enriched with low-valence Ti states (Ti^{2+} and Ti^{3+}). These states arise from the formation of abundant surface vacancies during the LiF/HCl synthesis process. However, pristine $Ti_3C_2T_x$ MXene is prone to restacking due to interlayer van der Waals forces [5, 6], which significantly reduces the number of exposed catalytically active sites and thus diminishes its catalytic performance. A promising strategy to overcome this limitation is heteroatom doping, which can modify both the surface texture and chemistry, effectively reducing restacking[7]. This approach not only increases the interlayer spacing but also exposes a larger surface area, thereby enhancing overall catalytic activity. Doping the $Ti_3C_2T_x$ framework with N or P has been shown to improve electrical conductivity and reduce the restacking issue. Although P and N share some chemical similarities as elements from the same group in the periodic table, P doping is particularly effective for AOPs for several reasons. Firstly, the larger covalent radius of the P atom compared to the C atom in the $Ti_3C_2T_x$ structure induces lattice distortion, which generates additional defects and reactive sites, ultimately boosting catalytic performance. Secondly, P doping introduces unique electronic effects due to the presence of vacant 3d orbitals and extra valence electrons in its third shell. Recent research demonstrates that kinetic studies in P-doped carbon materials require an activation energy of ~ 49.6 $kJ \cdot mol^{-1}$ for benzyl alcohol oxidation[8], which is lower than the 56.1 $kJ \cdot mol^{-1}$ observed for N-doped carbon catalysts. This result underscores the effectiveness of P doping in catalytic AOPs. Despite these advances, most investigations have focused on using $Ti_3C_2T_x$-based composites with metal compounds for PMS activation[9, 10], whereas the catalytic potential of heteroatom-doped $Ti_3C_2T_x$ for PMS activation has not been explored yet.

Recovering few-layer $Ti_3C_2T_x$ MXene nanosheets after catalytic experiments is particularly challenging, as they tend to be washed away during repeated centrifugation cycles for their excellent dispersion in aqueous medium and thin-layered structure. This issue complicates the assessment of their reusability. To overcome this limitation, researchers have developed 3D porous $Ti_3C_2T_x$ aerogels by integrating 2D $Ti_3C_2T_x$ MXene sheets into a foam-like architecture [11, 12]. These aerogels facilitate easier separation and recovery while preventing re-pollution, thereby offering a practical alternative compared to powder catalysts.

In this chapter, P-doped $Ti_3C_2T_x$ (P-$Ti_3C_2T_x$) nanosheets were synthesized via an in-situ

phosphating method, and their successful formation is confirmed by structural and morphological characterization. The P doping improves electrical conductivity and reduces the self-stacking issue of $Ti_3C_2T_x$ MXene nanosheets, as evidenced by BET characterization. Subsequently, a low-cost melamine sponge (MS) pre-treated with polyvinyl alcohol (PVA) was repeatedly immersed in the P-$Ti_3C_2T_x$ solution until its surface was coated entirely with the nanosheets, followed by freeze drying overnight. The resulting 3D architecture is used as a catalyst to activate PMS as an oxidant for the degradation of organic pollutants, specifically targeting CIP and various organic dyes. The study systematically monitored various parameters influencing CIP degradation, and the impact of P doping on pollutant degradation was further investigated using DFT studies.

3.2. Experimental Details

3.2.1. Synthesis of P-Doped $Ti_3C_2T_x$ Nanosheets

The synthesis of $Ti_3C_2T_x$ MXene nanosheets was carried out through a sequential chemical (LiF/HCl) etching and modification process. Initially, 0.8 g of LiF was dissolved in 10 mL of 9 M HCl and stirred for 10 min to ensure complete dissolution. Subsequently, 0.5 g of Ti_3AlC_2 was introduced into the prepared solution and subjected to continuous stirring at 35 °C for 24 h to facilitate the selective etching of the Al layer. After that, the obtained mixture was repeatedly washed with DI water to remove residual acids and by-products. The exfoliation of the etched material was then carried out via bath sonication under Ar bubbling for 1 h, resulting in a black colloidal solution. This dispersion was further centrifuged, and the supernatant was collected multiple times before freeze-drying for 24 h.

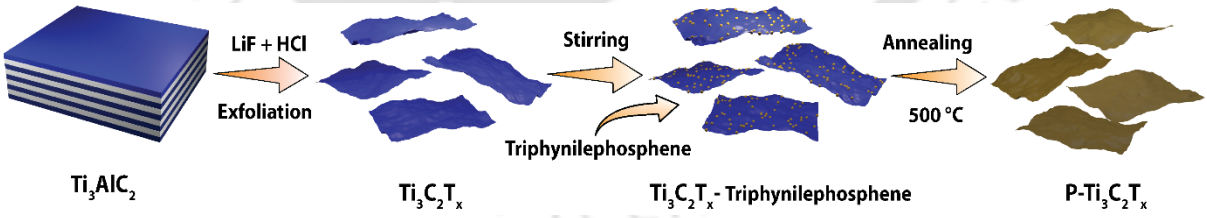

Fig. 3.1. Schematic representation of P doping in $Ti_3C_2T_x$ MXene nanosheets

For P doping, a specific quantity of triphenylphosphine was first dissolved in tert-butanol and gradually added dropwise to 10 mL of a $Ti_3C_2T_x$ suspension (5 mg mL^{-1}) under continuous stirring for 3 h. The obtained product was then freeze-dried and subsequently annealed at 500 °C in an Ar atmosphere (50 sccm) for 2 h to ensure the incorporation of P atoms into the MXene structure. A schematic illustration of P doping in $Ti_3C_2T_x$ MXene is shown in **Fig. 3.1**. The percentage of P doping was controlled by varying the amount of triphenylphosphine used (50,

100, and 200 mg), and the corresponding P-doped MXene samples were designated as MXP1, MXP2, and MXP4, respectively. The pristine $Ti_3C_2T_x$ MXene sample, without P doping, was referred to as MX.

3.2.2. Synthesis of P Doped $Ti_3C_2T_x$@PVA@MS Aerogel

The MS ($3 \times 2 \times 1$ cm^3) was initially subjected to a thorough cleaning process involving multiple washes and soaking in absolute ethanol, followed by rinsing with deionized water. The cleaned MS was then dried overnight to eliminate residual moisture. Subsequently, it was immersed in a 2 mg/mL PVA solution for 1 h, to ensure uniform coating of PVA on the MS surface, resulting in the formation of PVA@MS (PVMS). After the coating process, the substrate was removed from the solution and dried in an oven at 65 °C. To fabricate the MXP2@PVMS aerogel, the PVMS structure was repeatedly soaked in a 3 mg/mL MXP2 solution for 5 min to allow effective deposition of MXP2. A schematic illustration of the fabrication of MXP2@PVMS aerogel is shown in **Fig. 3.2**. The treated samples were then subjected to a freeze-drying process to obtain the final MXP2@PVMS aerogel.

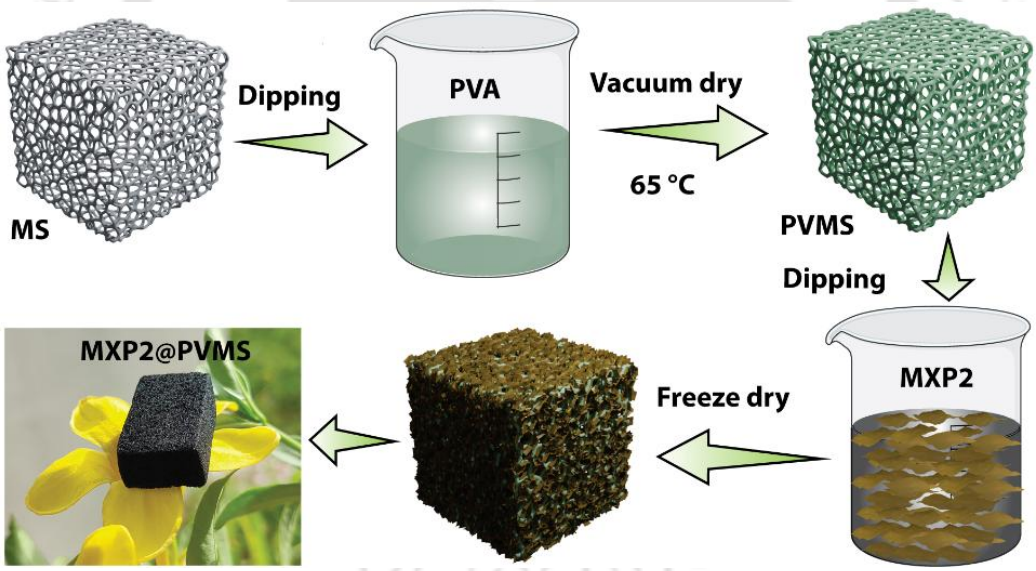

Fig. 3.2. Schematic representation of the formation process of the MXP2@PVMS hybrid aerogel.

3.2.3. Ciprofloxacin and Organic Dye Degradation Experiment

In this study, a 50 mL ciprofloxacin (CIP) solution with an initial concentration of 20 mg/L was utilized as the model system. The MXP@PVMS aerogel was introduced into the CIP solution, and after reaching adsorption-desorption equilibrium, a certain amount of PMS solution was added under gentle stirring at 200 rpm. To monitor the degradation process, 2 mL of CIP solution was extracted from the reaction mixture at an interval of 3 min and immediately

analyzed using a UV-Visible (UV-Vis) absorption spectrophotometer. In the case of organic dye degradation experiments, the initial dye concentration was maintained at 10 mg/L. The pH of the solutions was carefully adjusted using 0.1 M HCl and NaOH solutions to study their influence on the degradation process. The degradation efficiency was calculated using the following equation:

$$\text{Degradation (\%)} = \frac{C_0 - C_t}{C_0} \qquad (1)$$

where C_0 and C_t represent the absorbance of the pollutant solution initially and at any time t, respectively.

3.2.4. Characterization Techniques

The characterization details, including XRD, Raman spectroscopy, BET surface area analysis, FESEM, TEM, ESR spectroscopy, and UV-Vis absorption spectroscopy, are the same as those described in **Chapter 2**, **Section 2.2.3.** In addition, X-ray photoelectron spectroscopy (XPS) was performed using a PHI5000 VERSAPROBE III (ULVAC-PHI Inc., Japan) to investigate the oxidation states of elements present in MX and MXP2 samples. The acquired XPS spectra were analyzed using XPSPEAK 41 software.

3.2.5. Computational Details

The DFT calculations were carried out using the Vienna Ab Initio Simulation Package[13-15] (VASP). We used the Perdew-Burke-Ernzerhof functional to apply the generalized gradient approximation[16] (GGA) for exchange-correlation. A cut-off energy of 500 eV was set for all calculations. For Brillouin zone sampling, a Monkhorst-Pack[17] k-point grid of 8 × 8 × 1 was employed. Charge transfer was analyzed using Bader charge analysis, developed by Henkelman's group[18, 19]. The charge density distribution was visualized by VESTA software[20]. Additionally, the adsorption energy (E_{ads}) of the adsorbate molecule on various catalyst surfaces was calculated using the following formula:

$$E_{ads} = E_{total} - E_{surface} - E_{adsorbate} \qquad (2)$$

Where E_{total}, $E_{surface}$, and $E_{adsorbate}$ represent the energy of the combined system, the isolated substrate surface, and the adsorbate in its free state, respectively.

3.3. Results and Discussion

3.3.1. Morphology and Compositional Analysis

Fig. 3.3(a) illustrates the TEM image of pristine MX and reveals ultrathin, transparent

nanosheets with a random size distribution spanning from 100 nm to 1.5 µm. Additionally, the HRTEM analysis provides an interplanar spacing of 0.25 nm (**Fig. 3.3(b)**), corresponding to the (010) lattice planes[21]. The TEM image of the MXP2 in **Fig. 3.3(c)** exhibits a wrinkled nanosheet-like morphology while maintaining a layered structure. HRTEM analysis demonstrates an interlayer spacing of 0.25 nm, as shown in **Fig. 3.3(d)**. This observation suggests that P doping does not affect the interplanar spacing of the (010) planes [21], which is further supported by the XRD results as described below. The EDS mapping shown in **Fig. 3.3(e-j)** demonstrates the distribution of Ti, C, O, F, and P elements, thereby confirming the successful incorporation of P atoms into the MX framework.

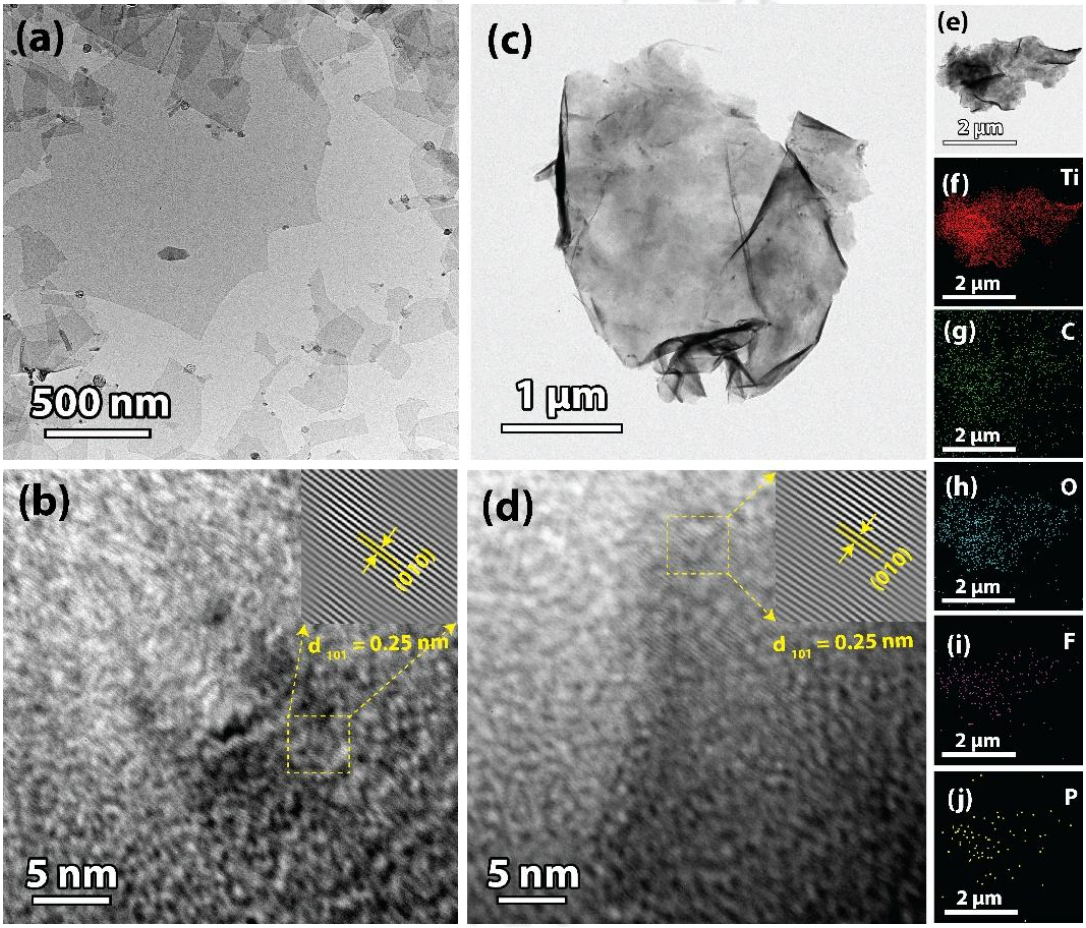

Fig. 3.3. The TEM and HRTEM images of (a, b) MX and (c, d) MXP2 nanosheets. (e-j) EDS elemental mapping of MXP2, illustrating the spatial distribution of individual elements.

3.3.2. Structural Characterizations

The XRD and Raman spectroscopy were employed to investigate the structural modifications induced by P doping. As depicted in **Fig. 3.4(a)**, the (002) diffraction peak of the P-doped MX sample (MXP2) appears at 5.9°, compared to 6.3° for the pristine MX nanosheet. This shift signifies an increased interlayer spacing, likely resulting from the incorporation of P

heteroatoms into the MX framework. In contrast, the position of (010) diffraction peaks does not change significantly, which is consistent with the HRTEM observations as discussed earlier. **Fig. 3.4(b)** shows the Raman spectra for both pristine MX and MXP2. In the MXP2 sample, the peaks at 201.5 and 730.1 cm^{-1} are attributed to the A_{1g} (out-of-plane)[22] vibrational modes of the Ti-C bonds. Additionally, the broad regions observed between 320 - 470 cm^{-1} and 515 - 680 cm^{-1} correspond to the E_g (in-plane) vibrational modes of the surface-terminated groups on the outer Ti layers[22]. Notably, the A_{1g} peak exhibits a blue shift from 199.8 cm^{-1} in the pristine MX to 201.5 cm^{-1} in MXP2, suggesting an enhancement in the Ti-C bond strength due to P doping[21]. Conversely, the E_g modes display a redshift, indicating that the incorporation of P weakens the bond strength between the functional groups and the surface Ti atoms[21]. These spectral shifts confirm the successful integration of P into the MX structure.

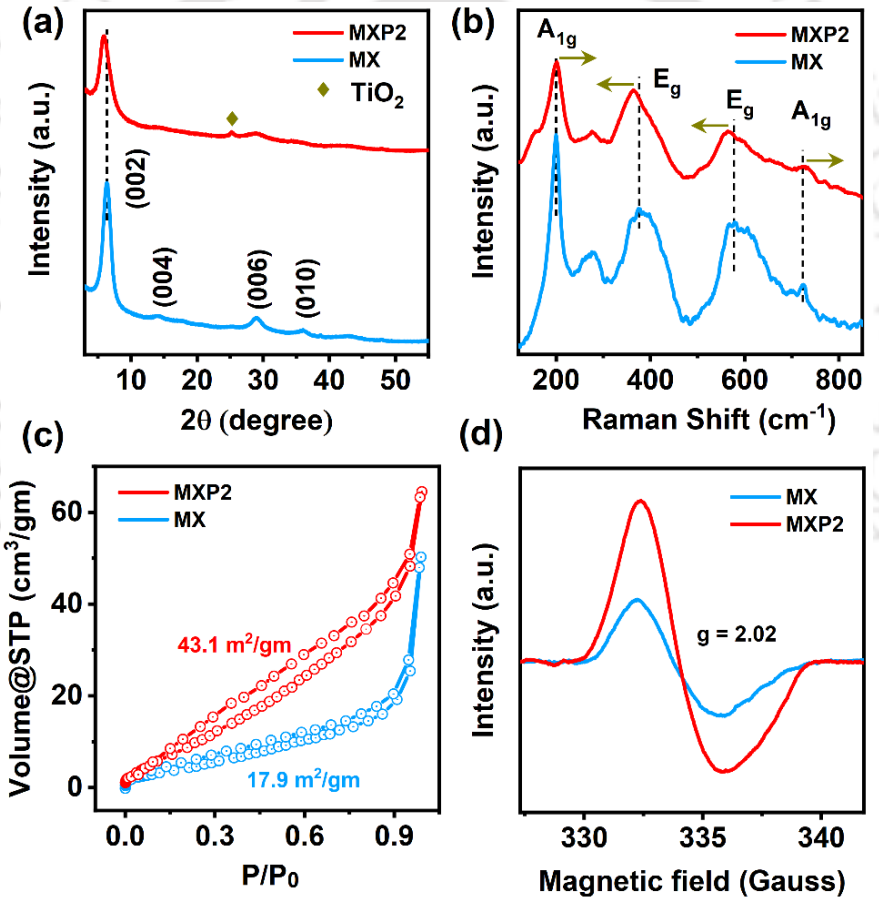

Fig. 3.4. Comparison of (a) XRD patterns, (b) Raman spectra, (c) nitrogen adsorption-desorption isotherms, and (d) ESR signal of MX and MXP2 nanosheets.

3.3.3. BET and ESR Analysis

Additionally, nitrogen adsorption/desorption measurements in **Fig. 3.4(c)** reveal that MXP2 has a significantly higher specific surface area of 43.1 m^2/g compared to 17.9 m^2/g for pristine MX. This enhancement is attributed to the enlarged interlayer spacing and the reduced

restacking of MX nanosheets[23], likely resulting from reduced interlayer van der Waals interactions. The larger surface area can provide more adsorption sites and improved adsorption kinetics, thereby possibly enhancing its catalytic activity. The ESR spectroscopy serves as direct evidence for the presence of oxygen vacancies (OVs) in both pristine MX and MXP2 samples. Distinct ESR signals with a g-value of 2.02 were observed in both cases (**Fig. 3.4(d)**), confirming the presence of trapped electrons associated with OVs[24, 25]. Moreover, a comparative evaluation of the peak areas at g = 2.02 in the ESR spectra of these samples indicates a higher concentration of OVs in the MXP2 sample compared to pristine MX nanosheets. This observation suggests that P doping enhances the formation of OV sites on the MX surface, which, in turn, provides active sites for PMS adsorption and dissociation, thereby improving the catalytic performance.

3.3.4. XPS Analysis

The chemical composition and oxidation states of various elements in the synthesized MXP2 nanosheets were analyzed using XPS. **Fig. 3.5(a)** illustrates a comparative survey scan XPS spectrum of MX and MXP2 nanosheets over the BE range of 100-800 eV, which confirms the

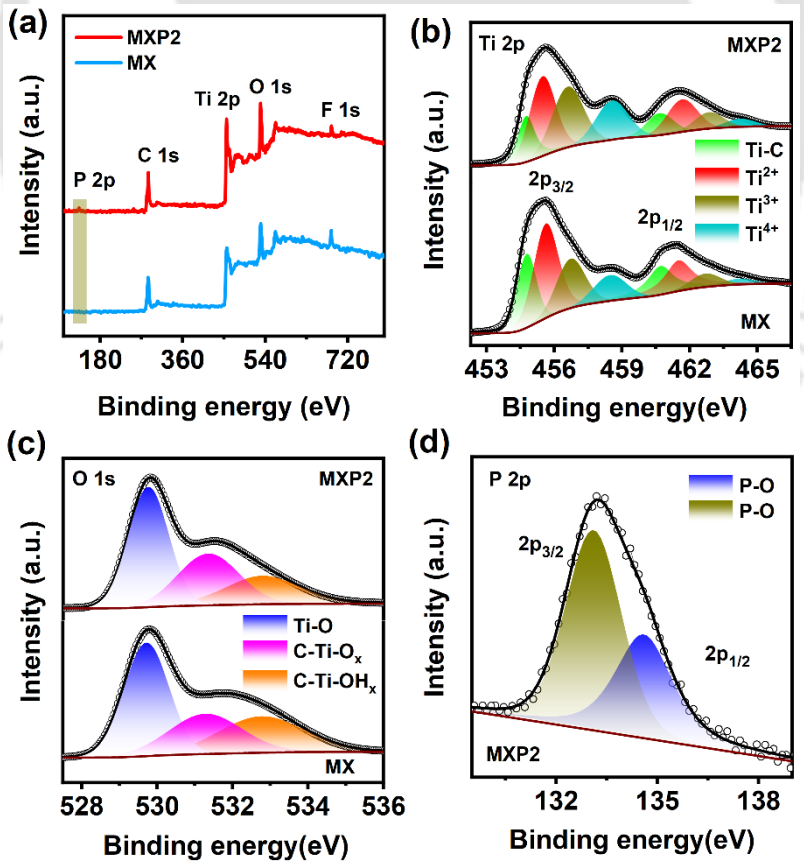

Fig. 3.5. Comparison of (a) the survey scan and high-resolution XPS spectra of (b) Ti 2p and (c) O 1s for MX and MXP2, along with (d) the P 2p spectrum for MXP2. The symbols represent experimental data, while the solid lines indicate Gaussian-Lorentzian fitted spectra with a Shirley background.

presence of Ti, C, O, F, along with the additional P element in MXP2. Based on the survey spectrum, the atomic percentages of Ti, C, O, F, and P in MXP2 were determined to be 41.1%, 29.2%, 25.1%, 3.3%, and 1.3%, respectively, indicating the successful incorporation of P atoms into the MXene structure. The high-resolution Ti 2p XPS spectrum of pristine MX nanosheets in **Fig. 3.5(b)** displays distinct peaks corresponding to Ti-C (454.7 and 460.7 eV), Ti^{2+} (455.5 and 461.7 eV), Ti^{3+} (456.6 and 462.8 eV), and Ti^{4+} (458.5 and 464.2 eV). In contrast, the MXP2 nanosheets exhibited similar peaks, with variations in the relative proportions of Ti^{2+}, Ti^{3+}, and Ti^{4+} states, as summarized in **Table 3.1**. The O 1s XPS spectrum of MX nanosheets in **Fig. 3.5(c)** shows three peaks attributed to Ti-O (529.7 eV), C-Ti-O_x (531.3 eV), and C-Ti-OH_x (532.8 eV)[26, 27]. For MXP2, a similar pattern was observed, but with an increased percentage of OVs, as summarized in **Table 3.1**. Furthermore, the P 2p XPS spectrum of MXP2 exhibited (**Fig. 3.5(d)**) two peaks at 133.1 eV and 134.6 eV, corresponding to P-O bonds[28, 29], confirming the incorporation of P atoms into the MXene framework. The presence of P-O bonding suggests that P atoms are primarily bound to surface O groups, contributing to an increase in OVs, which can serve as catalytically active sites. This is also confirmed by the ESR analysis, as discussed earlier. This enhancement in OV sites facilitates the AOPs by effective adsorption and dissociation of PMS molecules, highlighting the significance of P doping in improving catalytic performance.

Table 3.1. *The relative area (%) under the peaks from XPS data represents the various elemental states of pristine MX and MXP2.*

Sample	**Ti 2p (%)**				**O 1s (%)**		
	Ti-C	Ti^{2+}	Ti^{3+}	Ti^{4+}	Ti-O	Ti-OH_x	Ti-O_x
Pristine $Ti_3C_2T_x$	27.7	41	20	11.3	44.7	27.8	27.5
P-doped $Ti_3C_2T_x$	20.5	36	26	17.5	43.9	19.1	37

3.3.5. Morphology of MXP2@PVA@MS Aerogel

The FESEM images of pristine MS (**Fig. 3.6(a-b)**) reveal a porous structure with pore sizes exceeding 100 μm and smooth skeletons. As shown in **Fig. 3.6(c-d)**, PVA uniformly coats the MS skeletons while preserving the overall porous architecture. From **Fig. 3.6(e-f)**, it is notable that the incorporation of MXP2 into the PVMS skeletons imparts a rough texture, with MXP2 nanosheets uniformly distributed across the porous PVMS framework, facilitating the

development of a hierarchical MXP2@PVMS hybrid aerogel structure. Furthermore, EDS mapping (**Fig. 3.6 (g-l)**) confirms the homogeneous distribution of Ti, C, O, F, and P elements, demonstrating the successful anchoring of MXP2 nanosheets to the PVMS skeletons and the formation of a well-defined hierarchical porous aerogel structure.

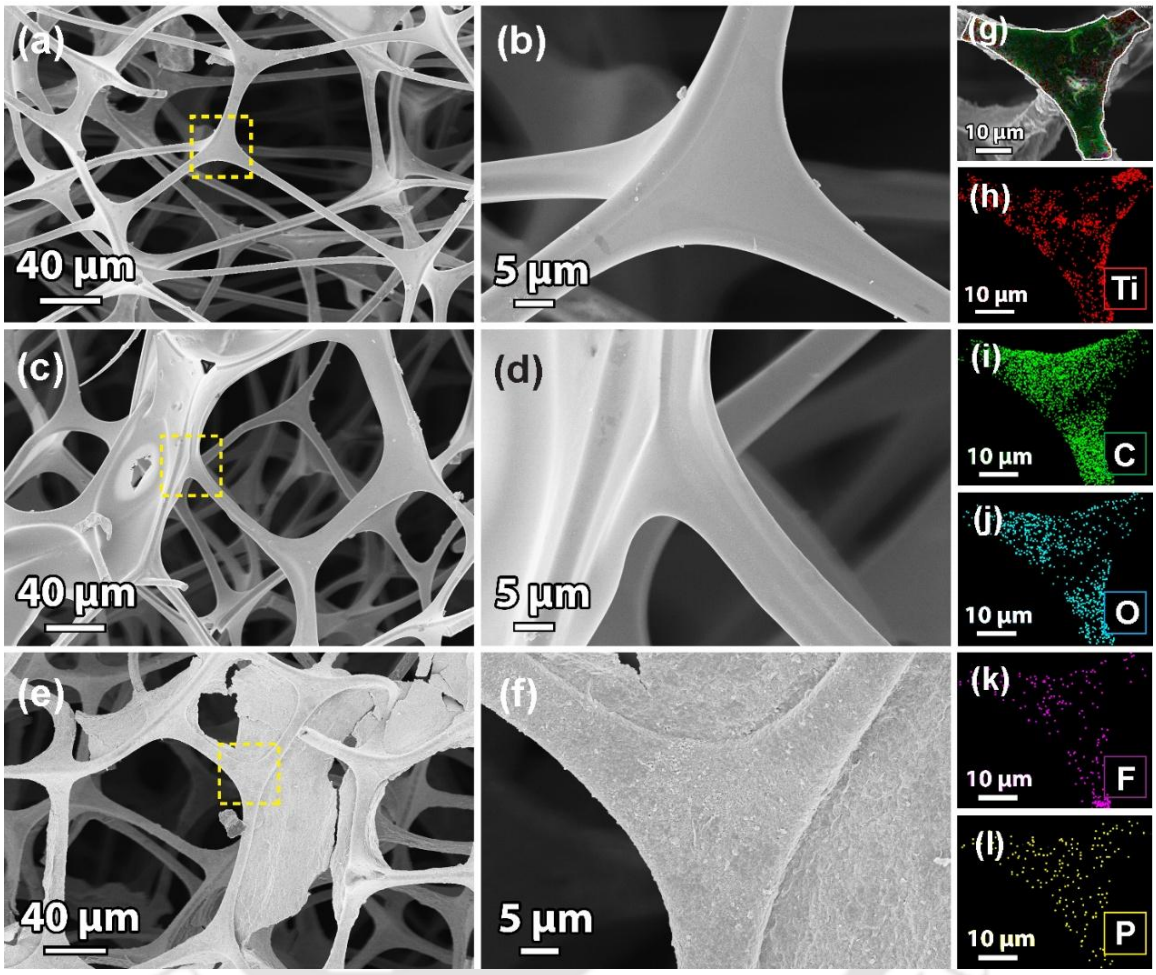

Fig. 3.6. (a, b) FESEM images of pristine MS along with its magnified view. (c, d) FESEM images of PVMS. (e, f) FESEM images of the MXP2@PVMS hybrid aerogel. (g-l) EDS elemental mapping of MXP2@PVMS, illustrating the distribution of individual elements.

3.3.6. Catalytic Activity

The oxidative degradation of CIP using MXP2@PVMS was investigated in the presence of a small amount of PMS as an oxidant. As shown in **Fig. 3.7(a)**, approximately 20% of CIP was removed by MXP2@PVMS in the absence of PMS, primarily due to surface adsorption, which reached equilibrium in 20 min. This observation suggests a relatively low adsorption capacity of the MXP2@PVMS aerogel. On the other hand, when only PMS was used as the oxidant, ~19% of CIP degradation occurred in 21 min (**Fig. 3.7(b)**), attributed to the combined effects of PMS and $_1O^2$ generated during PMS decomposition[30]. The CIP removal efficiency for MS/PMS and PVMS/PMS systems exhibited only slight improvements compared to PMS

alone (**Fig. 3.7(b)**), indicating the lack of catalytic activity in bare MS and PVMS. However,

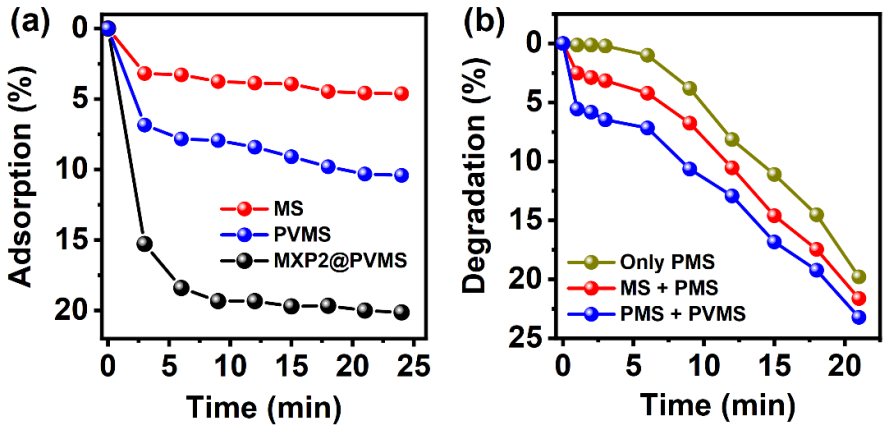

Fig. 3.7. (a) The CIP adsorption performance of pristine MS, PVMS, and MXP2@PVMS and (b) CIP degradation efficiency of PMS alone, MS, and PVMS along with PMS.

The MX@PVMS/PMS system achieved 75% CIP degradation in 21 min (**Fig. 3.8(a)**), highlighting the intrinsic catalytic activity of the aerogels in PMS activation, which can be attributed to the surface defect states present in pristine MX nanosheets. Notably, the MXP2@PVMS/PMS system demonstrated a significantly enhanced degradation efficiency, achieving ~96% CIP removal within the same time frame (**Fig. 3.8 (a)**). This improvement underscores the beneficial role of P doping in the MX framework for PMS activation. Furthermore, the CIP degradation efficiency increased with higher P doping levels in the MX nanosheets up to a saturation point, beyond which no further enhancement was observed. To further assess the catalytic performance, pseudo-first-order kinetic rate constants were determined based on the Langmuir-Hinshelwood model:

$$\mathrm{Ln}\,(C_t/C_0) = -kt \qquad (3)$$

Here, C_0 represents the initial absorbance, while C_t denotes the absorbance at time t after the addition of PMS, and k is the rate constant. As illustrated in **Fig. 3.8(b)**, the calculated rate constants for CIP degradation in the MX@PVMS/PMS, MXP2@PVMS/PMS, and MXP4@PVMS/PMS systems were determined to be 0.04, 0.1, and 0.09 min^{-1}, respectively. These observations indicate a substantial enhancement in the CIP degradation rate for the P-doped case, which is ~2.5 times higher than that observed for the undoped system. Thus, MXP2@PVMS was chosen as the optimal catalyst due to its comparable catalytic activity with MXP4@PVMS. **Table 3.2** presents a comparative analysis of the CIP degradation efficiency of the MXP2@PVMS hybrid aerogel, with previously reported values in the literature. Next, the influence of MXP2 nanosheet loading on PVMS for optimizing CIP degradation efficiency was systematically examined, as shown in **Fig. 3.8(c)**. It was observed that increasing the

MXP2 loading resulted in an improved CIP degradation efficiency. Specifically, increasing the loading from 4 to 5 mg/cc enhanced the degradation efficiency from 91% to 96% in 21 min. A further increase to 6 mg/cc led to a degradation efficiency of 96.7%; however, considering cost-effectiveness, a loading of 5 mg/cc was chosen for subsequent experiments. **Fig. 3.8(d)** illustrates the effect of PMS concentration on CIP degradation. An increase in PMS concentration from 0.9 mM to 1.2 mM resulted in enhanced degradation efficiency due to the higher generation of reactive radicals. However, further increasing the PMS concentration from

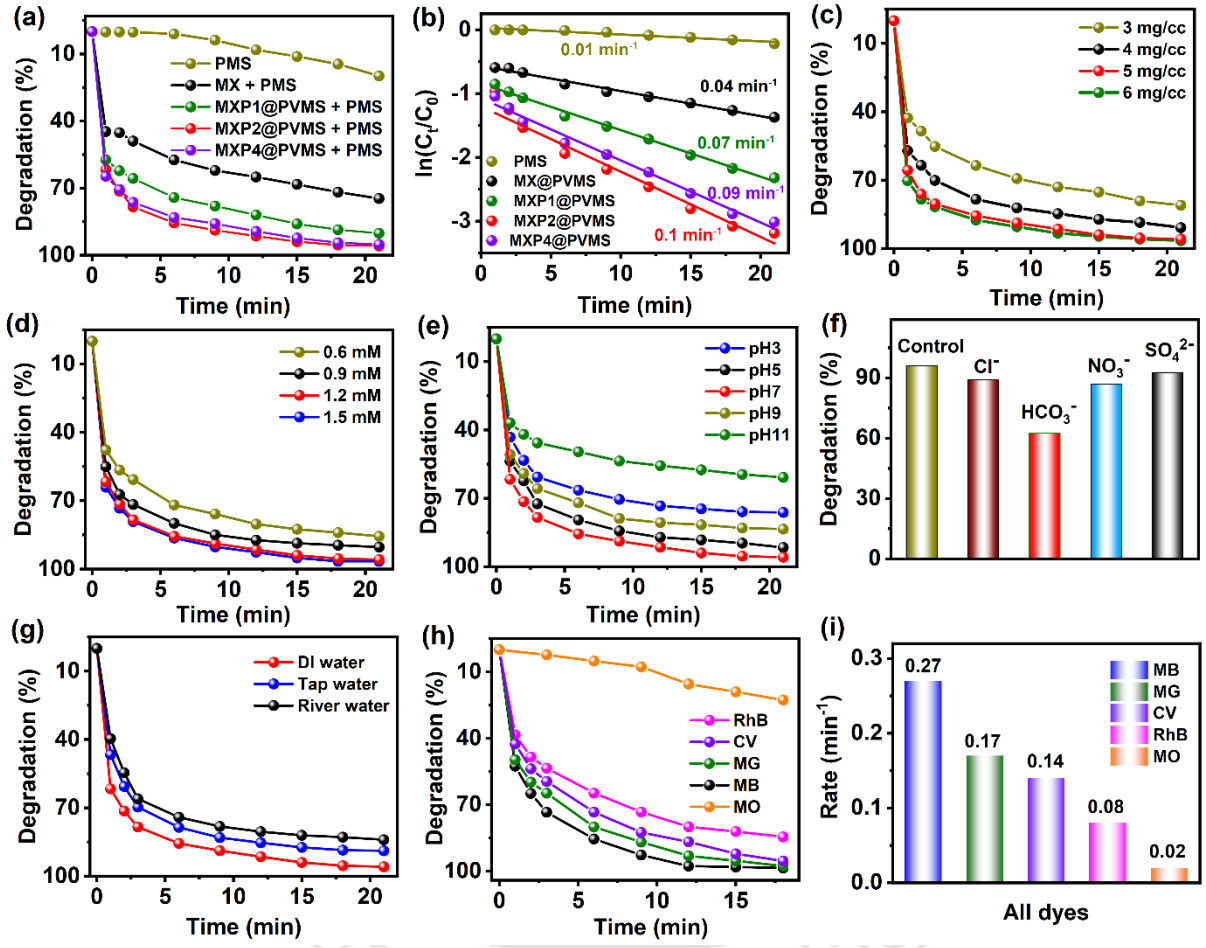

Fig. 3.8. (a) Comparison of the degradation performance of CIP in the presence of PMS and various hybrid aerogels. (b) ln (C_t/C_0) vs time (t) plot with linear fitting and the first order rate constant for CIP degradation. (c, d) The effect of MXP2 nanosheet loading and PMS concentration in CIP degradation. (e) The effect of solution pH in CIP degradation efficiency. (f) Effects of inorganic anions in CIP degradation for MXP2@PVMS/PMS system. (g) CIP removal efficiency from the tap and river water by MXP2@PVMS/PMS system. (h, i) Comparison in the degradation performance of MXP2@PVMS for MB, MG, CV, RhB, and MO dyes in the presence of PMS and their first order rate constant in a bar diagram.

1.2 mM to 1.5 mM led to only a marginal improvement in degradation efficiency. Consequently, 1.2 mM was identified as the optimal PMS concentration and was maintained for further studies. **Fig. 3.8(e)** illustrates the influence of pH on CIP degradation across a pH range of 3 to 11. The removal efficiency of CIP improved as the pH increased from 3 to 7, but declined at higher pH values. Notably, the degradation efficiency within the pH range of 3 to

7 exceeded that of conventional Fenton catalysts, which typically exhibit optimal performance only at a pH of ~ 3. The reduced efficiency observed under acidic conditions can be attributed to the formation of hydrogen bonds between H^+ ions and the O-O group of PMS, leading to an accumulation of positive charge on the PMS molecule's surface. Additionally, the higher concentration of H^+ ions induces a positive charge on the MXP2 surface, causing electrostatic repulsion of PMS molecules and thereby reducing degradation efficiency[31]. At a neutral pH of 7, the generation of $SO_4^{\cdot -}$ radical becomes more prominent, significantly enhancing CIP degradation. As a result, pH 7.0 was identified as the optimal condition for subsequent studies. Inorganic anions commonly present in wastewater, such as nitrate (NO_3^-), chloride (Cl^-), bicarbonate (HCO_3^-), and sulfate (SO_4^{2-}), play a significant role in influencing pollutant degradation rates through AOPs. These anions can impede the degradation process by rapidly reacting with reactive radicals through electron exchange mechanisms and altering the solution pH. As shown in **Fig. 3.8(f)**, the presence of these anions leads to a noticeable reduction in CIP degradation efficiency. Under optimal conditions, in the absence of interfering anions, a degradation efficiency of 96% was achieved. However, upon the introduction of 10 mM of each anion into the reaction system, the degradation efficiency decreased to 89.1% for Cl^-, 62.5% for HCO_3^-, 87.1% for NO_3^-, and 92.7% for SO_4^{2-} after 21 min. These anions interact with active species, thereby reducing their availability for organic pollutant degradation and leading to the formation of less reactive radicals with significantly lower oxidation potentials, ultimately diminishing the overall degradation efficiency[32]. Despite these effects, the MXP2@PVMS/PMS system exhibited strong resistance to interference from co-existing anions, highlighting its potential for effective antibiotic degradation in complex aquatic environments. Additionally, the system's performance was evaluated for CIP degradation in real water samples, including tap water and Brahmaputra River water, as shown in **Fig. 3.8(g)**. The degradation efficiencies achieved were 89% and 84% within 21 min, respectively, demonstrating the system's robustness and the favourable influence of actual water matrices on the degradation process.

Fig. 3.8(h) displays the degradation efficiency of various dyes, including methylene blue (MB), crystal violet (CV), malachite green (MG), rhodamine B (RhB), and methyl orange (MO). The results indicate that cationic dyes (MB, CV, MG, and RhB) exhibit significantly higher degradation rates compared to the anionic dye (MO). Among the cationic dyes, MB demonstrates the highest degradation rate, which can be attributed to its smaller molecular size and enhanced adsorption on the negatively charged catalyst surface. In contrast, MO exhibits

a considerably lower degradation efficiency of only 36%, likely due to electrostatic repulsion between the negatively charged MO molecules and the catalyst surface, which reduces adsorption and degradation efficiency. The degradation kinetics of MB, MG, CV, RhB, and MO are depicted in **Fig. 3.8(i)**. These results underscore the effectiveness of MXP2@PVMS as a catalyst for PMS activation, facilitating the degradation of organic dyes in industrial wastewater treatment applications. **Table 3.3** presents a comparative analysis of the MB degradation efficiency of the MXP2@PVMS hybrid aerogel with the reported literature.

3.3.7. DFT Analysis and PMS Adsorption Study

The DFT calculations were performed to investigate the modifications in the electronic states of P-doped $Ti_3C_2T_x$ and its enhanced catalytic activity for CIP degradation. The XPS survey spectrum (**Fig. 3.5 (a)**) indicates that the atomic percentage of -O surface groups is significantly higher than that of -F groups, leading to the modelling of $Ti_3C_2T_x$ as $Ti_3C_2O_2$. The influence of P doping on the $Ti_3C_2O_2$ surface was analyzed, which revealed the formation of P-O bonds. Furthermore, the charge density difference analysis, shown in **Fig. 3.9(a)**, illustrates charge accumulation in the yellow regions and charge depletion in the blue regions, indicating an electron transfer of 2.1|e| from P to the $Ti_3C_2O_2$ surface. The plane-averaged charge density difference plot (**Fig. 3.9(b)**) further confirms this trend, with pronounced peaks in the $Ti_3C_2O_2$ region corresponding to electron accumulation and smaller peaks in the P region suggesting charge depletion. Additionally, the density of states (DOS) analysis for $Ti_3C_2O_2$ and P-$Ti_3C_2O_2$ reveals that the total DOS at the Fermi energy level for P-$Ti_3C_2O_2$ is 12.45 states/eV, significantly higher than that of pristine $Ti_3C_2O_2$ MXene (9.31 states/eV). This increase in DOS suggests that P doping substantially increases the free electron density, thereby improving the electrical conductivity of the $Ti_3C_2O_2$ MXene[33]. An adsorption test was conducted through DFT to evaluate the efficiency of PMS molecule adsorption on different catalyst surfaces. As depicted in **Fig. 3.9(c)**, PMS adsorption was analyzed on pristine $Ti_3C_2O_2$, OV-$Ti_3C_2O_2$, and P-doped $Ti_3C_2O_2$ MXene surfaces. The results indicate that the O-O bond length in the PMS molecule increased from 1.44 Å on pristine $Ti_3C_2O_2$ to 1.46 Å on P-doped $Ti_3C_2O_2$ and further to 1.47 Å on the OV- $Ti_3C_2O_2$ (**Fig. 3.9(d)**). This elongation suggests that the O-O bond in the PMS molecule undergoes easier cleavage on P-doped and oxygen-deficient sites than on undoped $Ti_3C_2O_2$, leading to the generation of highly reactive $SO_4^{\cdot -}$ and $^{\cdot}OH$ radicals. Additionally, the calculated adsorption energies reveal that P-doped $Ti_3C_2O_2$ (- 4.26 eV) and OV-$Ti_3C_2O_2$ (-4.31 eV) exhibit significantly higher adsorption capacities compared to undoped $Ti_3C_2O_2$ (-0.56 eV), as illustrated in **Fig. 3.9(e)**. These observations highlight that P doping and

the introduction of OVs substantially enhance PMS adsorption and dissociation, thereby

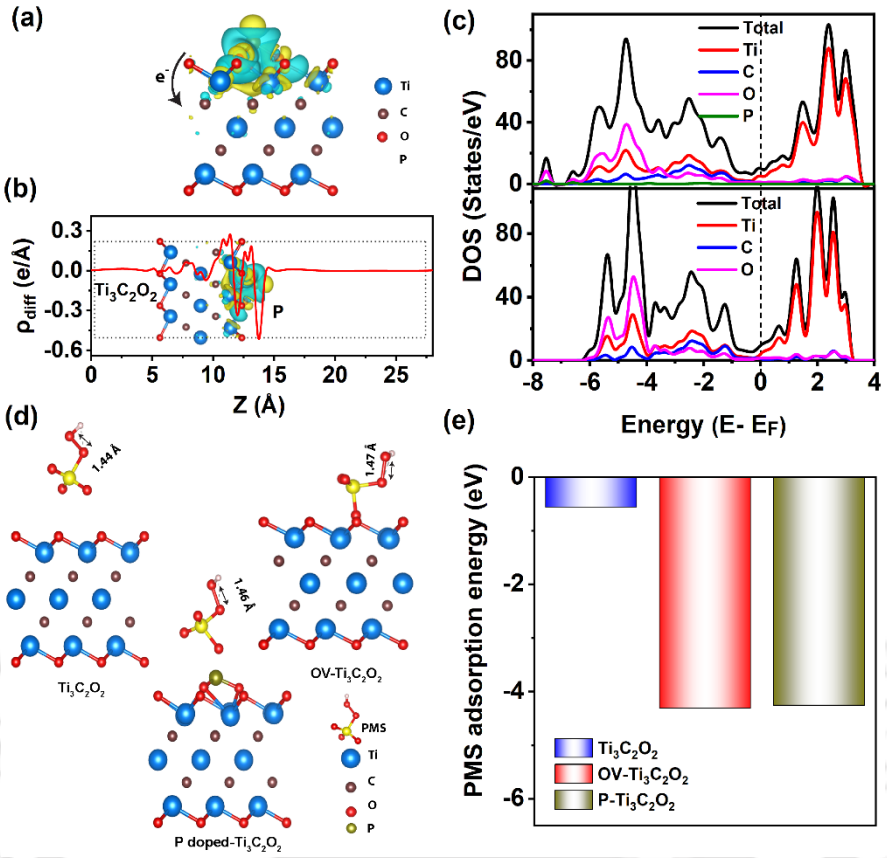

Fig. 3.9. (a) Charge density difference and (b) plane average charge density difference plot of P-$Ti_3C_2O_2$. (c) Comparison of the DOS of $Ti_3C_2O_2$ and P-$Ti_3C_2O_2$. (d) Optimized structure of PMS adsorbed $Ti_3C_2O_2$, OV-$Ti_3C_2O_2$, and P-$Ti_3C_2O_2$ showing the evolution of O-O bond length in PMS. (e) PMS adsorption energy on $Ti_3C_2O_2$, surface O vacant $Ti_3C_2O_2$, and P-doped $Ti_3C_2O_2$ surfaces.

accelerating the production of $SO_4^{\bullet-}$ and •OH radicals, which improves the efficiency of CIP degradation.

3.3.8. Cyclic Stability and Free Radical Scavenging Test

The recyclability of catalysts is a critical factor for their practical application in wastewater treatment. As illustrated in **Fig. 3.10(a)**, the cyclic stability of the MXP2@PVMS aerogel was evaluated in CIP degradation over multiple cycles. During the first cycle, 96% of CIP was degraded in 21 min. However, the degradation efficiency gradually declined in subsequent cycles, reducing to 87% in the 2nd cycle, 79% in the 3rd cycle, and further dropping to 70% in the 4th cycle for the same reaction time. This decline in catalytic performance with recycling can be attributed to the oxidation of metallic Ti species (Ti^{2+} and Ti^{3+}) to Ti^{4+}, along with the reduction of OVs sites due to pollutant adsorption. These factors lead to reduced PMS adsorption, subsequently hindering the formation of $SO_4^{\bullet-}$ and •OH radicals, thereby decreasing the overall degradation efficiency.

To confirm the generation of reactive radicals and their involvement in CIP degradation, a scavenging test was conducted, as depicted in **Fig. 3.10(b)**. The activation of PMS consistently

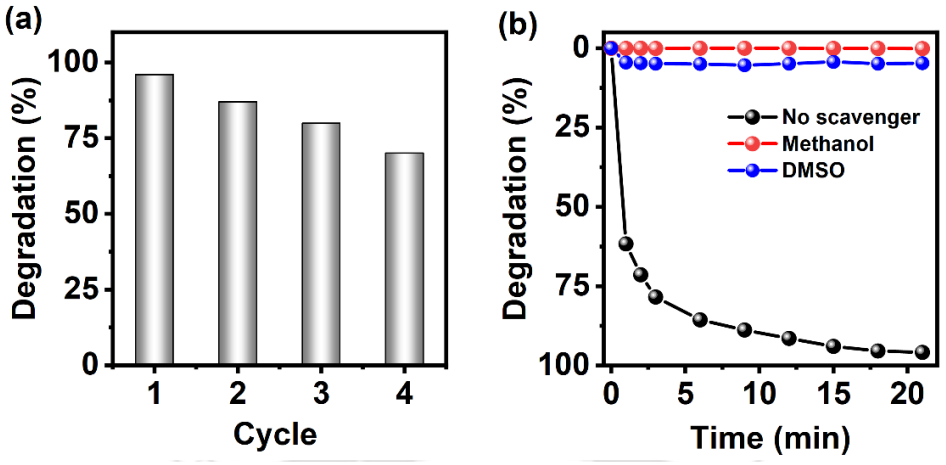

Fig. 3.10. (a) Cyclic stability of MXP2@PVMS aerogel, and (b) The effect of free radical scavenger in CIP degradation.

produces $SO_4^{\bullet-}$ and •OH radicals. To evaluate their contribution to the degradation process, methanol was used as a scavenger for both $SO_4^{\bullet-}$ and •OH radicals, while dimethyl sulfoxide (DMSO) was specifically employed to quench •OH radicals. Notably, the addition of 50 mM methanol completely inhibited CIP degradation, thereby confirming the crucial role of $SO_4^{\bullet-}$ and •OH radicals in the oxidation process. Additionally, the introduction of 50 mM DMSO resulted in a reduction in CIP degradation within the MXP2@PVMS/PMS system, although its inhibitory effect was less significant than that of methanol. These findings highlight that both $SO_4^{\bullet-}$ and •OH radicals play essential roles in facilitating CIP degradation.

3.3.9. Mechanism of CIP Degradation

To gain deeper insight into PMS activation and the catalytic CIP degradation mechanism for the MXP2@PVMS/PMS system, XPS analysis was conducted to examine the changes in the chemical states of various elements before and after the catalytic reaction. As depicted in **Fig. 3.11(a)**, the high-resolution Ti 2p XPS spectra obtained after the 2nd catalytic cycle reveal a decline in the proportions of Ti^{2+} (from 36% to 20.1%) and Ti^{3+} (from 26% to 13.3%), accompanied by a significant increase in Ti^{4+} content (from 17.5% to 60.3%). This transformation suggests the active participation of lower-valence Ti species in the catalytic degradation process. The substantial rise in Ti^{4+} confirms that Ti species serve as active sites for PMS activation, thereby facilitating the generation of reactive oxygen species (ROS). Further, the high-resolution O 1s XPS spectra, shown in **Fig. 3.11(b)**, reveal a reduction in the content of C-Ti-O_x and C-Ti-$(OH)_x$ from 37% and 19.1% to 26.4% and 14.6%, respectively.

This decrease underscores their involvement in PMS activation, highlighting the crucial role of surface functional groups in catalytic activity. Based on the identification of ROS and XPS analysis, a proposed mechanism for PMS catalytic activation is illustrated in **Fig. 3.11(c)**. The degradation of CIP follows a radical-mediated pathway, as revealed from the scavenging experiments. The hydrophilic nature of MXP2@PVMS facilitates PMS adsorption onto the low-valent Ti active sites, leading to the formation of Ti-O-O-SO_3 complexes[34]. These complexes interact with CIP molecules, ultimately degrading them into CO_2 and H_2O. Thus,

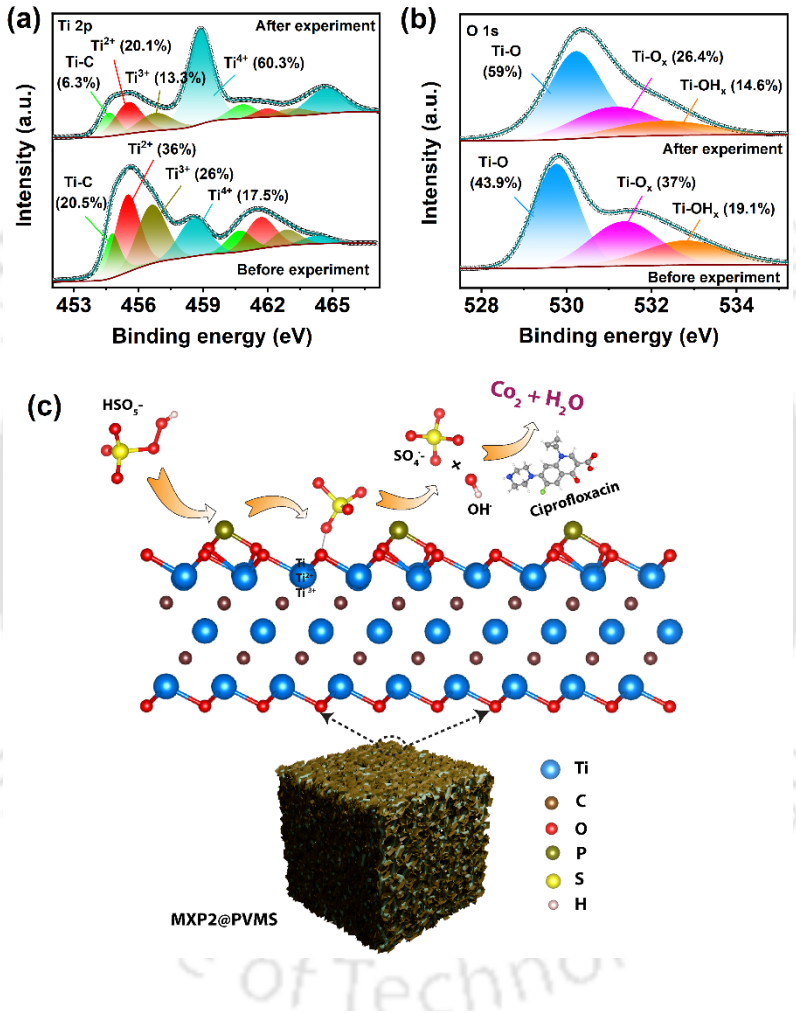

Fig. 3.11. (a) High-resolution XPS spectra of Ti 2p and (b) O 1s of MXP2, before and after CIP degradation. (c) A schematic illustration of CIP degradation on the surface of MXP2@PVMS in the presence of PMS.

the effective degradation of CIP is caused by the synergistic effect of both $SO_4^{\bullet-}$ and $^{\bullet}OH$ radicals. Additionally, P doping enhances catalytic efficiency by promoting PMS adsorption and dissociation, a process further supported by an increased concentration of OVs within the system.

Table 3.2. *A comparative analysis of the CIP degradation efficiency of the MXP2@PVMS hybrid aerogel, with previously reported literatures.*

Catalyst	Pollutant	Experimental Conditions	Degradation efficiency (%) (Time)	Ref.
$Bi_2WO_6/C_3N_4/ Ti_3C_2$	Ciprofloxacin (10 mg/L)	Catalyst (0.15 g/L) + 300 W Xe lamp irradiation	100 (50 min)	[35]
CN/MX/BP	Ciprofloxacin (20 mg/L)	Catalyst (0.2g /L) + 300 W Xe lamp irradiation	>99 (60 min)	[36]
$g\text{-}C_3N_4/Ti_3C_2$	Ciprofloxacin (20 mg/L)	Catalyst (0.2g /L) + 500 W Xe lamp irradiation	100 (150 min)	[37]
2D-2D BiOCl/ $Ti_3C_2T_x$	Ciprofloxacin (20 mg/L)	Catalyst (0.4g /L) + 300 W Xe lamp irradiation	90 (30 min)	[38]
VCo-MOF@MXene	Ciprofloxacin (40 mg/L)	Catalyst (0.1 gm/L) + PMS (0.6 mg/mL)	92.4 (30 min)	[39]
MXP2@PVMS aerogel	Ciprofloxacin (20 mg/L)	Catalyst (0.6 gm/L) + PMS (1.2 mM)	96 (21 min)	**This work**

Table 3.3. *A comparative analysis of the MB degradation efficiency of the MXP2@PVMS hybrid aerogel with the reported literature.*

Catalyst	Pollutant	Experimental Conditions	Degradation Time (min)	Degradation efficiency (%)/Adsorption capacity (mg/g)	Ref.
mp-MXene/TiO_{2-x} nanodots (NDs)	RhB (30mg/L)	Catalyst (150mg/L) + sunlight irradiation + H_2O_2 (0.7mM)	10	96%	[40]
MXene–Co_3O_4 nanoco-mposites	MB (12.5mg/L)	Catalyst (10 mg) + H_2O_2 (15 ml)	300	128.91 mg/g	[41]
Ti_3C_2- Fe_3O_4 MNPs	MB (20 mg/L)	Catalyst (0.5g/L) + H_2O_2 (50 mM/L)	6	100%	[42]
CdS@Ti_3C_2@TiO_2 nanocom-posite	MB (20mg/L)	Catalyst (250 mg/L) + vis light irradiations 300 W Xe lamp (λ < 400 nm)	88	100%	[43]
Fe/Ce-BDC@CS MOF	MB (30mg/L)	Catalyst (2.5 gm/L) + 0.25 ml H_2O_2 + 10 mg NH_2OH	20	100%	[44]
Ti^{3+}-TiO_2/Ti_3C_2	MB (10mg/L)	Catalyst (0.5gm/L) + H_2O_2 (4 mM) + visible light	100	99.2%	[45]
MXP2@PVMS aerogel	MB (10 mg/L)	Catalyst (0.6 gm/L) + PMS (1.2 mM)	12	98%	**This work**

3.4. Conclusions

A 3D porous aerogel structure of P-doped $Ti_3C_2T_x$ nanosheets was successfully fabricated by integrating them onto a 3D PVA-coated MS (MXP2@PVMS), as confirmed through comprehensive morphological characterization. This distinctive architecture provides enhanced surface properties and a high concentration of low-valence Ti states (Ti^{2+} and Ti^{3+}), as verified by XPS analysis, making it highly efficient for the degradation of CIP and organic dyes through AOPs. Under optimized conditions in the absence of light and with minimal PMS addition, the degradation efficiencies for CIP and MB reached 96% and 98% within 21 and 12 min, respectively. The degradation kinetics demonstrated outstanding rate constants of 0.1 min-

^{1} for CIP and 0.27 min^{-1} for MB. Notably, the MXP2@PVMS catalyst exhibited remarkable performance across a broad pH range (3-7) for CIP degradation, presenting a significant advantage over conventional Fenton catalysts in practical applications. DFT calculations provided further insight into the role of P doping in enhancing the electrical conductivity of $Ti_3C_2T_x$ nanosheets and its influence on PMS adsorption and dissociation, leading to superior degradation efficiency. Furthermore, radical scavenging experiments confirmed that both $SO_4^{\bullet-}$ and •OH radicals play a predominant role in the degradation process. In addition, degradation studies involving other dyes, including CV, MG, RhB, and MO, revealed that cationic dyes degrade more efficiently than anionic dyes, which is attributed to the negatively charged MXene surface promoting stronger electrostatic interactions with cationic dye molecules. In conclusion, the P-doped $Ti_3C_2T_x$@PVMS aerogel exhibits remarkable versatility as an advanced hybrid material, demonstrating efficient catalytic activity for the degradation of antibiotics and dyes. Its exceptional performance highlights its potential for environmental remediation applications, making it a promising candidate for addressing wastewater treatment challenges.

References

1. Giannakis, S.; Lin, K.-Y. A.; Ghanbari, F., A review of the recent advances on the treatment of industrial wastewaters by Sulfate Radical-based Advanced Oxidation Processes (SR-AOPs). *Chem. Eng. J.* **2021,** *406*, 127083.
2. Kohantorabi, M.; Moussavi, G.; Giannakis, S., A review of the innovations in metal- and carbon-based catalysts explored for heterogeneous peroxymonosulfate (PMS) activation, with focus on radical vs. non-radical degradation pathways of organic contaminants. *Chem. Eng. J.* **2021,** *411*, 127957.
3. Xin, Y.; Wang, H.; Xue, H.; Li, Q.; Li, H.; Zhang, Y.; Dong, Y.; Xie, H.; Ma, Y., Ti_3C_2-based MXene anchoring single-atom Co as a long-lasting peroxymonosulfate activator enabling efficient water decontamination: Deciphering the critical role of titanium vacancies. *Appl. Catal. B: Environ. Energy* **2025,** *365*, 124966.
4. Mi, X.; Wang, P.; Xu, S.; Su, L.; Zhong, H.; Wang, H.; Li, Y.; Zhan, S., Almost 100 % Peroxymonosulfate Conversion to Singlet Oxygen on Single-Atom CoN_{2+2} Sites. *Angew. Chem. Int. Ed.* **2021,** *60* (9), 4588-4593.
5. Bandpey, M.; Barz, D. P. J., Effects of interlayer space engineering and surface modification on the charge storage mechanisms of MXene nanomaterials: A review on recent developments. *Nanoscale* **2024,** *16* (32), 15078-15093.
6. Chen, W.; Liu, P.; Liu, Y.; Liu, Z., Recent advances in Two-dimensional $Ti_3C_2T_x$ MXene for flame retardant polymer materials. *Chem. Eng. J.* **2022,** *446*, 137239.
7. Jaberi, S. Y. S.; Asen, P.; Esfandiar, A.; Tolstoy, V. P., MXene/carbon hybrid nanostructures and heteroatom-doped derivatives for enhanced electrochemical energy storage. *J. Energy Storage* **2024,** *90*, 111751.

8. Patel, M. A.; Luo, F.; Khoshi, M. R.; Rabie, E.; Zhang, Q.; Flach, C. R.; Mendelsohn, R.; Garfunkel, E.; Szostak, M.; He, H., P-Doped Porous Carbon as Metal Free Catalysts for Selective Aerobic Oxidation with an Unexpected Mechanism. *ACS Nano* **2016,** *10* (2), 2305-2315.
9. Liu, Y.; Luo, R.; Li, Y.; Qi, J.; Wang, C.; Li, J.; Sun, X.; Wang, L., Sandwich-like Co_3O_4/MXene composite with enhanced catalytic performance for Bisphenol A degradation. *Chem. Eng. J.* **2018,** *347*, 731-740.
10. Ding, M.; Chen, W.; Xu, H.; Shen, Z.; Lin, T.; Hu, K.; Lu, C. h.; Xie, Z., Novel α-Fe_2O_3/MXene nanocomposite as heterogeneous activator of peroxymonosulfate for the degradation of salicylic acid. *J. Hazard. Mater.* **2020,** *382*, 121064.
11. Wu, L.; Li, Y.; Jia, Z.; Xu, L.; Sheng, G.; Wei, R.; Ye, K., Modification of melamine sponge by solid-phase esterification of citric acid-polyvinyl alcohol and its selective adsorption for cationic dyes. *Inorg. Chem. Commun.* **2024,** *161*, 112004.
12. Wang, X.; Xu, Q.; Zhang, L.; Pei, L.; Xue, H.; Li, Z., Adsorption of methylene blue and Congo red from aqueous solution on 3D MXene/carbon foam hybrid aerogels: A study by experimental and statistical physics modeling. *J. Environ. Chem. Eng.* **2023,** *11* (1), 109206.
13. Kresse, G.; Joubert, D., From ultrasoft pseudopotentials to the projector augmented-wave method. *Phys. Rev. B* **1999,** *59* (3), 1758.
14. Kresse, G.; Furthmüller, J., Efficient iterative schemes for ab initio total-energy calculations using a plane-wave basis set. *Phys. Rev. B* **1996,** *54* (16), 11169.
15. Blöchl, P. E., Projector augmented-wave method. *Phys. Rev. B* **1994,** *50* (24), 17953.
16. Perdew, J. P.; Burke, K.; Ernzerhof, M., Generalized gradient approximation made simple. *Phys. Rev. Lett.* **1996,** *77* (18), 3865.
17. Monkhorst, H. J.; Pack, J. D., Special points for Brillouin-zone integrations. *Phys. Rev. B* **1976,** *13* (12), 5188.
18. Tang, W.; Sanville, E.; Henkelman, G., A grid-based Bader analysis algorithm without lattice bias. *J. Phys.: Condens. Matter* **2009,** *21* (8), 084204.
19. Sanville, E.; Kenny, S. D.; Smith, R.; Henkelman, G., Improved grid-based algorithm for Bader charge allocation. *J. Comput. Chem.* **2007,** *28* (5), 899-908.
20. Momma, K.; Izumi, F., VESTA: a three-dimensional visualization system for electronic and structural analysis. *J. Appl. Crystallogr.* **2008,** *41* (3), 653-658.
21. Li, H.; Fan, K.; Xiong, P.; Zhou, H.; Lin, Z.; Tao, K.; Liu, T.; Guo, X.; Zhu, Y.; Zhuang, L.; Han, W.; Yang, C.; Liu, Y.; Meng-Jung Li, M.; Fu, M.; Wang, J.; Huang, H., Selective grafting of phosphorus onto $Ti_3C_2T_x$ MXene enables a two-proton process and enhanced charge storage. *J. Mater. Chem. A* **2024,** *12* (6), 3449-3459.
22. Sarycheva, A.; Gogotsi, Y., Raman Spectroscopy Analysis of the Structure and Surface Chemistry of $Ti_3C_2T_x$ MXene. *Chem. Mater.* **2020,** *32* (8), 3480-3488.
23. Wang, R.; Li, M.; Sun, K.; Zhang, Y.; Li, J.; Bao, W., Element-Doped Mxenes: Mechanism, Synthesis, and Applications. *Small* **2022,** *18* (25), 2201740.
24. Li, J.; Zhang, M.; Guan, Z.; Li, Q.; He, C.; Yang, J., Synergistic effect of surface and bulk single-electron-trapped oxygen vacancy of TiO_2 in the photocatalytic reduction of CO_2. *Appl. Catal. B: Environ.* **2017,** *206*, 300-307.
25. Yu, K.; Wang, S.; Li, Q.; Hou, T.; Xin, Y.; He, R.; Zhang, W.; Liang, S.; Wang, L.; Zhu, W., Au atoms doped in $Ti_3C_2T_x$ MXene: Benefiting recovery of oxygen vacancies towards photocatalytic aerobic oxidation. *Nano Res.* **2022,** *15* (4), 2862-2869.
26. Halim, J.; Cook, K. M.; Naguib, M.; Eklund, P.; Gogotsi, Y.; Rosen, J.; Barsoum, M. W., X-ray photoelectron spectroscopy of select multi-layered transition metal carbides (MXenes). *Appl. Surf. Sci.* **2016,** *362*, 406-417.

27. Natu, V.; Benchakar, M.; Canaff, C.; Habrioux, A.; Célérier, S.; Barsoum, M. W., A critical analysis of the X-ray photoelectron spectra of $Ti_3C_2T_z$ MXenes. *Matter* **2021,** *4* (4), 1224-1251.
28. Peng, W.; Han, J.; Lu, Y.-R.; Luo, M.; Chan, T.-S.; Peng, M.; Tan, Y., A General Strategy for Engineering Single-Metal Sites on 3D Porous N, P Co-Doped $Ti_3C_2T_x$ MXene. *ACS Nano* **2022,** *16* (3), 4116-4125.
29. Chao, M.; Zeng, K.; Lu, C.; Shi, Z.; Guo, J.; Chen, X.; Yang, R., Synergized N and P co-doped $Ti_3C_2T_x$ mxene enabling high-performance Li-air batteries. *J. Colloid Interface Sci.* **2024,** *657*, 46-53.
30. Yin, R.; Guo, W.; Wang, H.; Du, J.; Zhou, X.; Wu, Q.; Zheng, H.; Chang, J.; Ren, N., Selective degradation of sulfonamide antibiotics by peroxymonosulfate alone: Direct oxidation and nonradical mechanisms. *Chem. Eng. J.* **2018,** *334*, 2539-2546.
31. Noroozi, R.; Gholami, M.; Farzadkia, M.; Jonidi Jafari, A., Degradation of ciprofloxacin by $CuFe_2O_4$/GO activated PMS process in aqueous solution: performance, mechanism and degradation pathway. *Int. J. Environ. Anal. Chem.* **2022,** *102* (1), 174-195.
32. Li, W.; Li, S.; Tang, Y.; Yang, X.; Zhang, W.; Zhang, X.; Chai, H.; Huang, Y., Highly efficient activation of peroxymonosulfate by cobalt sulfide hollow nanospheres for fast ciprofloxacin degradation. *J. Hazard. Mater.* **2020,** *389*, 121856.
33. Xu, H.; Liu, H.; Guo, P.; Yang, W.; Li, M.; Li, C.; Wang, H.; Peng, W.; Liu, J., Multifunctional capacitive deionization removal of metal ions via crumpled phosphorus-doped $Ti_3C_2T_x$ MXene nanosheets. *Desalination* **2024,** *586*, 117861.
34. Wang, F.; Bian, Z.; Zhang, W.; Zheng, L.; Zhang, Y.; Wang, H., Fluorine-free MXene activate peroxymonosulfate to remove tetracyclic antibiotics. *Sep. Purif. Technol.* **2023,** *314*, 123549.
35. Wu, K.; Song, S.; Wu, H.; Guo, J.; Zhang, L., Facile synthesis of $Bi_2WO_6/C_3N_4/Ti_3C_2$ composite as Z-scheme photocatalyst for efficient ciprofloxacin degradation and H_2 production. *Appl. Catal. A: General* **2020,** *608*, 117869.
36. Zhou, Y.; Yu, M.; Liang, H.; Chen, J.; Xu, L.; Niu, J., Novel dual-effective Z-scheme heterojunction with g-C_3N_4, Ti_3C_2 MXene and black phosphorus for improving visible light-induced degradation of ciprofloxacin. *Appl. Catal. B: Environ.* **2021,** *291*, 120105.
37. Liu, N.; Lu, N.; Su, Y.; Wang, P.; Quan, X., Fabrication of g-C_3N_4/Ti_3C_2 composite and its visible-light photocatalytic capability for ciprofloxacin degradation. *Sep. Purif. Technol.* **2019,** *211*, 782-789.
38. Chen, Z.; Ma, Y.; Chen, W.; Tang, Y.; Li, L.; Wang, J., Enhanced photocatalytic degradation of ciprofloxacin by heterostructured BiOCl/$Ti_3C_2T_x$ MXene nanocomposites. *J. Alloys Compd.* **2023,** *950*, 169797.
39. Li, Z.; Ning, S.; Hu, F.; Zhu, H.; Zeng, L.; Chen, L.; Wang, X.; Fujita, T.; Wei, Y., Preparation of VCo-MOF@MXene composite catalyst and study on its removal of ciprofloxacin by catalytically activating peroxymonosulfate: Construction of ternary system and superoxide radical pathway. *J. Colloid Interface Sci.* **2023,** *629*, 97-110.
40. Cheng, X.; Zu, L.; Jiang, Y.; Shi, D.; Cai, X.; Ni, Y.; Lin, S.; Qin, Y., A titanium-based photo-Fenton bifunctional catalyst of mp-MXene/TiO_{2-x} nanodots for dramatic enhancement of catalytic efficiency in advanced oxidation processes. *Chem. Commun.* **2018,** *54* (82), 11622-11625.
41. Luo, S.; Wang, R.; Yin, J.; Jiao, T.; Chen, K.; Zou, G.; Zhang, L.; Zhou, J.; Zhang, L.; Peng, Q., Preparation and Dye Degradation Performances of Self-Assembled MXene-Co3O4 Nanocomposites Synthesised via Solvothermal Approach. *ACS Omega* **2019,** *4* (2), 3946-3953.
42. Liu, Q.; Tan, X.; Wang, S.; Ma, F.; Znad, H.; Shen, Z.; Liu, L.; Liu, S., MXene as a non-metal charge mediator in 2D layered CdS@Ti_3C_2@TiO_2 composites with superior Z-

scheme visible light-driven photocatalytic activity. *Environ. Sci.: Nano* **2019,** *6* (10), 3158-3169.
43. Cui, Y.; Liu, M.; Huang, H.; Zhang, D.; Chen, J.; Mao, L.; Zhou, N.; Deng, F.; Zhang, X.; Wei, Y., A novel one-step strategy for preparation of Fe_3O_4-loaded Ti_3C_2 MXenes with high efficiency for removal organic dyes. *Ceram. Int.* **2020,** *46* (8, Part B), 11593-11601.
44. Zheng, Y.; Ran, L.; Zhang, X.; Zhu, L.; Zhang, H.; Xu, J.; Zhao, Q.; Zhou, L.; Ye, Z., Enhanced Fenton catalytic degradation of methylene blue by the synergistic effect of Fe and Ce in chitosan-supported mixed-metal MOFs (Fe/Ce-BDC@CS). *Int. J. Biol. Macromol.* **2024,** *279*, 134872.
45. Zhong, Q.; Li, Y.; Liu, J.; Li, J.; Zhang, G., In situ construction of Ti^{3+} self-doped TiO_2/Ti_3C_2 Schottky heterojunctions for highly selective photo-Fenton-like degradation of organic pollutants: Surface/interface effect and mechanism insight. *Appl. Surf. Sci.* **2024,** *667*, 160376.

Chapter 4

Efficient Reduction of Organic Pollutants and Photo-Electrochemical Hydrogen Production by $Bi_2S_3/Ti_3C_2T_x$ Nanocomposite

In the previous two chapters, the treatment of wastewater containing organic pollutants was explored using AOPs, specifically employing transition metal Ti-based $Ti_3C_2T_x$ MXenes. Although low-valent Ti states, in combination with an oxidizing agent such as hydrogen peroxide and peroxymonosulfate, have demonstrated excellent performance in degrading organic dyes and CIP antibiotics. However, they have proven ineffective for the removal of 4-nitrophenol (4-NP). Considering this limitation, catalytic reduction presents as a promising alternative for wastewater treatment. Unlike oxidation-based approaches, catalytic reduction involves the electron transfer process, leading to the formation of less harmful products. These final products can have potential applications in pharmaceutical synthesis and environmentally sustainable processes. Typically, catalytic reduction requires $NaBH_4$ as a reducing agent in the presence of an active catalyst to reduce organic pollutants, as discussed in **Chapter 1**, **Section 1.5.2**. Previous studies demonstrate the incapability of pristine $Ti_3C_2T_x$ MXene in the reduction of organic pollutants in the presence of $NaBH_4$. To address this limitation, we synthesized a cost-effective semimetal sulfide-based MXene composite, $Bi_2S_3/Ti_3C_2T_x$, via a single-step hydrothermal method. The catalytic performance of this composite was systematically investigated for the reduction of organic pollutants in the presence of $NaBH_4$. Additionally, DFT simulations were employed to elucidate the underlying reduction mechanism, which is discussed in detail in this chapter. Beyond catalytic reduction, the study also explores the photoelectrocatalytic water-splitting performance of the synthesized composite material. The $Bi_2S_3/Ti_3C_2T_x$ composite demonstrated enhanced hydrogen evolution activity under visible-near infrared (Vis-NIR) light illumination. The mechanistic insights into this improved performance are comprehensively analyzed in subsequent sections of this chapter.

4.1. Introduction

Environmental pollution, particularly the contamination of freshwater sources, presents a serious threat to human health and has become a critical issue on a global scale [1-4]. Among various pollutants, nitrophenol compounds, such as 4-NP, are widely used as key raw materials in the production of dyes, pesticides, and pharmaceuticals [5]. The discharge of industrial

effluents containing 4-NP poses significant risks due to its toxic, carcinogenic properties and its potential to cause allergic reactions and skin inflammation [5, 6]. The conversion of the highly toxic 4-NP to the less harmful 4-aminophenol (4-AP) is therefore essential for both industrial applications and the treatment of wastewater contaminated with 4-NP. The by-product, 4-AP, has a lower environmental impact and can be reused in the synthesis of aniline and paracetamol [7]. The selection of an appropriate catalyst is crucial in facilitating this reduction process. Typically, the catalytic reduction of 4-NP to 4-AP involves the use of $NaBH_4$ as a reducing agent, in combination with an active catalyst. However, the widespread use of precious metal catalysts[6-8] poses a limitation to their practical application due to high costs. Thus, the development of highly efficient non-precious metal catalysts is essential to advance the field of catalytic reduction and broaden its applicability.

Photoelectrochemical water splitting is a sustainable approach for generating clean energy, playing a crucial role in advancing the hydrogen economy and achieving carbon neutrality. Hydrogen production in alkaline media offers several advantages, including enhanced electrode stability, consistent power output, cost-effective electrolyzers, and the prevention of acidic corrosion, making it a highly promising method for industrial applications. In alkaline systems, the Volmer step [9] ($H_2O + e^- \rightarrow H_{ads} + OH^-$) represents the rate-limiting step in hydrogen evolution due to the challenges associated with water dissociation and inappropriate hydrogen adsorption. Therefore, an efficient HER catalyst must effectively promote both water splitting and hydrogen adsorption processes. Although noble metal-based catalysts exhibit superior performance[10, 11], their high cost and limited durability restrict their widespread application. This has driven significant interest in the development of non-precious metal catalysts as more sustainable and cost-effective alternatives for long-term use.

Low-cost, earth-abundant metal sulfides have garnered significant attention for their potential in catalytic and optoelectronic applications, owing to their exceptional surface properties and light absorption capabilities[12-14]. Recent research has emphasized the potential of bismuth nanoparticles (Bi NPs) and bismuth sulfide (Bi_2S_3)-based composites in the degradation of organic pollutants and the advancement of optoelectronic devices. Bi_2S_3 is particularly notable for its distinctive properties, including a direct bandgap ranging from 1.3 to 1.7 eV[15], a high absorption coefficient[16] (~10^5 cm^{-1}), and excellent carrier mobility[16] (~200 $cm^2/V{\cdot}s$), which collectively enhance light absorption and facilitate efficient electron transfer. Furthermore, Bi NPs exhibit localized surface plasmon resonance[17, 18] (LSPR), significantly enhancing their ability to absorb visible light. Despite these advantages, the low-cost and scalable hydrothermal

synthesis of Bi_2S_3 is often hindered by severe agglomeration due to its high surface energy[19], negatively impacting its catalytic performance. To reduce this challenge, $Ti_3C_2T_x$ nanosheets can be employed as a supporting material. These nanosheets provide a stable substrate that prevents agglomeration and promotes interfacial charge transfer, thereby enhancing the catalytic efficiency of the composite materials.

In this study, a simple hydrothermal method is employed for the in-situ growth of Bi_2S_3 nanorods on the surface of $Ti_3C_2T_x$ MXene nanosheets. The successful synthesis of $Ti_3C_2T_x$ MXene nanosheets integrated with Bi_2S_3 nanorods is confirmed through TEM and XPS analyses. Furthermore, the catalytic efficiency of the $Bi_2S_3/Ti_3C_2T_x$ composite is evaluated for the reduction of 4-NP, MB, MO, RhB, and CIP in the presence of $NaBH_4$, where all pollutants exhibit excellent reduction rates except for CIP. Additionally, the reduction mechanism of 4-NP is supported by DFT calculations. Moreover, optical studies reveal that the $Bi_2S_3/Ti_3C_2T_x$ composite facilitates excellent light absorption and efficient separation of photogenerated charge carriers, leading to a significant enhancement in photoelectrochemical HER performance under both dark and Vis-NIR light illumination. Notably, the composite demonstrates a lower overpotential of 73 mV and a Tafel slope of 84 mV/dec, outperforming pristine Bi_2S_3 nanorods. This study provides a comprehensive understanding of the exceptional HER performance and the underlying charge transfer mechanism.

4.2. Experimental Details

4.2.1. Synthesis of $Ti_3C_2T_x$ Nanosheets

The synthesis of $Ti_3C_2T_x$ MXene nanosheets via LiF/HCl etching method is similar to **Chapter 3**, **Section 3.2.1.**

4.2.2. Synthesis of $Bi_2S_3/Ti_3C_2T_x$ MXene Composite

Herein, a one-step hydrothermal approach was adopted, as schematically illustrated in **Fig. 4.1**. In a typical synthesis, varying amounts of $Ti_3C_2T_x$ (MX) nanosheets (7, 14, and 21 mg) were dispersed in 25 mL of DI water. Subsequently, 1 mM $Bi(NO_3)_3 \cdot 5H_2O$ was introduced into the dispersion, followed by sonication and vigorous stirring at room temperature. After complete adsorption of Bi^{3+} ions onto the negatively charged MX surface, 2 mM thiourea (CH_4N_2S) was added, and the solution was stirred continuously for another 1 h. The resulting mixture was then transferred to a Teflon-lined stainless-steel autoclave and subjected to hydrothermal treatment at 140°C for 10 h in a vacuum oven. After cooling, the black precipitate was collected

and purified through multiple centrifugation cycles using ethanol and DI water. The obtained product was vacuum-dried at 70°C overnight, and the final composite material was obtained

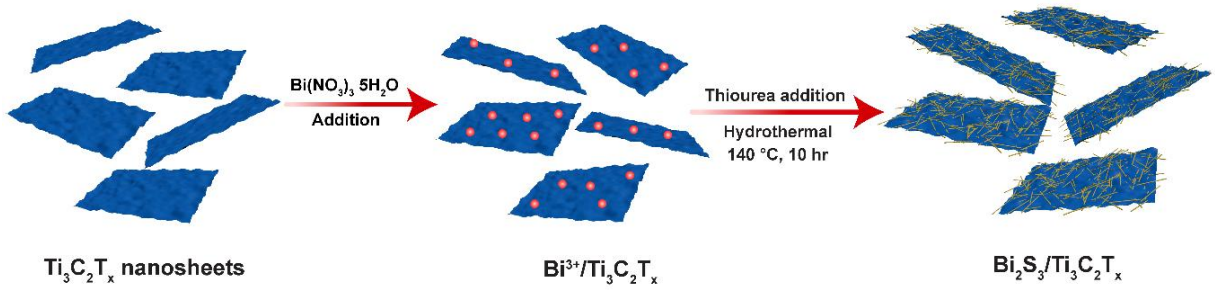

Fig. 4.1. A schematic illustration of the synthesis of $Bi_2S_3/Ti_3C_2T_x$ nanocomposite.

as black powder, which was subsequently stored in a desiccator for further characterization. For comparison, pristine Bi_2S_3 (BS) nanorods were synthesized using the same procedure, except for the addition of MX nanosheets. The possible reaction pathway[20] for the synthesis is provided below:

$$Bi(NO_3)_3 + H_2O \longleftrightarrow 2HNO_3 + BiONO_3 \quad (1)$$

$$2BiONO_3 + 3S^{2-} + H_2O \longleftrightarrow Bi_2S_3 + 4OH^- + 2NO^{3-} \quad (2)$$

$$nBi_2S_3 \longleftrightarrow Bi_2S_3 \text{ nanorods} \quad (3)$$

It is important to note that all experimental procedures were carried out under an Ar atmosphere to reduce the oxidation of MX nanosheets. Additionally, the pH of the solution is a crucial factor in ensuring the complete dissolution of $Bi(NO_3)_3 \cdot 5H_2O$, facilitating the formation of Bi^{3+} ions. In this synthesis, MX nanosheets play a crucial role by facilitating nucleation sites on their surface, thereby preventing the aggregation of Bi_2S_3 nanorods. Additionally, the dispersion of Bi_2S_3 nanorods was controlled by modulating the MX loading, leading to the formation of composites designated as BSMX7, BSMX14, and BSMX21.

4.2.3. Catalytic Reduction Procedure for Organic Pollutants

The catalytic activity of the synthesized composite for the reduction of 4-NP was evaluated in the presence of $NaBH_4$. Initially, 0.2 mL of $NaBH_4$ solution (0.2 mM) was introduced into 2.3 mL of 4-NP solution (25 mg/mL). Subsequently, a predetermined amount of catalyst suspension was added to the reaction mixture, and the progress of the catalytic reduction was monitored through UV-Vis spectroscopy by measuring the absorption spectrum of 4-NP. Furthermore, to assess the catalyst's efficiency in degrading other pollutants such as MB, MO, and CIP, a catalyst dosage of 0.2 mg was employed while maintaining the pollutant concentration at 15 mg/mL under constant experimental conditions.

4.2.4. Electrochemical Experiments

Electrochemical characterizations were carried out using a three-electrode setup, comprising a Pt wire as the counter electrode, an Ag/AgCl reference electrode, and a catalyst-integrated graphite sheet (1×1 cm^2) as the working electrode. For the fabrication of the working electrode, 4 mg of catalyst and a certain amount of carbon black with a ratio of 1:4 were combined in 190 µL of ethanol, and a specific volume of Nafion was added to the mixture. This solution was sonicated for 30 min to form a uniform ink, which was then coated onto the graphite sheet and vacuum-dried overnight. Electrochemical measurements were conducted using a 1 M KOH solution at room temperature, both in the dark and under Vis-NIR light illumination.

4.2.5. Characterization Techniques

To analyze the crystal structure, morphology, and surface properties of the $Bi_2S_3/Ti_3C_2T_x$ composites, XRD, Raman spectroscopy, and TEM analyses were performed. However, the characterization procedures are the same as those described in **Chapter 2**, **Section 2.2.3** and **Chapter 3**, **Section 3.2.4.** Furthermore, temporal photocurrent response (I-t) measurements were carried out using a microprobe station (ECOPIA, EPS-500), an 808 nm laser with TTL modulation (CNI Laser), and a source-measure unit (Keithley 2400). Linear sweep voltammetry (LSV) and electrochemical impedance spectroscopy (EIS) were conducted using an electrochemical workstation (CH Instruments, CHI6044E), and the EIS data were subsequently analyzed using an EIS Spectra analyzer. Photoelectrochemical characterization was performed with a solar simulator (Photo Emission Tech, Model: 300WSS-PC, Class AAA), providing a solar flux of 1 sun (1 kW m^{-2}).

4.2.6. Computational Details

The DFT calculations were carried out using VASP[21-23]. The PBE functional was employed within the GGA for exchange-correlation[24]. A 500-eV kinetic energy cut-off was used for all calculations. Grimme-D3 van der Waals corrections[25] were included for computations involving the BSMX composite. A Monkhorst-Pack k-point[26] grid of 8 × 8 × 1 was used for Brillouin zone sampling. Bader charge analysis, developed by Henkelman's group[27, 28], was used to investigate charge transfer. The charge density distribution was visualized with VESTA software[29], and the charge density difference (ρ_{cdd}) was calculated using the corresponding formula:

$$\rho_{cdd} = \rho_{AB} - \rho_A - \rho_B \ , \qquad (4)$$

where, ρ_{AB}, ρ_A, and ρ_B represent the charge density of the composite material and its constituent materials.

4.3. Results and Discussion

4.3.1. Morphological Characterizations

The surface texture and morphological characteristics of the synthesized materials were analyzed using AFM, TEM, and FESEM. The TEM and AFM images, illustrated in **Fig. 4.2**,

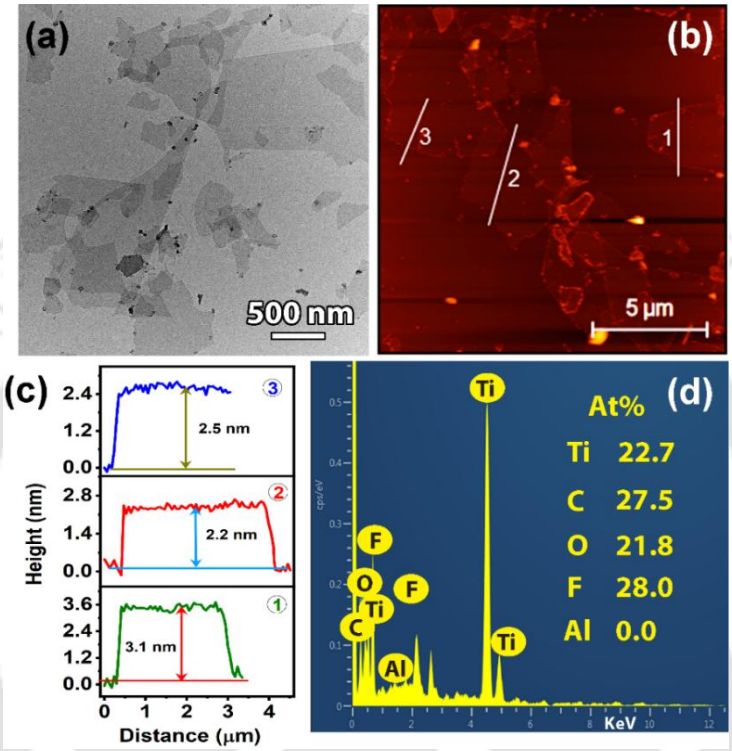

Fig. 4.2. (a) TEM image, (b-c) AFM image and corresponding height profile, and (d) EDS spectra of MX nanosheets.

indicate that the MX nanosheets exhibit a lateral dimension ranging between ~ 0.2 and 1 µm, with an average thickness of ~2.5 nm, corresponding to monolayer MX nanosheets[30].

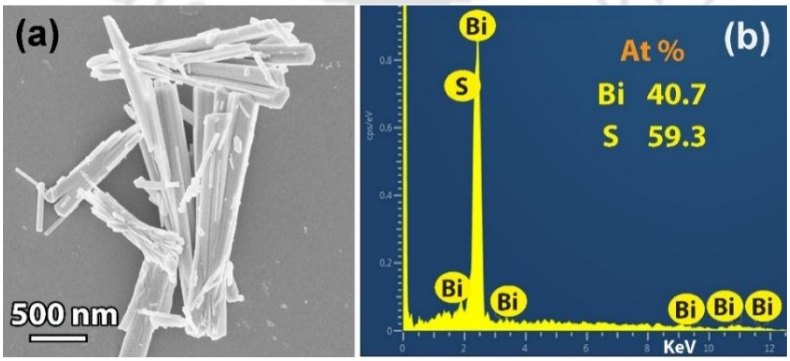

Fig. 4.3. (a) FESEM image, (b) EDS spectra of BS nanorods showing the atomic percentage of different elements.

Furthermore, EDS analysis in **Fig. 4.2(d)** confirms the absence of Al, validating the successful removal of Al layers. The atomic composition of Ti, C, O, and F is determined to be 22.7%, 27.5%, 21.8%, and 28.0%, respectively. The FESEM image of pristine BS in **Fig. 4.3(a)** displays a nanorod bundle with extreme aggregation. This aggregation is attributed to the high surface energy of BS nanorods, which inherently tend to cluster to minimize their surface energy. The EDS analysis (**Fig. 4.3(b)**) of BS nanorods further reveals atomic percentages of Bi (40.7%) and S (59.3%). The TEM image in **Fig. 4.4(a)** illustrates that the aggregated

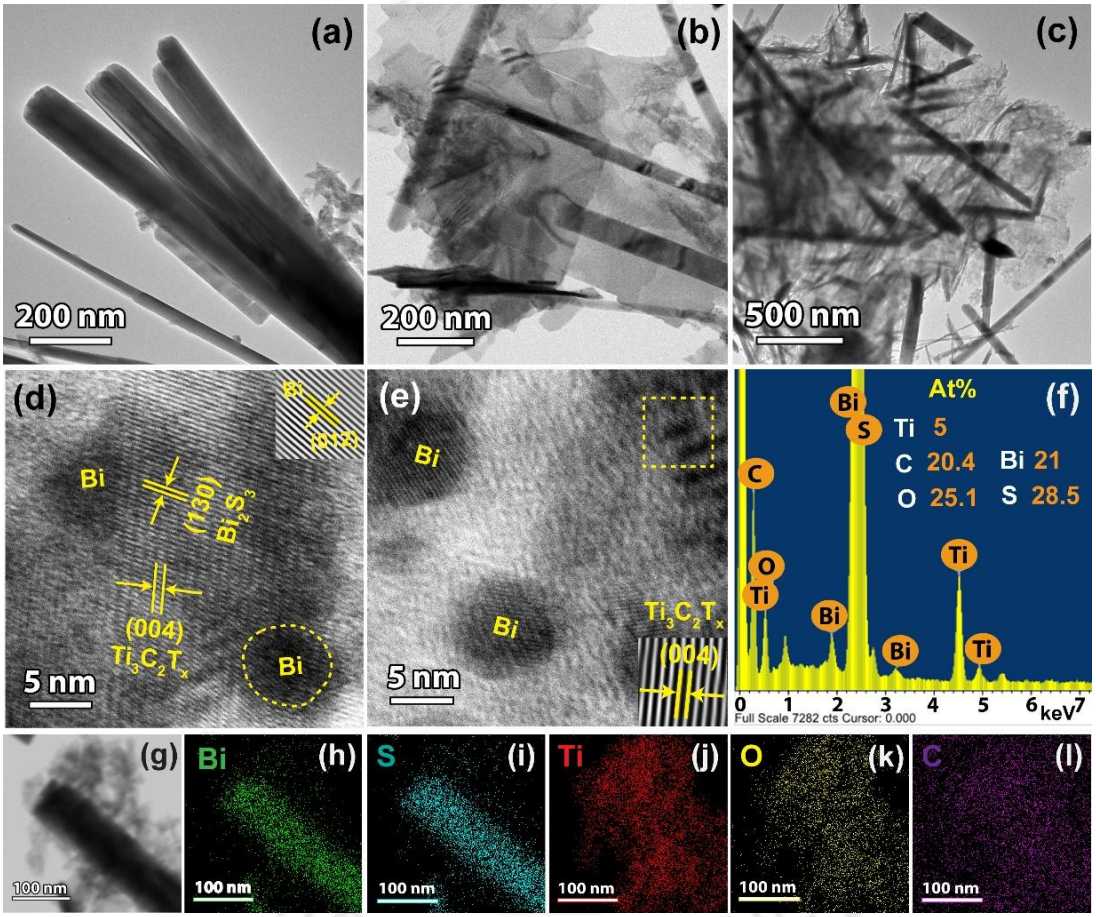

Fig. 4.4. The TEM images of BSMX composites with various loading amounts of MX nanosheets: (a) 7, (b) 14, and (c) 21 mg. (d) HRTEM image of BSMX14; the top right inset shows the IFFT lattice image of Bi NPs. (e) HRTEM image of BSMX14 illustrating Bi NPs over MX nanosheets; the bottom inset shows the IFFT lattice image of MX nanosheets. (f) EDS spectra of BSMX14 show the atomic percentage of different elements. (g-l) elemental mapping of Bi, S, Ti, O, and C elements in BSMX14 nanocomposite.

morphology of BSMX7 is likely due to the absence of sufficient nucleation sites arising from a lower MX nanosheet loading. Conversely, BSMX14 in **Fig. 4.4(b)** demonstrates a well-dispersed morphology of BS nanorods over MX nanosheets, whereas BSMX21 **(Fig. 4.4 (c))** exhibits an excess presence of MX nanosheets, leading to a bird's nest-like morphology. The HRTEM image in **Fig. 4.4(d)** identifies distinct lattice planes corresponding to BS, MX, and

metallic Bi NPs, with interplanar spacings of 0.36 nm, 0.51 nm, and 0.32 nm, which correspond with the (130), (004), and (012) crystal planes[31, 32], respectively. The inset in the upper section of **Fig. 4.4(d)** displays the inverse fast Fourier transform (IFFT) lattice image of a Bi NP, corresponding to the (012) crystal plane. Additionally, **Fig. 4.4 (e)** depicts Bi NPs with an average particle size of ~ 6 nm, while the inset at the bottom shows the IFFT lattice image of an MX nanosheet corresponding to the (004) crystal planes. Based on prior research, metallic Bi NPs exhibit superior catalytic activity compared to bulk Bi[31, 33]. Hence, the presence of self-reduced Bi NPs in BSMX14 is expected to provide substantial advantages in various catalytic applications. The EDS spectrum of BSMX14 in **Fig. 4.4(f)** demonstrates the atomic percentages of Bi (21%), S (28.5%), Ti (5%), O (25.1%), and C (20.4%). Furthermore, the elemental mapping images (**Fig. 4.4(g-l)**) verify the homogeneous distribution of these elements within BSMX14. The morphological analysis of BSMX composites underscores the necessity of maintaining an optimal balance between BS nanorods and MX nanosheets to achieve a well-dispersed structure. Such a balanced configuration is critical for enhanced light absorption and efficient charge transfer among Bi NPs, BS nanorods, and MX layers, promoting stronger interfacial interactions and improved catalytic performance.

4.3.2. Structural Characterizations

The XRD patterns corresponding to MX nanosheets, BS nanorods, and BSMX14 composites are depicted in **Fig. 4.5(a)**. In the case of MX nanosheets, distinct diffraction peaks are observed at 2θ = 5.9°, 17.4°, 29.4°, 34.2°, and 45°, corresponding to the (002), (004), (006), (101), and (106) crystal planes, respectively. Additionally, the XRD pattern of BS nanorods matches with its orthorhombic phase (JCPDS No. 01-075-1306). The BSMX14 composite exhibits an XRD pattern similar to that of pristine BS but with higher peak intensities. This suggests that the presence of MX nanosheets during the in-situ growth of BS nanorods enhances their crystallinity without altering their crystal structure. However, no distinct diffraction peaks corresponding to MX nanosheets or Bi NPs are detected, likely due to their low concentration within the composite. To further validate the structural phases of the samples, Raman spectroscopy was performed. The Raman spectra of pristine MX nanosheets are similar, as discussed in **section 3.3.2**. The comparative Raman spectra of MX nanosheets, BS nanorods, and BSMX14 composites are shown in **Fig. 4.5(b)**. The orthorhombic phase of BS exhibits four Raman-active modes (A_g, B_{1g}, B_{2g}, and B_{3g}) and a single infrared-active mode (B_{3u}), as predicted by Tanner et al.[34]. The Raman spectrum of BS nanorods features peaks at 71.4, 100.5, 237.2, and 257.4 cm^{-1}, which correspond to the A_g optical phonon mode[34]. For

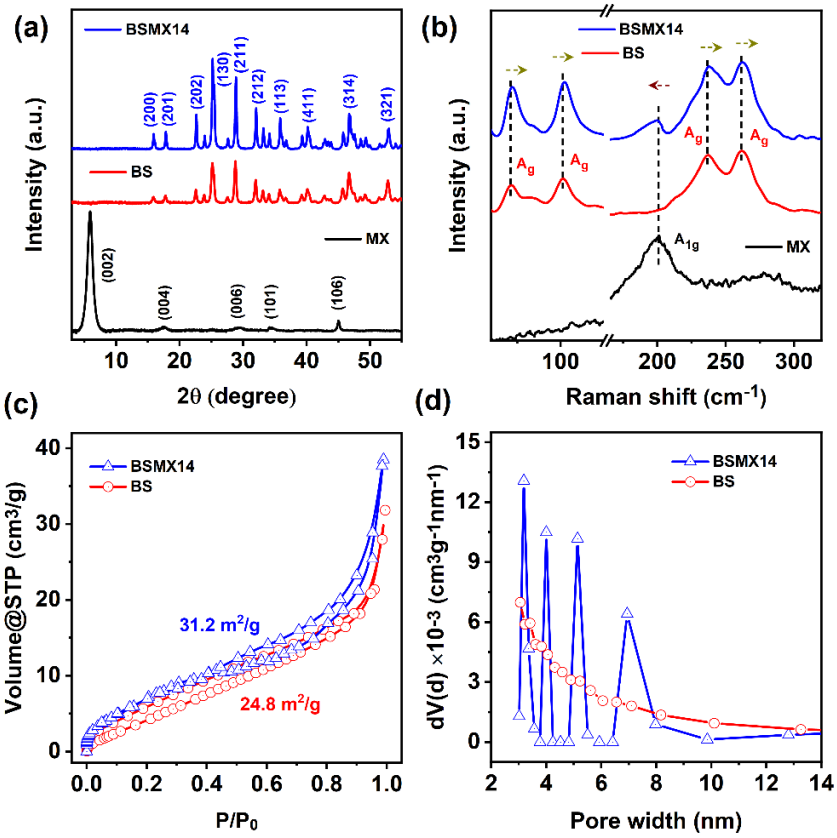

Fig. 4.5. Comparison of (a) XRD patterns, and (b) Raman spectra of MX nanosheets, BS nanorods, and BSMX14 composite at 532 nm laser excitation. (c) Nitrogen adsorption-desorption isotherm, and (d) BJH pore size distribution in BS nanorods and BSMX14 composite.

BSMX14, the Raman spectrum exhibits characteristic bands of both BS (A_g) and MX (A_{1g}), confirming their coexistence within the composite. Interestingly, a red shift in the A_{1g} vibrational mode of MX from 201.2 cm^{-1} to 199.8 cm^{-1} is observed, which can be attributed to the tensile strain introduced in the MX lattice upon composite formation. In contrast, all A_g modes of BS nanorods exhibit a blue shift compared to pristine BS nanorods, indicating the presence of compressive strain in the BS lattice. This strain is likely induced by the interaction between BS nanorods and MX nanosheets. Collectively, these Raman spectral observations confirm the structural stability and strong interfacial interaction between BS nanorods and MX nanosheets in the BSMX14 composite.

Additionally, the nitrogen adsorption-desorption isotherm analysis was conducted to evaluate the specific surface area and pore size distribution of the synthesized materials, as illustrated in **Fig. 4.5(c).** The isotherms for BS nanorods and BSMX14 exhibit a Type IV pattern, indicating a mesoporous structure. The Brunauer-Emmett-Teller (BET) surface area was determined to be 24.8 m^2/g for BS nanorods and 31.2 m^2/g for BSMX14, highlighting a

significant enhancement in surface area upon MX nanosheet incorporation. Moreover, Barrett-Joyner-Halenda (BJH) pore size distribution analysis confirms the mesoporous nature of both BS nanorods and BSMX14. Notably, the composite material exhibits larger pore sizes, (**Fig. 4.5(d)**) reaching up to 7 nm, compared to pristine BS nanorods. These findings underscore the role of MX nanosheets in increasing both surface area and porosity, which in turn provides a higher density of active sites for catalytic reactions, ultimately contributing to enhanced catalytic efficiency.

4.3.3. XPS Analysis

The XPS analysis was conducted to investigate the elemental composition and valence states of the synthesized materials. The survey XPS spectra of MX, BS, and BSMX14 within the energy range of 100-750 eV are illustrated in **Fig. 4.6(a)**. The pristine MX nanosheets exhibit characteristic XPS peaks corresponding to Ti, C, F, and O, while BS nanorods show the presence of Bi and S. In contrast, the BSMX14 composite displays peaks associated with Bi, S, Ti, O, and C, confirming the successful integration of BS and MX within the composite.

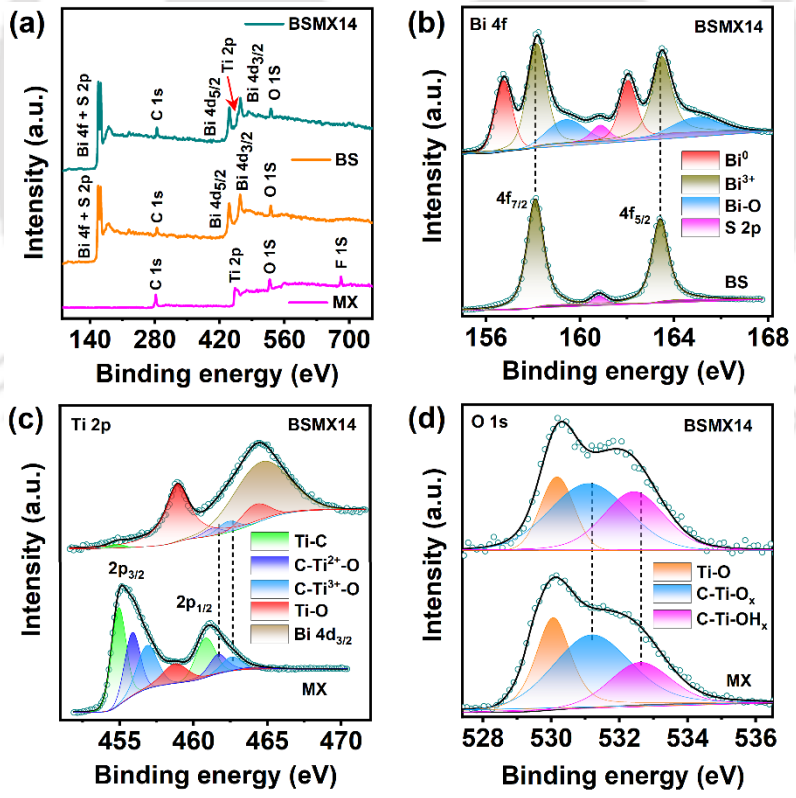

Fig. 4.6. (a) Survey scan XPS spectra of MX, BS, and BSMX14. High-resolution XPS spectra of (b) Bi 4f from BS and BSMX14, (c) Ti 2p, and (d) O 1s of MX and BSMX14. The symbols represent the experimental data, and the solid lines correspond to the Gaussian-Lorentzian fitted spectra with Shirley baseline.

However, no peaks corresponding to F are detected, and the possible reasons for its absence

are discussed later. To further understand the electronic states, high-resolution XPS spectra of Bi 4f and S 2p for both pristine BS and BSMX14 are compared in **Fig. 4.6(b)**. The BS nanorods exhibit two prominent peaks at BE of 158.1 eV and 163.4 eV, corresponding to Bi $4f_{7/2}$ and Bi $4f_{5/2}$ of Bi^{3+} respectively[35], in addition to a smaller peak at 160.8 eV corresponding to the S^{2-} orbital[35]. In contrast, the XPS spectrum of the BSMX14 composite demonstrates significant modifications compared to pristine BS. Two additional peaks at 156.8 eV and 162.1 eV are characteristic of metallic bismuth[36] (Bi^0). Furthermore, new peaks at 159.4 eV and 164.9 eV, corresponding to Bi-O bonds[35], have appeared. These findings indicate the self-reduction of Bi^{3+} to Bi^0 on the MX nanosheet surface and the formation of covalent bonds between Bi and O-containing groups in MX. Moreover, a shift toward higher BE is observed in the deconvoluted Bi^{3+} and S^{2-} peaks of BSMX14 compared to pristine BS, suggesting a strong interaction between BS nanorods and MX nanosheets. The high-resolution Ti 2p XPS spectrum[37] of pristine MX nanosheets, depicted in **Fig. 4.6(c)**, consists of four fitted peaks assigned to Ti-C (454.9 and 460.9 eV), C-Ti^{2+}-O (455.8 and 461.9 eV), C-Ti^{3+}-O (456.8 and 462.8 eV), and Ti-O (458.8 eV). In contrast, BSMX14 exhibits similar peaks such as Ti-C (454.8 eV), C-Ti^{2+}-O (461.3 eV), C-Ti^{3+}-O (462.4 eV), and Ti-O (458.9 and 464.2 eV) respectively. Additionally, a broad peak at 464.8 eV, attributed to Bi $4d_{3/2}$, is observed, indicating an increased presence of oxygen-containing surface groups in BSMX14 compared to pristine MX nanosheets. Further, the O 1s XPS spectrum[37] of MX nanosheets in **Fig. 4.6(d)** exhibits three characteristic peaks at 530 eV (Ti-O), 531.2 eV (C-Ti-O_x), and 532.6 eV (C-Ti-OH_x). In BSMX14, these peaks are slightly shifted to 530.2 eV (Ti-O), 531.1 eV (C-Ti-O_x), and 532.4 eV (C-Ti-$(OH)_x$), with relative weight percentages of 24.8%, 49.6%, and 25.6%, respectively. This suggests the presence of -O_x and -OH_x functional groups in a ratio of ~3:1. Additionally, the peaks corresponding to C-Ti-O_x and C-Ti-$(OH)_x$ in BSMX14 experience a shift toward lower BE. The shift observed in the XPS spectra is attributed to changes in the local electronic charge density within BS and MX. This indicates that the intimate contact between BS nanorods and MX nanosheets facilitates spontaneous electron migration from BS to the MX surface, leading to the formation of a Schottky-type junction, which arises from the metallic nature of the MX nanosheets.

To elucidate the role of MX surface groups in facilitating Bi^{3+} reduction to Bi^0 during in-situ growth, a DFT analysis was performed. Three structural models, $TiC_{0.66}F_{0.66}$, $TiC_{0.66}O_{0.66}$, and $TiC_{0.66}(OH)_{0.66}$, were examined with adsorbed $BiO(NO_3)$ to study interfacial charge distribution. Bader charge analysis revealed that $TiC_{0.66}F_{0.66}$ and $TiC_{0.66}O_{0.66}$ gained net charges

of 0.28e and 0.6e, whereas $TiC_{0.66}(OH)_{0.66}$ lost 0.33e, which was acquired by $BiO(NO_3)$ as illustrated in the iso-surface plot in **Fig. 4.7**, which highlights the pivotal role of -OH surface groups of MX nanosheets in the reduction of Bi^{3+} to Bi^0. Previous studies reported that $BiO(NO_3)$ is a potential inorganic anion exchanger, particularly reactive with -F groups[38] due

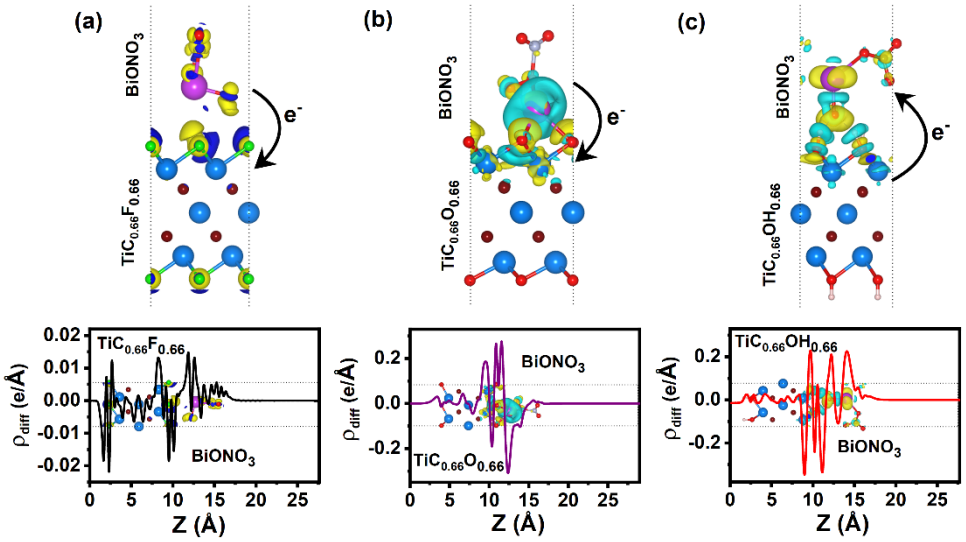

Fig. 4.7. DFT calculated charge density difference (CDD) and plane average charge density plot for (a) $TiC_{0.66}F_{0.66}$@$BiONO_3$, (b) $TiC_{0.66}O_{0.66}$@$BiONO_3$ and (c) $TiC_{0.66}OH_{0.66}$@$BiONO_3$.

to its high electronegativity. In the present study, after the attachment of $BiO(NO_3)$ to the -F site of MX nanosheets, an ion exchange reaction led to the formation of an intermediate BiOF@MX complex. Under thermal treatment, this unstable intermediate transformed into Bi-O@MX. As a result, the final composite materials primarily contain O-based functional groups, with no detectable F groups, further validating the strong interaction between BS nanorods and MX nanosheets. These findings are consistent with Raman spectral observations, corroborating the structural stability of the BSMX14 composite.

4.3.4. Optical Characterization

To investigate the charge carrier dynamics in BS and BSMX composites, steady-state PL measurements were carried out, which are shown in **Fig. 4.8(a)**. The pristine BS nanorods exhibit a broad PL spectrum with a peak at ~ 940 nm, indicating excitonic recombination near the band edge. Interestingly, the BSMX composites demonstrate substantial PL quenching relative to pristine BS nanorods, with BSMX14 exhibiting the most pronounced quenching effect. This substantial PL quenching is attributed to the efficient separation and transport of photogenerated charge carriers at the Bi/MX/BS interfaces, thereby minimizing radiative recombination and enhancing charge separation in the composite materials. The I-t measurements, performed under an applied bias of 3V and 808 nm laser illumination, are

shown in **Fig. 4.8(b)**. Compared to pristine BS, all BSMX composites exhibit a considerable improvement in the on-off ratio (I_{light}/I_{dark}). Among the composites, BSMX14 achieves the highest photocurrent gain, which is consistent with its superior PL quenching effect. The optical absorption spectra of MX nanosheets, illustrated in **Fig. 4.8(c)**, display a broad peak in the 700-875 nm range, which is attributed to localized surface plasmon resonance (LSPR)

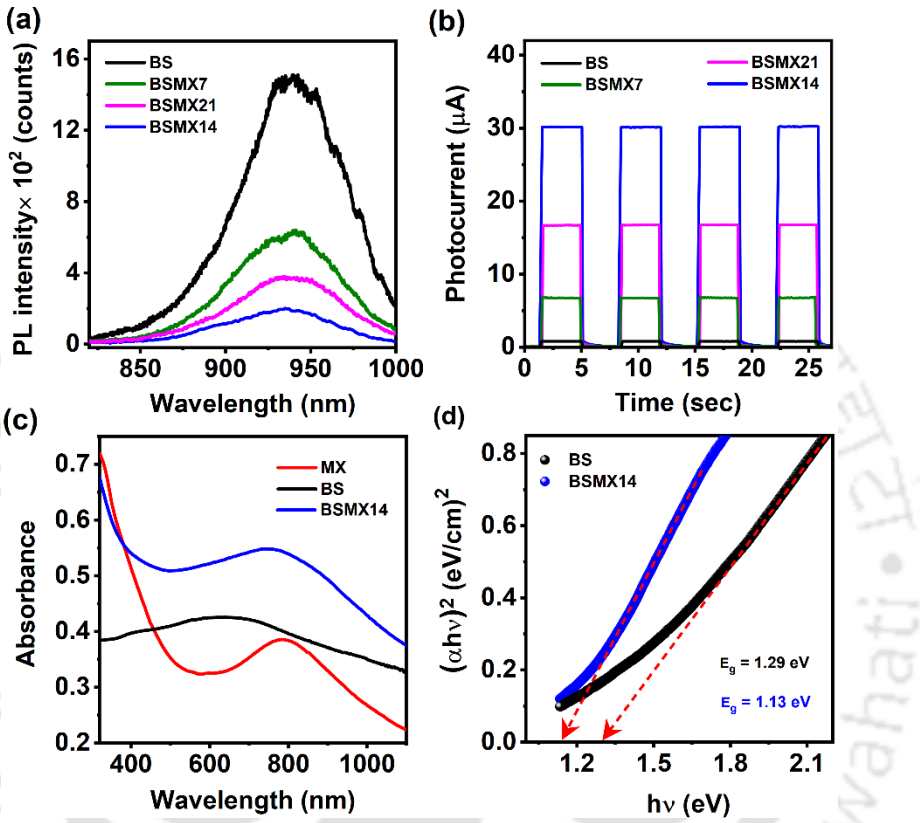

Fig. 4.8. (a) The steady-state micro-PL spectra under 532 nm laser excitation, and (b) temporal photocurrent response (I-t) of BS, BSMX7, BSMX14, and BSMX21 under 808 nm laser excitation. (c) Comparison of UV-Vis absorption spectra of MX, BS, and BSMX14 composites. (d) A comparison of Tauc's plots for BS and BSMX14 shows the respective bandgap.

effects[39]. In contrast, BS nanorods exhibit a broad absorption spectrum extending across the Vis-NIR region, with a distinct peak centred at ~650 nm. Notably, the BSMX14 composite synthesized via in-situ growth exhibits significantly enhanced absorption in the Vis-NIR region compared to pristine BS nanorods. This increased absorption is attributed to the synergistic effect of well-dispersed BS nanorods on the MX nanosheets, as well as the LSPR effects of self-reduced Bi NPs and MX nanosheets. The bandgap of the BS nanorods and BSMX14 composites is calculated by utilizing the Tauc plot for direct bandgap materials:

$$(\alpha h\nu)^2 = A\,(h\nu - E_g) \qquad (5)$$

Where α signifies the absorption coefficient, E_g represents the bandgap, A is a constant of

proportionality, and hν denotes the incident photon energy. The calculated bandgap values for pristine BS and BSMX14 are ~1.3 eV and 1.1 eV, respectively, as presented in **Fig. 4.8(d)**. The observed reduction in bandgap upon composite formation is primarily attributed to the combined influence of ultra-thin MX nanosheets and the quantum confinement effect induced by Bi NPs.

4.4. Catalytic 4-NP Reduction Performance

4.4.1. 4-Nitrophenol Reduction

The catalytic performance of the synthesized composite materials was assessed through the reduction of 4-NP to 4-AP in the presence of $NaBH_4$. This reduction process was monitored by a time-dependent UV-Vis absorption spectroscope. The aqueous 4-NP solution exhibited a pale-yellow colouration with a distinct absorption peak at 317 nm, which shifted to 400 nm upon the introduction of $NaBH_4$. This shift is attributed to the formation of 4-nitrophenolate (4-NPh) ions under alkaline conditions. In the absence of a catalyst, the absorption intensity at 400 nm remained unchanged, indicating that $NaBH_4$ alone is insufficient to facilitate the reduction of 4-NP. Similarly, pristine BS, MX, and BSMX composites were unable to catalyze 4-NP reduction in the absence of $NaBH_4$. However, upon introducing the catalyst in the presence of $NaBH_4$, a rapid reduction of 4-NP was observed, as confirmed by a gradual decrease in the absorption peak at 400 nm, accompanied by the emergence of a new peak at 300 nm, corresponding to 4-AP (**Fig. 4.9(a)**). The BS nanorods achieved a 69% conversion efficiency within 4 min, whereas the MX nanosheets exhibited only ~5% adsorption, with no observable reduction activity (**Fig. 4.9(b)**). The absence of catalytic activity in MX nanosheets is likely due to their significantly higher negative zeta potential (-34.1 mV) compared to BS nanorods (-14.7 mV). The negatively charged surface functional groups (-F, -O, and -OH) on MX nanosheets create an electrostatic repulsion effect, preventing the adsorption of 4-NP and, consequently, its reduction. Additionally, the BSMX7, BSMX14, and BSMX21 catalysts demonstrated excellent reduction efficiencies of 82%, 97%, and 69%, respectively, within 2.6 min. Furthermore, BSMX14 achieved 100% conversion within 4 min, whereas BSMX7 and BSMX21 exhibited conversion efficiencies of ~ 90% and 80%, respectively, over the same duration (**Fig. 9(b)**). The superior catalytic performance of BSMX14 is attributed to its well-dispersed morphology of Bi NPs and the synergistic effects of BS nanorods and MX nanosheets. In contrast, the reduced catalytic efficiency of BSMX7 is likely due to the agglomeration of BS nanorods, which decreases the available active surface area. Similarly, the lower catalytic activity of BSMX21 can be ascribed to the excessive loading of MX

nanosheets, which blocks the active sites of BS nanorods, thereby hindering the catalytic reaction. A comparison of the 4-NP reduction performance using the BSMX14 catalyst with other materials and MX-based composites is summarized in **Table 4.1.** To further quantify the reaction kinetics, the reduction rate was analyzed using the Langmuir-Hinshelwood model:

$$Ln\left(\frac{C_t}{C_0}\right) = -kt \qquad (6)$$

where C_0 is the initial concentration, C_t is the concentration of 4-NP solution after the addition of the catalyst after a time t (min), and k is the rate constant. The rate constants for BS, BSMX7, BSMX14, and BSMX21 were determined to be 0.3, 0.55, 1.14, and 0.35 min^{-1}, respectively (**Fig. 4.9(c)**). The highest reduction rate observed for BSMX14 is correlated with its elevated Bi^0/Bi^{3+} ratio, as illustrated in **Table 4.2.** However, an excessive amount of metallic Bi leads to a decline in catalytic performance by covering the active sites, highlighting the necessity of optimizing the Bi^0/Bi^{3+} ratio for optimal reduction efficiency.

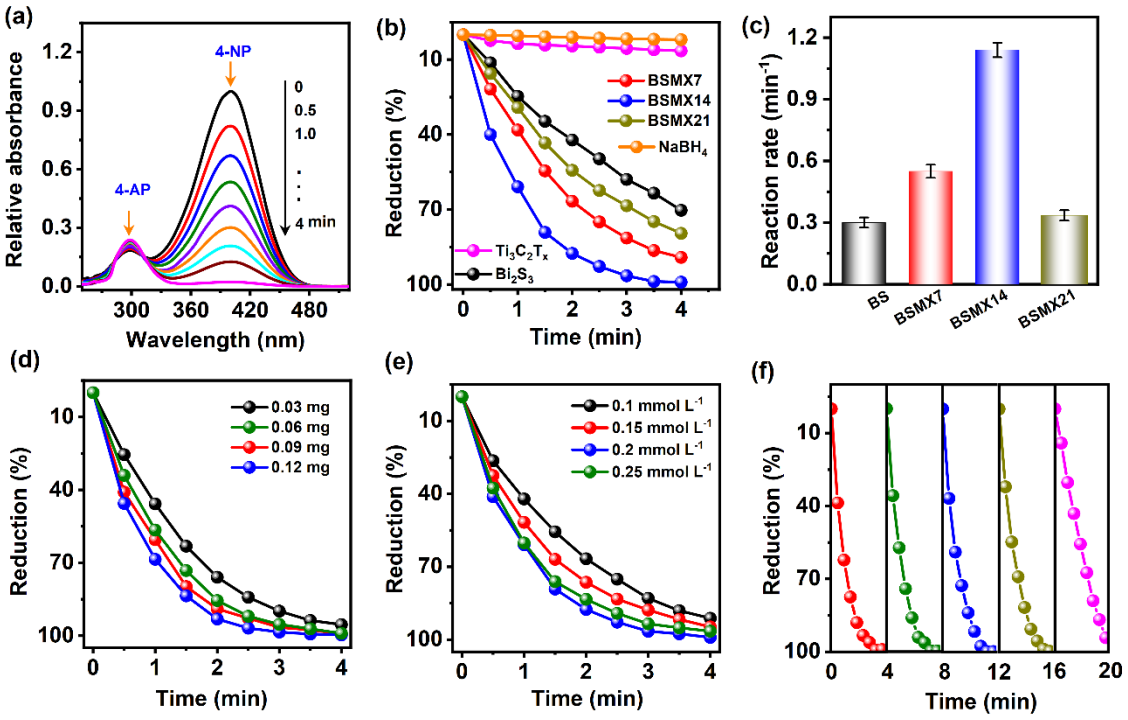

Fig. 4.9. (a) Evolution of UV-Vis absorption spectra of 4-NP with the addition of $NaBH_4$ and BSMX14 catalyst after different time durations. (b) Comparison of the catalytic 4-NP reduction efficiency of different catalysts under dark conditions, (c) 4-NP reduction rate of various catalysts. (d) Effect of BSMX14 catalyst loading amount and (e) Effect of $NaBH_4$ concentration on the reduction efficiency of 4-NP. (f) Cyclic stability of BSMX14 catalyst in 4-NP reduction.

Further, the catalytic reduction efficiency was found to increase with higher catalyst loading **(Fig. 4.9(d))**. Specifically, the reaction rate improved from 1.14 min^{-1} to 1.45 min^{-1} as the

catalyst dosage increased from 0.09 mg to 0.12 mg. This enhancement is attributed to the greater availability of active catalytic sites. However, since the reduction rates for 0.09 mg and 0.12 mg catalyst loadings were comparable, 0.09 mg was deemed optimal for this study. Additionally, the role of $NaBH_4$ concentration in the catalytic reduction process was further explored (**Fig. 4.9(e)**). It was observed that increasing $NaBH_4$ concentration from 0.2 to 0.25 mmol L^{-1} led to a decline in reaction rate from 1.4 min^{-1} to 0.85 min^{-1}. This reduction in efficiency is attributed to the excessive generation of hydrogen gas (H_2) bubbles, which disrupt the uniform adsorption and reduction processes, thereby lowering the overall catalytic rate. The stability and recyclability of the BSMX14 catalyst were evaluated through multiple consecutive cycles of 4-NP reduction (**Fig. 4.9(f)**). The catalyst maintained a high conversion efficiency of 94% even after 5th successive cycles, demonstrating excellent catalytic stability. These results suggest that BSMX14 is a highly efficient and reusable catalyst for the reduction of 4-NP to 4-AP in the presence of a minimal $NaBH_4$ concentration.

4.4.2. Post-reduction Stability of the Catalyst

The structural and chemical stability of the BSMX14 catalyst was evaluated after five consecutive cycles of 4-NP reduction. The XRD pattern of BSMX14 (**Fig. 4.10(a)**) reveals a significant reduction in BS peak intensities and the emergence of a distinct peak corresponding to bulk Bi. This observation suggests that $NaBH_4$ facilitates the reduction of BS to bulk Bi.

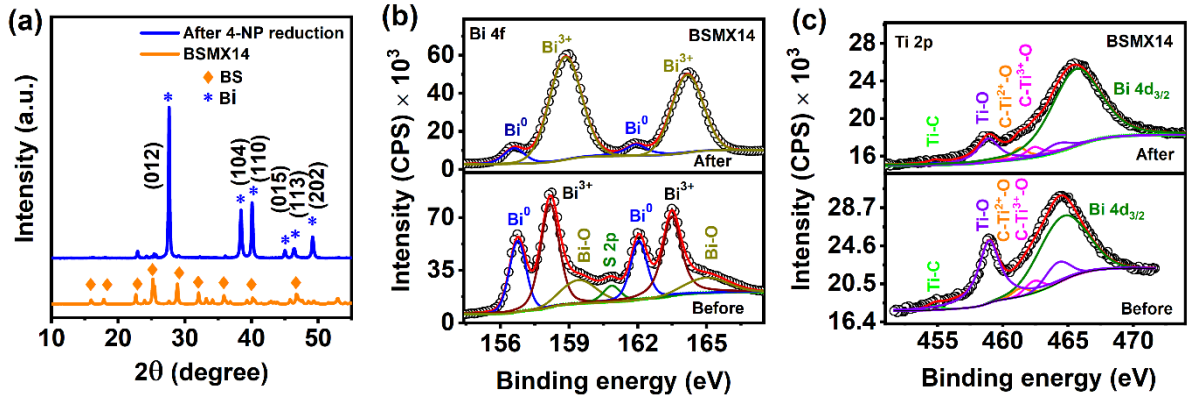

Fig. 4.10. (a) XRD patterns, (b, c) High-resolution XPS spectra of Bi 4f and Ti 2p in BSMX14 before and after 4-NP reduction. The symbols represent experimental data, and the solid lines correspond to the Gaussian-Lorentzian fitted spectra with Shirley baseline.

Furthermore, the high-resolution XPS analysis of the Bi 4f region (**Fig. 4.10(b)**) after the reduction process exhibits a considerable decrease in the Bi^0 peak intensity, indicating its active involvement in the catalytic reduction of 4-NP. The broadening of the Bi 4f peaks implies the formation of Bi_2O_3 due to oxidation. Additionally, the high-resolution Ti 2p XPS spectra (**Fig. 4.10(c)**) reveal broadened and diminished Ti-O peaks at binding energies of 458.9 eV and 464.2

eV, respectively. This finding suggests that the -O functional groups present on the MX nanosheets serve as active sites for H* adsorption, thereby playing a crucial role in the reduction mechanism.

4.4.3. DFT Analysis and Mechanistic Study

The reduction of 4-NP typically involves electron transfer from $NaBH_4$ to 4-NP via the catalyst surface, as widely reported in the literature. To investigate this process, DFT calculations were

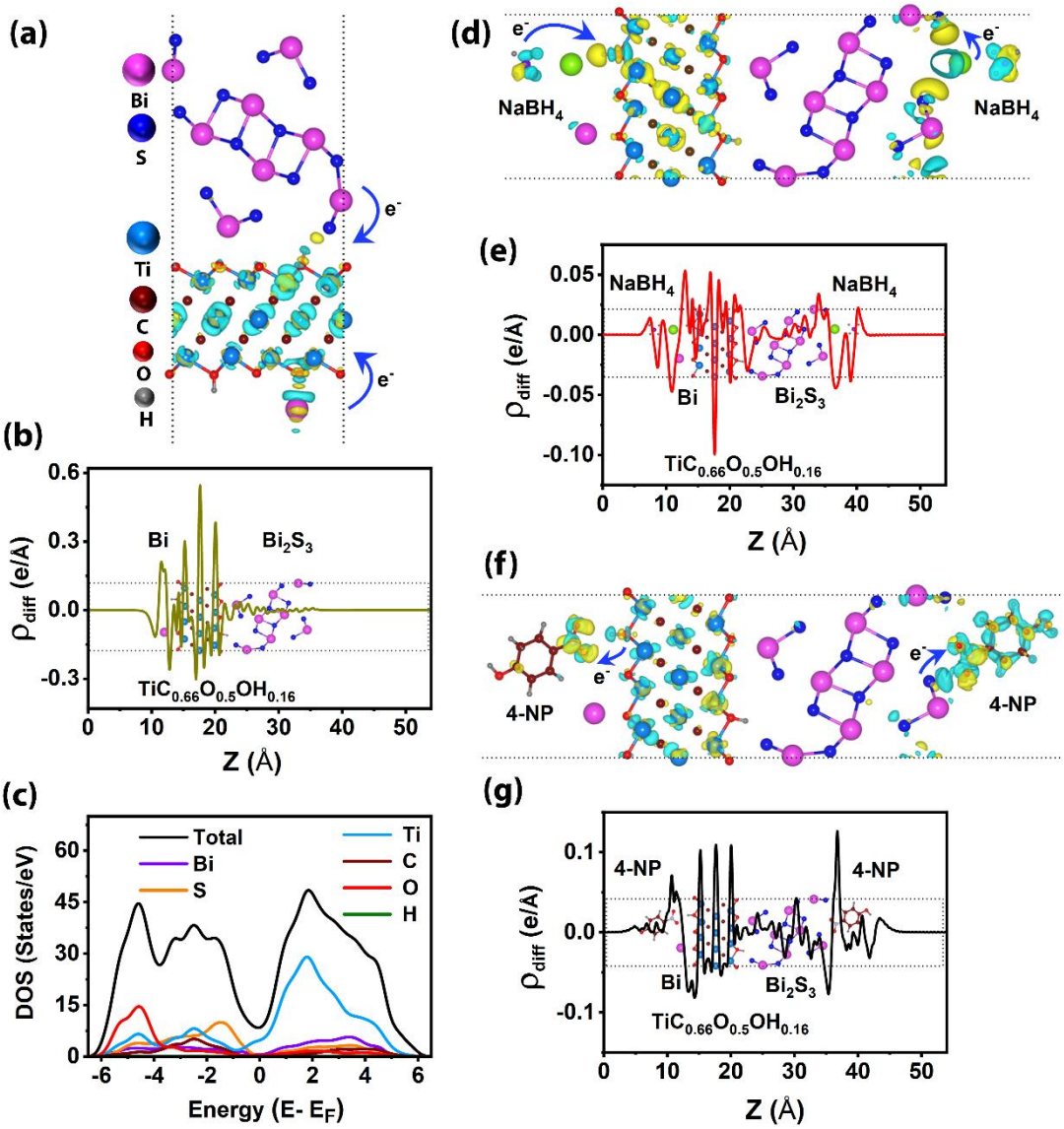

Fig. 4.11. (a) CDD plot of $Bi/BSTC_{0.66}O_{0.5}OH_{0.16}$ composite from DFT calculation, where the charge accumulation and depletion are represented by yellow and cyan colour shades in two regions. (b) The plane average charge density difference plot at the $Bi/TC_{0.66}O_{0.5}OH_{0.16}/BS$ interface. (c) DOS of $Bi/BSTC_{0.66}O_{0.5}OH_{0.16}$. The CDD and plane average charge density difference plot of (d, e) $NaBH_4$ adsorbed on $Bi/BSTC_{0.66}O_{0.5}OH_{0.16}$ and (f, g) 4-NP adsorbed on $Bi/BSTC_{0.66}O_{0.5}OH_{0.16}$.

performed on the $Bi_2S_3/Ti_3C_2T_x$ composite with adsorbed Bi on the $Ti_3C_2T_x$ surface, where MX is modelled as $TiC_{0.66}O_{0.5}OH_{0.16}$ with a -O to -OH ratio of 3:1, as confirmed by O 1s XPS

analysis (**Fig. 4.6(d)**). The CDD analysis in **Fig. 4.11 (a)** indicates electron depletion from Bi and BS to the $TiC_{0.66}O_{0.5}OH_{0.16}$ site. The plane-averaged charge density difference plot (**Fig. 4.11(b)**) highlights three pronounced peaks in the $TiC_{0.66}O_{0.5}OH_{0.16}$ region, suggesting electron accumulation, while Bi and BS exhibit less intense peaks, confirming charge loss. Bader charge analysis further reveals net charge losses of 0.48e and 0.45e per unit cell from Bi and BS, respectively, with $TiC_{0.66}O_{0.5}OH_{0.16}$ acquiring this charge, suggesting a lower work function of BS and forming a Schottky junction. The total TDOS of the composite (**Fig. 4.11(c)**) exhibits a nonzero density of states near the Fermi level, in contrast to the semiconducting BS nanorods. This indicates enhanced electrical conductivity, which can be attributed to the incorporation of MX nanosheets.

Further, CDD analysis of $NaBH_4$ adsorption on BS and Bi/$TiC_{0.66}O_{0.5}OH_{0.16}$ (**Fig. 4.11(d)**) reveals electron depletion from $NaBH_4$ and charge accumulation in the catalyst, corroborated by the plane-averaged charge density plot (**Fig. 4.11(e)**). Bader analysis shows a net charge transfer of 0.17e and 0.16e per unit cell from $NaBH_4$ to BS and Bi/$TiC_{0.66}O_{0.5}OH_{0.16}$, respectively, indicating effective charge absorption. Similarly, CDD analysis for 4-NP adsorption (**Fig. 4.11(f)**) shows charge depletion from BS and Bi/$TiC_{0.66}O_{0.5}OH_{0.16}$, whereas charge accumulation in 4-NP, supported by the plane-averaged charge density plot (**Fig. 4.11(g)**). Bader charge analysis indicates 0.15e and 0.24e charge depletion from BS and Bi/$TiC_{0.66}O_{0.5}OH_{0.16}$, respectively, highlighting 1.5 times higher electron transfer from the latter, which accelerates the 4-NP reduction. According to the investigation, a proposed mechanism for 4-NP reduction is illustrated in **Fig. 4.12(a).** In a weakly alkaline medium, 4-NP forms 4-NPh, which adsorbs onto the catalyst surface. Simultaneously, $NaBH_4$ hydrolyzes, releasing BH_4^- ions and electrons. These species, along with 4-NPh, are adsorbed onto active sites, where BH_4^- dissociates to generate H* species. These H* species and electrons facilitate the reduction of 4-NP to 4-AP by replacing O in the $-NO_2$ group with H* atoms. The desorption of 4-AP and subsequent H_2 formation, indicated by bubble generation, completes the reaction. The unique electronic structure of MX nanosheets enhances H* adsorption on the BSMX14 surface and improves 4-NP reduction efficiency.

4.4.4. Catalytic Reduction of Organic Dyes and CIP Antibiotic

To evaluate the BSMX14 catalyst's effectiveness in reducing organic dyes (MB, RhB, and MO) further experiments were carried out in the presence of $NaBH_4$, which revealed a rapid decrease in absorption intensity for both dyes, indicating the catalyst's strong reduction ability (**Fig.**

4.12(b)). MO is reduced faster than MB and RhB. The reduction efficiencies for MO, RhB, and MB are 99%, 41%, and 98% within 5 min, with rates of 0.82, 0.11, and 0.76 min^{-1}, respectively (**Fig. 4.12(c)**). However, the reduction of CIP was not observed, which may be attributed to the alkaline medium. The lower degradation efficiency of CIP under highly alkaline conditions has been previously discussed in **Chapter 3, Section 3.3.6**. The reduction mechanism involves the adsorption of dyes and $NaBH_4$ onto the catalyst, followed by $NaBH_4$ hydrolysis and electron transfer through the BSMX14 surface, resulting in pollutant reduction. These findings confirm the catalyst's versatility in wastewater treatment.

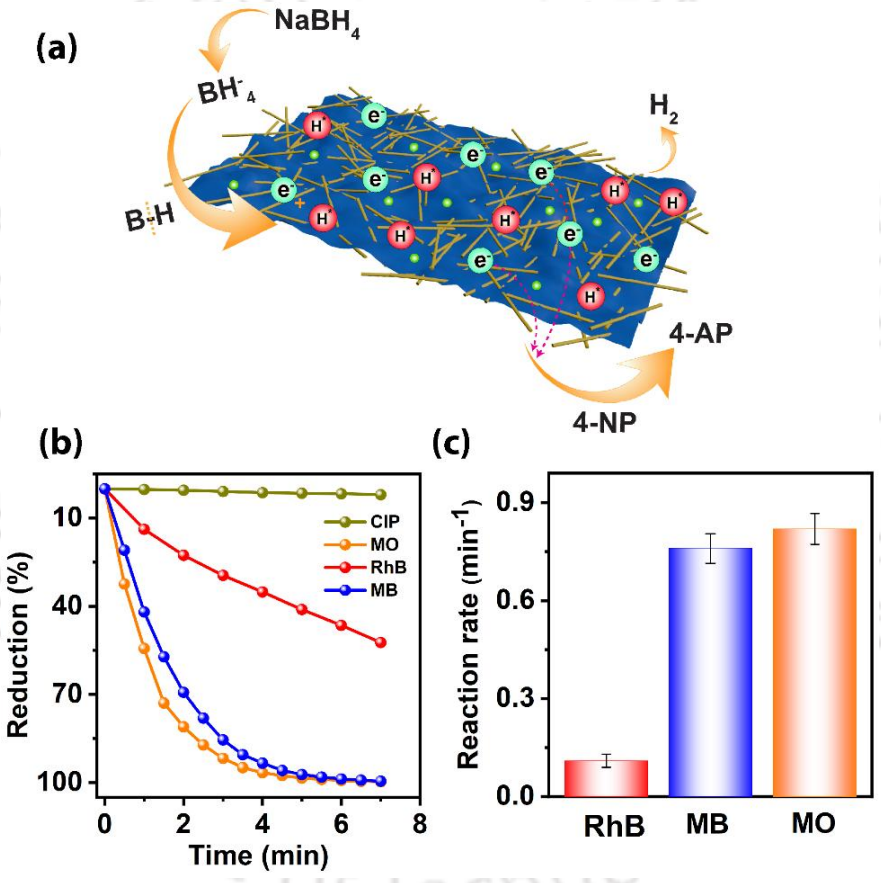

Fig. 4.12. (a) A schematic illustration of 4-NP reduction. (b) Comparison of the MO, MB, RhB, and CIP reduction efficiency by BSMX14 under dark conditions, (c) RhB, MB, and MO reduction rate by BSMX14.

Table 4.1. *Comparison of the 4-NP reduction performance of BSMX14 catalyst with some recently reported catalysts.*

Catalyst	Catalyst amount (mg)	4-NP concentration (mM)	$NaBH_4$ (mM)	Rate constant K (min^{-1})	Reference
MXene@Ag-12%	0.01	0.144		0.1	[7]
Bi-1.0% $Ti_3C_2T_x$	1	0.07	0.1	0.41	[31]
CQD@Ag/MXene	0.004	10	66	0.022	[40]
Fe_3O_4/Ag	1	5	15	0.45	[41]
CuPd	4	0.1	20	0.33	[42]
GO/Ag-Fe_3O_4	0.2	10		0.026	[43]
Ag/ZrGp NPs	10	0.1		0.096	[44]
Bi_2S_3@Fe_3O_4	7	0.1	0.2	0.004	[45]
BSMX14	0.09	0.2	0.2	1.14	***This work***

4.5. Photo Electrochemical Hydrogen Production Performance

The electrochemical HER performance of BS and BSMX14 catalysts was assessed through LSV measurements (**Fig. 4.13(a)**) in 1 M KOH solution using a three-electrode setup, both in the dark and under Vis-NIR light. The BSMX14 demonstrated superior HER performance, with overpotentials of ~87 mV in the dark and ~73 mV under light, compared to ~140 mV and ~129 mV for BS nanorods (**Fig. 4.13(b)**). However, commercial Pt/C demonstrates a much lower overpotential of 24 mV. Additionally, the lower Tafel slope (**Fig. 4.13(c)**) of BSMX14 indicates more favourable HER kinetics, with the Tafel slope decreasing from ~113 mV/dec in the dark to ~84 mV/dec after 10 min of light exposure, suggesting an accelerated charge transfer rate under the light. The overpotentials and Tafel slopes of the catalysts are tabulated in **Table 4.2** below. The enhanced HER activity of BSMX14 is attributed to the synergistic effect of BS, Bi NPs, and MX nanosheets, which improves thermodynamics and reaction kinetics under light illumination via the photothermal effect. The combined LSPR effect of Bi NPs [46] and MX nanosheets [32] introduces a photothermal effect and further enhances the electron transfer rate. The LSV and Tafel analysis of various BSMX composites revealed that an optimal Bi^0/Bi^{3+} ratio (**Table 4.2**) improves HER performance, but excessive metallic Bi

reduces it by covering active sites. The electrochemically active surface area (ECSA) is directly proportional to the double-layer capacitance (C_{dl}). As shown in **Fig. 4.13(d)**, the BSMX14 composite exhibits a higher C_{dl} value (12.8 mF/cm²) compared to BS, indicating its superior HER performance. Additionally, the EIS measurements (**Fig. 4.13(e)**) revealed that BSMX14 has a lower charge transfer resistance (R_{ct}) of ~62 Ω in the dark, which decreases further to ~37 Ω after 10 min of light exposure. This decrease in R_{ct} correlates with improved charge transfer and faster HER kinetics, consistent with the results from the Tafel slope and the photothermal effect. The conductivity of hybrid materials significantly influences their electrocatalytic HER performance. MX nanosheets with abundant -O-containing groups also improve electron transfer and provide active sites for hydrogen adsorption [47-49], boosting electrocatalytic efficiency. Long-term stability tests (**Fig. 4.13(f)**) show minimal degradation in the LSV curve after 1000 cycles, indicating the durability of BSMX14 in alkaline HER. Additionally, the photothermal effect of the BS and BSMX14 samples is presented in **Fig. 4.14 (a)**. Notably, the BSMX14 composite exhibits enhanced photothermal activity, which

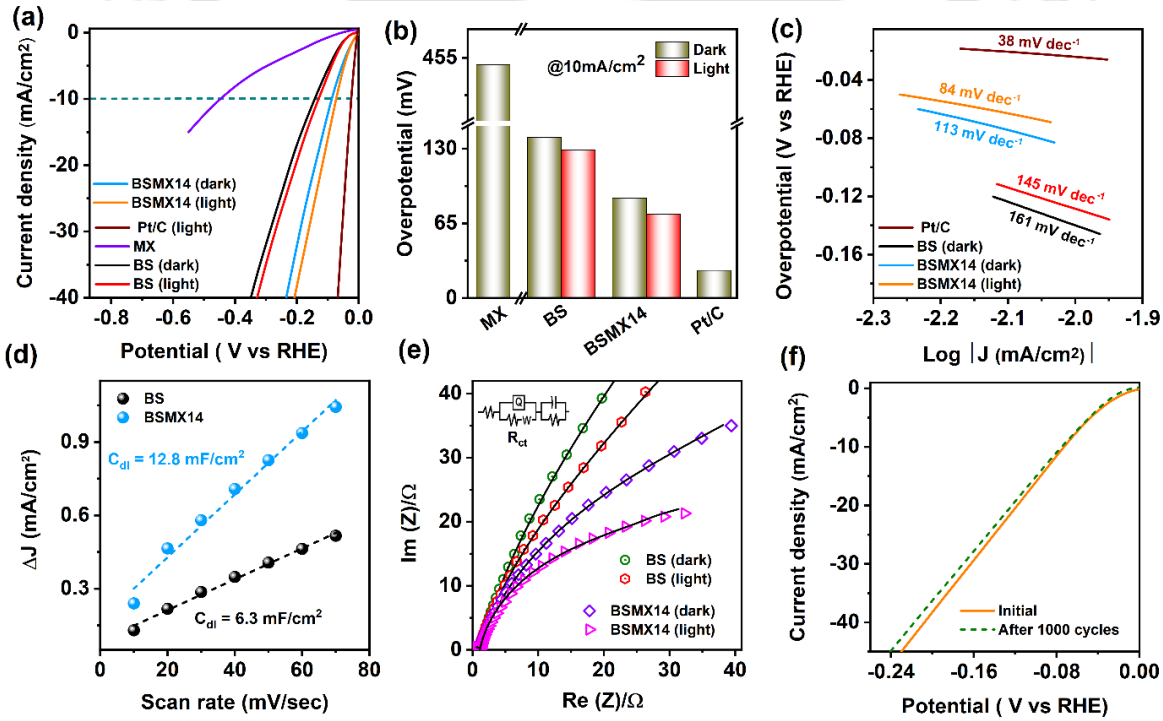

Fig. 4.13. Comparison of (a) LSV curves and (b) overpotentials (at 10 mA/cm²) of MX, BS, BSMX14, and Pt/C, (c) Corresponding Tafel plots and slopes, (d) Plots of capacitive current density difference vs. scan rate for BS and BSMX14 catalysts. (e) Nyquist plot of BS and BSMX14 under dark, and light illumination. (f) LSV curve of the BSMX14 catalyst before and after 1000 cycles under Vis-NIR light illumination in 1 M KOH solution.

consequently leads to superior HER performance under light illumination. From the above characterizations, a band alignment and charge transfer process is proposed in **Fig. 4.14(b)**.

Upon exposure to Vis-NIR light, electrons in the valence band of BS are energized to the conduction band. In contrast, the positive force experienced by holes in the valence band propels them swiftly toward the MX surface and gets separated from the electrons. Moreover, the separated electrons can then efficiently reduce water molecules to generate H_2 gas, by following the reaction mechanism:

Volmer reaction: $BSMX14 + H_2O + e^- \rightarrow BSMX14\text{-}H_{ads} + 2OH^-$ (9)

Heyrovsky reaction: $BSMX14\text{-}H_{ads} + H_2O + e^- \rightarrow BSMX14 + OH^- + H_2$ (10)

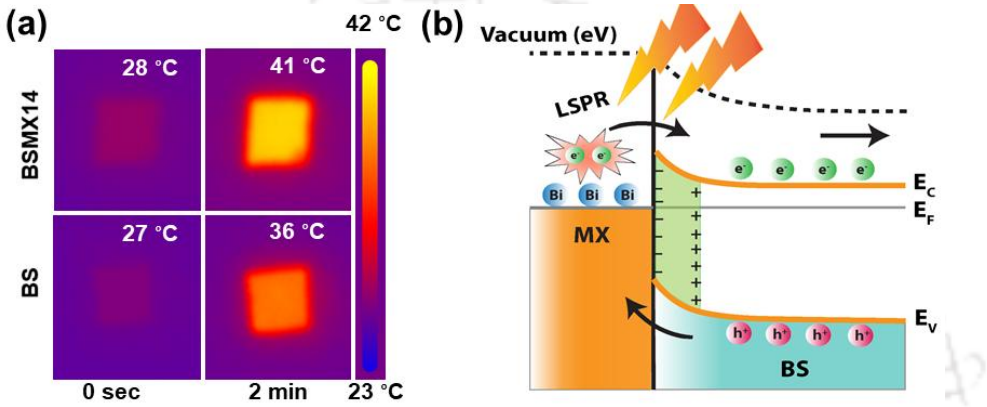

Fig. 4.14. (a) Optical images of the photothermal effect in BS and BSMX14. (b) A schematic illustration of the charge transfer mechanism in BSMX composite under Vis-NIR light illumination.

the combined LSPR effect of MX nanosheets and Bi NPs in BSMX14 composite generates a photothermal effect[50] that speeds up reaction kinetics and substantially enhances their electrocatalytic performance. These observations underscore the potential of BSMX14 as an efficient photoelectrocatalyst for the HER.

Table 4.2. *Summary of Bi^0/Bi^{3+} ratio, catalytic performance, and C_{dl} values of different catalysts.*

Catalyst	Bi^0/Bi^{3+} ratio	4-NP reduction rate (min^{-1})	Photoelectrochemical hydrogen production		Double layer capacitance (C_{dl}) (mF/cm^2)
			Overpotential (mV) at 10 mA/cm^2 (Dark & Light)	Tafel slope (mV/dec) (Dark & Light)	
BS	0	0.3	140 & 129	161 & 145	6.3
BSMX7	0.30	0.55	-		
BSMX14	0.46	1.14	87 & 73	113 & 84	12.8
BSMX21	0.78	0.35	-		

4.6. Conclusions

We have successfully synthesized 2D $Ti_3C_2T_x$ (MX) nanosheets and 1D Bi_2S_3 (BS) nanorod-based composite material $Bi_2S_3/Ti_3C_2T_x$ (BSMX) by a simple hydrothermal method, where the aggregation of 1D BS nanorods is reduced by varying the loading percentage of MX nanosheets. The Raman and XPS analysis corroborate the structural integrity and strong interaction between BS nanorods and MX nanosheets in optimized BSMX14. The efficient photo-induced charge transfer/separation capability of BSMX14 was substantiated by PL and photo-response studies. The UV-Vis absorption spectra confirm the enhanced light absorption ability of the BSMX14 composite compared to the pristine BS nanorods. The DFT calculation corroborated the efficient charge transfer and the formation of a local Schottky junction. Furthermore, the superior reduction capability of organic pollutants (4-NP, MB, MO, and RhB) by the BSMX14 was characterized in the presence of $NaBH_4$, which demonstrates an outstanding reduction rate (up to 1.1 min^{-1}) of 4-NP with long cyclic stability. The reduction mechanism was further supported by DFT analysis. Additionally, BSMX14 demonstrates excellent photo-electrochemical HER performance under both dark and light illumination, with an overpotential of 87 and 73 mV, along with a Tafel slope of 113 and 84 mV/dec, respectively. Therefore, the noble-metal-free BSMX14 nanocomposite is a highly promising candidate for reducing organic pollutants and facilitating photoelectrochemical hydrogen evolution.

References

1. Lin, J.; Tian, W.; Guan, Z.; Zhang, H.; Duan, X.; Wang, H.; Sun, H.; Fang, Y.; Huang, Y.; Wang, S., Functional Carbon Nitride Materials in Photo-Fenton-Like Catalysis for Environmental Remediation. *Advanced Functional Materials* **2022,** *32* (24), 2201743.
2. Liu, M.; Niu, B.; Chen, X.; Lin, X.; Chen, Z.; Guo, H., One-step simple calcination of Ni@C(N) core-shell microspheres: Catalytic reduction of 4-nitrophenol, supercapacitor and electrocatalytic hydrogen production. *Journal of Alloys and Compounds* **2023,** *937*, 168467.
3. Zainal, B. S.; Ker, P. J.; Mohamed, H.; Ong, H. C.; Fattah, I. M. R.; Rahman, S. M. A.; Nghiem, L. D.; Mahlia, T. M. I., Recent advancement and assessment of green hydrogen production technologies. *Renewable and Sustainable Energy Reviews* **2024,** *189*, 113941.
4. Panchenko, V. A.; Daus, Y. V.; Kovalev, A. A.; Yudaev, I. V.; Litti, Y. V., Prospects for the production of green hydrogen: Review of countries with high potential. *International Journal of Hydrogen Energy* **2023,** *48* (12), 4551-4571.
5. Chen, F.; Yan, X.; Hu, X.; Feng, R.; Li, T.; Li, X.; Zhao, G., Enhanced catalytic reduction of p-nitrophenol and azo dyes on copper hexacyanoferrate nanospheres decorated copper foams. *Journal of Environmental Management* **2022,** *314*, 115075.

6. Dan, H.; Song, Y.; Xu, Y.; Gao, Y.; Kong, W.; Huang, Y.; Yue, Q.; Gao, B., Green synthesis of Cu nanoparticles supported on straw-graphene composite for catalytic reduction of p-nitrophenol. *Journal of Cleaner Production* **2021,** *283*, 124578.
7. Qin, X.; Ding, C.; Tian, Y.; Dong, J.; Cheng, B., Multifunctional $Ti_3C_2T_x$ MXene/Silver Nanowire Membranes with Excellent Catalytic, Antifouling, and Antibacterial Properties for Nitrophenol-Containing Water Purification. *ACS Applied Materials & Interfaces* **2023,** *15* (41), 48154-48167.
8. Mejía, Y. R.; Reddy Bogireddy, N. K., Reduction of 4-nitrophenol using green-fabricated metal nanoparticles. *RSC Advances* **2022,** *12* (29), 18661-18675.
9. Zhu, Q.; Qu, Y.; Liu, D.; Ng, K. W.; Pan, H., Two-Dimensional Layered Materials: High-Efficient Electrocatalysts for Hydrogen Evolution Reaction. *ACS Applied Nano Materials* **2020,** *3* (7), 6270-6296.
10. Mishra, K.; Devi, N.; Siwal, S. S.; Thakur, V. K., Insight perspective on the synthesis and morphological role of the noble and non-noble metal-based electrocatalyst in fuel cell application. *Applied Catalysis B: Environmental* **2023,** *334*, 122820.
11. Cui, Z.; Jiao, W.; Huang, Z.; Chen, G.; Zhang, B.; Han, Y.; Huang, W., Design and Synthesis of Noble Metal-Based Alloy Electrocatalysts and Their Application in Hydrogen Evolution Reaction. *Small* **2023,** *19* (35), 2301465.
12. Yang, W.; Yang, J.; Zhao, K.; Gao, Q.; Liu, L.; Zhou, Z.; Hou, S.; Wang, X.; Shen, G.; Pang, X., Low-Noise Dual-Band Polarimetric Image Sensor Based on 1D Bi_2S_3 Nanowire. *Advanced Science* **2021,** *8* (14), 2100075.
13. Han, P.; Mihi, A.; Ferre-borrull, J.; Pallares, J.; Marsal, L. F., Interplay between morphology, optical properties, and electronic structure of solution-processed Bi_2S_3 colloidal nanocrystals. *The Journal of Physical Chemistry C* **2015,** *119* (19), 10693-10699.
14. Tahir, A. A.; Ehsan, M. A.; Mazhar, M.; Wijayantha, K. U.; Zeller, M.; Hunter, A., Photoelectrochemical and photoresponsive properties of Bi_2S_3 nanotube and nanoparticle thin films. *Chemistry of Materials* **2010,** *22* (17), 5084-5092.
15. Bernechea, M.; Cao, Y.; Konstantatos, G., Size and bandgap tunability in Bi_2S_3 colloidal nanocrystals and its effect in solution processed solar cells. *Journal of Materials Chemistry A* **2015,** *3* (41), 20642-20648.
16. Xu, J.; Li, H.; Fang, S.; Jiang, K.; Yao, H.; Fang, F.; Chen, F.; Wang, Y.; Shi, Y., Synthesis of bismuth sulfide nanobelts for high performance broadband photodetectors. *Journal of Materials Chemistry C* **2020,** *8* (6), 2102-2108.
17. He, W.; Xiong, J.; Tang, Z.; Wang, Y.; Wang, X.; Xu, H.; Zhao, Z.; Liu, J.; Wei, Y., Localized surface plasmon resonance effect of bismuth nanoparticles in Bi/TiO_2 catalysts for boosting visible light-driven CO_2 reduction to CH_4. *Applied Catalysis B: Environment and Energy* **2024,** *344*, 123651.
18. Hao, J.; He, H.; Gong, S.; Fan, J.; Xu, Q.; Min, Y., WN Coupled with Bi Nanoparticles to Enhance the Localized Surface Plasmon Resonance Effect for Photocatalytic Hydrogen Evolution. *ACS Applied Materials & Interfaces* **2021,** *13* (17), 19884-19893.
19. Wang, Y.; Chen, J.; Wang, P.; Chen, L.; Chen, Y.-B.; Wu, L.-M., Syntheses, growth mechanism, and optical properties of [001] growing Bi_2S_3 nanorods. *The Journal of Physical Chemistry C* **2009,** *113* (36), 16009-16014.
20. Yu, Y.; Jin, C. H.; Wang, R. H.; Chen, Q.; Peng, L. M., High-Quality Ultralong Bi_2S_3 Nanowires: Structure, Growth, and Properties. *The Journal of Physical Chemistry B* **2005,** *109* (40), 18772-18776.
21. Kresse, G.; Joubert, D., From ultrasoft pseudopotentials to the projector augmented-wave method. *Physical Review B* **1999,** *59* (3), 1758-1775.
22. Kresse, G.; Furthmüller, J., Efficient iterative schemes for ab initio total-energy calculations using a plane-wave basis set. *Physical Review B* **1996,** *54* (16), 11169-11186.

23. Blöchl, P. E., Projector augmented-wave method. *Physical Review B* **1994,** *50* (24), 17953-17979.
24. Perdew, J. P.; Burke, K.; Ernzerhof, M., Generalized Gradient Approximation Made Simple. *Physical Review Letters* **1996,** *77* (18), 3865-3868.
25. Moellmann, J.; Grimme, S., DFT-D3 study of some molecular crystals. *The Journal of Physical Chemistry C* **2014,** *118* (14), 7615-7621.
26. Monkhorst, H. J.; Pack, J. D., Special points for Brillouin-zone integrations. *Physical Review B* **1976,** *13* (12), 5188.
27. Tang, W.; Sanville, E.; Henkelman, G., A grid-based Bader analysis algorithm without lattice bias. *Journal of Physics: Condensed Matter* **2009,** *21* (8), 084204.
28. Sanville, E.; Kenny, S. D.; Smith, R.; Henkelman, G., Improved grid-based algorithm for Bader charge allocation. *Journal of Computational Chemistry* **2007,** *28* (5), 899-908.
29. Momma, K.; Izumi, F., VESTA: a three-dimensional visualization system for electronic and structural analysis. *Journal of Applied Crystallography* **2008,** *41* (3), 653-658.
30. Lipatov, A.; Alhabeb, M.; Lukatskaya, M. R.; Boson, A.; Gogotsi, Y.; Sinitskii, A., Effect of synthesis on quality, electronic properties and environmental stability of individual monolayer Ti_3C_2 MXene flakes. *Advanced Electronic Materials* **2016,** *2* (12), 1600255.
31. Yu, C.; Peng, L.; Zhu, Y.; Xie, G.; Wu, Z.; Xie, X.; Zhang, N., Electrostatically confined $Bi/Ti_3C_2T_x$ on a sponge as an easily recyclable and durable catalyst for the reductive transformation of nitroarenes. *Journal of Materials Chemistry A* **2021,** *9* (35), 19847-19853.
32. Li, J.; Li, Z.; Liu, X.; Li, C.; Zheng, Y.; Yeung, K. W. K.; Cui, Z.; Liang, Y.; Zhu, S.; Hu, W.; Qi, Y.; Zhang, T.; Wang, X.; Wu, S., Interfacial engineering of $Bi_2S_3/Ti_3C_2T_x$ MXene based on work function for rapid photo-excited bacteria-killing. *Nature Communications* **2021,** *12* (1), 1224.
33. Liang, Y.; Manioudakis, J.; Macairan, J.-R.; Askari, M. S.; Forgione, P.; Naccache, R., Facile Aqueous-Phase Synthesis of an Ultrasmall Bismuth Nanocatalyst for the Reduction of 4-Nitrophenol. *ACS Omega* **2019,** *4* (12), 14955-14961.
34. Zhao, Y.; Chua, K. T. E.; Gan, C. K.; Zhang, J.; Peng, B.; Peng, Z.; Xiong, Q., Phonons in Bi_2S_3 nanostructures: Raman scattering and first-principles studies. *Physical Review B* **2011,** *84* (20), 205330.
35. Qu, C.; Li, H.; Zhou, S.; Li, G.; Wang, C.; Snyders, R.; Bittencourt, C.; Li, W., Bi_2S_3/rGO composite based electrochemical sensor for ascorbic acid detection. *Chemosensors* **2021,** *9* (8), 190.
36. Chen, L.; He, J.; Yuan, Q.; Zhang, Y.-W.; Wang, F.; Au, C.-T.; Yin, S.-F., CuS–Bi 2 S 3 hierarchical architectures: controlled synthesis and enhanced visible-light photocatalytic performance for dye degradation. *RSC Advances* **2015,** *5* (43), 33747-33754.
37. Halim, J.; Cook, K. M.; Naguib, M.; Eklund, P.; Gogotsi, Y.; Rosen, J.; Barsoum, M. W., X-ray photoelectron spectroscopy of select multi-layered transition metal carbides (MXenes). *Applied Surface Science* **2016,** *362*, 406-417.
38. Kabay, N.; Kodama, H., Ion exchange properties of $BiO(NO_3)\cdot 0.5H_2O$ towards fluoride ions. *Solvent Extraction and Ion Exchange* **2000,** *18*, 583-603.
39. Naguib, M.; Gogotsi, Y., Synthesis of two-dimensional materials by selective extraction. *Accounts of chemical research* **2015,** *48* (1), 128-135.
40. Chen, Y.; Yang, C.; Huang, X.; Li, L.; Yu, N.; Xie, H.; Zhu, Z.; Yuan, Y.; Zhou, L., Two-dimensional MXene enabled carbon quantum dots@Ag with enhanced catalytic activity towards the reduction of p-nitrophenol. *RSC Advances* **2022,** *12* (8), 4836-4842.
41. Xing, Y.; Bai, X.-H.; Gong, Y.; Peng, M.-L.; Zhang, Y.-Y.; Ma, X.-R.; Zhang, Y., Enhanced catalytic properties of Fe_3O_4/Ag magnetic microspheres synthesized by a novel

thermal co-reduction method. *Journal of Magnetism and Magnetic Materials* **2020,** *510*, 166951.
42. Saikia, H.; Borah, B. J.; Yamada, Y.; Bharali, P., Enhanced catalytic activity of CuPd alloy nanoparticles towards reduction of nitroaromatics and hexavalent chromium. *Journal of Colloid and Interface Science* **2017,** *486*, 46-57.
43. Qu, J.-c.; Ren, C.-l.; Dong, Y.-l.; Chang, Y.-p.; Zhou, M.; Chen, X.-g., Facile synthesis of multifunctional graphene oxide/AgNPs-Fe_3O_4 nanocomposite: A highly integrated catalysts. *Chemical Engineering Journal* **2012,** *211-212*, 412-420.
44. Zhou, A.; Li, J.; Wang, G.; Xu, Q., Preparation of Ag/ZrGP nanocomposites with enhanced catalytic activity for catalytic reduction of 4-nitrophenol. *Applied Surface Science* **2020,** *506*, 144570.
45. Yetim, N. K.; Aslan, N.; Koc, M. M., Structural and catalytic properties of Fe_3O_4 doped Bi2S3 novel magnetic nanocomposites: p-Nitrophenol case. *Journal of Environmental Chemical Engineering* **2020,** *8* (5), 104258.
46. Dong, X.; Xu, L.; Ma, J.; Li, Y.; Yin, Z.; Chen, D.; Wang, Q.; Han, J.; Qiu, J.; Yang, Z.; Song, Z., Enhanced interfacial charge transfer and photothermal effect via in-situ construction of atom co-sharing Bi plasmonic/$Bi_4O_5Br_2$ nanosheet heterojunction towards improved full-spectrum photocatalysis. *Chemical Engineering Journal* **2023,** *459*, 141557.
47. Huang, L.; Ai, L.; Wang, M.; Jiang, J.; Wang, S., Hierarchical MoS_2 nanosheets integrated Ti_3C_2 MXenes for electrocatalytic hydrogen evolution. *International Journal of Hydrogen Energy* **2019,** *44* (2), 965-976.
48. Khalil, M.; Lesa, M.; Juandito, A. G.; Sanjaya, A. R.; Ivandini, T. A.; Kadja, G. T. M.; Mahyuddin, M. H.; Sookhakian, M.; Alias, Y., A SBA-15-templated mesoporous $NiFe_2O_4$/MXene nanocomposite for the alkaline hydrogen evolution reaction. *Materials Advances* **2023,** *4* (17), 3853-3862.
49. Yu, M.; Wang, Z.; Liu, J.; Sun, F.; Yang, P.; Qiu, J., A hierarchically porous and hydrophilic 3D nickel–iron/MXene electrode for accelerating oxygen and hydrogen evolution at high current densities. *Nano Energy* **2019,** *63*, 103880.
50. Liu, Y.; Lu, X.; Ma, Z.; Guo, K.; Guo, C.; Han, M.; Bao, J., Hetero-coupling and photothermal effects co-modulated reaction kinetics for highly-efficient electrocatalytic hydrogen evolution reaction. *Electrochimica Acta* **2022,** *403*, 139693.

Chapter 5

Synergistic Effect of Ru Nanoclusters on N-Doped $Ti_3C_2T_x$ Nanoribbons for High-Performance Photoelectrochemical Water Splitting

In this chapter, we have synthesized an ultra-small Ru nanocluster (NC) anchored hierarchical N-doped $Ti_3C_2T_x$ (Ru@N-$Ti_3C_2T_x$) MXene nanoribbon (MXNR)-based composite material. The high aspect ratio and defective sites of partially oxidized MXNRs provide an abundance of active sites, effectively preventing the aggregation of Ru NCs and enabling superior photoelectrochemical hydrogen production in an alkaline medium. The in-situ formation of a small amount of TiO_2 nanoparticles (TiO_2 NPs) during 1D structuring and N doping enhances UV-Vis light absorption, further contributing to its role as an efficient photo-electrocatalyst.

The electrochemical hydrogen evolution performance of the Ru@N-$Ti_3C_2T_x$ catalyst was systematically investigated under dark and visible light illumination in an alkaline medium (1M KOH). The results demonstrate that Ru@N-$Ti_3C_2T_x$ exhibits outstanding hydrogen evolution reaction (HER) activity, surpassing the performance of commercially available Pt/C (20%). This chapter highlights the development of a cost-effective and robust Ru@N-$Ti_3C_2T_x$ MXene-based composite material, presenting a promising strategy for sustainable hydrogen production.

5.1. Introduction

Hydrogen is a sustainable alternative to fossil fuels due to its zero carbon emissions and high energy density[1]. However, conventional hydrogen production primarily relies on the steam reforming of fossil fuels, contributing to CO_2 emissions. Water splitting has emerged as a clean and efficient approach for high-purity hydrogen generation. Among various methods, electrocatalytic water splitting is particularly promising due to its scalability, zero CO_2 emissions, and high purity[2, 3]. The performance of this process is mainly determined by the electrocatalyst's intrinsic properties. While Pt-based catalysts are the benchmark for HER in acidic media, their high cost, scarcity, and poor kinetics in neutral and alkaline media limit their application[4-6]. On the other hand, Ru has been explored as an alternative due to its favourable hydrogen bonding energy and low water dissociation barrier. However, its strong

binding energy can cause nanocluster aggregation, compromising HER performance. Therefore, developing stable and efficient electrocatalysts remains crucial for advancing green hydrogen production.

To overcome this challenge, integrating Ru with highly conductive substrates offers a promising strategy to enhance the HER performance. This approach facilitates uniform Ru dispersion, minimizes catalyst usage, and maintains high catalytic efficiency. Extensive research has been conducted on carbon-based nanomaterials[7-10], including graphene, carbon nitride, and carbon nanotubes, due to their ability to prevent Ru nanocluster aggregation while preserving excellent electrocatalytic properties. Therefore, the development of cost-effective Ru-based catalysts with superior electrical conductivity and enhanced catalytic activity remains a key focus for advancing practical hydrogen production technologies.

Two-dimensional (2D) $Ti_3C_2T_x$ MXenes have garnered substantial attention due to their remarkable combination of metallic conductivity, hydrophilicity, and tuneable surface chemistry. As a result, $Ti_3C_2T_x$ MXenes have found widespread applications in energy storage, electromagnetic interference (EMI) shielding, renewable energy, sensing, and related fields. However, 2D $Ti_3C_2T_x$ has non-uniform flake distribution as well as restacking issues due to interlayer van der Waals interaction, which significantly reduces its catalytically active surface area, and hence it yields low catalytic activity[11, 12]. As an alternative, one-dimensional (1D) $Ti_3C_2T_x$ MXene nanoribbon has been gaining attention as an extension of 2D MXene, offering new opportunities for diverse applications[13]. The high aspect ratio of 1D MXenes significantly improves their electrical conductivity, mechanical flexibility and provides an increased surface area, which enhances their functionality in various catalytic applications by facilitating efficient electron transport, which further boosts the catalytic activity[13]. However, the synthesis of 1D $Ti_3C_2T_x$ MXene involves various etching techniques that face various challenges, while simultaneously exposing a more significant number of active sites, thereby enhancing their catalytic performance[13]. During the synthesis of 1D MXene, its conductivity significantly reduces due to the formation of TiO_2 nanoparticles (NPs) on its surface. To improve its conductivity, heteroatom doping plays a crucial role. Additionally, the synergistic combination of 1D MXenes with noble metals such as Ru, Pt, etc, can further enhance their catalytic activity by reducing their agglomeration effect, leading to superior performance in catalytic HER application. Moreover, 1D MXene exhibits excellent photothermal properties under laser irradiation[13, 14] which can boost its electrochemical performance by boosting electron mobility and faster charge transfer. Additionally, it demonstrates good biocompatibility, making it

highly promising for various sustainable catalytic applications.

In this study, Ru NCs anchored hierarchical N-doped $Ti_3C_2T_x$ (Ru@N-$Ti_3C_2T_x$) MXene nanoribbon-based composite catalyst was successfully synthesized through a combination of etching and annealing techniques. The presence of oxygen vacancies (OVs) facilitates the formation of ultra-small Ru NCs (~ 0.4 nm), effectively reducing their agglomeration and thereby significantly improving the electronic metal support interaction (EMSI) effect. We show that the 5% Ru@N-$Ti_3C_2T_x$ catalyst exhibits significantly enhanced electrocatalytic activity with an overpotential of 22 and 12 mV under dark and Vis-NIR light illumination as compared to conventional Pt/C (20%) catalysts. Also, it exhibits long-term durability for the HER in an alkaline medium. The Ru NCs are effectively stabilized at the defect sites of the MXene nanoribbons, which substantially improves the catalytic performance toward HER. This study underscores the critical role of atomic-scale engineering of Ru NCs over MXene nanoribbons in optimizing their catalytic activity by precisely tailoring the electronic and structural properties of the material at the atomic level.

5.2. Experimental

5.2.1. Preparation of $Ti_3C_2T_x$ Nanoribbons

The synthesis of $Ti_3C_2T_x$ MXene nanoribbons is illustrated in **Fig. 5.1**. Initially, 1 g of Ti_3AlC_2 MAX phase powder was subjected to 20 mL of a 40 wt% HF solution while being continuously stirred at 250 rpm for 48 h. After etching, the resulting mixture was repeatedly centrifuged with Milli-Q water at 4500 rpm until the pH reached ~6. The collected sediment was then freeze-dried for 24 h to obtain black, multi-layered $Ti_3C_2T_x$ MXene powder. For the subsequent synthesis of $Ti_3C_2T_x$ MXene nanoribbons, 0.5 g of the as-prepared MXene powder was dispersed in 60 mL of 6 M KOH solution and stirred at 400 rpm for 120 h in a sealed container under an Ar atmosphere at room temperature. Finally, the obtained product was thoroughly washed and subjected to an additional freeze-drying step for 24 h. The as-prepared $Ti_3C_2T_x$ MXene nanoribbons are abbreviated as MXNR.

5.2.2. Preparation of N-Doped $Ti_3C_2T_x$ Nanoribbons

In a standard synthesis process, 0.6 g of HCl-treated melamine was introduced into a 50 mL suspension of MXNR (3 mg mL^{-1}) and stirred continuously for 1 h. The resulting mixture was then stored at -15 °C overnight, followed by freeze-drying for 24 h. The dried material was subsequently annealed at 500 °C for 2 h under an Ar atmosphere, maintaining a controlled heating rate of 5°C min^{-1}. Finally, the obtained product was thoroughly washed multiple times

with distilled water and ethanol and then vacuum-dried at 60°C to obtain N-doped MXNR. The prepared doped material is abbreviated as N-MXNR.

5.2.3. Preparation of Ru@N-Doped $Ti_3C_2T_x$ Nanoribbons

In this process, a 50 mL suspension of N-MXNR (3 mg mL^{-1}) was prepared by sonication continuously for 1 h. Then, a specific volume of $RuCl_3 \cdot xH_2O$ solution was gradually added dropwise into the above solution under vigorous stirring in an ice bath for another 1 h. The resulting mixture was then stored at -15 °C overnight, followed by freeze-drying for 24 h. The dried samples were subsequently annealed at 500°C for 1 h under an Ar/H_2 atmosphere by maintaining a fixed heating rate of 5°C min^{-1}. Finally, the product was washed with DI water and ethanol and then vacuum-dried at room temperature to obtain Ru@N-doped $Ti_3C_2T_x$

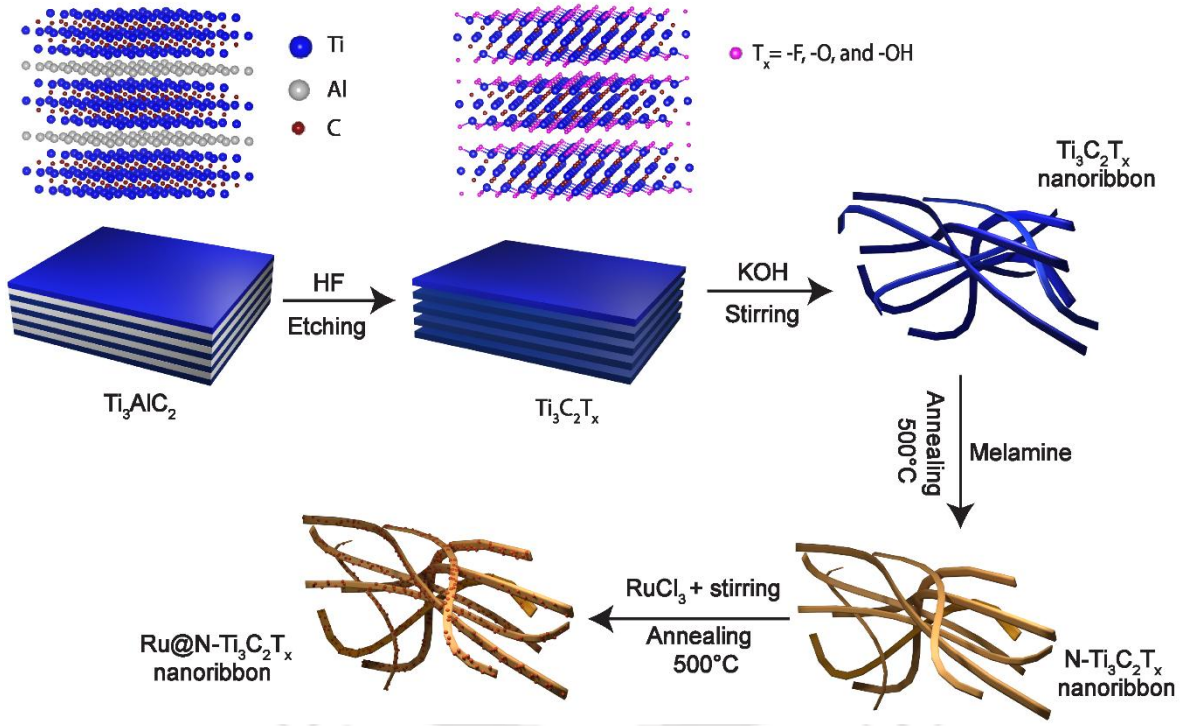

Fig. 5.1. Schematic representation of the synthesis of Ru-anchored N-doped $Ti_3C_2T_x$ nanoribbon nano composite (Ru@N-$Ti_3C_2T_x$).

nanoribbons in powder form. According to the loading percentages of Ru, these materials are abbreviated as 3%, 5%, and 7% Ru@N-MXNR. A schematic representation of the synthesis of ultra-small Ru NCs anchored on N-doped $Ti_3C_2T_x$ MXene nanoribbons (Ru@N-MXNR) is illustrated in **Fig. 5.1**.

5.2.4. Electrochemical Experiment

Electrochemical characterization was conducted using a conventional three-electrode setup. In this system, a platinum (Pt) wire functioned as the counter electrode, while an Ag/AgCl

electrode served as the reference. The working electrode consisted of a catalyst-integrated graphite sheet (1×1 cm^2), selected for its excellent electronic conductivity. To prepare the working electrode, 3.3 mg of the synthesized catalyst and 0.7 mg of carbon black were dispersed in 235 µL of ethanol, followed by the addition of 15 µL of Nafion. The resulting mixture underwent sonication for 30 min to achieve a homogeneous dispersion. This catalyst ink was subsequently coated onto the graphite sheet and subjected to vacuum drying overnight. Electrochemical measurements were then performed in a 1 M KOH electrolyte at room temperature, both in the absence of light (dark conditions) and under visible-near infrared (Vis-NIR) illumination. Linear sweep voltammetry (LSV) was carried out at a scan rate of 5 mV s^{-1}, while the cyclic voltammetry (CV) test was performed over a scan rate range of 20 to 60 mV s^{-1} to determine the double-layer capacitance (C_{dl}). The electrode potential referenced to Ag/AgCl was converted to the reversible hydrogen electrode (RHE) potential using the following equation[15]:

$$E_{RHE} = E_{Ag/AgCl} + 0.0591 \times pH + 0.2045 \quad (1)$$

Additionally, all polarization curves were corrected for iR compensation to account for solution resistance.

5.2.5. Characterization Techniques

The morphology, crystal structure, and surface properties of the as-prepared materials were investigated using FESEM, TEM, XRD, Raman spectroscopy**,** BET, and XPS analysis. The characterization procedures followed the methodologies detailed in **Sections 2.2.3** and **3.2.4.** of **Chapters 2 & 3**, respectively. Electron Spin Resonance (ESR) spectroscopy was conducted using a JEOL JES-FA200 spectrometer to investigate the defect states associated with OVs in the as-prepared samples. The electrochemical measurements were performed using an electrochemical workstation (CH Instruments, CHI6044E). Photoelectrochemical characterization was performed with a solar simulator (Photo Emission Tech, Model: 300WSS-PC, Class AAA), providing a solar flux of 1 sun (1 kW m^{-2}).

5.3. Results and Discussion

5.3.1. Morphological Characterizations

The morphological characteristics of the synthesized materials were examined using FESEM and TEM. The FESEM analysis of MXNRs revealed a porous three-dimensional (3D) network**,** where the nanoribbons are intricately entangled, forming a highly interconnected structure, as

depicted in **Fig. 5.2(a, b)**. In contrast, the TEM images of Ru@N-MXNR, shown in **Fig. 5.2(c)**, reveal the formation of a porous, net-like structure composed of MXNRs, extending several micrometres in length, similar to MXNRs, while their widths were between 7 - 20 nm. Additionally, high-angle annular dark-field (HAADF) imaging, presented in **Fig. 5.2(d)**, confirms an interconnected MXene nanoribbon network and also supports the observations. A

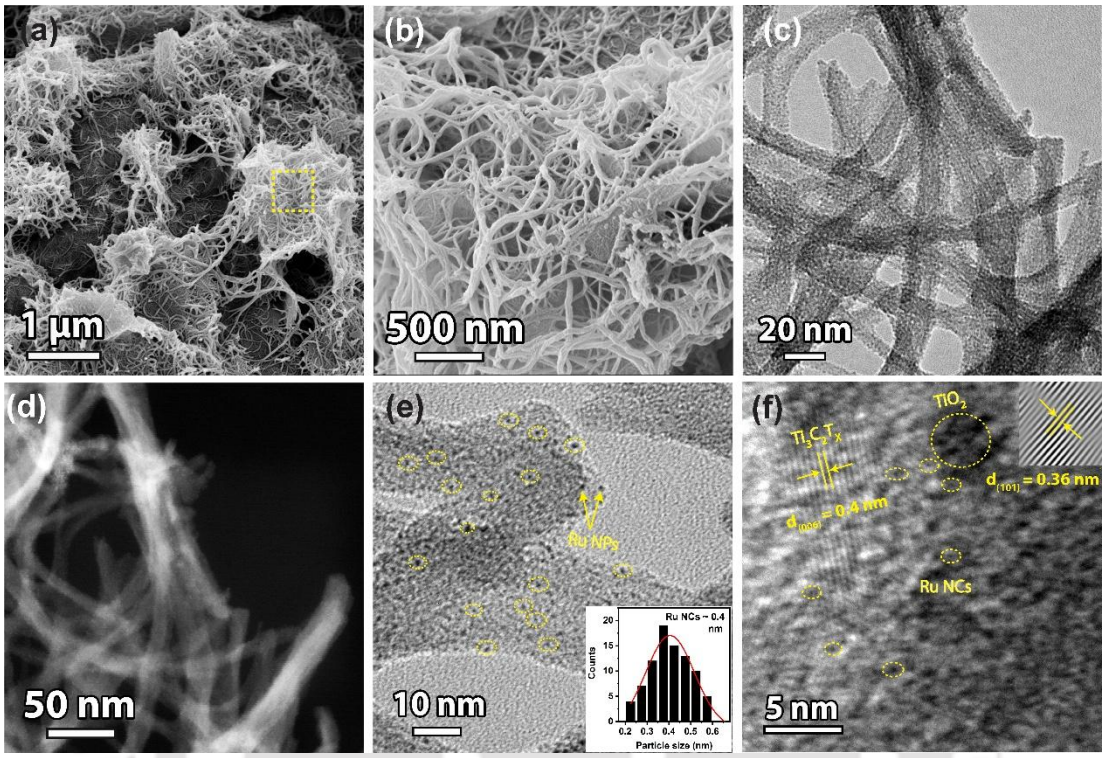

Fig. 5.2. FESEM images of (a) MXNR and (b) magnified view of the MXNR from highlighted area. (c) TEM and (d) HAADF image of 5% Ru@N-MXNR; (e) Magnified TEM image of 5% Ru@N-MXNR, where the inset illustrates the average Ru NCs size ~ 0.4 nm; (f) HRTEM lattice image of 5% Ru@N-MXNR. The inset in the top right corner displays the inverse fast Fourier transform (IFFT) lattice images of TiO_2 NPs.

magnified TEM image in **Fig. 5.2(e)** further illustrates that Ru NCs are homogeneously distributed on the surface of MXNRs, with an average Ru NC size of ~ 0.4 nm. Furthermore, the high-resolution TEM (HRTEM) image in **Fig. 5.2(f)** reveals distinct interplanar spacings of 0.4 and 0.36 nm corresponding to the (006) and (101) lattice planes of MXNRs and TiO_2 NPs, respectively. Notably, partial oxidation of the MX surface was observed during nanoribbon formation, heteroatom doping, and the Ru NCs anchoring process. The inverse fast Fourier transform (IFFT) patterns, displayed at the top corner of **Fig. 5.2(f)**, distinctly highlight the (101) lattice planes corresponding to TiO_2 NPs[16].

5.3.2. Structural Characterizations

The structural purity and crystallinity of the synthesized materials were assessed using XRD and Raman spectroscopy. The XRD pattern of multi-layered $Ti_3C_2T_x$ (m-$Ti_3C_2T_x$) powder is

shown in **Fig. 5.3(a)**. Notably, the (104) peak of m-$Ti_3C_2T_x$ at ~39° vanishes after the HF treatment, while the (002) peak undergoes a shift toward a lower 2θ value in multi-layered $Ti_3C_2T_x$. This shift indicates an increase in interlayer spacing due to the removal of Al layers and the introduction of surface functional groups (-O, -OH, -F). The diffraction peaks centred at 2θ = 9°, 18.5°, 37.8°, 37.1°, and 60.6° correspond to the (002), (004), (006), (010), and (110) crystallographic planes. Additionally, a further downward shift in the (002) peak after KOH treatment suggests the intercalation of K^+ ions, leading to an increment in interlayer spacing. Although the Ar atmosphere effectively suppressed oxidation, slight surface oxidation was observed, as evidenced by a minor peak at 2θ = 26°, corresponding to anatase TiO_2, which was previously confirmed through HRTEM analysis. As illustrated in **Fig. 5.3(a)**, the (002) diffraction peak of N-MXNR appears at 7.2°, which is a little lower than that of pristine MXNRs (7.5°). This shift implies an additional increase in interlayer spacing, likely attributed to the incorporation of N heteroatoms into the MXNR framework. Interestingly, the XRD pattern of 5%Ru@N-MXNR exhibits a similar pattern to those of MXNR and N-MXNRs. However, the (002) peak downshifts further to 7.0° as compared to 7.2° in N-MXNR, suggesting that Ru anchoring further increases the interlayer spacing. This observation confirms that the synergistic effect of N doping and Ru anchoring improves the interlayer distance, thereby increasing the surface area, which is beneficial for catalytic HER applications. Next, the crystallinity and phase of the as-prepared materials are investigated by Raman spectroscopy. The m-$Ti_3C_2T_x$ in **Fig. 5.3(b)** exhibits characteristic peaks at 209.4 cm^{-1} (Ti, C, O) and 700.8 cm^{-1} (Ti, C), which correspond to the A_{1g} out-of-plane vibrational modes[17]. The broad bands observed in the range 230-470 cm^{-1} and 540-730 cm^{-1} can be attributed to the E_g in-plane vibrational modes associated with surface functional groups bonded to Ti atoms[17]. Further, a broad Raman band appearing in the range 1200-1600 cm^{-1} can be ascribed to C-C bonding, likely resulting from minor surface oxidation and the presence of amorphous carbon[18]. The Raman spectra of MXNRs display characteristic peaks at ~206, 272, 376, 574, and 734 cm^{-1}, which align well with those typically observed for m-$Ti_3C_2T_x$. Additionally, MXNRs exhibit two distinct bands at ~1364 cm^{-1} and ~1549 cm^{-1}, corresponding to the D band (disordered carbon) and G-band (graphitic carbon), respectively[18]. In the case of N-doped MXNRs, a well-defined D-band at 1355 cm^{-1} and G-bands at 1565 cm^{-1} were observed compared to pristine MXNRs, suggesting that N doping increases the structural disorder due to high-temperature annealing. The Raman spectrum of 5% Ru@N-MXNR exhibits similar features to those of N-MXNR, as well as a reduction in disorder within the MXNR framework upon Ru anchoring. The I_D/I_G intensity ratio, a widely used parameter for evaluating the degree

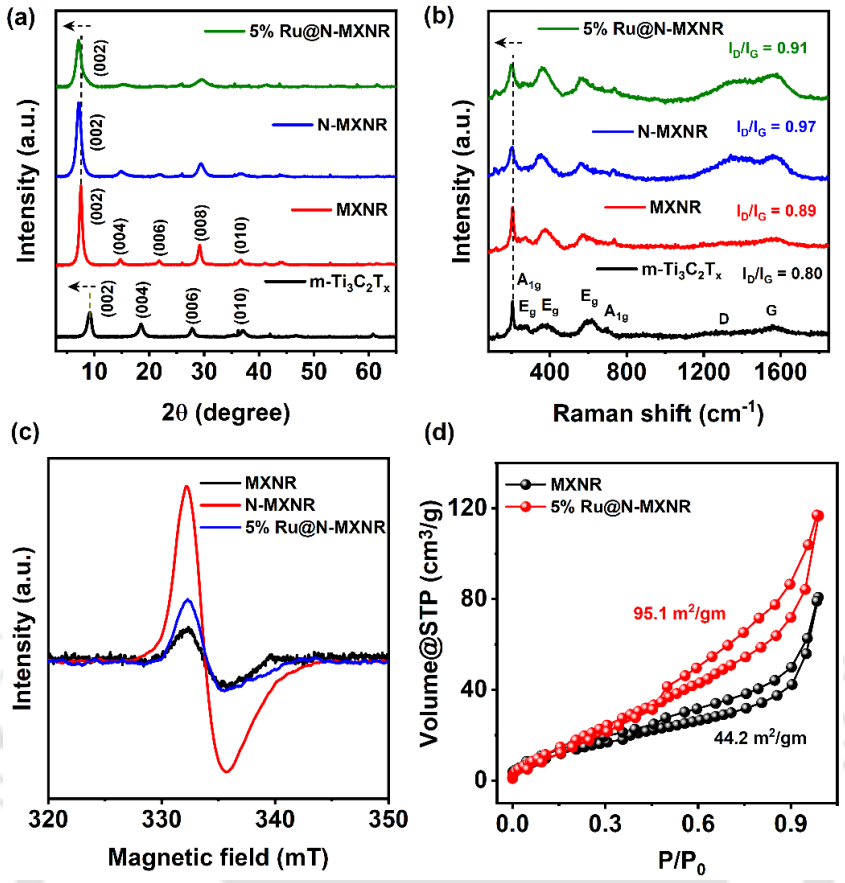

Fig. 5.3. Comparisons in (a) XRD patterns and (b) Raman spectra of m-$Ti_3C_2T_x$, MXNR, N-MXNR, and 5% Ru@N-MXNR. (c) comparisons in the ESR signal of MXNR, N-MXNR, and 5% Ru@N-MXNR. (d) Nitrogen adsorption-desorption isotherm of MXNR and 5% Ru@N-MXNR.

of graphitization and defect density in carbon structures indicate that a higher I_D/I_G ratio corresponds to increased defect density within the carbon lattice[19]. The calculated I_D/I_G ratios for pristine MXNR, N-MXNR, and 5%Ru@N-MXNR are 0.89, 0.97, and 0.91, respectively. These findings suggest that increased graphitization and more defect formation occur during high-temperature processing, potentially enhancing the catalyst's activity by providing additional active sites. Highly graphitized carbon also facilitates stronger π-π interactions, thereby improving charge transfer kinetics. Moreover, the introduction of defective sites plays a crucial role in tuning the electronic structure and surface characteristics, optimizing the adsorption energies of reaction intermediates during catalytic processes. Interestingly, the reduction in the I_D/I_G ratio after Ru anchoring indicates improved structural purity. Consequently, Ru NC-decorated MXene nanoribbons, which exhibit a lower I_D/I_G ratio, are expected to show lower charge transfer resistance and, thus, enhanced catalytic activity.

5.3.3. BET and ESR Analysis

ESR spectroscopy was employed to analyze the presence of OVs in the synthesized materials. The ESR spectra exhibited resonance signals at g = 2.02, as shown in **Fig. 5.3(c)**, confirming the existence of OVs in all the samples[20, 21]. However, pristine MXNRs displayed a relatively low concentration of OVs. In contrast, N doping significantly increased the density of OVs within the lattice. Furthermore, a noticeable reduction in the ESR signal was observed after Ru NCs incorporation, compared to N-doped MXNRs. This suggests that Ru species can integrate into the MXNR lattice, effectively occupying OV sites during the synthesis process. This phenomenon facilitates the formation of Ru-Ti bonds, enhancing interfacial chemical interactions between Ru and the MXNR support. Consequently, this structural modification contributes to an enhanced electrocatalytic HER performance, further emphasizing the importance of controlled Ru NCs incorporation in tuning the electronic and catalytic properties of MXNR-based catalysts.

Next, the nitrogen adsorption-desorption isotherm analysis was conducted to evaluate the specific surface area of MXNR and 5% Ru@N-MXNR, as illustrated in **Fig. 5.3(d)** The Brunauer-Emmett-Teller (BET) surface area was calculated to be 44.2 m^2/g for MXNR and 95.1 m^2/g for 5% Ru@N-MXNR, highlighting a significant enhancement in surface area with doping, which in turn provides a higher density of active sites for catalytic reactions, and enhanced catalytic efficiency.

5.3.4. XPS Analysis

XPS was employed to analyze the chemical composition and modifications in the as-prepared samples before and after functionalization. The XPS survey spectrum in **Fig. 5.4(a)** reveals Ti, C, and O in both MXNRs and 5%Ru@N-MXNR, while the F 1s peak is diminished, indicating the substitution of F with -O/-OH groups after alkalization, leading to -O terminated MXNRs. Additionally, the survey XPS spectra of 5%Ru@N-MXNR show the presence of a small peak corresponding to N 1s. However, no Ru 3d peak is observed separately because of the overlap of the energy range of C 1s and Ru 3d. The high-resolution Ti 2p XPS spectra (**Fig. 5.4(b)**) of N-MXNRs show four peaks corresponding to Ti-C (454.3, 460.7 eV), Ti^{2+} (455.3, 461.8 eV), Ti^{3+} (456.6, 463.3 eV) and Ti-O (458.6, 464.6 eV). Similarly, the Ti 2p high-resolution XPS spectra of 5%Ru@N-MXNR show similar peaks, but with a noticeable shift toward higher binding energies, attributed to interfacial charge transfer from Ru NCs to the N-doped MXene matrix via strong metal-support interactions. The intensity of the Ti-O peak at 458.6 eV is slightly improved after Ru anchoring, which can be attributed to the conversion of all the surface groups to -O terminated groups at the surface of MXNRs, followed by KOH treatment

and annealing, as confirmed earlier from TEM and XRD analysis. The O 1s XPS spectrum of the N-MXNRs (**Fig. 5.4(c)**) shows three peaks corresponding to Ti-O (529.9 eV), C-Ti-O_x (531.3 eV), and C-Ti-OH_x (532.8 eV). A similar pattern was observed for 5%Ru@N-MXNR, but the percentage of OVs is altered. The decrease in the order of OVs is N-MXNR (16.9%) > N-MXNR@Ru (13.7%), respectively. Furthermore, the N 1s XPS spectrum for N-MXNR

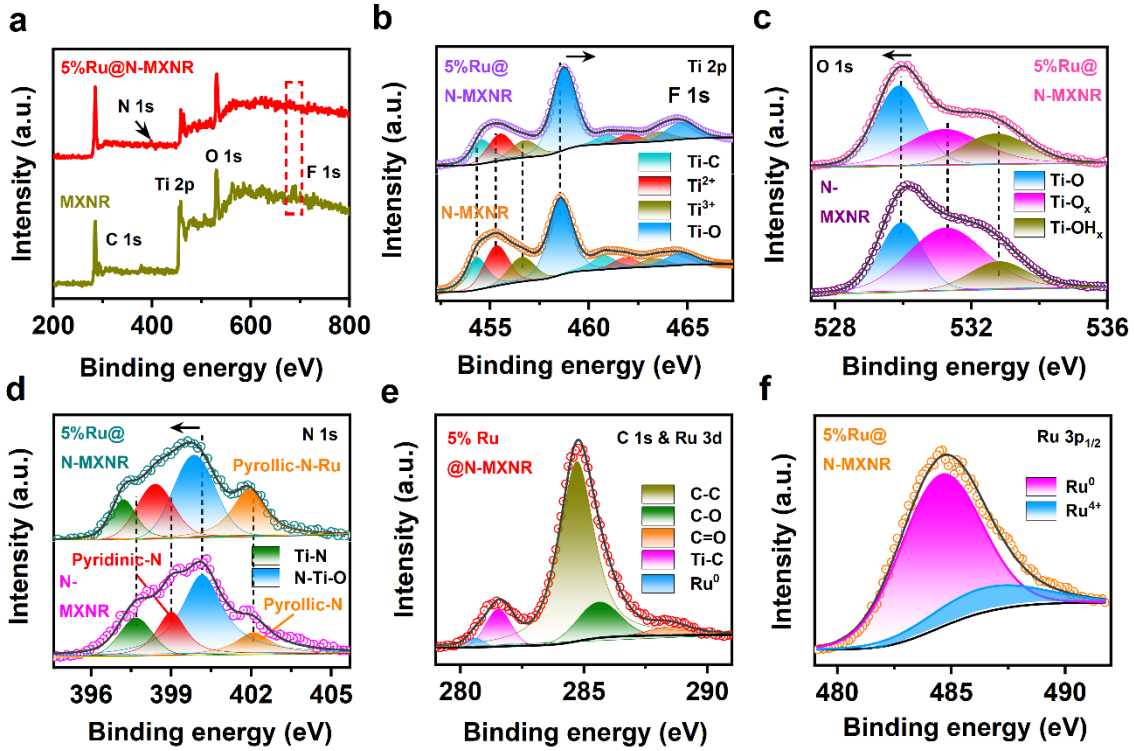

Fig. 5.4. Comparison of (a) the survey scan XPS spectra of MXNR and 5%Ru@N-MXNR. (c) Comparison of the high-resolution (b) Ti 2p, (c) O 1s and (d) N 1s XPS spectra of N-MXNR and 5%Ru@ N-MXNR. The high-resolution XPS spectra of (e) C 1s & Ru 3d and (f) Ru $3p_{1/2}$ for 5%Ru@N-MXNR.

shows (**Fig. 5.4(d)**) two prominent nitrogen states: pyridinic N (398.3 eV) and pyrrolic N (401.4 eV), with two additional peaks at BE values 397.0 and 399.5 eV, attributed to Ti-N and N-Ti-O bonds[22], respectively, confirming the successful incorporation of nitrogen into the MXNR framework. In 5%Ru@N-MXNR, all these N 1s states are retained with a notable shift toward lower binding energies, along with an enhanced intensity of the pyrrolic-N-Ru peak, suggesting Ru NCs preferentially anchor at N-rich defect sites, thereby strengthening the interaction with support material. The high-resolution XPS spectra of the C 1s and Ru 3d regions (**Fig. 5.4(e)**) exhibit peaks assigned to Ti-C (281.4 eV), C-C (284.7 eV), C-O (285.6 eV), and O=C-O (288.4 eV). Additionally, the Ru $3d_{5/2}$ signal is also detected at 280.5 eV, corresponding to Ru^0.[23]

Further, the Ru 3p region[24] demonstrates two primary Ru $3p_{1/2}$ peaks at BE of 484.5 eV and 486.3 eV. The higher BE peak corresponds to RuO_2, while the lower energy peak is attributed

to metallic Ru^0, as illustrated in **Fig. 5.4(f)**.

5.3.5. UV-Vis Absorption and Photothermal Characterizations

The optical absorption spectra of MXNR, N-MXNR, and 5% Ru@N-MXNR are depicted in **Fig. 5.5(a)**. A broad absorption peak in the spectral range of 740-1240 nm range for MXNR is attributed to localized surface plasmon resonance (LSPR) effects. In comparison, N-MXNR exhibits a similar absorption profile to MXNR but with a slight enhancement in the visible and UV regions. This improvement is ascribed to the presence of OVs, which enable higher visible light absorption[25], while the increased absorption in the UV region is likely due to slight surface oxidation and the formation of TiO_2 NPs on the MXNR surface, as confirmed by XRD and XPS analyses. Notably, 5% Ru@N-MXNR exhibits significantly higher light absorption spanning from the UV to NIR regions, which can be attributed to the synergistic effect of MXNR, N doping, and Ru NCs.

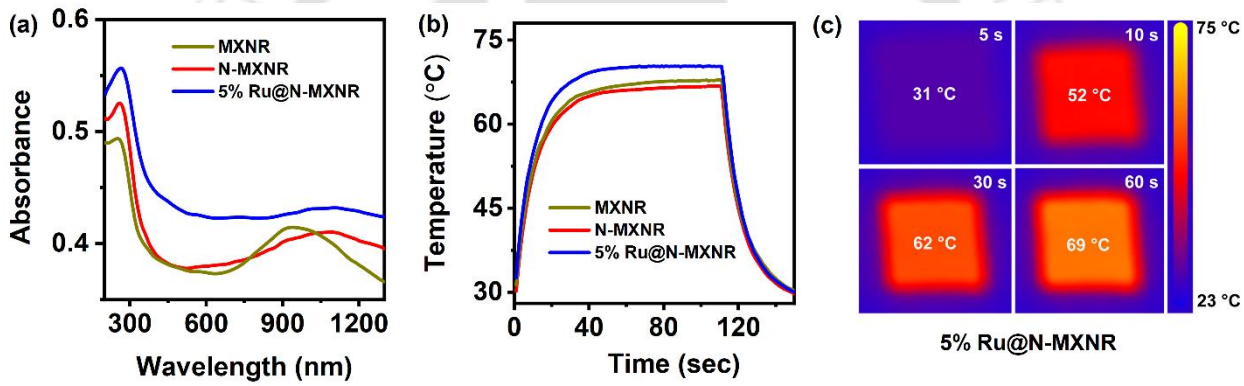

Fig. 5.5. (a) Comparison of UV-Vis absorption spectra (b) Light to temperature conversion curves of MXNR, N-MXNR, and 5%Ru@N-MXNR composites. (d) A digital image of the photothermal effect for 5%Ru@N-MXNR.

Furthermore, the light-to-heat conversion capability of the synthesized materials was evaluated by exposing them to a xenon lamp source (Vis-NIR). The results (**Fig. 5.5(b)**) reveal that 5% Ru@N-MXNR demonstrates substantially higher photothermal conversion efficiency compared to both MXNR and N-MXNR, owing to their enhanced light absorption and the LSPR effect of MXNRs. Additionally, the digital images of the photothermal effect in **Fig. 5.5(c)** indicate that under Vis-NIR light illumination, 5% Ru@N-MXNR rapidly attains a temperature of 69°C within 1 min, highlighting its excellent photothermal conversion efficiency.

5.3.6. Electrocatalytic HER Performance

The electrochemical HER performance of the synthesized catalysts was evaluated in an

alkaline medium using a standard three-electrode setup in 1 M KOH at room temperature. The corresponding LSV curves for MXNR, N-MXNR, 5%Ru@MXNR, 3%, 5%, and 7% Ru loaded N-MXNR are illustrated in **Fig. 5.6(a)**. A comparative analysis of the overpotential at a current density of 10 mA cm^{-2} of the as-prepared catalysts is summarized in **Table 5.1**. Among the catalysts, 5%Ru@N-MXNR exhibited the highest catalytic performance, achieving an exceptionally low overpotential of ~22 mV at a current density of 10 mA cm^{-2}. This overpotential is significantly lower than that of 5% Ru@MXNR (61 mV). The negligible HER activity observed for pure MXNR highlights the crucial role of Ru NCs as electrocatalytically active sites. The strong metal-support interactions between Ru NCs and the distinct Ti sites in the MXNR substrate effectively modulate the adsorption/dissociation kinetics of H_2O as well as the desorption of OH* and H* species at the 5%Ru@N-MXNR active sites, thereby optimizing the overall catalytic efficiency.

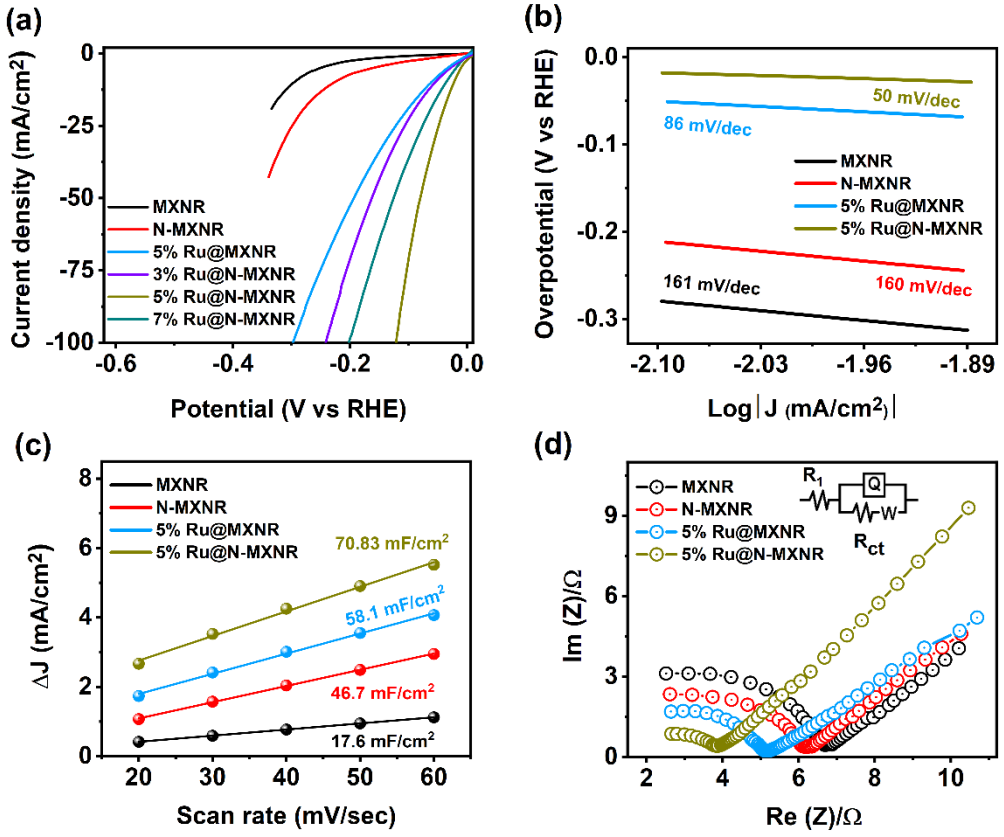

Fig. 5.6. Comparison of (a) LSV curves of MXNR, N-MXNR, 5% Ru@MXNR, 3%, 5% and 7% Ru loaded N-MXNR composites (b) Tafel plots and slopes, (c) Plots of capacitive current density difference vs. scan rate, (d) Nyquist plot for MXNR, N-MXNR, 5% Ru@MXNR, 5% Ru@N-MXNR catalysts in 1 M KOH solution.

To gain deeper insights into the kinetics of the HER, the Tafel slopes of the synthesized electrocatalysts were analyzed. The MXNR catalyst exhibited a Tafel slope of 161 mV dec^{-1}, suggesting that the water dissociation step is the rate-determining step. In **Fig. 5.6(b)**, the 5%

Ru@MXNR and 5% Ru@N-MXNR catalysts demonstrated a Tafel slope of 86 and 50 mV dec^{-1}, signifying the effectiveness of Ru NCs in faster HER reaction. The Tafel slope analysis indicates that the HER in alkaline electrolytes follows the Volmer-Heyrovsky pathway[26, 27]. Additionally, Ru NCs demonstrate superior water dissociation capability due to their low energy barrier for water dissociation. Moreover, the EMSI in 5% Ru@N-MXNR catalyst enhances the desorption of adsorbed H*, further improving HER performance[28]. Additionally, the catalytic HER performance of the synthesized materials follows a volcanic trend as the Ru concentration increases in Ru@N-MXNR. This behaviour can be attributed to the fact that an optimal amount of Ru NCs provides more active sites for HER, whereas an excessive Ru loading leads to NCs aggregation, which diminishes the EMSI effect and subsequently reduces the catalytic performance.

The electrochemically active surface area (ECSA) can be determined by evaluating the electrochemical double-layer capacitance (C_{dl}), which is directly proportional to ECSA. As depicted in **Fig. 5.6(c)**, the C_{dl} values for MXNR, N-MXNR, 5% Ru@MXNR, and 5% Ru@N-MXNR were measured as 17.6, 46.7, 58.1, and 70.83 mF cm^{-2}, respectively. Among these, 5% Ru@N-MXNR exhibited the highest ECSA, indicating that it can provide the largest number of active sites for electrocatalytic HER. This result further corroborates the superior catalytic activity of 5% Ru@N-MXNR in HER. Additionally, the EIS provides valuable insights into the charge-transfer kinetics involved in the HER process, which is illustrated in **Fig. 5.6(d)**. Compared to MXNR, the charge transfer resistance (R_{ct}) of Ru@MXNR is significantly reduced, which is summarised in **Table 5.1**, indicating improved electron transfer efficiency. Among the catalysts, 5% Ru@N-MXNR shows the lowest R_{ct} value of 1.72 Ω, which can be attributed to the enhanced water dissociation capability of Ru NCs and the charge redistribution induced by the EMSI effect. These findings are consistent with the observed alkaline HER activity, further confirming the crucial role of Ru NCs and the EMSI effect in facilitating efficient charge transfer and catalytic performance.

5.3.7. Photoelectrochemical HER Activity

The photoelectrochemical (PEC) HER performance of the 5% Ru@N-MXNR catalyst was further evaluated under simulated solar irradiation to explore the impact of its strong light absorption, efficient separation of photogenerated charge carriers, and light-to-heat conversion capabilities on HER performance. The LSV was employed to investigate the PEC hydrogen evolution performance of 5% Ru@N-MXNR and commercial Pt/C (20%) photocathodes, as shown in **Fig. 5.7(a)**. Notably, 5% Ru@N-MXNR exhibited a significantly higher HER

activity, achieving an overpotential of ~12 mV @10 mA cm^{-2} under Vis-NIR light illumination, which is significantly lower than the overpotential observed under dark. In contrast, HER performance of commercial Pt/C (20%) demonstrates a lower HER performance in both dark and under light illumination, with an overpotential of ~23 mV. Additionally, a significant reduction in the Tafel slope (**Fig. 5.7 (b)**) of 5% Ru@N-MXNR (34 mV/dec) was observed under illumination, whereas the Tafel slopes of Pt/C (20%) (41 mV/dec) is significantly higher, which makes 5% Ru@N-MXNR an excellent photo electrocatalyst over the commercial Pt/C catalyst in alkaline medium. The above results indicate that the 5% Ru@N-MXNR catalyst exhibits significantly improved HER kinetics compared to the commercial Pt/C catalyst. The

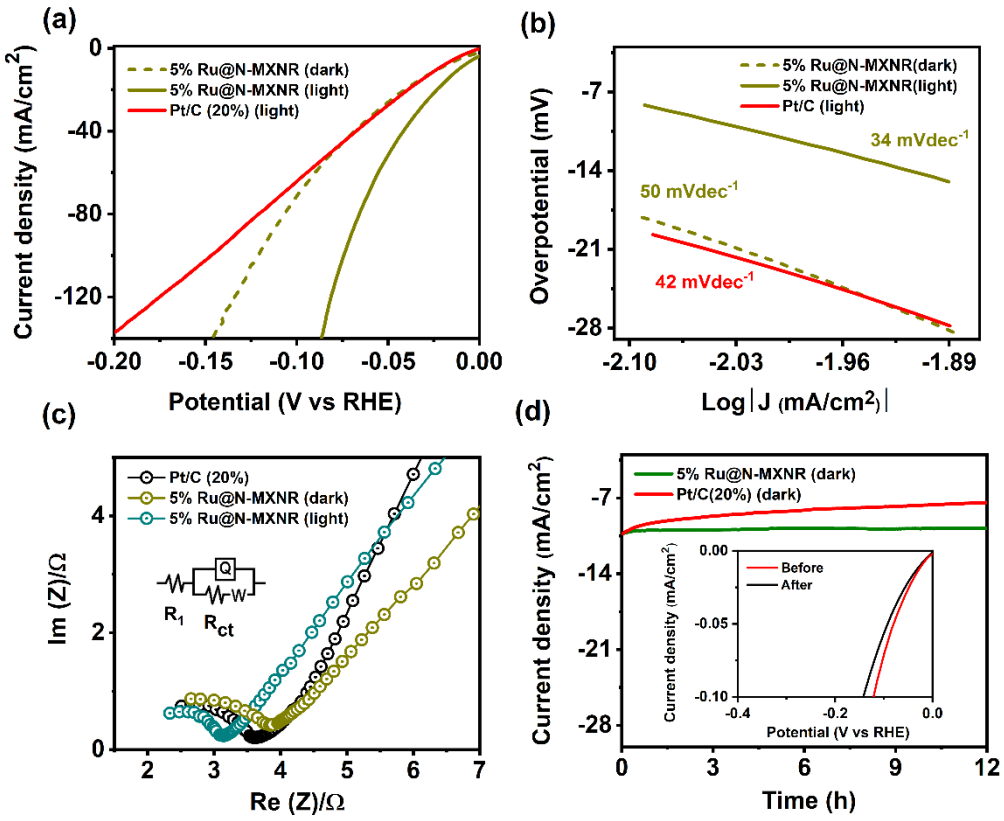

Fig. 5.7. Comparison of (a) LSV curves of 5% Ru@N-MXNR and commercial Pt/C catalysts under dark and light illumination, corresponding to (b) Tafel plots and (c) Nyquist plot in 1 M KOH solution. (d) The chronoamperometry curve shows long-term stability up to 12 h and the LSV curve of 5% Ru@N-MXNR catalyst before and after 5000 cycles under Vis-NIR light illumination in 1 M KOH solution.

superior HER activity under light illumination can be attributed to its enhanced light absorption and the generation of photogenerated charge carriers by TiO_2 NPs. Additionally, the efficient charge separation and transfer facilitated by Ru NCs and MXNR further contribute to its high catalytic performance. Upon Vis-NIR light illumination, the photothermal effect of the 5% Ru@N-MXNR plays a crucial role in improving both the thermodynamic and kinetic aspects of the electrocatalytic process. This enhancement arises from the LSPR effect and the presence

of OV states of MXNRs. These defects facilitate the redistribution of thermal energy through electron-electron and electron-phonon scattering, leading to a rapid increase in the localized surface temperature. As a result, the electron transfer rate is significantly accelerated, ultimately boosting the overall HER efficiency.

Further, EIS was conducted to analyze the electron transfer kinetics of the catalyst during the electrocatalysis process. As anticipated, the 5% Ru@N-MXNR catalyst exhibited the lowest charge transfer resistance (R_{ct}**)** of 1.4 Ω (**Fig. 5.7(c)**), which can be attributed to the enhanced separation of photogenerated charge carriers facilitated by Ru NCs and N-MXNR surfaces, along with their photothermal effect. This synergistic interaction effectively accelerates interface electron transfer kinetics. Additionally, the stability of the catalyst was evaluated under prolonged electrochemical conditions. After 5000 CV cycles in 1.0 M KOH, the catalytic performance remained nearly unchanged, indicating excellent durability (**Fig. 5.7(d)**). Additionally, a chronoamperometry test conducted at a constant current density of 10 mA cm^{-2} for 12 h showed no significant degradation, further confirming the catalyst's long-term stability.

5.3.8. Mechanism of Enhanced HER Activity

The EIS measurements (**Fig. 5.7(c)**) reveal that the 5% Ru@N-MXNR catalyst exhibits a lower charge transfer resistance (R_{ct}) of ~ 1.72 Ω in the dark, which further decreases to ~1.4 Ω after 5 min of light exposure. This reduction in R_{ct} indicates enhanced charge transfer dynamics and accelerated hydrogen HER kinetics, aligning with the trends observed in the LSV curve and Tafel slope analysis. The electrical conductivity of hybrid materials plays a crucial role in determining their electrocatalytic HER efficiency.

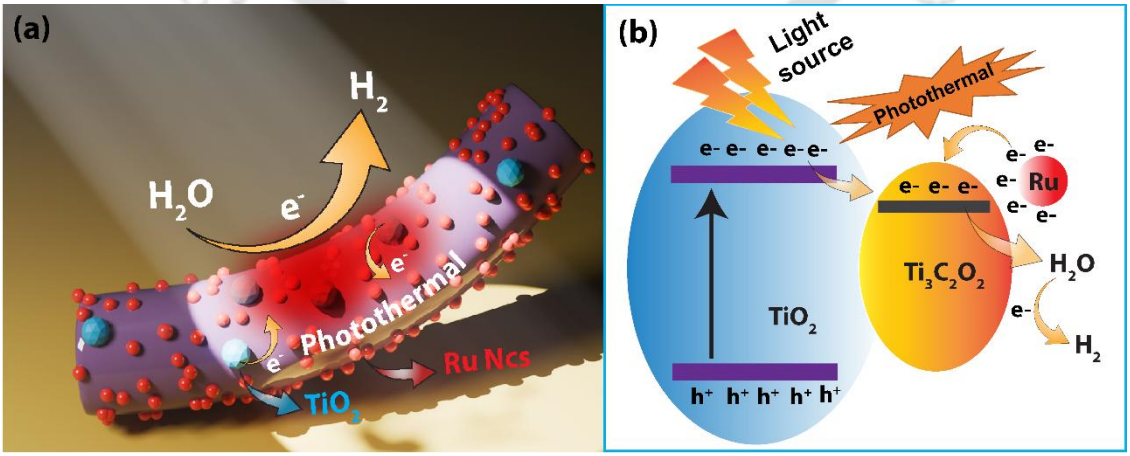

Fig. 5.8. (a) A schematic illustration of HER and (b) charge transfer mechanism in Ru@N-MXNR composite under Vis-NIR light illumination.

The presence of oxygen-containing functional groups on MXNRs provides active sites for

hydrogen adsorption, while TiO_2 NPs on the surface contribute additional photoelectrons under light illumination. This enhanced electron transfer is attributed to the formation of a Schottky junction at the MXNR/TiO_2 interface, which significantly boosts electrocatalytic performance. Moreover, the photothermal effect further enhances electron mobility at the interface, thereby increasing the electron transfer rate. Based on these findings, a band alignment and charge transfer process is proposed, as illustrated in **Fig. 5.8 (a, b)**. Under Vis-NIR light irradiation, electrons in the valence band of TiO_2 NPs are excited to the conduction band and subsequently migrate to the N-MXNR surfaces due to the Schottky junction formation. The separated electrons efficiently participate in water reduction, facilitating hydrogen evolution via the following reaction mechanism:

Volmer reaction: $Ru@N\text{-}MXNR + H_2O + e^- \rightarrow Ru@N\text{-}MXNR\text{-}H_{ads} + 2OH^-$

Heyrovsky reaction: $Ru@N\text{-}MXNR\text{-}H_{ads} + H_2O + e^- \rightarrow Ru@N\text{-}MXNR + OH^- + H_2$

Additionally, the LSPR effect of MXNRs, coupled with the presence of OVs, induces a photothermal effect that accelerates reaction kinetics and significantly enhances electrocatalytic performance. These findings highlight the potential of 5% Ru@N-MXNR as an efficient photo-electrocatalyst for alkaline HER.

Table 5.1. *A summary of catalytic activity and R_{ct} values of different catalysts studied here.*

Catalysts	**Photoelectrochemical hydrogen production**					
	Overpotential (mV) at 10 mA/cm^2		**Tafel slope (mV/dec)**		**Charge transfer resistance (R_{ct}, Ω)**	
	Dark	Light	Dark	Light	Dark	Light
MXNR	295	-	161	-	6.25	-
N-MXNR	227	-	160	-	4.63	-
5%Ru@MXNR	61	-	86	-	4.05	-
5%Ru@N-MXNR	22	12	50	34	1.72	1.4
Pt/C (20%)	23	23	42	42	1.58	1.58

5.4. Conclusions

We have successfully synthesized ultra-small Ru NCs anchored onto hierarchical N-doped $Ti_3C_2T_x$ MXene nanoribbons (Ru@N-MXNR). Structural characterization through Raman and ESR spectroscopy confirms the presence of OVs associated with defect states induced by N

doping. These defects serve as active sites for Ru anchoring. However, their concentration significantly decreases after Ru loading, which effectively inhibits the aggregation of Ru NCs. Further, XPS and TEM analysis reveal the formation of TiO_2 NPs on the MXNR surface and a strong interfacial interaction between Ru NCs and MXNRs in the 5% Ru@N-MXNR composite. The UV-Vis absorption spectra demonstrate enhanced light absorption capabilities of 5% Ru@N-MXNR compared to pristine MXNR and N-MXNR. Electrochemical studies highlight the exceptional HER performance of 5% Ru@N-MXNR under both dark and light-illuminated conditions. The catalyst exhibits low overpotentials of 22 mV and 12 mV, along with Tafel slopes of 50 mV/dec and 34 mV/dec, respectively. Notably, these values surpass the performance of the commercial 20% Pt/C catalyst, which demonstrates an overpotential of ~23 mV and a Tafel slope of 42 mV/dec. The superior catalytic activity of 5% Ru@N-MXNR can be attributed to the synergistic effects of Ru NCs' excellent water dissociation ability and the electronic metal-support interaction, which facilitates the efficient desorption of adsorbed H* intermediates. Additionally, under Vis-NIR light illumination, the generation of additional photogenerated charge carriers, coupled with photothermal effects, enhances electron mobility and further improves HER activity. A long-term stability assessment confirms the stable hydrogen production capability of 5% Ru@N-MXNR, as evidenced by a consistent current density over the extended operation. Therefore, the 5% Ru@N-MXNR emerges as a highly promising and cost-effective alternative to conventional 20% Pt/C catalysts for photoelectrochemical hydrogen evolution in alkaline media, offering a sustainable pathway for efficient hydrogen production.

References

(1) Dresselhaus, M. S.; Thomas, I. L. Alternative energy technologies. *Nature* **2001**, *414* (6861), 332-337.
(2) Yin, H.; Tang, Z. Ultrathin two-dimensional layered metal hydroxides: an emerging platform for advanced catalysis, energy conversion and storage. *Chemical Society Reviews* **2016**, *45* (18), 4873-4891.
(3) Turner, J. A. Sustainable Hydrogen Production. *Science* **2004**, *305* (5686), 972-974.
(4) Yin, H.; Zhao, S.; Zhao, K.; Muqsit, A.; Tang, H.; Chang, L.; Zhao, H.; Gao, Y.; Tang, Z. Ultrathin platinum nanowires grown on single-layered nickel hydroxide with high hydrogen evolution activity. *Nature Communications* **2015**, *6* (1), 6430.
(5) Gray, H. B. Powering the planet with solar fuel. *Nature Chemistry* **2009**, *1* (1), 7-7.
(6) Wang, P.; Zhang, X.; Zhang, J.; Wan, S.; Guo, S.; Lu, G.; Yao, J.; Huang, X. Precise tuning in platinum-nickel/nickel sulfide interface nanowires for synergistic hydrogen evolution catalysis. *Nature Communications* **2017**, *8* (1), 14580.

(7) Chen, W.; Pei, J.; He, C.-T.; Wan, J.; Ren, H.; Zhu, Y.; Wang, Y.; Dong, J.; Tian, S.; Cheong, W.-C.; et al. Rational Design of Single Molybdenum Atoms Anchored on N-Doped Carbon for Effective Hydrogen Evolution Reaction. *Angewandte Chemie International Edition* **2017**, *56* (50), 16086-16090.
(8) Han, A.; Chen, W.; Zhang, S.; Zhang, M.; Han, Y.; Zhang, J.; Ji, S.; Zheng, L.; Wang, Y.; Gu, L.; et al. A Polymer Encapsulation Strategy to Synthesize Porous Nitrogen-Doped Carbon-Nanosphere-Supported Metal Isolated-Single-Atomic-Site Catalysts. *Advanced Materials* **2018**, *30* (15), 1706508.
(9) Li, Q.; Chen, W.; Xiao, H.; Gong, Y.; Li, Z.; Zheng, L.; Zheng, X.; Yan, W.; Cheong, W.-C.; Shen, R.; et al. Fe Isolated Single Atoms on S, N Codoped Carbon by Copolymer Pyrolysis Strategy for Highly Efficient Oxygen Reduction Reaction. *Advanced Materials* **2018**, *30* (25), 1800588.
(10) Fei, H.; Dong, J.; Arellano-Jiménez, M. J.; Ye, G.; Dong Kim, N.; Samuel, E. L. G.; Peng, Z.; Zhu, Z.; Qin, F.; Bao, J.; et al. Atomic cobalt on nitrogen-doped graphene for hydrogen generation. *Nature Communications* **2015**, *6* (1), 8668.
(11) Bandpey, M.; Barz, D. P. J. Effects of interlayer space engineering and surface modification on the charge storage mechanisms of MXene nanomaterials: A review on recent developments. *Nanoscale* **2024**, *16* (32), 15078-15093.
(12) Chen, W.; Liu, P.; Liu, Y.; Liu, Z. Recent advances in Two-dimensional $Ti_3C_2T_x$ MXene for flame retardant polymer materials. *Chemical Engineering Journal* **2022**, *446*, 137239.
(13) Kumar, S.; Mehdi, S. M. Z.; Seo, Y. 1D MXenes: Synthesis, Properties, and Applications. *Small* **2024**, *20* (49), 2405576.
(14) Saidur, R. M.; Mushtaq, A.; Huang, S.; Zhang, R.; Lu, Y.; Le, Y.; Jing, G.; Ahmad, Z.; Iqbal, M. Z.; Kong, X. Synthesis of ultra-small MXene nanorods for enhanced photothermal therapy of breast cancer in vitro. *Materials Letters* **2023**, *353*, 135324.
(15) Cui, C.; Cheng, R.; Zhang, H.; Zhang, C.; Ma, Y.; Shi, C.; Fan, B.; Wang, H.; Wang, X. Ultrastable MXene@Pt/SWCNTs' Nanocatalysts for Hydrogen Evolution Reaction. *Advanced Functional Materials* **2020**, *30* (47), 2000693.
(16) Yamunasree, B.; Kim, S.; Park, Y. H.; Modigunta, J. K. R.; Kim, J.; Astakala, A. K.; Lee, S. J.; Murali, G.; Lee, W.; In, I. Ultrasensitive and highly selective NO_2 gas sensing of porous MXene nanoribbon assemblies. *Carbon* **2024**, *228*, 119364.
(17) Sarycheva, A.; Gogotsi, Y. Raman Spectroscopy Analysis of the Structure and Surface Chemistry of $Ti_3C_2T_x$ MXene. *Chemistry of Materials* **2020**, *32* (8), 3480-3488.
(18) Naguib, M.; Mashtalir, O.; Lukatskaya, M. R.; Dyatkin, B.; Zhang, C.; Presser, V.; Gogotsi, Y.; Barsoum, M. W. One-step synthesis of nanocrystalline transition metal oxides on thin sheets of disordered graphitic carbon by oxidation of MXenes. *Chemical Communications* **2014**, *50* (56), 7420-7423.
(19) Rajput, G.; Rawat, A.; Chourasia, N. K.; Jalendra, G.; Gupta, G.; Yadav, A.; Kulriya, P. K. Engineering the decay time of $Ti_3C_2T_x$ MXene by gold nanoparticle decoration. *Nanotechnology* **2025**, *36* (15), 155702.
(20) Li, J.; Zhang, M.; Guan, Z.; Li, Q.; He, C.; Yang, J. Synergistic effect of surface and bulk single-electron-trapped oxygen vacancy of TiO_2 in the photocatalytic reduction of CO_2. *Applied Catalysis B: Environmental* **2017**, *206*, 300-307.
(21) Yu, K.; Wang, S.; Li, Q.; Hou, T.; Xin, Y.; He, R.; Zhang, W.; Liang, S.; Wang, L.; Zhu, W. Au atoms doped in $Ti_3C_2T_x$ MXene: Benefiting recovery of oxygen vacancies towards photocatalytic aerobic oxidation. *Nano Research* **2022**, *15* (4), 2862-2869.
(22) Liu, H.; Hu, Z.; Liu, Q.; Sun, P.; Wang, Y.; Chou, S.; Hu, Z.; Zhang, Z. Single-atom Ru anchored in nitrogen-doped MXene ($Ti_3C_2T_x$) as an efficient catalyst for the hydrogen evolution reaction at all pH values. *Journal of Materials Chemistry A* **2020**, *8* (46), 24710-24717.

(23) Zhou, L.; Shao, Y.; Yin, F.; Li, J.; Kang, F.; Lv, R. Stabilizing non-iridium active sites by non-stoichiometric oxide for acidic water oxidation at high current density. *Nature Communications* **2023**, *14* (1), 7644.
(24) Antonetti, C.; Oubenali, M.; Raspolli Galletti, A. M.; Serp, P.; Vannucci, G. Novel microwave synthesis of ruthenium nanoparticles supported on carbon nanotubes active in the selective hydrogenation of p-chloronitrobenzene to p-chloroaniline. *Applied Catalysis A: General* **2012**, *421-422*, 99-107.
(25) Zhang, D.; Wang, M.; Wei, G.; Li, R.; Wang, N.; Yang, X.; Li, Z.; Zhang, Y.; Peng, Y. High visible light responsive $ZnIn_2S_4/TiO_{2-x}$ induced by oxygen defects to boost photocatalytic hydrogen evolution. *Applied Surface Science* **2023**, *622*, 156839.
(26) Cai, J.; Zong, L.; Fan, K.; Song, F.; Gao, J.; Wang, Z.; Chen, Y.; Wang, L. High temperature shock synthesis of superfine Ru nanoparticles anchored on TiO_2 @nitrogen-doped carbon for pH-universal hydrogen evolution reaction. *Journal of Alloys and Compounds* **2023**, *969*, 172279.
(27) Khalil, M.; Lesa, M.; Juandito, A. G.; Sanjaya, A. R.; Ivandini, T. A.; Kadja, G. T. M.; Mahyuddin, M. H.; Sookhakian, M.; Alias, Y. A SBA-15-templated mesoporous $NiFe_2O_4$/MXene nanocomposite for the alkaline hydrogen evolution reaction. *Materials Advances* **2023**, *4* (17), 3853-3862.
(28) Sun, Y.; Xue, Z.; Liu, Q.; Jia, Y.; Li, Y.; Liu, K.; Lin, Y.; Liu, M.; Li, G.; Su, C. Y. Modulating electronic structure of metal-organic frameworks by introducing atomically dispersed Ru for efficient hydrogen evolution. *Nature Communications* **2021**, *12* (1), Article.

Chapter 6

High-Performance Schottky Junction Photodetector Based on $Bi_2S_3/Ti_3C_2T_x$ MXene for Broadband Photodetection

This chapter investigates the role of $Ti_3C_2T_x$ MXene nanosheets as a robust metallic support in enhancing the optoelectronic device performance of $Ti_3C_2T_x$-based composites. In this context, the $Bi_2S_3/Ti_3C_2T_x$ composite material, previously discussed in **Chapter 4**, has been utilized, considering its low cost, exceptional light absorption properties, and efficient photogenerated charge separation capabilities. The fabricated low-cost $Bi_2S_3/Ti_3C_2T_x$-based Schottky junction photodetector exhibits outstanding broadband responsivity, covering a spectral range from ultraviolet to near-infrared (300-1550 nm). The device achieves peak responsivity values of 36.7 A/W at 300 nm and 26.2 A/W at 780 nm. Additionally, it demonstrates a high external quantum efficiency of ~ 3.9×10^3% and a rapid response time of ~300 μs under an applied bias of 3 V, highlighting its remarkable performance. Moreover, the fabricated photodetector exhibits excellent long-term stability under ambient conditions. This study provides valuable insights into the superior charge transport properties and ultra-broadband photodetection capabilities of $Ti_3C_2T_x$ MXene-based composites, underscoring their potential for high-performance optoelectronic applications.

6.1. Introduction

Photodetectors (PDs) are optoelectronic devices that transform photon energy into electrical signals. They are extensively used in advanced applications such as optical communication [1], remote sensing [2], and biological imaging[3]. Semiconducting materials with suitable band gaps can detect light signals in specific wavelength ranges, from ultraviolet (UV) to near-infrared (NIR). Wide bandgap semiconductors like TiO_2, ZnO, and GaN are ideal for UV detection[4], whereas narrow bandgap materials like InGaAs and Sb_2Se_3 are better suited for visible (Vis) and NIR light detection[5]. Broadband PDs have recently attracted considerable attention due to their ability to detect light across a broad spectrum, from UV to Vis to NIR. The active research in this field primarily focuses on materials such as Si[6], organic-inorganic perovskites[7], graphene [8], black phosphorus [9], TMDs [10], and their hybrid structures, owing to their distinctive electrical and optical properties. However, Si-based PDs exhibit limitations in broadband detection due to their low optical sensitivity in the UV and NIR regions, as well as high

reflectivity [10]. Organic-inorganic metal halide perovskites, recognized for their high absorption coefficient, excellent charge carrier mobility, and suitable bandgap, have gained significant attention for broadband PD applications. Despite these advantages, their instability in the presence of oxygen and moisture poses a significant challenge to their commercial viability [11].

A graphene-based PD capable of detecting light across a broad spectral range from 300 to 6000 nm is reported by Muller and co-others [12]. However, despite its extensive spectral sensitivity, the device exhibits low responsivity and limited gain, primarily due to high dark current and insufficient light absorption. Similarly, black phosphorus-based PDs, while highly effective for mid-infrared detection, suffer from poor environmental stability, which restricts their widespread application in optoelectronic devices[13]. The TMDs, known for their high absorption coefficient and excellent charge carrier mobility, have shown enhanced responsivity and specific detectivity in the Vis to NIR region. However, their atomically ultrathin structure [14] results in inadequate light absorption, leading to reduced responsivity in the NIR region, thereby limiting their potential for broadband detection. Additionally, the high costs associated with material synthesis and device fabrication, coupled with environmental instability, pose significant challenges. Therefore, there is an urgent need for a cost-effective material with an optimal bandgap and broad spectral sensitivity to drive advancements in broadband photodetection technologies.

The PDs based on $Ti_3C_2T_x$ MXene have demonstrated exceptional performance due to their outstanding electrical and optical properties. For instance, Nabet et al. [15] fabricated an MXene-GaAs-MXene PD by spin-coating a $Ti_3C_2T_x$ transparent electrode onto a patterned GaAs substrate, effectively replacing the conventional high-cost Au electrodes. This device exhibited superior photodetection performance compared to its counterpart incorporating Au electrodes. Similarly, Yang et al.[16] developed a large-area flexible PD on a paper substrate by integrating $CsPbBr_3$ with $Ti_3C_2T_x$ nanosheets, achieving an impressive on/off ratio of approximately 2.3×10^3, a response time of ~18 ms, a maximum responsivity of 44.9 mA W^{-1} at a bias voltage of 10 V, and a specific detectivity of 6.4×10^8 Jones. Zhang et al.[17] fabricated a self-driven Schottky junction PD based on a $Ti_3C_2T_x$/GaAs heterostructure, demonstrating an on/off ratio of ~5.6×10^5, a responsivity of 1.4 A/W, and a specific detectivity of 1.23×10^{13} Jones. Additionally, this device exhibited a broad photodetection range extending up to 980 nm. However, most studies on $Ti_3C_2T_x$ MXene-based PDs have reported photodetection capabilities limited to specific spectral regions, either from UV to Vis or from Vis to NIR. To date, no reports have documented the development of a truly broadband $Ti_3C_2T_x$ MXene-based

PD capable of covering the entire UV-Vis-NIR spectrum.

In this study, a planar PD was fabricated utilizing a $Bi_2S_3/Ti_3C_2T_x$ composite material. During the in-situ growth process, a Schottky junction was established at the interface between $Ti_3C_2T_x$ and Bi_2S_3. The presence of a built-in electric field at this junction effectively facilitates the separation of photogenerated charge carriers by minimizing recombination and trapping, thereby enhancing charge transfer across the interface. The broadband photodetection characteristics of the composite material were evaluated by spin-casting the as-synthesized $Bi_2S_3/Ti_3C_2T_x$ onto an Au inter-digitated electrode (IDE) patterned on an alumina substrate. The fabricated Schottky PD exhibited exceptionally high values of responsivity, specific detectivity, and external quantum efficiency. Additionally, the photoresponse was analyzed through pulsed photoresponse measurements, revealing rapid switching characteristics. The spectral response of the device demonstrated a broad detection range covering UV, Vis, and NIR regions. Furthermore, the room-temperature storage stability of the $Bi_2S_3/Ti_3C_2T_x$ PD, without any encapsulation, was assessed over an extended period. The exceptional performance and long-term stability of the PD were further investigated through a combination of density functional theory (DFT) calculations, microscopic imaging, and spectroscopic analysis.

6.2. Experimental Details

6.2.1. Synthesis of $Ti_3C_2T_x$ MXene Nanosheets

The synthesis of $Ti_3C_2T_x$ MXene nanosheets is similar to that discussed in **Chapter 3, Section 3.2.1**.

6.2.2. Synthesis of $Bi_2S_3/Ti_3C_2T_x$ MXene Composites

The synthesis of the $Bi_2S_3/Ti_3C_3T_x$ composite follows a methodology similar to that outlined in **Chapter 4, Section 4.2.2**. However, the precursor concentrations were adjusted, with bismuth nitrate pentahydrate ($Bi(NO_3)_3{\cdot}5H_2O$) at 0.75 mM and thiourea at 1.5 mM, with a total solution volume of 20 mL. The resulting composites are abbreviated as BSMX1, BSMX4, and BSMX7, corresponding to $Ti_3C_2T_x$ (MX) MXene loading of 1, 4, and 7 wt% relative to $Bi(NO_3)_3{\cdot}5H_2O$. Additionally, pristine bismuth sulfide (Bi_2S_3) was synthesized using the same precursor concentrations, but the mixing time of the two precursors was kept at 10 min before the hydrothermal treatment.

6.2.3. Fabrication of Photodetector Device

A planar photodetector device was fabricated utilizing commercially available IDE-patterned

gold (Au) electrodes with a channel gap of 80 μm on an alumina substrate. The sample solutions of BS and BSMX4, prepared at a concentration of 0.5 mg/mL, were subjected to sonication for 30 min. Subsequently, 50 μL of each solution was spin-coated onto a localized region of the IDE. The resulting films were then dried at 60 °C for 2 h before further characterization.

6.2.4. Computational Details

The density functional theory (DFT) calculations were carried out by using Quantum Espresso software[18]. The exchange-correlation interaction was treated by using generalized gradient approximation (GGA) with the Perdew-Burke-Ernzerhof (PBE) functional [19]. The van der Walls correction, Grimme-D3, was applied in all the calculations [20] of BSMX composite. The plane wave cut-off energy of 70 Ry and a Monkhorst-Pack k-point 8 × 8 × 1 grid were used for the Brillouin zone [21]. Additionally, in the reciprocal space, Vanderbilt ultra-soft pseudopotential was used to describe the atomic electronic configuration. The energy convergence threshold was set to 1×10^{-6} Ry.

In particular, the partial density of states (PDOS), the density of states (DOS), the band structure, and the charge density distribution were analyzed. Further, the charge density distribution was visualized by VESTA software [22], and the charge density difference (CDD) (ρ_{cdd}) was calculated by using the formula:

$$\rho_{cdd} = \rho_{BSMX} - \rho_{BS} - \rho_{MX} \quad (1)$$

Where, ρ_{BSMX}, ρ_{BS}, and ρ_{MX} represents the charge density of the BSMX composite, BS, and MX

6.2.5. Characterization Techniques

To analyze the crystal structure, morphology, and surface properties of the $Bi_2S_3/Ti_3C_2T_x$ composites, XRD, Raman spectroscopy, FESEM, TEM, and BET analyses were performed. Additionally, the reduction of organic pollutants was characterized using UV-Vis absorption spectroscopy. However, the characterization procedures are similar to those described in **Chapter 3**, **Section 3.2.4.** The UV-Vis absorption spectra of the synthesized materials were recorded using a PerkinElmer Lambda 950 absorption spectrometer. Electrochemical impedance spectroscopy (EIS) measurements were conducted with a CHI6044E electrochemical workstation; the current-voltage (I-V) characteristics and temporal photoresponse (I-t) of the photodetector devices were evaluated using a microprobe station (ECOPIA, EPS-500), an 808 nm laser with TTL modulation (CNI Laser), and a Keithley 2400

source-measure unit. The spectral photo-responsivity of the photodetector was determined utilizing a Xenon lamp (Newport) coupled with a manual monochromator (Newport) for measurements in the UV-Vis range. For the near-infrared (NIR) region, multiple laser sources with wavelengths of 808, 980, 1064, 1350, and 1550 nm were utilized, along with a Keithley 2400 source-measure unit.

6.3. Results and Discussion

6.3.1. Morphological Characterizations

The morphological characteristics of the synthesized materials were examined using FESEM and TEM. The TEM image of pristine MX reveals a nanosheet-like morphology, as described previously in **Chapter 4, Section 4.3.1.** FESEM image of pristine BS exhibits an aggregated

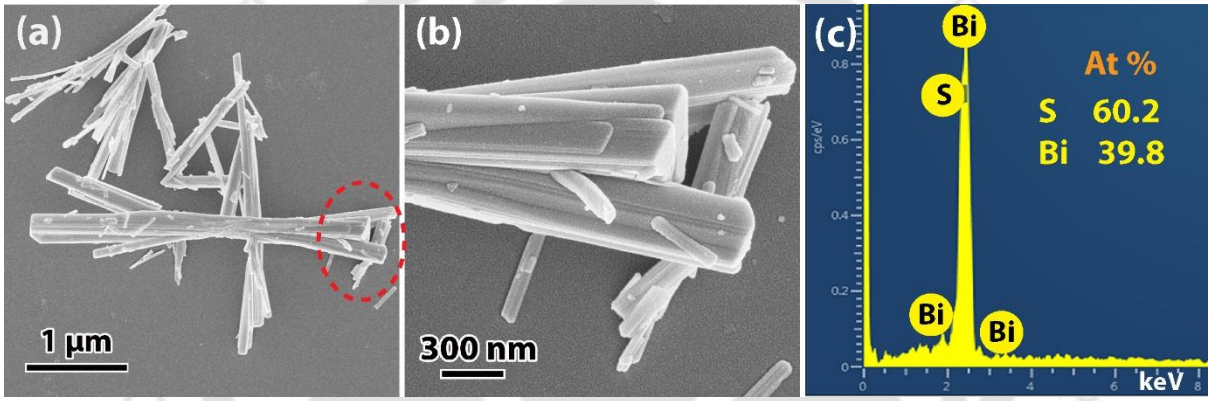

Fig. 6.1. (a) FESEM image, (b) magnified view of the selected region (red) of the BS nanorods. (c) EDS spectra of BS nanorods showing a good stoichiometry.

nanorod-like morphology, as illustrated in **Fig. 6.1(a, b).** This pronounced aggregated morphology is attributed to the high surface energy of BS nanorods, which drives their natural tendency to aggregate in order to minimize surface energy[23]. Additionally, the EDS analysis of the BS (**Fig. 6.1(c)**) reveals that the atomic percentage of Bi and S is 60.2 and 42.1%, respectively. However, the TEM image of BSMX composites with 4 wt% MX (**Fig. 6.2(a)**) loading demonstrates a significant reduction in BS nanorod aggregation. This reduction in agglomeration is primarily facilitated by the negatively charged functional groups present on MX nanosheets, which play a crucial role in providing nucleation sites while simultaneously preventing the aggregation of BS nanorods by reducing their surface energy through electron transfer from BS to MX nanosheets. This mechanism was further validated through density functional theory (DFT) simulations and experimental ultraviolet photoelectron spectroscopy (UPS) analysis, as discussed in a later section. A magnified view of an individual BS nanorod

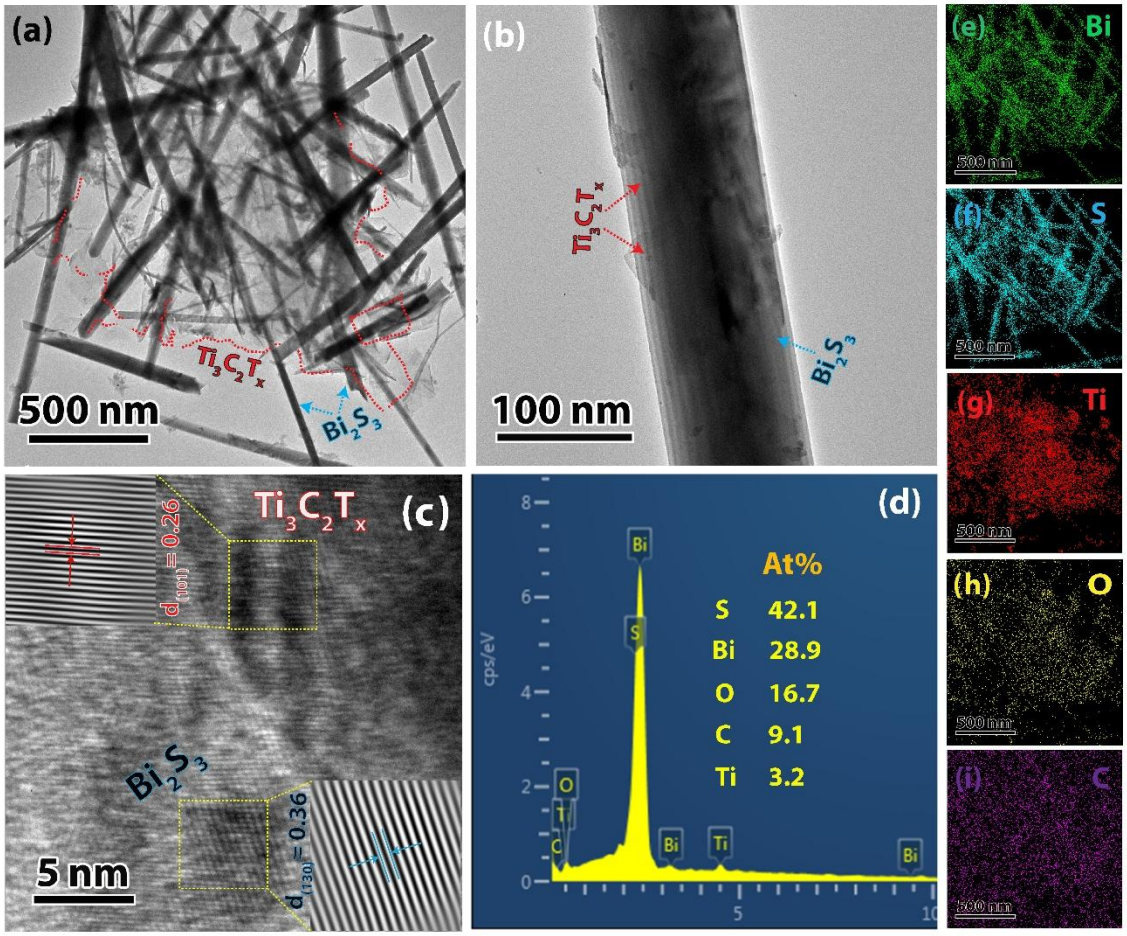

Fig. 6.2. (a, b) TEM images of BSMX4 composite. (c) HRTEM image of BSMX4, where the inset in the top and bottom corner shows the inverse fast Fourier transform lattice image of MX and BS. (d) EDS spectrum of BSMX4 composite and (e-i) elemental mapping of Bi, S, Ti, O, and C elements of BSMX4 composite.

from the BSMX4 composite (**Fig. 6.2 (a)**) is presented in **Fig. 6.2 (b)**, confirming that MX nanosheets wrap around the BS nanorods in BSMX4. These nanosheets act as a transparent layer under the electron beam, as reported in literature[24]. Furthermore, the high-resolution TEM (HRTEM) image of the BSMX4 composite (**Fig. 6.2 (c)**) displays lattice planes corresponding to both BS and MX nanosheets. The measured interplanar spacings of 0.26 nm and 0.36 nm correspond to the (101) and (130) crystal planes of MX and BS, respectively[25, 26]. This observation is further corroborated by XRD analysis, which is discussed later. The EDS analysis of the BSMX4 composite (**Fig. 6.2 (d)**) reveals the atomic percentage of Bi (28.9 %), S (42.1 %), Ti (3.2 %), O (16.7 %), and C (9.1 %). Furthermore, EDS mapping confirms the homogeneous distribution of Bi, S, Ti, C, and O elements within the BSMX4 composite, corresponding to **Fig. 6.2(e-i)**. However, the strong attachment between BS nanorods and MX layers enhances both light absorption and charge transfer processes, which are elaborated in subsequent sections.

6.3.2. Structural Characterizations

The phase structure and crystallinity of the synthesized materials were analyzed using X-ray diffraction (XRD) and Raman spectroscopy. The XRD pattern of MX nanosheets in **Fig. 6.3(a)** exhibits five primary diffraction peaks at 2θ = 6°, 17°, 29.1°, 34.11°, and 35.8°, which correspond to the (002), (004), (006), (101), and (106) crystal planes of MX, respectively. In contrast, the XRD pattern of BS aligns well with the standard reference card for Bi_2S_3 (JCPDS No. 01-075-1306), confirming its orthorhombic phase. Notably, the XRD pattern of the BSMX4 composite (**Fig. 6.3 (a)**) closely resembles that of pristine BS but with enhanced peak intensity. This observation indicates that during the in-situ growth of BS nanorods, the presence of MX nanosheets contributes to improved crystallinity without altering the intrinsic crystal structure of BS nanorods. However, characteristic XRD peaks associated with MX nanosheets are absent in the BSMX composite, likely due to the ultrathin layered structure or the relatively low concentration of MX nanosheets compared to BS. Furthermore, the Raman spectra of MX,

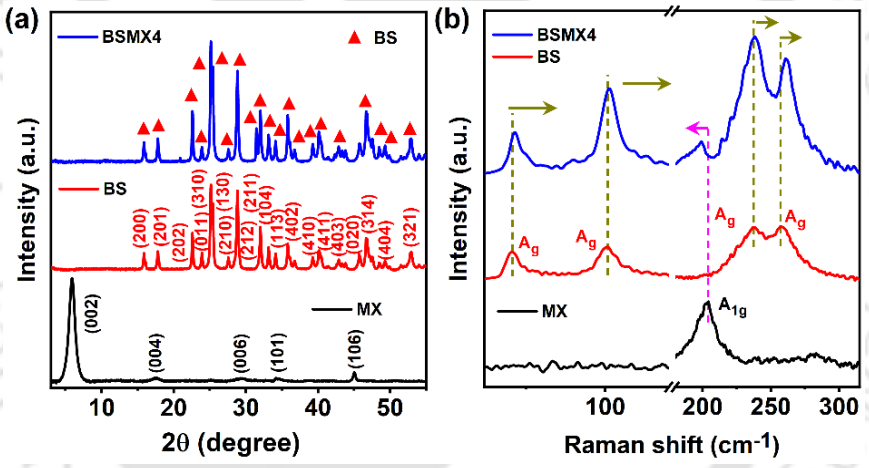

Fig. 6.3. Comparison of (a) XRD patterns and (b) Raman spectra of MX nanosheets (black), BS nanorods (red), and BSMX4 composite (blue). The arrows in (b) indicate the shift of the Raman modes in the composite.

BS and BSMX4 were recorded within the spectral range of 60-315 cm^{-1}, as depicted in **Fig. 6.3 (b)**. The Raman spectrum of the BSMX4 composite confirms the presence of vibrational modes corresponding to both BS (A_g) and MX (A_{1g}). However, both Raman modes (A_{1g} and A_g) exhibit a noticeable shift from their original positions. This shift may be attributed to the introduction of tensile strain in the MX lattice, resulting from the removal of oxygen vacancies (OVs) during the hydrothermal reaction. Additionally, all A_g peaks of BS in the BSMX4 composite undergo a blue shift relative to pristine BS, which could be a consequence of compressive strain in the BS lattice after the attachment of MX nanosheets. This structural alteration and strain effect are elaborated in **Chapter 4**, **Section 4.3.2**. These experimental

findings confirm the structural integrity of the BSMX4 composite.

6.3.3. XPS Analysis

The elemental composition and valence states of the constituent elements in pristine BS, MX, and the BSMX4 composite were further examined using XPS analysis. **Fig. 6.4(a)** demonstrates a comparative high-resolution XPS spectrum for Bi 4f and S 2p peaks in BS and BSMX4. The pristine BS spectrum exhibits two prominent peaks at binding energies (BE) of 158.4 eV and 163.7 eV, which correspond to Bi $4f_{7/2}$ and Bi $4f_{5/2}$ of Bi^{3+}, respectively[27], with a spin-orbit coupling separation of 5.3 eV. Additionally, two smaller peaks at BE values of 156.9 eV and 162.2 eV are assigned to Bi $4f_{7/2}$ and Bi $4f_{5/2}$ of metallic bismuth (Bi^0)[28]. Another peak at 161.1 eV corresponds to the 2p orbital of S^{2-}.[27] The high-resolution Bi 4f XPS spectrum of the BSMX4 composite (**Fig. 6.4(a)**) displays similar peaks to those observed in pristine BS, along with two additional peaks at BE values of 159.6 eV and 164.9 eV, which correspond to Bi-O bonds[27]. This suggests the interaction of Bi with oxygen-containing surface groups of MXene, leading to the formation of Bi-O chemical bonds. Notably, all peaks in the BSMX4 composite are shifted towards higher BE compared to pristine BS; the expected reason for this shift is discussed in a later section. The high-resolution Ti 2p XPS spectrum of MXene, shown

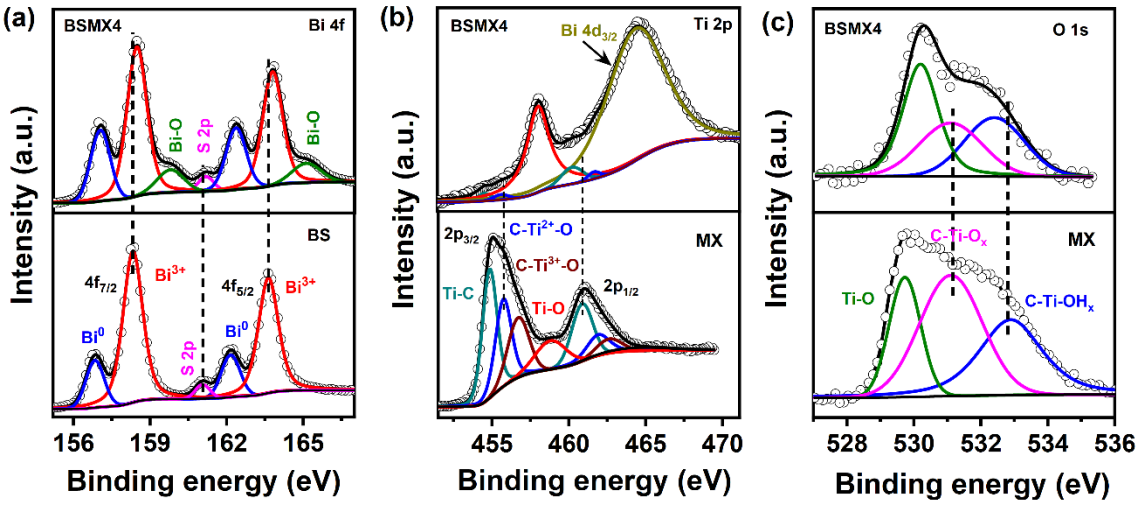

Fig. 6.4. High-resolution XPS spectrum of (a) Bi 4f from BS and BSMX4, (b) Ti 2p, and (c) O 1s of MX and BSMX4. The symbols represent the experimental data, and the solid lines correspond to the Gaussian-Lorentzian fitted spectra with a Shirley baseline.

in **Fig. 6.4(b)**, is fitted with four peaks corresponding to Ti-C (454.9 eV and 460.9 eV), C-Ti^{2+}-O (455.8 eV and 461.8 eV), C-Ti^{3+}-O (456.8 eV and 462.8 eV), and Ti-O (459 eV and 465.1 eV) [29, 30]. In contrast, the high-resolution Ti 2p spectrum of BSMX4 (**Fig. 6.4(b)**) primarily consists of three peaks attributed to C-Ti^{2+}-O (455.6 and 456.3 eV), Ti-C (454.5 and 460.2 eV),

and Ti-O (459 eV). The Ti-O peak arises from oxygen-containing surface groups, which are significantly more pronounced compared to pristine MXene nanosheets. Additionally, the decreased intensity of the C-Ti^{2+}-O peak suggests the removal of low-valent Ti states through hydrothermal oxidation. A comparison of the high-resolution O 1s XPS spectra of MX and BSMX4 is depicted in **Fig. 6.4(c)**. The O 1s spectrum of MXene is deconvoluted into three peaks corresponding to Ti-O (529.6 eV), C-Ti-O_x (531.1 eV), and C-Ti-OH_x (532.5 eV). Similarly, the O 1s spectrum of BSMX4 exhibits three peaks at 530.2 eV, 531.1 eV, and 532.2 eV, assigned to Ti-O, C-Ti-O_x, and C-Ti-$(OH)_x$, respectively[29, 30], with respective proportions of 29.1%, 38.1%, and 32.8%. These findings indicate the presence of -O_x and -OH_x groups in the BSMX4 composite in an approximate 2:1 ratio. Notably, the deconvoluted peaks associated with C-Ti-O_x and C-Ti-$(OH)_x$ in BSMX4 shift toward lower BE values.

6.3.4. Optical Characterization

To gain insight into the dynamics of photogenerated charge carriers in BS and BSMX composites, steady-state photoluminescence (PL) measurements were conducted. The PL spectra of pristine BS and BSMX composites with varying MX nanosheet loadings are presented in **Fig. 6.5 (a)**. BS nanorods exhibit a broad PL spectrum with an emission peak at ~ 940 nm, which corresponds to excitonic recombination near the band edge. However, in BSMX composites, a significant reduction in PL intensity is observed compared to pristine BS nanorods. The PL quenching efficiency follows the trend: BSMX4 (85%) > BSMX7 (80%) > BSMX1 (68%). The highest quenching efficiency in BSMX4 suggests the most effective separation and transfer of photogenerated charge carriers at the BSMX interface, thereby minimizing radiative recombination. Notably, no PL emission is detected in MX, likely due to its metallic nature.

To further substantiate the efficient charge separation and transfer rate in BSMX composites, electrochemical impedance spectroscopy (EIS) was carried out. **Fig. 6.5(b)** illustrates the Nyquist plots for BS, BSMX1, BSMX4, and BSMX7 samples, fitted using Z-view software. The results indicate that BSMX4 exhibits the smallest semi-circular arc radius, signifying the most efficient interfacial charge transfer[25] and enhanced separation of electron-hole pairs. The overall resistance at the electrode-electrolyte interface is denoted as R_s, while R_{ct} represents the interfacial charge transfer resistance. The R_{ct} values for the different materials follow the trend of: BS (184 kΩ) > BSMX1 (79.4 kΩ) > BSMX7 (60.4 kΩ) > BSMX4 (46 kΩ). These findings confirm that charge transfer kinetics are significantly enhanced upon the incorporation of MX

nanosheets at an optimal loading of 4 wt%. This improved charge transfer characteristic of the junction is subsequently leveraged for photodetection applications.

To evaluate the broadband light absorption capability of the MX, BS, and BSMX4 samples, UV-Vis absorption spectroscopy was conducted, and the corresponding results are illustrated

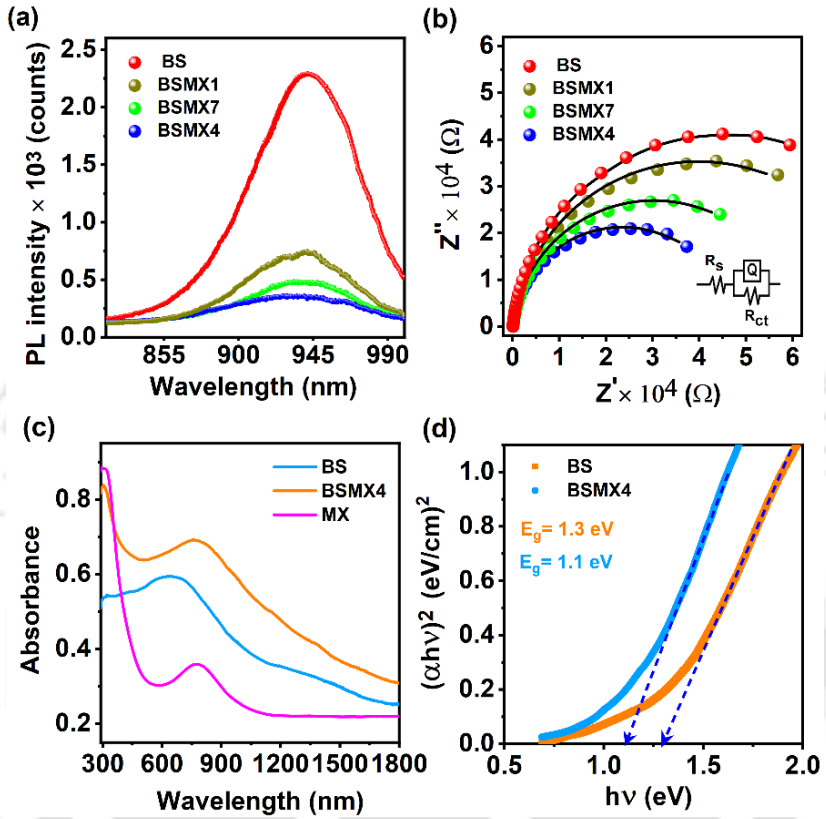

Fig. 6.5. (a) Comparison of the steady-state micro-PL spectra of BS, BSMX1, BSMX4, and BSMX7 under 532 nm laser excitation. (b) The electrochemical impedance spectra of the corresponding samples under 760 nm light irradiation. (c) Comparison of UV-Vis absorption spectra of BSMX4, BS, and MX, (d) Comparison of Tauc plots of BS and BSMX4 to calculate the respective bandgap.

in **Fig. 6.5(c)**. The absorption spectra of MX nanosheets exhibit two distinct peaks: a broad peak in the range of ~ 700-850 nm, which is attributed to the LSPR effect[31], and another peak at around 302 nm, associated with surface oxidation[32]. In contrast, BS nanorods display broadband absorption spanning the UV to NIR region (300-1800 nm), with a prominent peak at~ 650 nm. Notably, the BSMX4 composite exhibits a broad absorption spectrum similar to that of pristine BS nanorods. Moreover, the BSMX4 composite demonstrates significantly enhanced absorption across the entire spectral range (300-1800 nm) compared to pure BS nanorods, with a peak centred around 780 nm. Further, the band gap of the as-synthesized materials was calculated by using Tauc's formula:

$$(\alpha h\nu)^n = A\,(h\nu - E_g) \quad (2)$$

where α is the absorption coefficient, E_g is the bandgap, A is a proportionality constant, and n = 2. The calculated bandgap values, **Fig. 6.5(d)** of BS and BSMX4 are 1.3 eV and 1.1 eV, respectively. The observed bandgap reduction in BSMX4 is likely due to the synergistic effects of thin MX nanosheets and quantum confinement. The enhanced light absorption across the UV-NIR spectrum in BSMX4 facilitates efficient electron-hole pair generation, making it highly suitable for broadband photodetection applications

6.3.5. Theoretical DFT Study

To gain deeper insight into the electronic structure and interfacial charge transfer mechanism between BS and MX in BSMX composites, DFT calculations were performed. In this study, MX was modelled as $TC_{0.66}O_{0.66}$ ($T_x = O_2$), considering the high proportion of -O functional groups (67.2%) present in BSMX4, as confirmed by the O 1s XPS spectrum in **Fig. 6.4(c)**. The electronic band structure of BS, depicted in **Fig. 6.6(a),** reveals a direct bandgap of 1.33 eV, which aligns well with experimental observations. Conversely, the electronic band structure of $TC_{0.66}O_{0.66}$ in **Fig. 6.6(b)** shows overlapping bands near the Fermi level, indicative of its metallic nature. Notably, the band structure of $BSTC_{0.66}O_{0.66}$, presented in **Fig. 6.6(c)**, also exhibits band overlap near the Fermi level. This phenomenon is attributed to the introduction of $TC_{0.66}O_{0.66}$, which introduces additional electronic states within the bandgap of BS, thereby reducing its effective bandgap. Further analysis of the total density of states (TDOS) and projected density of states (PDOS) for BS and $TC_{0.66}O_{0.66}$ is provided in **Fig. 6.6(d**, **e)**, respectively. The calculated bandgap of BS from TDOS is 1.34 eV, which is consistent with the band structure plot. Similarly, the TDOS of $TC_{0.66}O_{0.66}$ confirms its metallic behaviour due to the overlap of electronic states near the Fermi level. Furthermore, the TDOS of $BSTC_{0.66}O_{0.66}$ (**Fig. 6.6(f)**) highlights the dominant contribution of $TC_{0.66}O_{0.66}$. A noticeable shift of the TDOS in the conduction band towards the Fermi level is observed in $BSTC_{0.66}O_{0.66}$ compared to pristine BS, suggesting an increased density of available electronic states near the Fermi level. This enhancement is expected to facilitate more efficient electron transport, leading to improved optoelectronic performance of $BSTC_{0.66}O_{0.66}$ relative to pristine BS. To further investigate charge separation and migration at the BS/$TC_{0.66}O_{0.66}$ interface, charge density difference (CDD) calculations were conducted, as shown in **Fig. 6.6(g)**. The regions of charge accumulation are represented in yellow, while the blue regions indicate charge depletion, confirming electron transfer from BS to the $TC_{0.66}O_{0.66}$ surface via the Bi-O bond.

Additionally, the plane-averaged charge density plot in **Fig. 6.6(h)** reveals two distinct peaks: one in the depletion region, indicating electron loss, and another in the accumulation region, signifying electron gain. These findings confirm that interfacial charge transfer occurs from BS to $TC_{0.66}O_{0.66}$. Furthermore, Bader charge analysis quantitatively verifies this charge transfer. It was determined that BS donates a total charge of 0.390 e per unit cell, or ~ 2.83×10^{-4} e/Å^3, which is subsequently acquired by $TC_{0.66}O_{0.66}$. Given that the estimated volume of a single BS nanorod in the practical system is approximately 1.907×10^{10} Å^3, the overall charge transfer per nanorod is calculated to be 5.39×10^6 e, which is significantly high.

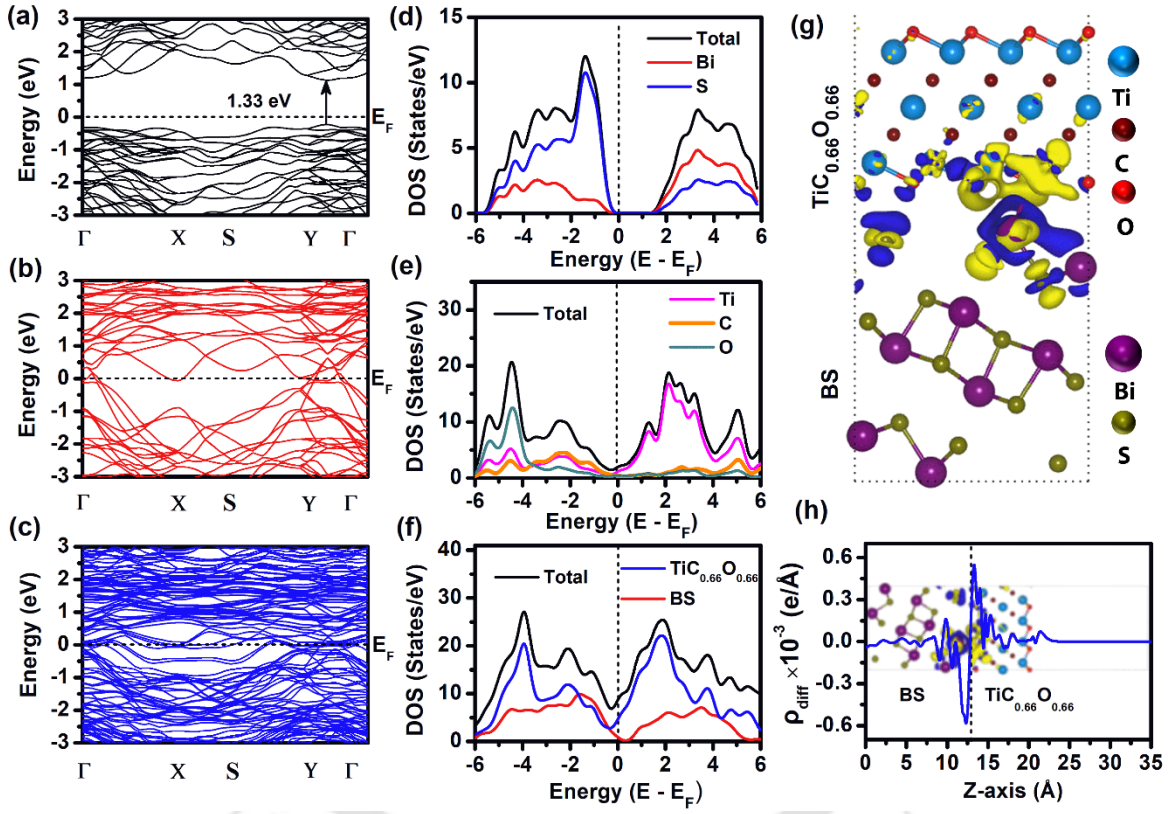

Fig. 6.6. (a, b, c) DFT calculated electronic band structure of BS, $TC_{0.66}O_{0.66}$, and $BSTC_{0.66}O_{0.66}$ composite, respectively. (d, e, f) The corresponding electronic DOS of these samples. (g) CDD plot of $BSTC_{0.66}O_{0.66}$ composite from DFT calculation, where the charge accumulation and depletion are represented by yellow and blue colour shades in two regions. (h) The plane average charge density difference plot indicates two spikes corresponding to charge depletion (at the BS site) and charge accumulation (at the $TC_{0.66}O_{0.66}$ site), and the dotted line indicates the interface between BS and $TC_{0.66}O_{0.66}$.

6.3.6. UPS Study

To further gain deeper insights into the interfacial charge transfer mechanism at the BS/MX interface in BSMX4, UPS analysis was conducted. The relative band positions and work function of the synthesized samples were examined using UPS. The corresponding UPS spectra for BS, MX, and BSMX4 are presented in **Fig. 6.7(a, b)**. The work function (φ) can be determined by using the formula:

$$\varphi = h\nu - E_{cut\ off} \quad (3)$$

where hν is the source energy (He I, 21.2 eV), and E_{cutoff} is determined by the intersection of the secondary electron cut-off occurs at a high binding energy value. For MX nanosheets, the measured secondary electron cut-off energy was found to be 16.61 eV, providing a work function of 4.59 eV. Similarly, for BS nanorods, the cut-off energy was determined to be 16.8 eV, corresponding to a work function of 4.4 eV. The energy separation between the Fermi level (E_F) and the valence band maximum (E_V) was obtained by extrapolating the linear portion of the spectrum to the energy axis in the low-binding energy region. For BS nanorods, this energy separation (E_F - E_V) was found to be 1.1 eV. Upon the formation of interfacial contact between BS nanorods and MX nanosheets, the cut-off energy shifted to 16.6 eV, leading to a work function of 4.6 eV, while the E_F - E_V value decreased to 1.0 eV. Using these parameters, a schematic band diagram was constructed to illustrate the band alignment of BS nanorods and MX nanosheets before and after contact, as shown in **Fig. 6.7(c)**. Before establishing contact, the E_F of BS nanorods was close to the conduction band, confirming its n-type semiconductor

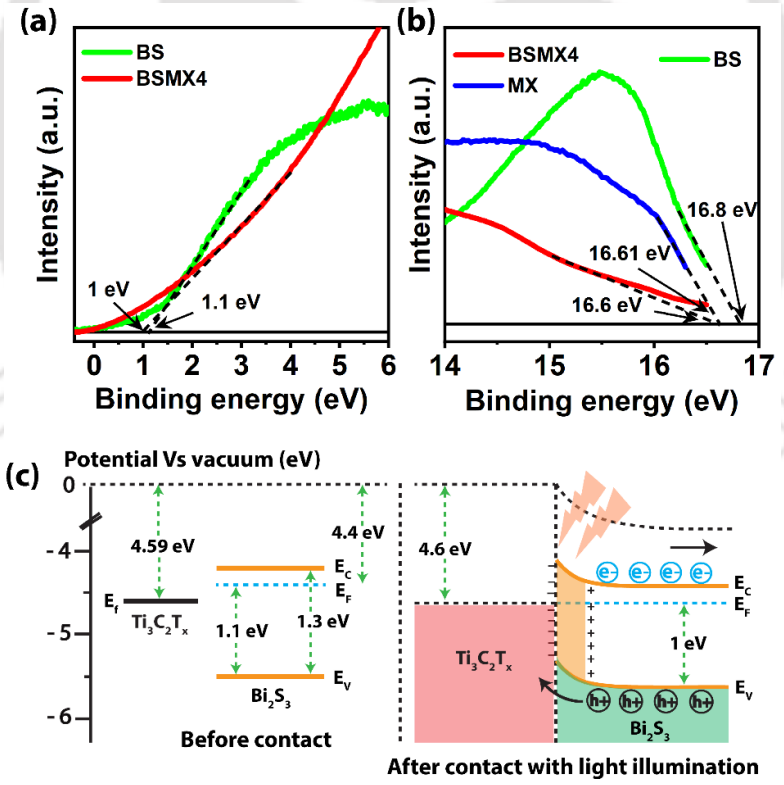

Fig. 6.7. UPS spectra of (a, b) BS, MX, and BSMX4 composite. (c) Energy band alignment derived from the UPS spectra and possible charge transfer mechanism in BSMX4 across the junction under light illumination.

nature. Meanwhile, the Fermi level of MX nanosheets was located below that of BS nanorods, suggesting the formation of a Schottky junction at the BS/MX interface. Upon interfacial

contact, electron transfer occurred spontaneously from the BS nanorods to the surface of MX nanosheets due to the higher E_F of BS. This electron migration continued until equilibrium was established, resulting in the formation of a positively charged layer on the BS surface and an accumulation of negatively charged electrons on the MX nanosheets. Consequently, a depletion region was formed, accompanied by an upward band bending near the interface. This phenomenon led to the development of a built-in electric field and a Schottky barrier at the junction, which is consistent with the DFT calculations discussed earlier. In the above system, upon illumination with a NIR light source, electrons in the valence band of BS nanorods are excited to the conduction band, leading to the generation of electron-hole pairs. Simultaneously, the built-in electric field at the BS/MX interface exerts a positive force on the photogenerated holes, facilitating their rapid transfer to the surface of the MX nanosheets. Consequently, the photogenerated electrons in the conduction band are efficiently separated under an applied external bias voltage, enhancing charge carrier extraction and transport. On the other hand, photogenerated holes facilitate their rapid transfer to the surface of the MX nanosheets. Consequently, the photogenerated electrons in the conduction band are efficiently separated under an applied external bias voltage, enhancing charge carrier extraction and transport.

Considering both the computational and experimental findings, it is evident that the BSMX4 composite exhibits remarkable potential for photodetection applications. To validate its practical utility, a PD device was fabricated using the BSMX4 composite material, and its broadband photodetection performance was systematically investigated, as discussed in the subsequent sections.

6.4. Application of BSMX Composite for Broadband Photodetection

A schematic representation of the BSMX4 composite-based PD is provided in **Fig. 6.8(a)**. The current-voltage (I-V) characteristics of both pristine BS and BSMX4-based PDs are depicted in **Fig. 6.8(b)** under dark conditions and upon illumination with an 808 nm laser at a power density of 6.3 mW cm^{-2} (Y-axis plotted on a logarithmic scale). The I-V curve of pristine BS demonstrates a symmetric behaviour, which indicates a back-to-back Schottky contact formation. Similarly, the BSMX4-based PD exhibits a symmetric I-V pattern with significant enhancement in photocurrent compared to the pristine BS PD, attributed to superior charge separation and enhanced light-matter interaction. It is noteworthy that the dark current in BSMX4 is slightly higher than that of the pristine BS PD due to the incorporation of MX

nanosheets, which contribute to an overall increase in system conductivity. **Fig. 6.8(c)** illustrates an intensity-dependent temporal photoresponse (I-t) study under 808 nm laser excitation with a bias voltage of 3 V. The inset illustrates the photocurrent as a function of laser intensity on a logarithmic scale, where the data have been fitted using a power-law relation:

$$I_{ph} = AP^{\theta} \quad (4)$$

where I_{ph} and P are the photocurrent and intensity of incident light, while A is a constant and exponent θ determines the photoinduced charge collection efficiency with light. In the low-intensity region (0.03-0.55 mW cm^{-2}), the value of exponent θ is ~ 0.88, suggesting an almost linear correlation between the incident photon flux and the generation of charge carriers. This behaviour indicates efficient charge separation with minimal recombination losses. However, in the higher power density range (0.55-8.5 mW cm^{-2}), the exponent θ decreases to ~ 0.35, which is attributed to increased carrier trapping and recombination effects. The linear dynamic range (LDR) provides a quantitative measure of the device's sensitivity across varying light

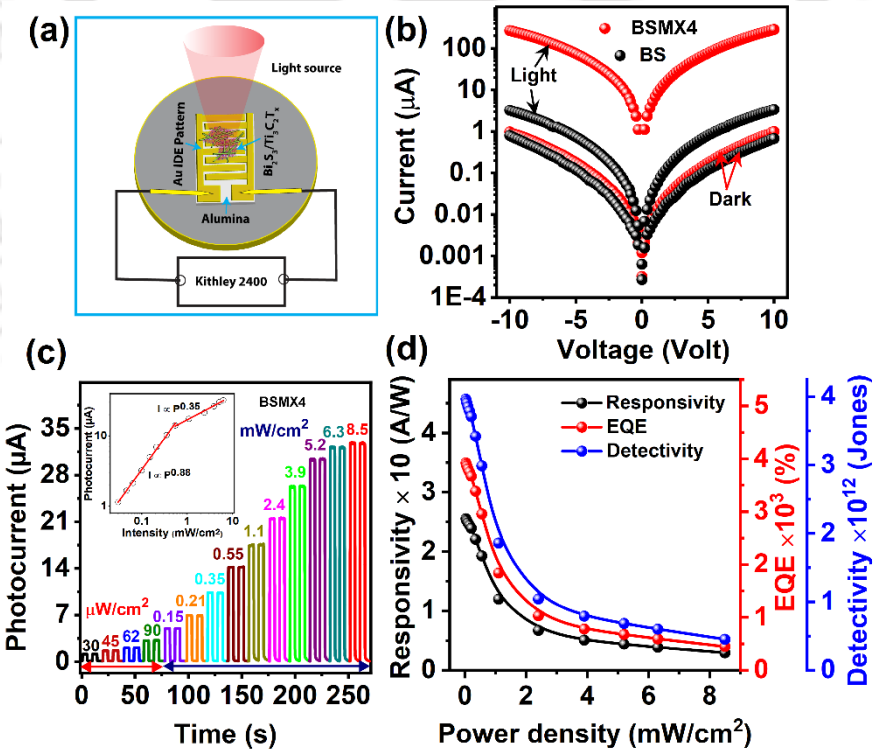

Fig. 6.8. (a) Schematic illustration of the PD configuration and photocurrent measurement, (b) Semi-log plot of dark current and photocurrent as a function of the voltage applied on BS and BSMX4 PDs. (c) Power-dependent photocurrent in BSMX4 PD; the inset shows a logarithmic photocurrent vs. intensity plot. (d) Responsivity, detectivity, and EQE BSMX4 PD as a function of incident power density.

intensities, as described by the corresponding mathematical relation:

$$LDR = 20 \log (I^*_{ph}/I_{dark}), \quad (5)$$

where I_{dark} is the current in the absence of any light, and I^*_{ph} is the photocurrent at a particular intensity from which the photocurrent starts deviating from linearity. In BSMX4 PD, the photocurrent increases from ~1.14 μA to 14.1 μA at an applied bias of 3 V as the incident light intensity rises from 0.03 to 0.55 mW cm^{-2}, giving an LDR of 40.7, which is notably high. The overall performance of a PD is primarily characterized by three key parameters: responsivity (R), external quantum efficiency (EQE), and specific detectivity (D*), which are defined by the following equations.

$$R = \frac{(I_{ph-I_{dark}})}{A \times P} \quad (6)$$

$$D^* = \frac{R}{\sqrt{2ej_d}} \quad (7)$$

$$EQE\% = (1240 \times \frac{R_\lambda}{\lambda}) \times 100\% \quad (8)$$

Where I_{ph} is photocurrent, I_{dark} is the dark current, P is the intensity of the incident light illumination and A is the effective area of the photodetector, whereas j_d refers to the dark current density, and e is the electronic charge. Based on the above equation, the responsivity (R), specific detectivity (D*), and external quantum efficiency (EQE) of the BSMX4 PD were determined under 808 nm excitation, with the results depicted in **Fig. 6.8(d)**. Notably, the responsivity of BSMX4 PD exhibits a decreasing trend with increasing laser intensity, reaching a maximum value of approximately 25.5 A/W at a low power density of 0.03 mW cm^{-2}. The decline in R at higher intensities is attributed to the presence of trap states within BS nanorods. At elevated light intensities, some photogenerated electrons may become trapped at interface states, leading to an increase in recombination processes. This, in turn, reduces the overall

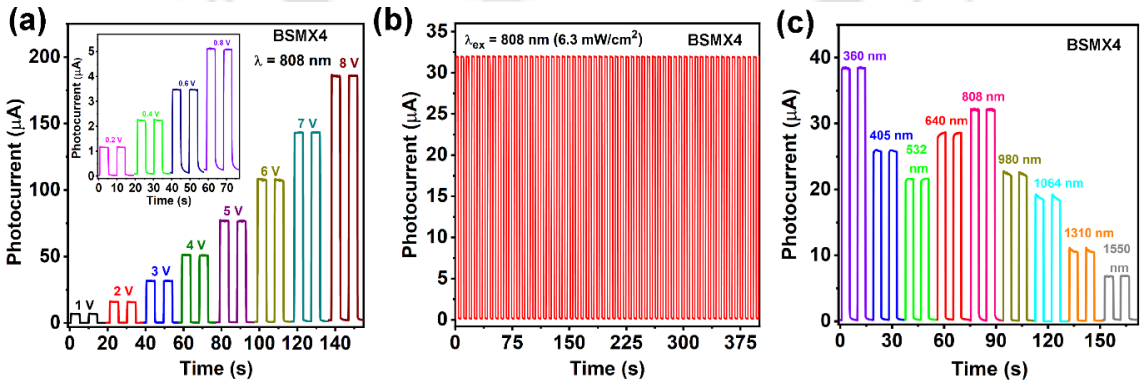

Fig. 6.9. (a) The photoresponse of BSMX4 PD at different applied bias voltages ranging from 1 to 8 V, with the inset depicting the photoresponse at lower bias voltages (0.2 to 0.8 V) under 808 nm laser excitation with a power density of 6.3 mW/cm^2. (b) The device exhibited high stability under prolonged exposure to 808 nm laser pulses. (c) The photoresponse was further examined under illumination from laser sources of varying wavelengths, including 360, 405, 532, 640, 808, 980, 1064, 1310, and 1550 nm, under identical experimental conditions.

photocurrent, thereby lowering the responsivity of the device. Since D* and EQE are directly

proportional to R, their values also decrease as laser intensity increases. However, at a low power density of 0.03 mW cm^{-2}, exceptionally high EQE and D* values of ~ 3.9 × 10^3% and 3.9 × 10^{12} Jones, respectively, were achieved, surpassing many previously reported devices.

To further explore the influence of applied bias on the photoresponse, measurements were conducted while maintaining a constant laser power of 6.3 mW cm^{-2}. **Fig. 6.9(a)** illustrates the photoresponse of BSMX4 PD under varying bias voltages (1-8 V), with the inset showing the photoresponse at lower bias voltages (0.2-0.8 V). A systematic increase in photocurrent was observed with increasing bias voltage. However, it is important to note that a higher bias voltage also leads to an increase in the dark current, thereby reducing the on-off ratio. Additionally, the photo-stability of BSMX4 PD was evaluated using an 808 nm pulsed laser, as depicted in **Fig. 6.9(b)**, demonstrating excellent stability under prolonged laser exposure. Furthermore, the broadband photoresponse of the BSMX4-based PD was evaluated under illumination with various wavelengths ranging from UV to Vis to NIR light at an intensity of 6.3 mW cm^{-2} with an applied bias of 3 V, as depicted in **Fig. 6.9(c)**.

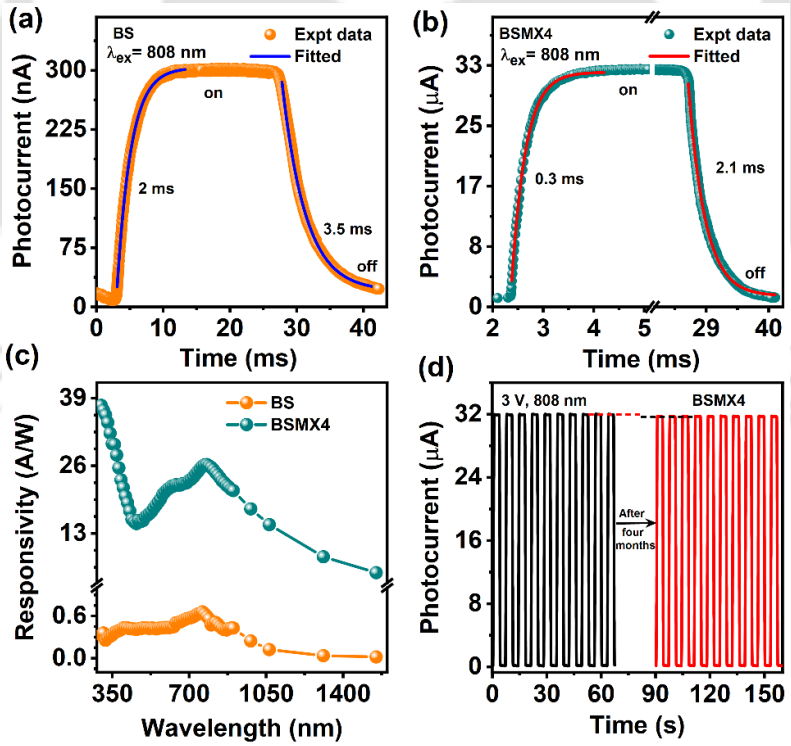

Fig. 6.10. The photocurrent growth and decay profiles of the devices with (a) BS and (b) BSMX4 at 808 nm excitation with a power density of 6.3 mW/cm^2. (c) The wavelength-dependent responsivity of BS and BSMX4 PDs at 3 V bias. (d) Storage stability of BSMX4 photodetector after four months without any encapsulation.

Further, **Fig. 6.10(a** and **b)** illustrates the photoresponse of bare BS and BSMX4 PDs under 808 nm pulsed laser excitation, with a peak intensity of 6.3 mW/cm^2 at an applied bias of 3 V.

To determine the temporal response characteristics, including the rise and decay time constants, the experimental data were fitted using a single exponential function.

$$I(t) = I_0 + A \exp\left(-\frac{t}{\tau}\right), \quad (9)$$

where τ is the time constant and I_0, and A are the constants. The photocurrent rise and decay time constants for the BS PD were determined to be 2.0 and 3.5 ms, respectively. In comparison, the BSMX4 PD exhibited significantly shorter time constants of 0.3 and 2.1 ms, indicating ~6.7-fold enhancement in photocurrent switching speed. This rapid photoresponse in BSMX4 is primarily attributed to the efficient separation of photogenerated charge carriers, facilitated by the incorporation of MX nanosheets. The broadband photodetection capability of BSMX4 PD, spanning from the UV to NIR regions, was further analyzed through a wavelength-dependent photoresponse study under an applied bias of 3 V, as presented in **Fig. 6.10(c)**. Notably, BSMX4 PD demonstrated a high responsivity of ~ 36.7 A/W in the UV region, which can be attributed to the presence of MX nanosheets and their surface oxidation induced by hydrothermal treatment. Additionally, in the Vis to NIR range, a significant increase in responsivity was observed due to enhanced light absorption and efficient charge carrier separation. A peak responsivity of ~26.2 A/W was obtained in the Vis to NIR region. The exceptional photoresponse across the UV to NIR spectrum can be associated with the improved light absorption and efficient separation of photogenerated carriers. This highlights BSMX4 as a highly promising candidate for broadband photodetection applications, with a broad coverage of wavelengths from 300 to 1550 nm. Furthermore, the long-term stability of BSMX4 PD was evaluated by monitoring its temporal photoresponse after four months of storage under ambient conditions using an 808 nm laser with a power density of 6.3 mW cm^{-2}, as depicted in **Fig. 6.10(d)**. Remarkably, the device exhibited only a ~0.6% reduction in photocurrent after four months, demonstrating its excellent stability and reliability for long-term photodetection in ambient environments.

Table 6.1. *Comparison of the performance of our $Bi_2S_3/Ti_3C_2T_x$-based broadband PD with recently reported PDs.*

Photodetector materials	**Synthesis technique**	**Wavelength (nm)**	**Responsivity (AW^{-1})**	**Detectivity (Jones)**	**Refs.**
Bi_2S_3 nanosheet	Chemical vapour deposition (CVD)	NIR (785)	16	10^{10}	[33]
Bi_2S_3 NFM	Hydrothermal	NIR (850 and 940)	2.23×10^{-3}	2.89×10^{9}	[34]
$Bi_2Te_3/Bi_2Se_3/Bi_2S_3$	Sequential vapour phase deposition	475	0.103	8.96×10^{9}	[35]
Bi_2S_3 nanowire	Vapour transport method	360 -1064	32		[36]
MXene/InGaN	Dry ion etching and chemical	Visible (470)	6	9×10^{11}	[37]
$MoSe_2/Ti_3C_2T_x$	Hydrothermal	554 - 780	6.58×10^{-3} (Visible) 9.82×10^{-3} (NIR light)	2.27×10^{9} (Visible) 3.39×10^{9} (NIR)	[38]
$ReS_2/Ti_3C_2T_x$	Hydrothermal (ReS_2) + MILD etching ($Ti_3C_2T_x$) + Spin casting ($ReS_2/Ti_3C_2T_x$)	Visible - NIR	40.8 (Visible) 26.9 (NIR Light)	1.07×10^{12} (Visible) 7.08×10^{11} (NIR)	[39]
$MoS_2/Ti_3C_2T_x$	Monolayer MoS_2 + $Ti_3C_2T_x$ dispersion spin casting	700 - 800	1.9 (Negative photo responsivity)	2.1×10^{10}	[40]
$Ti_3C_2T_x$-TiO_2	Hydrothermal	300 - 800	0.078×10^{-3}	8.4×10^{4}	[41]
$Ti_3C_2T_x/CsPbBr_3$	Spray Processed	450 - Visible	44.9×10^{-3}	6.4×10^{8}	[42]
$Si/SnO_2/Ti_3C_2T_x$	Electro spinning technique	Visible	64	3.09×10^{9}	[43]
Ti_3C_2/ZnO	Spin casting	200 - 400	128.3×10^{-3}	5.7×10^{11}	[44]
$Bi_2S_3/Ti_3C_2T_x$	Hydrothermal and spin casting	300 - 1550	36.7 (300 nm) 26.2 (780 nm) 25.5 (808 nm)	3.9×10^{12} (808 nm)	*This Work*

6.5. Conclusions

Using the optimized $Bi_2S_3/Ti_3C_2T_x$ composite, we successfully fabricated a high-performance broadband Schottky junction PD. The performance of the PD was characterized by using an 808 nm laser source. At 808 nm, the peak responsivity, detectivity and EQE of 25.5 A/W, 3.9×10^{12} Jones, and 3.9×10^{3}%, respectively, were achieved in the composite system. The broadband (UV-Vis-NIR) photodetector exhibits higher responsivity at 300 nm (~ 36.7 A/W) as well as at 780 nm (~ 26.2 A/W). The optimized BSMX4 planar PD exhibited very high storage stability in the ambient atmosphere. The above results confirm the superior photodetection performance of BSMX4 MXene composites in a broad range (300 -1550 nm); hence, it can be a potential candidate for broadband optoelectronic device applications.

References

1. Zhao, Z.; Liu, J.; Liu, Y.; Zhu, N., High-speed photodetectors in optical communication system. *Journal of Semiconductors* **2017,** *38* (12), 121001.
2. Huang, J.; Lee, J.; Vollbrecht, J.; Brus, V. V.; Dixon, A. L.; Cao, D. X.; Zhu, Z.; Du, Z.; Wang, H.; Cho, K., A high-performance solution-processed organic photodetector for near-infrared sensing. *Advanced Materials* **2020,** *32* (1), 1906027.
3. Ozsahin, I.; Uzun, B.; Ozsahin, D., Selection of photodetectors in nuclear medical imaging using MCDM methods. *Journal of Instrumentation* **2022,** *17* (06), C06003.
4. Sang, L.; Liao, M.; Sumiya, M., A comprehensive review of semiconductor ultraviolet photodetectors: from thin film to one-dimensional nanostructures. *Sensors* **2013,** *13* (8), 10482-10518.
5. Huang, S.-M.; Huang, S.-J.; Yan, Y.-J.; Yu, S.-H.; Chou, M.; Yang, H.-W.; Chang, Y.-S.; Chen, R.-S., Extremely high-performance visible light photodetector in the Sb_2SeTe_2 nanoflake. *Scientific Reports* **2017,** *7* (1), 45413.
6. Malik, A.; Vieira, M.; Fernandes, M., Surface-barrier Si-based photodetectors fabricated by the spray pyrolysis technique. *Philosophical Magazine B* **2000,** *80* (4), 781-790.
7. Ma, C.; Shi, Y.; Hu, W.; Chiu, M. H.; Liu, Z.; Bera, A.; Li, F.; Wang, H.; Li, L. J.; Wu, T., Heterostructured $WS_2/CH_3NH_3PbI_3$ photoconductors with suppressed dark current and enhanced photodetectivity. *Advanced Materials* **2016,** *28* (19), 3683-3689.
8. Echtermeyer, T.; Britnell, L.; Jasnos, P.; Lombardo, A.; Gorbachev, R.; Grigorenko, A.; Geim, A.; Ferrari, A. C.; Novoselov, K., Strong plasmonic enhancement of photovoltage in graphene. *Nature Communications* **2011,** *2* (1), 458.
9. Butler, S. Z.; Hollen, S. M.; Cao, L.; Cui, Y.; Gupta, J. A.; Gutiérrez, H. R.; Heinz, T. F.; Hong, S. S.; Huang, J.; Ismach, A. F., Progress, challenges, and opportunities in two-dimensional materials beyond graphene. *ACS nano* **2013,** *7* (4), 2898-2926.
10. Tsai, D.-S.; Lin, C.-A.; Lien, W.-C.; Chang, H.-C.; Wang, Y.-L.; He, J.-H., Ultra-high-responsivity broadband detection of Si metal–semiconductor–metal schottky photodetectors improved by ZnO nanorod arrays. *ACS nano* **2011,** *5* (10), 7748-7753.
11. Hu, X.; Zhang, X.; Liang, L.; Bao, J.; Li, S.; Yang, W.; Xie, Y., High-performance flexible broadband photodetector based on organolead halide perovskite. *Advanced Functional Materials* **2014,** *24* (46), 7373-7380.

12. Mueller, T.; Xia, F.; Avouris, P., Graphene photodetectors for high-speed optical communications. *Nature Photonics* **2010,** *4* (5), 297-301.
13. Mu, H.; Yu, W.; Yuan, J.; Lin, S.; Zhang, G., Interface and surface engineering of black phosphorus: a review for optoelectronic and photonic applications. *Materials Futures* **2022,** *1* (1), 012301.
14. Eda, G.; Yamaguchi, H.; Voiry, D.; Fujita, T.; Chen, M.; Chhowalla, M., Photoluminescence from chemically exfoliated MoS_2. *Nano Letters* **2011,** *11* (12), 5111-5116.
15. Montazeri, K.; Currie, M.; Verger, L.; Dianat, P.; Barsoum, M. W.; Nabet, B., Beyond gold: spin-coated Ti_3C_2-based MXene photodetectors. *Advanced Materials* **2019,** *31* (43), 1903271.
16. Deng, W.; Huang, H.; Jin, H.; Li, W.; Chu, X.; Xiong, D.; Yan, W.; Chun, F.; Xie, M.; Luo, C., All-sprayed-processable, large-area, and flexible perovskite/MXene-based photodetector arrays for photocommunication. *Advanced Optical Materials* **2019,** *7* (6), 1801521.
17. Zhang, X.; Shao, J.; Yan, C.; Wang, X.; Wang, Y.; Lu, Z.; Qin, R.; Huang, X.; Tian, J.; Zeng, L., High performance broadband self-driven photodetector based on MXene ($Ti_3C_2T_x$)/GaAs Schottky junction. *Materials & Design* **2021,** *207*, 109850.
18. Giannozzi, P.; Baroni, S.; Bonini, N.; Calandra, M.; Car, R.; Cavazzoni, C.; Ceresoli, D.; Chiarotti, G. L.; Cococcioni, M.; Dabo, I.; Dal Corso, A.; de Gironcoli, S.; Fabris, S.; Fratesi, G.; Gebauer, R.; Gerstmann, U.; Gougoussis, C.; Kokalj, A.; Lazzeri, M.; Martin-Samos, L.; Marzari, N.; Mauri, F.; Mazzarello, R.; Paolini, S.; Pasquarello, A.; Paulatto, L.; Sbraccia, C.; Scandolo, S.; Sclauzero, G.; Seitsonen, A. P.; Smogunov, A.; Umari, P.; Wentzcovitch, R. M., QUANTUM ESPRESSO: a modular and open-source software project for quantum simulations of materials. *Journal of Physics: Condensed Matter* **2009,** *21* (39), 395502.
19. Perdew, J. P.; Burke, K.; Ernzerhof, M., Generalized gradient approximation made simple. *Physical Review Letters* **1996,** *77* (18), 3865.
20. Moellmann, J.; Grimme, S., DFT-D3 study of some molecular crystals. *The Journal of Physical Chemistry C* **2014,** *118* (14), 7615-7621.
21. Monkhorst, H. J.; Pack, J. D., Special points for Brillouin-zone integrations. *Physical Review B* **1976,** *13* (12), 5188.
22. Momma, K.; Izumi, F., VESTA: a three-dimensional visualization system for electronic and structural analysis. *Journal of Applied Crystallography* **2008,** *41* (3), 653-658.
23. Wang, Y.; Chen, J.; Wang, P.; Chen, L.; Chen, Y.-B.; Wu, L.-M., Syntheses, growth mechanism, and optical properties of [001] growing Bi_2S_3 nanorods. *The Journal of Physical Chemistry C* **2009,** *113* (36), 16009-16014.
24. Lee, S.; Kim, E. H.; Yu, S.; Kim, H.; Park, C.; Lee, S. W.; Han, H.; Jin, W.; Lee, K.; Lee, C. E., Polymer-laminated $Ti_3C_2T_x$ MXene electrodes for transparent and flexible field-driven electronics. *ACS nano* **2021,** *15* (5), 8940-8952.
25. Li, J.; Li, Z.; Liu, X.; Li, C.; Zheng, Y.; Yeung, K. W. K.; Cui, Z.; Liang, Y.; Zhu, S.; Hu, W., Interfacial engineering of $Bi_2S_3/Ti_3C_2T_x$ MXene based on work function for rapid photo-excited bacteria-killing. *Nature Communications* **2021,** *12* (1), 1224.
26. Feng, A.; Hou, T.; Jia, Z.; Zhang, Y.; Zhang, F.; Wu, G., Preparation and characterization of epoxy resin filled with $Ti_3C_2T_x$ MXene nanosheets with excellent electric conductivity. *Nanomaterials* **2020,** *10* (1), 162.
27. Qu, C.; Li, H.; Zhou, S.; Li, G.; Wang, C.; Snyders, R.; Bittencourt, C.; Li, W., Bi_2S_3/rGO composite based electrochemical sensor for ascorbic acid detection. *Chemosensors* **2021,** *9* (8), 190.

28. Chen, L.; He, J.; Yuan, Q.; Zhang, Y.-W.; Wang, F.; Au, C.-T.; Yin, S.-F., CuS–Bi $_2S_3$ hierarchical architectures: controlled synthesis and enhanced visible-light photocatalytic performance for dye degradation. *RSC Advances* **2015,** *5* (43), 33747-33754.
29. Ghosh, K.; Ghosh, J.; Giri, P., Accordion-like Multilayered Two-Dimensional Ti_3C_2T x MXenes for Catalytic Elimination of Organic Dyes from Wastewater via the Fenton Reaction. *ACS applied nano materials* **2022,** *5* (11), 16451-16461.
30. Park, G. S.; Ho, D. H.; Lyu, B.; Jeon, S.; Ryu, D. Y.; Kim, D. W.; Lee, N.; Kim, S.; Song, Y. J.; Jo, S. B., Comb-type polymer-hybridized MXene nanosheets dispersible in arbitrary polar, nonpolar, and ionic solvents. *Science Advances* **2022,** *8* (13), eabl5299.
31. Naguib, M.; Gogotsi, Y., Synthesis of two-dimensional materials by selective extraction. *Accounts of chemical research* **2015,** *48* (1), 128-135.
32. Satheeshkumar, E.; Makaryan, T.; Melikyan, A.; Minassian, H.; Gogotsi, Y.; Yoshimura, M., One-step solution processing of Ag, Au and Pd@ MXene hybrids for SERS. *Scientific Reports* **2016,** *6* (1), 32049.
33. Chitara, B.; Kolli, B. S. C.; Yan, F., Near-Infrared photodetectors based on 2D Bi_2S_3. *Chemical Physics Letters* **2022,** *804*, 139876.
34. Rong, P.; Gao, S.; Ren, S.; Lu, H.; Yan, J.; Li, L.; Zhang, M.; Han, Y.; Jiao, S.; Wang, J., Large-Area Freestanding Bi_2S_3 Nanofibrous Membranes for Fast Photoresponse Flexible IR Imaging Photodetector. *Advanced Functional Materials* **2023,** *33* (24), 2300159.
35. Lu, C.; Luo, M.; Dong, W.; Ge, Y.; Han, T.; Liu, Y.; Xue, X.; Ma, N.; Huang, Y.; Zhou, Y.; Xu, X., Bi_2Te_3/Bi_2Se_3/Bi_2S_3 Cascade Heterostructure for Fast-Response and High-Photoresponsivity Photodetector and High-Efficiency Water Splitting with a Small Bias Voltage. *Advanced Science* **2023,** *10* (6), 2205460.
36. Yang, W.; Yang, J.; Zhao, K.; Gao, Q.; Liu, L.; Zhou, Z.; Hou, S.; Wang, X.; Shen, G.; Pang, X.; Xu, Q.; Wei, Z., Low-Noise Dual-Band Polarimetric Image Sensor Based on 1D Bi2S3 Nanowire. *Advanced Science* **2021,** *8* (14), 2100075.
37. Kong, D.; Lin, T.; Chai, J.; Zhu, Z.; Liu, P.; Lin, Z.; Lin, T.; Li, L.; Chen, L.; Li, G.; Wang, W., A self-powered MXene/InGaN van der Waals heterojunction mini-photodetector for visible light communication. *Applied Physics Letters* **2023,** *122* (14).
38. Polumati, G.; Adepu, V.; Kolli, C. S. R.; Reji, J.; Sahatiya, P., Band alignment study of 2D-2D heterointerface of $MoSe_2$ with $Ti_3C_2T_x$ (transport layer) for flexible broadband photodetection. *Materials Science in Semiconductor Processing* **2023,** *153*, 107161.
39. Selamneni, V.; Adepu, V.; Raghavan, H.; Sahatiya, P., Ultra-High Responsivity and Enhanced Trap Assisted Charge Transfer by utilizing $Ti_3C_2T_x$(MXene) as a Transport Layer for ReS_2 based Flexible Broadband Photodetector: A better Alternative to Graphene. *FlatChem* **2022,** *33*, 100363.
40. Zhu, J.; Wang, H.; Ma, L.; Zou, G., Observation of ambipolar photoresponse from 2D MoS_2/MXene heterostructure. *Nano Research* **2021,** *14* (10), 3416-3422.
41. Xiong, D.; Deng, W.; Tian, G.; Zhang, B.; Zhong, S.; Xie, Y.; Yang, T.; Zhao, H.; Yang, W., Controllable in-situ-oxidization of 3D-networked $Ti_3C_2T_x$-TiO_2 photodetectors for large-area flexible optical imaging. *Nano Energy* **2022,** *93*, 106889.
42. Deng, W.; Huang, H.; Jin, H.; Li, W.; Chu, X.; Xiong, D.; Yan, W.; Chun, F.; Xie, M.; Luo, C.; Jin, L.; Liu, C.; Zhang, H.; Deng, W.; Yang, W., All-Sprayed-Processable, Large-Area, and Flexible Perovskite/MXene-Based Photodetector Arrays for Photocommunication. *Advanced Optical Materials* **2019,** *7* (6), 1801521.
43. Adepu, V.; Kunchur, A.; Kolli, C. S. R.; Siddhartha, S.; Mattela, V.; Sahatiya, P., High-Performance Visible Light Photodetector Based on 1D SnO_2 Nanofibers with a $Ti_3C_2T_x$ (MXene) Electron Transport Layer. *ACS Applied Nano Materials* **2022,** *5* (5), 6852-6863.

44. Song, W.; Liang, Z.; Guo, Y.; Luo, X.; He, X.; Liu, Q.; Sun, Y.; Li, S., 2D Ti_3C_2 nanoflakes anchored ZnO photodetector with substantially improved deep-ultraviolet photoresponse and on/off ratio. *Journal of Alloys and Compounds* **2022,** *909*, 164816.

Chapter 7

Summary and Outlooks

This chapter provides a comprehensive summary of this thesis's key contributions, emphasizing novel findings related to the functionalization of two-dimensional (2D) $Ti_3C_2T_x$ nanostructures and their composite with earth-abundant semiconductor Bi_2S_3 and noble metal Ru**.** This study explores their applications in catalytic wastewater treatment, photoelectrochemical hydrogen production, and broadband photodetection. Additionally, potential directions for future research are discussed in the concluding section.

7.1. Summary and Highlights of the Thesis Contribution

We have conducted a systematic investigation into the modulation of surface defect states in $Ti_3C_2T_x$ MXenes to evaluate their catalytic performance in the degradation of various organic pollutants, including the antibiotic ciprofloxacin (CIP), organic dyes, and 4-nitrophenol (4-NP) from wastewater. The optimization of chemical etching parameters, particularly hydrofluoric acid (HF) concentration, was carried out to achieve an accordion-like microstructure of $Ti_3C_2T_x$ with a well-balanced combination of low valent Ti states (Ti^{3+}) or oxygen vacancy (OVs)-rich surface defect states and their crystallinity. Furthermore, the catalytic activity of the accordion-like $Ti_3C_2T_x$ was explored in the degradation of organic pollutants as a Fenton catalyst (Chapter 2). The beneficial impact of phosphorus doping in $Ti_3C_2T_x$ MXene nanosheets has been investigated, particularly in reducing multilayer restacking, modulating surface oxygen vacancy (OV) states, and facilitating the formation of a porous aerogel structure. These modifications contribute significantly to enhancing the degradation efficiency of organic pollutants through advanced oxidation processes (Chapter 3). Formation of suitable composite material by integrating two-dimensional (2D) $Ti_3C_2T_x$ MXene nanosheets with one-dimensional (1D) Bi_2S_3 nanorods to enhance interfacial charge transfer and improve light absorption for effective catalytic reduction of organic pollutants and photoelectrochemical hydrogen production (Chapter 4). Ultrasmall Ru nanoclusters (NCs) anchored onto an oxygen vacancy (OV)-rich, nitrogen-doped $Ti_3C_2T_x$ MXene nanoribbon support facilitate strong electron-metal support interactions, enhanced light absorption, and an improved photothermal effect. These synergistic effects collectively contribute to the enhancement of photoelectrochemical hydrogen production in an alkaline medium, as discussed in Chapter 5.

Finally, the role of $Ti_3C_2T_x$ MXene nanosheets as a robust metallic support has been investigated, along with the formation of a local Schottky junction with cost-effective Bi_2S_3 nanorods. This integration enhances broadband light absorption, minimizes photogenerated charge carrier recombination, and facilitates efficient separation and transport of charge carriers, thereby improving the broadband photodetection performance (Chapter 6).

The significant contribution of the thesis is listed below.

A. Surface Defect Engineered Multi-layered $Ti_3C_2T_x$ MXenes as Advanced Fenton Catalyst for Organic Pollutant Degradation

We demonstrate a simple and effective approach to modulate the low valent Ti states (Ti^{3+}) or OVs states in multi-layered $Ti_3C_2T_x$ (m-$Ti_3C_2T_x$) by modulating the HF concentration. The catalytic performance of the m-$Ti_3C_2T_x$ as a Fenton catalyst was subsequently investigated for the degradation of organic dyes, with methylene blue (MB) exhibiting the highest degradation efficiency. The influence of various parameters on MB degradation was systematically investigated. Under optimized conditions, complete degradation (100%) of MB was achieved within 24 min using only a minimal amount of H_2O_2 as an oxidant. Interestingly, m-$Ti_3C_2T_x$ demonstrates enhanced degradation efficiency under both acidic and basic pH conditions compared to conventional Fenton catalysts that are primarily effective in acidic media (pH ~ 3). This unique characteristic, coupled with good reusability, highlights its potential advantages. Furthermore, the negatively charged surface of m-$Ti_3C_2T_x$ facilitates selective degradation of cationic dyes (MB and RhB) over anionic dyes (MO), promoting favourable electrostatic interactions. These observations underscore the potential of m-$Ti_3C_2T_x$ MXenes as highly effective Fenton catalysts for wastewater treatment applications. *This work has been published in ACS Appl. Nano Mater. 2022, 5(11), 16451-16461.*

B. Phosphorous-doped Ti_3C_2Tx MXene/Carbon Foam Hybrid Aerogel for the Degradation of Organic Pollutants Through Advanced Oxidation Process

In this study, we presented an innovative and effective strategy to reduce multilayer restacking in $Ti_3C_2T_x$ MXene nanosheets through phosphorus doping while simultaneously constructing a hierarchical three-dimensional (3D) porous aerogel by grafting the doped nanosheets onto a PVA-coated flexible melamine sponge. This porous aerogel serves as an efficient alternative to powder-based $Ti_3C_2T_x$ nanosheets, which are prone to being washed away during multiple cycles and exhibit poor reusability. The phosphorous doping in $Ti_3C_2T_x$ nanosheets effectively

reduces restacking, enhancing the active surface area for catalytic reactions and improving surface oxygen vacancy states, which act as active sites for the degradation of organic pollutants via advanced oxidation processes (AOPs). Under optimized conditions, with minimal peroxymonosulfate (PMS) addition, the degradation efficiencies of Ciprofloxacin (CIP) and methylene blue (MB) reached 96% and 98% within 21 and 12 min, respectively. Interestingly, the porous aerogel catalyst exhibited outstanding performance over a wide pH range (3-7) for CIP degradation, offering a significant advantage over conventional Fenton catalysts in practical applications. Furthermore, density functional theory (DFT) calculations provided deeper insights into the role of phosphorus doping in enhancing the degradation efficiency. In the case of organic dyes, cationic dyes were degraded more effectively than anionic dyes, attributed to the negatively charged surface of the aerogel and stronger electrostatic interactions with cationic dye molecules. Thus, the hybrid aerogel highlights its potential for environmental remediation applications, making it a promising candidate for addressing wastewater treatment challenges. *This work has been published in Carbon* 238, 120258 (2025).

C. $Bi_2S_3/Ti_3C_2T_x$ Nanocomposite for Efficient Reduction of Organic Pollutants and Photo-Electrochemical Hydrogen Production

Here, we investigated the interfacial charge transfer dynamics in 1D Bi_2S_3 and 2D $Ti_3C_2T_x$-based composite material. Generally, Bi_2S_3 nanorods pose severe agglomeration in hydrothermal synthesis, but the surface groups (-F, -OH, and -O) of $Ti_3C_2T_x$ act as nucleation centers and enable the well dispersion of Bi_2S_3 nanorods on its surface. Interestingly, fewer Bi^{3+} are reduced to metallic Bi nanoparticles, attributed to the self-reduction capability of $Ti_3C_2T_x$ MXene, which is also supported by DFT calculation. The excellent catalytic reduction capability of organic pollutants 4-nitrophenol (4-NP), Methylene blue (MB), Methyl orange (MO), and Rhodamine B (RhB) by the composite was characterized in the presence of $NaBH_4$, which demonstrates an outstanding reduction rate (up to 1.1 min^{-1}) of 4-NP with long cyclic stability. The reduction mechanism and effective charge transfer were further supported by DFT analysis. Additionally, it demonstrates excellent photo-electrochemical HER performance under both dark and light illumination, with an overpotential of 87 and 73 mV, along with a Tafel slope of 113 and 84 mV/dec, respectively, attributed to the formation of a local Schottky junction, reduced radiative recombination and efficient separation of photogenerated charge carriers, further supported by DFT analysis. Therefore, the noble-metal-free $Bi_2S_3/Ti_3C_2T_x$

nanocomposite shows great promise for reducing organic pollutants and facilitating photoelectrochemical hydrogen production. *This work has been published in ACS Appl. Mater. Interfaces 2024, 16, 32, 42007-42020.*

D. Synergistic Effect of Ru Nanoclusters on N-Doped $Ti_3C_2T_x$ Nanoribbons for High-Performance Photoelectrochemical Water Splitting

In this study, we synthesized an ultrasmall Ru nanocluster (NC)-anchored hierarchical N-doped $Ti_3C_2T_x$ (Ru@N-$Ti_3C_2T_x$) MXene nanoribbon (MXNR) composite. The high aspect ratio and oxygen vacancy (OV) defects in partially oxidized MXNRs provide abundant active sites, preventing Ru NC aggregation and enabling strong electron-metal support interactions. The in-situ formation of TiO_2 nanoparticles (TiO_2 NPs) and OV defects during 1D structuring and N doping enhances visible light absorption, improving photocatalytic efficiency. Electrochemical studies demonstrate the exceptional hydrogen evolution reaction (HER) performance of 5% Ru@N-MXNR under both dark and illuminated conditions, with low overpotentials of 22 mV and 12 mV and Tafel slopes of 50 mV/dec and 34 mV/dec, respectively. These values surpass the performance of the commercial 20% Pt/C catalyst, which exhibits an overpotential of ~23 mV and a Tafel slope of 42 mV/dec. The superior activity of 5% Ru@N-MXNR is attributed to the synergistic effects of Ru NCs' efficient water dissociation and strong electronic metal-support interactions, facilitating rapid desorption of hydrogen intermediates (H*). Furthermore, under Vis-NIR illumination, enhanced charge carrier generation and photothermal effects improve electron mobility, further boosting HER efficiency. Additionally, these catalysts offer prolonged operational stability by maintaining a consistent current density, which is beneficial for stable hydrogen production. This study highlights the development of a MXene -based cost-effective, high-performance photocatalyst as a viable alternative to commercial Pt/C.

E. High-Performance $Bi_2S_3/Ti_3C_2T_x$ MXenes-Based Schottky Junction Photodetector for Broadband Photodetection

Here, we investigate the role of $Ti_3C_2T_x$ MXene nanosheets as a robust metallic support in enhancing the optoelectronic device performance of $Ti_3C_2T_x$-based composites. In this context, the $Bi_2S_3/Ti_3C_2T_x$ composite material has been utilized, considering its low cost, exceptional light absorption properties, and efficient photogenerated charge separation capabilities. The fabricated low-cost $Bi_2S_3/Ti_3C_2T_x$-based Schottky junction photodetector (PD) exhibits outstanding broadband responsivity, covering a spectral range from ultraviolet to near-infrared

(300-1550 nm). The device achieves peak responsivity values of 36.7 A/W at 300 nm and 26.2 A/W at 780 nm. Additionally, it demonstrates a high external quantum efficiency of ~ 3.9 × 10^3% and a rapid response time of ~300 μs under an applied bias of 3 V, highlighting its remarkable performance. Moreover, the fabricated PD exhibits excellent long-term stability under ambient conditions. The formation of the Schottky junction was verified by ultraviolet photoelectron spectroscopy and supported by DFT calculations. The electronic band structure and electronic density of states were investigated to justify the excellent photodetection performance of the composite material. This study provides valuable insights into the superior charge transport properties and ultra-broadband photodetection capabilities of $Ti_3C_2T_x$ MXene-based composites, underscoring their potential for high-performance optoelectronic applications. *This work has been published in Carbon, 216 (2024) 118515.*

7.2. Scope of Future Work

This thesis focused on enhancing the catalytic activity of pristine $Ti_3C_2T_x$ through various approaches, including the optimization of surface defect states via controlled synthesis parameters, doping, composite formation, and 1D nanostructuring, followed by functionalization. Furthermore, $Ti_3C_2T_x$-based composites have been investigated for broadband photodetection applications. The findings of this research provide a foundation for further advancements in multiple directions, as discussed below.

1. In Chapters 2 and 3, it is observed that pollutant degradation through advanced oxidation processes leads to the partial oxidation of $Ti_3C_2T_x$, resulting in the formation of TiO_2. While this transformation adversely affects its catalytic activity, TiO_2 itself is a well-established photocatalyst. By strategically modifying the surface, particularly by tuning the oxygen vacancy states and optimizing the TiO_2 content, the material can be repurposed as a photo-Fenton catalyst for long-term applications. This approach opens new avenues for further research in this domain.

2. In catalytic advanced oxidation processes, the oxidation of $Ti_3C_2T_x$ within an aerogel-like architecture can degrade its performance. To overcome this issue, a co-catalyst layer can be introduced to shield the $Ti_3C_2T_x$ nanosheets, ensuring enhanced interfacial charge transport. This strategy not only preserves the structural integrity of the

nanosheets but also improves their long-term cyclic stability, making it a promising direction for further investigation.

3. This thesis primarily focuses on the degradation of organic pollutants for wastewater treatment. However, pollutant adsorption by catalysts is also an important area of research in this field. $Ti_3C_2T_x$ MXene nanosheets exhibit the ability to adsorb various cationic pollutants due to their negatively charged surface functional groups. However, van der Waals restacking reduces their accessible surface area, thereby limiting their adsorption efficiency. In contrast, $Ti_3C_2T_x$ MXene nanoribbons offer a significantly higher surface area and feature defective edges, which serve as beneficial active sites for enhanced adsorption. Therefore, investigating the adsorption behaviour of MXene nanoribbons can provide insights into their superior performance, while studying their adsorption kinetics and modelling may further elucidate the underlying mechanisms.

4. The partially oxidized $Ti_3C_2T_x$ MXenes obtained after the catalytic reaction can be reused as photodetector materials for UV light detection. The in-situ formation of TiO_2 facilitates UV light absorption while promoting efficient charge separation due to the synergistic interaction between $Ti_3C_2T_x$ MXene and TiO_2. Which can also be considered for further exploration.

5. The fabrication and optimization of planar asymmetric junction photodetectors utilizing $Ti_3C_2T_x$ MXene nanosheets in combination with suitable metals such as Al, Ag, or Au, along with transition metal dichalcogenides (TMDs) like $MoSe_2$, WS_2, and WSe_2, can be promising for enhancing device performance. The incorporation of an asymmetric heterojunction structure can facilitate efficient charge separation, thereby improving the overall functionality of the photodetector. Further studies in this direction may provide valuable insights into optimizing the device's efficiency.

6. The formation of a Schottky junction with a suitable hydrogen evolution reaction (HER) catalyst, such as $Ni(OH)_2$, can be explored to evaluate its photoelectrochemical HER performance. This performance is expected to be enhanced by minimizing agglomeration, improving light absorption, and facilitating the efficient separation of photogenerated charge carriers. Further investigations in this area may provide valuable insights into optimizing the catalytic efficiency of the system.

Appendix 1

List of Publications

a. In peer-reviewed journals:

Thesis relevant publications:

1. Koushik Ghosh, Joydip Ghosh, P. K. Giri, Accordion-like Multilayered Two-Dimensional $Ti_3C_2T_x$ MXenes for Catalytic Elimination of Organic Dyes from Wastewater *via* the Fenton Reaction, ACS Appl. Nano Mater. 5, 16451–16461 (2022).

2. Koushik Ghosh, P. K. Giri, Experimental and theoretical study on the role of 2D $Ti_3C_2T_x$ MXenes on superior charge transport and ultra-broadband photodetection in MXene/Bi_2S_3 nanorod composite through local Schottky junctions, Carbon, 216, 118515 (2024).

3. Koushik Ghosh, Sanjoy Sur Roy, P. K. Giri, Fast Reduction of 4-Nitrophenol and Photoelectrochemical Hydrogen Production by Self-Reduced Bi/$Ti_3C_2T_x$/Bi_2S_3 Nanocomposite: A Combined Experimental and Theoretical Study, ACS Appl. Mater. Interfaces, 16, 42007–42020 (2024).

4. Koushik Ghosh, Sanjoy Sur Roy, Sirsendu Ghosal, Debabrata Shau, P. K. Giri, Phosphorous Doped $Ti_3C_2T_x$ MXene/Carbon Foam Hybrid Aerogel as a Versatile Platform for Industrial Waste Treatment, Strain Sensing and Oil-Water Separation *Carbon*, 238, 120258 (2025).

5. Koushik Ghosh, Sanjoy Sur Roy, P. K. Giri, Ru Nanocluster Anchored Vacancy-Engineered Nitrogen Doped $Ti_3C_2T_x$ MXene Nanoribbons for Photothermal-Driven Efficient Hydrogen Generation and Solar Water Evaporation (**Under review**).

Other publications

1. Dilip K. Singh, Rakesh K. Prasad, Koushik Ghosh, P. K. Giri, Dai-Sik Kim, High-Efficiency Photodetector Based on a CVD-Grown WS_2 Monolayer, *ACS Appl. Electron. Mater*. 5, 3634−3640 (2023).

2. Subhankar Debnath, Koushik Ghosh, M Meyyappan, P. K. Giri, A fully printed ultrafast Si/WS_2 quantum dot photodetector with very high responsivity over the UV to near-infrared region, *Nanoscale*, 15, 13809-13821 (2023).

3. Sanjoy Sur Roy, Koushik Ghosh, M Meyyappan, P. K. Giri, MXene-PEDOT: PSS Nanocomposite-Based Electromagnetic Interference Shields with Ultrahigh Absolute Shielding Effectiveness, *ACS Appl. Nano Mater*, 6, 23357-23369 (2023).

4. Sanju Nandi, Koushik Ghosh, M Meyyappan, P. K. Giri, 2D MXene Electrode-Enabled High-Performance Broadband Photodetector Based on a CVD-Grown 2D Bi2Se3 Ultrathin Film on Silicon, *ACS Appl. Electron. Mater.* 5, 6985-6995 (2023).

5. Shipra Aswal, Koushik Ghosh, P. K. Giri, Borophene Quantum Dots with Strong Photoluminescence for Selective Metal Ion Sensing, *ACS Appl. Nano Mater.* 7, 11634-11644 (2024).

6. Sanjoy Sur Roy, Koushik Ghosh, M Meyyappan, P. K. Giri, High green index electromagnetic interference shields with semiconducting Bi_2S3 fillers in a PEDOT: PSS matrix, *Mater. Horiz*, 11, 3695-3705 (2024).

7. Joydip Ghosh, Naveen Kumar Tailor, Koushik Ghosh, Jayana Jayarathne, Shivani Choudhary, Carol Crean, P. K. Giri, Soumitra Satapathi, and Paul Sellin, $Cs_2AgBiBr_6$ double perovskite single crystal/$CsPbBr_3$ perovskite nanocrystals heterojunction for high-performance X-ray detection. *Adv. Opt. Mater.*, 2025, 13(5), 2402497.

8. Sanjoy Sur Roy, Koushik Ghosh, M Meyyappan, P. K. Giri, MXene Nanoribbon Aerogel-based Gradient Conductivity Electromagnetic Interference Shields with Unprecedented Combination of High Green Index and Shielding Effectiveness. *Small* 2025, 2500003.

9. Koushik Ghosh, Sanjoy Sur Roy, P. K. Giri. (2025). Phosphorus-doped $Ti_3C_2T_x$ MXene/PEDOT: PSS aerogel-based electromagnetic interference shields with unique combination of high green index and shielding effectiveness. *Mater. Today Adv.*, *26*, 100576.

10. Debabrata Sahu, Sanjoy Sur Roy, Koushik Ghosh, P. K. Giri. (2025). Asymmetric Contact Enabled Self-Powered Flexible Photodetector on Formamidinium-Based Perovskite with 2D MXene Electrode. *J. Mater. Chem. C.* 2025, 13, 9317-9331.

11. Sanjoy Sur Roy, Koushik Ghosh, M Meyyappan, P. K. Giri, MXene Nanoribbon-PEDOT: PSS Aerogel-Based Piezoresistive Sensors for Human Motion Detection and Thermal Insulation. *ACS Appl. Nano Mater*, 2025, 8, 14, 7164-7174.

12. Subhajit Roy Chowdhury, Suman Santra, Koushik Ghosh, Sudipta Chakrabarty, Jyoti Mandal, P. K. Giri, Syed Minhaz Hossain, Visible Electroluminescence from nanostructured Silicon based Schottky junction LED: Role of metal contacts. *J. Lumin.* 282, 121249 (2025).

b. Patent Granted:

1. "AN ELECTROMAGNETIC INTERFERENCE SHIELDING FILM WITH HIGH GREEN INDEX", Patent No: 564492, Application No: 202431004374 (Date of Filing: 22.01.2024).

c. Conferences attended:

1. International Conference on Light-Matter Interaction (**ICLMIN-2021**), organized by Indira Gandhi Centre for Atomic Research (IGCAR), Kalpakkam, India during May 19-21, 2021.

2. 33rd AGM of MRSI and 4th Indian Material Conclave; **IUMRS-ICA,** organized by IIT Jodhpur, Rajasthan, India from 19-23rd Dec 2022. (Poster presentation)

3. Advanced materials for better tomorrow (**AMBT 2023**), organized by Banaras Hindu University (BHU), Varanasi, India from 10-13th Oct 2023. (Poster presentation)